UNIVERSITAT POLITÈCNICA
DE CATALUNYA
BARCELONATECH

Hyperspectral imaging system for the fast recording of the ocular fundus

Tommaso Alterini

ADVERTIMENT La consulta d'aquesta tesi queda condicionada a l'acceptació de les següents condicions d'ús: La difusió d'aquesta tesi per mitjà del repositori institucional UPCommons (http://upcommons.upc.edu/tesis) i el repositori cooperatiu TDX (http://www.tdx.cat/) ha estat autoritzada pels titulars dels drets de propietat intel·lectual **únicament per a usos privats** emmarcats en activitats d'investigació i docència. No s'autoritza la seva reproducció amb finalitats de lucre ni la seva difusió i posada a disposició des d'un lloc aliè al servei UPCommons o TDX. No s'autoritza la presentació del seu contingut en una finestra o marc aliè a UPCommons (*framing*). Aquesta reserva de drets afecta tant al resum de presentació de la tesi com als seus continguts. En la utilització o cita de parts de la tesi és obligat indicar el nom de la persona autora.

ADVERTENCIA La consulta de esta tesis queda condicionada a la aceptación de las siguientes condiciones de uso: La difusión de esta tesis por medio del repositorio institucional UPCommons (http://upcommons.upc.edu/tesis) y el repositorio cooperativo TDR (http://www.tdx.cat/?locale-attribute=es) ha sido autorizada por los titulares de los derechos de propiedad intelectual **únicamente para usos privados enmarcados** en actividades de investigación y docencia. No se autoriza su reproducción con finalidades de lucro ni su difusión y puesta a disposición desde un sitio ajeno al servicio UPCommons No se autoriza la presentación de su contenido en una ventana o marco ajeno a UPCommons (*framing*). Esta reserva de derechos afecta tanto al resumen de presentación de la tesis como a sus contenidos. En la utilización o cita de partes de la tesis es obligado indicar el nombre de la persona autora.

WARNING On having consulted this thesis you're accepting the following use conditions: Spreading this thesis by the institutional repository UPCommons (http://upcommons.upc.edu/tesis) and the cooperative repository TDX (http://www.tdx.cat/?locale- attribute=en) has been authorized by the titular of the intellectual property rights **only for private uses** placed in investigation and teaching activities. Reproduction with lucrative aims is not authorized neither its spreading nor availability from a site foreign to the UPCommons service. Introducing its content in a window or frame foreign to the UPCommons service is not authorized (framing). These rights affect to the presentation summary of the thesis as well as to its contents. In the using or citation of parts of the thesis it's obliged to indicate the name of the author.

DOCTORAL THESIS

FOR OBTAINING THE DOCTORAL DEGREE

IN THE FIELD OF OPTICAL ENGINEERING FROM THE

UNIVERSITAT POLITÈCNICA DE CATALUNYA

UPC-BARCELONATECH

DEPARTMENT OF OPTICS AND OPTOMETRY

HYPERSPECTRAL IMAGING SYSTEM FOR THE FAST RECORDING OF THE OCULAR FUNDUS

Author:

TOMMASO ALTERINI

Thesis Directors:

PROF. DR. MERITXELL VILASECA RICART

DR. FERNANDO DÍAZ DOUTÓN

Terrassa, February 2021

“Feina de formiga, força d’elefant”

Lema dels Castellers de Sants

“Antlike work, elephant’s strength”

Sants Castellers Motto

Assessment results for the doctoral thesis

Academic year:

Full name

____

Doctoral programme

____

Structural unit in charge of the programme

____

Decision of the committee[i]

In a meeting with the examination committee convened for this purpose, the doctoral candidate presented the topic of his/her doctoral thesis entitled________________________
____.
Once the candidate had defended the thesis and answered the questions put to him/her, the examiners decided to award a mark of:

☐ FAIL ☐ PASS ☐ GOOD ☐ EXCELLENT

(Full name and signature)	(Full name and signature)

(Full name and signature) Member	(Full name and signature) Member	(Full name and signature) Member

_______________, _______________________________________

The votes of the members of the examination committee were counted by the Standing Committee of the Doctoral School, and the result is to award the CUM LAUDE DISTINCTION:

☐ YES ☐ NO

(Full name and signature)	(Full name and signature)

Barcelona, _______________________________________

International doctorate mention

As the secretary of the examination committee, I hereby state that the thesis was partly (at least the summary and conclusions) written and presented in a one of the languages commonly used in scientific communication in the relevant field of knowledge, which must not be an official language of Spain. This rule does not apply to stays, reports and experts from a Spanish-speaking country.

(Full name and signature)

Supervisor’s Certificate

Dr. Meritxell Vilaseca Ricart, full professor at the Universitat Politècnica de Catalunya (UPC), and Dr. Fernando Díaz Doutón, researcher at the Universitat Politècnica de Catalunya (UPC)

CERTIFY

that the work reported in the thesis entitled

HYPERSPECTRAL IMAGING SYSTEM FOR THE FAST RECORDING OF THE OCULAR FUNDUS

which is submitted by Tommaso Alterini in fulfilment of the requirements for the degree of Doctor by the Universitat Politècnica de Catalunya (UPC) has been carried out under our supervision within the framework of the PhD program in Optical Engineering.

Meritxell Vilaseca Ricart	Fernando Díaz Doutón

Table of Contents

List of Figures

List of Tables

ABSTRACT

Vision loss affects physical, psychological, and emotional wellbeing and social life as well. High life expectancy and health policies are translated into an aging population worldwide, which has higher risk of eye's disorders and diseases. Therefore, new systems able to contribute at non-invasive objective diagnosis of ocular diseases are demanded. In this context, optical imaging techniques have a primary role as they allow obtaining information from almost any part of the eye. In particular, many important eye and systemic diseases early manifest themselves in the retina and, since the pioneer study of Helmholtz, many resources have been spent to acquire good images of the ocular fundus. In common clinics, fundus photography is restricted to color imaging sensors with only three spectral bands, and, due to metamerism, many structures might remain hidden. Recently, hyperspectral imaging techniques have come to view as a promising and powerful tool for the spectral analysis of several retinal diseases, increasing the amount of information extractable from fundus photography. However, in the literature, examples are restricted to the visible range of the electromagnetic spectrum, have few bands and/or make use of modified commercial fundus cameras. Accordingly, the goal of this project is to build a novel hyperspectral fundus camera based on light-emitting diodes allowing the fast imaging of the retina both in the visible and in the near infrared region of the spectrum, which has never been explored, through a considerable number of spectral bands. This fundus camera has been designed, tested and developed with new custom-made illumination and detection strategies combined with novel cutting-edge technology at the Center for Sensors, Instruments and Systems Development (CD6) of the Universitat Politècnica de Catalunya (UPC, Terrassa). Finally, after a scrupulous clinical study carried out at the Instituto de Microcirugía Ocular (IMO, Barcelona) and at the University Vision Center of UPC (CUV-UPC, Terrassa), qualitative and quantitative results are presented for healthy and diseased eyes. The available spectroscopic information and the visualization of retinal structures and lesions, especially those affecting the choroidal vasculature and retinal pigment epithelium that are hardly visible in conventional color fundus images, underline the clinical potential of this system as a new tool for ophthalmic diagnosis.

Keywords: hyperspectral imaging, fundus camera, retina, ocular fundus.

1 INTRODUCTION

In common day living, the eye is one of the most important and definitely necessary organs to have a good quality of life. In the modern world, the longer life expectancy brings the emergence of new diseases that affect this organ in different manners. Accordingly, in research and industry, attention has been drawn to the investigation and management of medical diagnostic tools and several techniques have been developed to fulfill the clinical demand [1].

The eye is a complex biological system of our body. As shown in Figure 1.1, it consists of several specialized structures involved in the formation of images on the retina. It is also responsible of the transformation of light into a nerve signal that the optic nerve transports to the brain, allowing us to have the final perception of the scene.

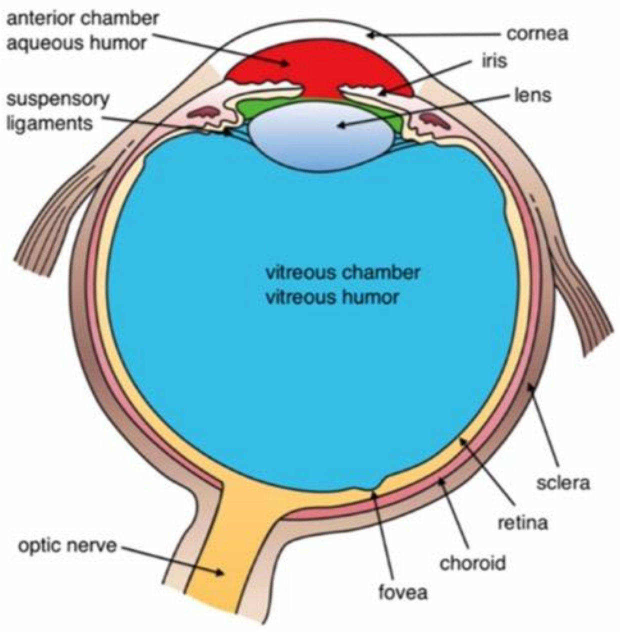

Figure 1.1: Principal structures of the eye.

Firstly, the collected photons coming from the external objects strike on the cornea and enter the anterior segment of the eye. This segment consists of several structures with different refractive indexes which are, besides the cornea, the aqueous humor, iris and crystalline lens. The posterior segment, located behind the lens, begins with the vitreous humor, a jelly-like liquid that completely fills the ocular globe, and ends with a multi-layered structure, within which there are the retina, the choroid and the sclera.

The aforementioned structures, essentially the cornea and the lens, are responsible for the formation of the image on the retina while the iris acts as a natural diaphragm to control the light entering the eye. The retina acts as a converter of the information in form of photons to electric signals readable by the brain, by means of very specialized cells called cones and rods. This process is known as phototransduction. Cones and rods are irregularly distributed on the retinal mosaic. The cones, more densely arranged in the central region of the retina called fovea, are able to discern among colors, thanks to their differentiated spectral sensitivity in three main zones of the VISible spectrum (spectral range between 400 nm and 700 nm approximately, in this work indicated as VIS). These cells play a central role in the so-called photopic vision, and require certain light level to work properly. When the light level is not sufficient to activate the cones (scotopic vision conditions), the rods are the cells involved in the visual process. The distribution of rods is quasi-complementary to that of cones and they are spread in the peripheral zones of the retina with the minimum of concentration in the fovea. Rods provide a unique response throughout the whole VIS, so they cannot be used to distinguish colors. Cones and rods have synaptic terminals connected to other neurons, essentially bipolar and ganglion cells, which in turn form a bundle of nerves that emerge out of the eyeball through the optic disk (located 15° nasally relative to the fovea) and transport the transformed nerve signal to the part of the brain called visual cortex.

A series of veins and arteries in the retina and a strong vasculature in the choroid, located between the retina and the sclera, provide nutrients and necessary substances for retinal cells maintenance. The choroid plays an important role in the sustaining and regulation of the eye pressure, which must be kept constant. On the other hand, the sclera, frequently referred as the white of the eye, is the most rigid eye layer and covers the entire eye globe. This part serves as a support and provides protection to mechanical stresses.

From the former description it is easy to understand that, for a non-invasive investigation and study of both the dynamics and structures of the eye, optical and photonic tools allowing the fast recording of images of the retina might be very helpful. In fact, several optical techniques have been developed to study the eye. Ophthalmoscopes were the first instruments used to examine the ocular media, mainly the fundus of the eye, by means of a white light illumination and a viewing system with a magnifying glass to compensate for the observer's and patient's refraction. Later on, fundus cameras – also known as retinographs - were developed and are widely used nowadays by ophthalmologists in their daily clinical practice for the early diagnosis of retinal diseases. Fundus cameras allowing for ocular fundus color photography (Figure 1.2 a) are also currently commercially available, which provide a picture of the main important structures of the retina. Nevertheless, they have spectral information limited to three spectral zones (red, green and blue), similarly to the visual encoding process in the human eye.

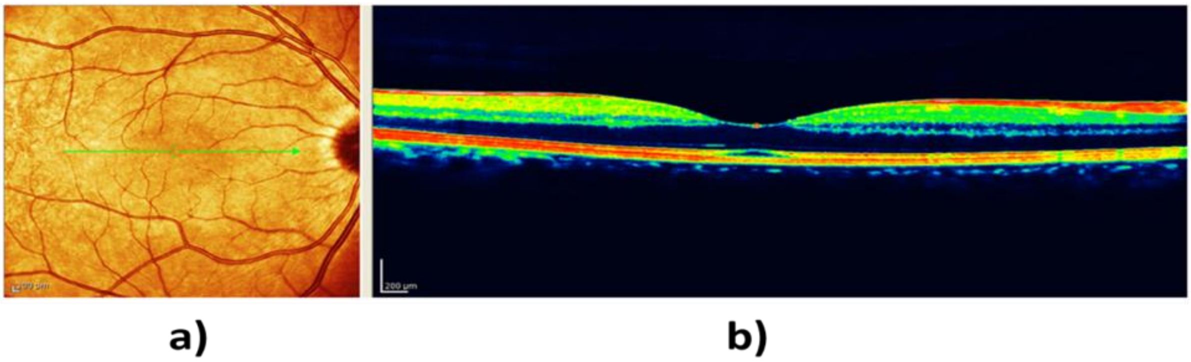

Figure 1.2: a) Common color fundus image, centered at the fovea. b) OCT image of the retinal section underlined by the green arrow in the fundus image a), adapted from [2].

In the last 20 years, thanks to the development of Optical Coherence Tomography (OCT) (Figure 1.2 b) and confocal Scanning Laser Ophthalmoscopy (cSLO), it is also possible to reconstruct and view 2D and 3D images of the ocular fundus with high resolution, thus increasing the diagnostic tools available for the clinician. In particular, OCT, based on interferometry, permits to obtain axial sections of the eye with high spatial resolution and penetration depth around 1 millimeter. cSLO, based on the same principle as confocal microscopy, allows acquiring high contrasted images at a specific depth with the highest lateral resolution in comparison with the rest of ophthalmic imaging systems. However, its clinical use is more restricted than OCT due to its cost, specificity, complexity and because the performance of traditional fundus cameras is rather acceptable.

Both aforementioned techniques can be combined with adaptive optics to reduce the impact of the patient's eye aberrations and to improve their performance considerably. Unfortunately, none of these techniques provides spectral information and the only spectroscopic data available from the retina comes out from the poor sampling of the color fundus camera.

This reduced spectral information also limits the diagnostic potential of current fundus cameras. Adding a spectral dimension permits to reconstruct the spectrum - e.g., in terms of reflectance values - of structures and substances of the eye, allowing the study of oxygenation and other metabolic dynamics of the ocular fundus whose spectral properties (e.g., the absorbance) change with the wavelength (λ). In general, common systems that permit to obtain spectrally resolved images of a sample are called HyperSpectral Imaging (HSI) systems and are generally composed by: a white broadband light source, an imaging system and a spectral filtering device that allows performing the spectral sampling (through more than three bands) of the object under analysis (Figure 1.3).

The use of HSI techniques spans a wide range of applications. In fact, although originally developed for remote sensing, mining and geology, it has already been applied into fields as widespread as ecology, agriculture, art conservation, surveillance as well as medicine and biophotonics [3]–[10]. Along the history, several approaches have been developed to increase the number of bands and speed of such systems; nevertheless, some limitations of the current configurations remain and the trade-off between different characteristics such as the speed, resolution and spectral bands must still be improved.

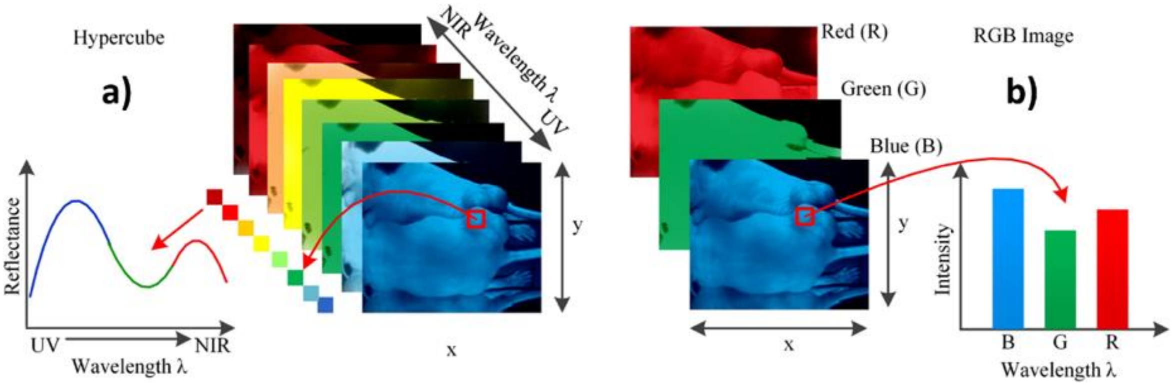

Figure 1.3: his imaging a) vs. color imaging b), adapted from [11].

Accordingly, this work aims at developing a fast HSI system for the imaging of the eye fundus that overcomes some of the limitations of conventional fundus cameras. The system increases the number of spectral bands up to 15 to provide accurate spectroscopic retinal information and widens the spectral sensitivity beyond the VIS and up to the Near InfraRed (NIR) (from 400 nm to 1300 nm), ultimately limited only by the absorption of the ocular media in between the retina and the exterior world. This might help in the investigation of the properties of the eye, such as the reflectance of different substances and cells, and be used as a precise diagnostic tool to improve detection and follow-up of certain ocular diseases. In order to broaden the spectral range and to increase the number of channels of the developed system while ensuring a good operation, our purpose is to increase the speed of common HSI systems, so as to avoid the effects of the undesirable eye movements that can produce artifacts and image misalignments.

Recently, a series of such kind of devices for HSI of the ocular fundus have been already developed, but they are mostly limited by the compromise between spectral sampling, spatial resolution and acquisition time [12], [13]. The ocular fundus has also been imaged with a system that makes use of Light Emitting Diodes (LEDs) for the spectral sampling in the VIS [14], instead of the more classical configuration with optical filters and a white light source. Although the latter system provides very good contrasted images at some wavelengths, it strongly suffers from the limited numbers of bands and the reduced spectral range of silicon-based cameras. Only one of the most recent spectral fundus cameras performs measurements up to 850 nm [15].

From a practical point of view and to increase the speed and resolution of the state-of-the-art HSI fundus cameras, we designed a light source composed of LEDs emitting at different wavelengths. Combining this light source with fast Complementary Metal-Oxide Semiconductor (CMOS) and Indium Gallium Arsenide (InGaAs) imaging detectors, the system covers a wide spectral range (400 nm to 1300 nm) in a short time, allowing for the analysis of the fundus along the entire optically accessible spectral window. In particular, we developed the entire hardware and software architecture for the acquisition of spectral images, and built customized processing algorithms for their correct visualization and quantitative analysis. Moreover, the system was used to collect and study images from healthy and diseased eyes in a clinical study.

This PhD project was carried out within the framework of the European Project BE-OPTICAL "Advanced BiomEdical OPTICAL Imaging and Data Analysis" (EU European Commission, Innovative Training Networks [ITN] call H2020-MSCA-ITN-2015) (2015-2019). It comprised several leading academic groups and non-academic partners in different countries bringing together an interdisciplinary team of physicists, engineers, medical doctors and optometrists, with complementary expertise in vision, optical engineering, nanotechnology, computer science, complex systems and data analysis, in order to share and improve knowledge in imaging technologies and data analysis for biomedical applications [16].

This document is organized as follows: in the second chapter, after a brief introduction to color science, the state of the art of HSI systems and retinal imaging techniques - with special emphasis on fundus cameras - are presented. In the third chapter, the developed experimental prototype is introduced, including details of its design, hardware and software architectures, and optical characterization. Its standardization according to international regulations for optical system safeness are also presented. In chapter 4, the clinical study conducted for the validation of the system and the developed tools for image processing and spectral analysis are described, whereas chapter 5 describes the qualitative and quantitative results obtained for healthy and diseased eyes. Chapters 6 and 7 contain the most relevant conclusions of this work and lines of future research. In chapters 8 and 9, the complete lists of publications and conference presentations related with this work and the bibliography are given. Finally, details and references for all used components can be found in the appendices of this work, as well as the written informed consent forms used in the performed clinical study.

2 STATE OF THE ART

In this chapter, some concepts, definitions and examples that are useful for a rough comprehension of the current state of the art of imaging science and spectral techniques are given. After a brief introduction of the basic concepts related to color vision and color imaging systems, the advantages that HSI systems offer are discussed. Finally, focusing on the main topic of this work, the principal features of current available fundus cameras are described as well as modern optical systems used for the ocular fundus investigation.

2.1 Color vision and color imaging theory

What is color? One definition was given by the Committee on Colorimetry of the Optical Society of America, reported by Hardenberg [17], citing Nimeroff (1972):

"Color consists of the characteristics of light other than spatial and temporal inhomogeneities; light being that aspect of radiant energy of which a human observer is aware through the visual sensations which arise from the stimulation of the retina of the eye."

From this definition is evident that color is very difficult to describe, as it is a sensation, i.e., an interaction between the physical world and our senses. Color actually results from the interaction of a light source, an object, the eye and the brain or, in other words, the visual system (Figure 2.1a).

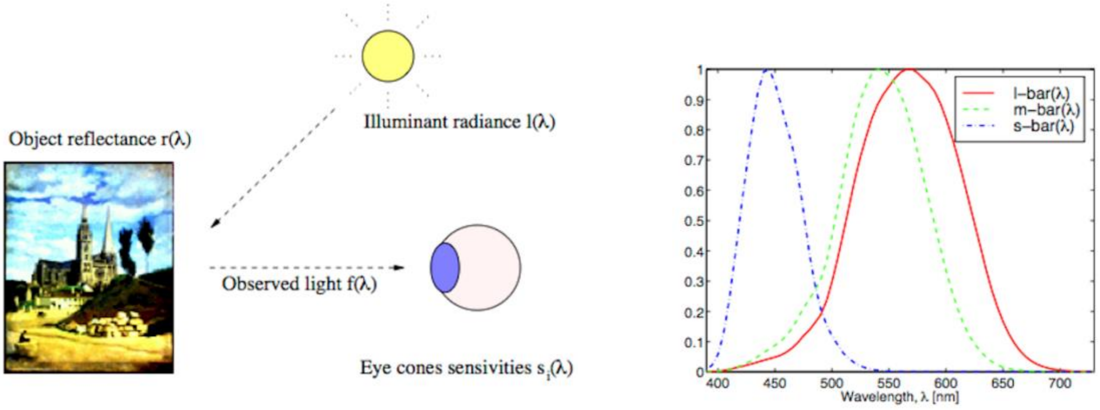

a)

b)

Figure 2.1: a) Color results from the interaction of a light source, the light reflected (or transmitted or emitted) by an object and the cone sensitivities. b) Normalized spectral sensitivity curves of the three different types of cones, (l=long, m=medium, s=short wavelength cones) responsible of the photopic vision, [17].

As already mentioned in the introduction, the eye is able to convert the light signal (photons) to a brain-readable signal of action potentials thanks to rods and cones. In particular, photopic vision is regulated by the presence of three different cone pigments that are in the retina. These pigments are linked to different sensitivity through the VIS and their responses enable having color perception (Figure 2.1 b). Taking this into account, it is easy to understand that a three components vector, C(λ) = (c_r(λ), c_g(λ), c_b(λ)), is needed to represent any color, where the subscripts r, g and b stand for red, green and blue, respectively. This is what is known as trichromacy of the visual system.

Because of trichromacy, almost all image sensors have three acquisition channels (Red, Green, Blue - RGB), trying to emulate the retinal cones performance. And also because of trichromacy of the eye and cameras, there is metamerism [18]. This is a phenomenon in which spectrally different stimuli produce the same color and occurs when there are equal cone or RGB camera responses. Because of both color encoding and metamerism, there is a loss of spectral information from the sample under analysis.

Metamerism can have a great impact in some fields such as quality control in the industry or biomedical applications, in which spectroscopic information can be very useful due to its relationship with chemicals and components of tissue such as hemoglobin or melanin. Mathematically and from a physical point of view, the phenomenon of color can be expressed as follows:

$$c_i = \int_{\lambda_{min}}^{\lambda_{max}} f(\lambda) s_i(\lambda)\, d\lambda \qquad 2.1$$

where c_i is the i−th component of the vector that represents each of the three cone responses, S_i is the i-th single pigment spectral sensitivity, λ_{max} and λ_{min} denote the interval of wavelengths of the VIS outside of which the spectral sensitivities of cones are zero, and $f(\lambda)$ is the product between the light source spectrum $l(\lambda)$ and the reflectance (or transmittance) of the object $r(\lambda)$:

$$f(\lambda) = l(\lambda) r(\lambda) \qquad 2.2$$

From this equation, it is simple to understand how much we can learn from the reflectance (or transmittance) spectrum of an object, sampled at many wavelengths, rather than only considering color, which is only expressed by means of 3 values.

It is important to note that in this simplified and intuitive representation we are neglecting some important dependencies of the reflected (or transmitted) light such as angular distribution, spatial distribution and positions of the source and the detector. Moreover, in this case we are neglecting physical phenomena arising from the interaction of light with every kind of material such as the axial penetration dependency of wavelength, fluorescence emission, regular and diffuse reflectance, light polarization etc. The discussion of all these phenomena falls outside of the scope of this dissertation. For a detailed and more complete description of them, we resend the reader to fundamental books as [19]–[24].

2.2 Spectral imaging systems

Spectroscopic techniques have a huge applicability, especially HSI systems, which add spatial resolution to conventional spectrometers based on a single sensor. As previously pointed out, the spectroscopic techniques combined with an imaging system permit to improve the quality control in several fields such as in the food industry, mapping the earth for environmental, defense and monitoring purposes or, for instance, increasing the contrast and the specificity of some diagnostic tools in medical imaging [3], [4], [25], [26]. As aforementioned, for many applications, spectral information can be more appropriate than color. Scenes or objects can be characterized by their spectral properties (reflectance, transmittance, radiance etc.). In particular, reflectance strongly depends on the properties of the material that is under analysis. For this reason, spectral imaging technology is a unique opportunity to add an extra dimension to imaging devices, the “λ” axis. These devices sample the object through numerous spectral bands and create a dataset in three dimensions where, besides the spatial (x, y) coordinates, a third spectral dimension is added. All this information is described by the, so called, hyperspectral datacube (Figure 2.2) and a single element of this datacube is referred as a "voxel" [27].

Spectral imaging systems are classified by their characteristics of spatial and spectral resolution, acquisition rates, etc. A first classification among spectral imaging systems is made on the basis of the number of spectral bands that they contain. Generally, systems that are named Multispectral (MSI) include from three to ten bands, HSI from tens to hundreds, and Ultraspectral (USI) thousands of them.

Other two classifications are commonly made in the literature based on the continuous or discontinuous spectral sampling of the electromagnetic spectrum and on the spectral/spatial sampling technique. In the first of these classifications, hyperspectral systems provide a continuous scanning of the sample over the spectrum, acquiring several hundreds of spectral points one after the other. Instead, we refer to multispectral systems if they provide a discontinuous acquisition, probing the sample only in well separated parts of the spectrum.

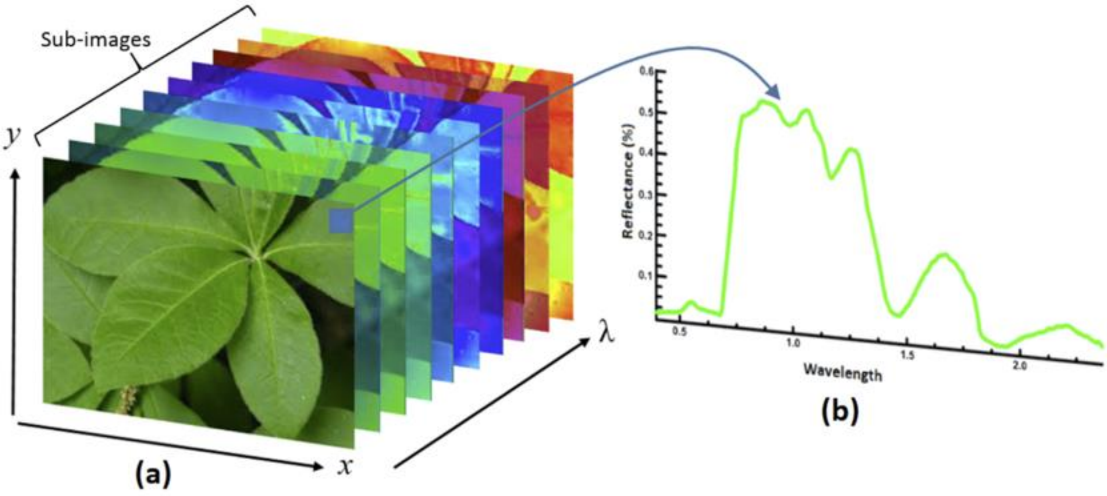

Figure 2.2: a) Layout of the hyperspectral datacube and b) spectral curve corresponding to a pixel [28].

In the second one, the difference between the spectral imaging classes is the acquisition mode of the spatial and spectral information, or more precisely, the used spectral/spatial sampling approach. This allows spectral imaging systems to be divided into four main classes: whiskbroom, pushbroom, staring, and snapshot methods (Figure 2.3).

Whiskbroom systems acquire spectral information from a single spatial point at a time and change the measurement position by moving the sample or the system; alternatively, they can perform the spatial scanning by means of, for example, galvanometric mirrors. The collection of the spectrum from each single spatial location is made as in conventional spectroscopy, that is, with a point or linear sensor and a wavelength disperser device, such as a prism or a diffraction grating. Whiskbroom imagers are robust, affordable and with very good spectral resolution. For these reasons, they are commonly used in fields such as satellite investigation and in systems where the spatial resolution is not as important as the spectral one.

Pushbroom imagers allow the simultaneous acquisition of an entire plane of the datacube. This method implements the same idea of the whiskbroom approach, maintaining the robustness with increased speed, but using a 2D camera to acquire both the spatial and spectral information of one line of the sample in one shot. In this way, a dimension of the camera identifies the position along a single spatial line, while the other dimension is used to sample the spectral coordinates. Furthermore, a pushbroom scanner can get more light than the whiskbroom one for each single voxel, since it can stay at a particular area for a longer time (if the total acquisition time is kept constant) as it only requires scanning in one spatial direction. Anyway, even if speed is increased compared to the whiskbroom method, this time-consuming approach still limits its possibilities.

On the other hand, staring imagers use the entire 2D sensor to acquire an image of the sample at a precise wavelength for each frame and then, build the wavelength dimension of the datacube by scanning the wavelength. This technique improves the image spatial resolution and is generally used when the highest spectral resolution and a continuous spectral scanning are not necessary.

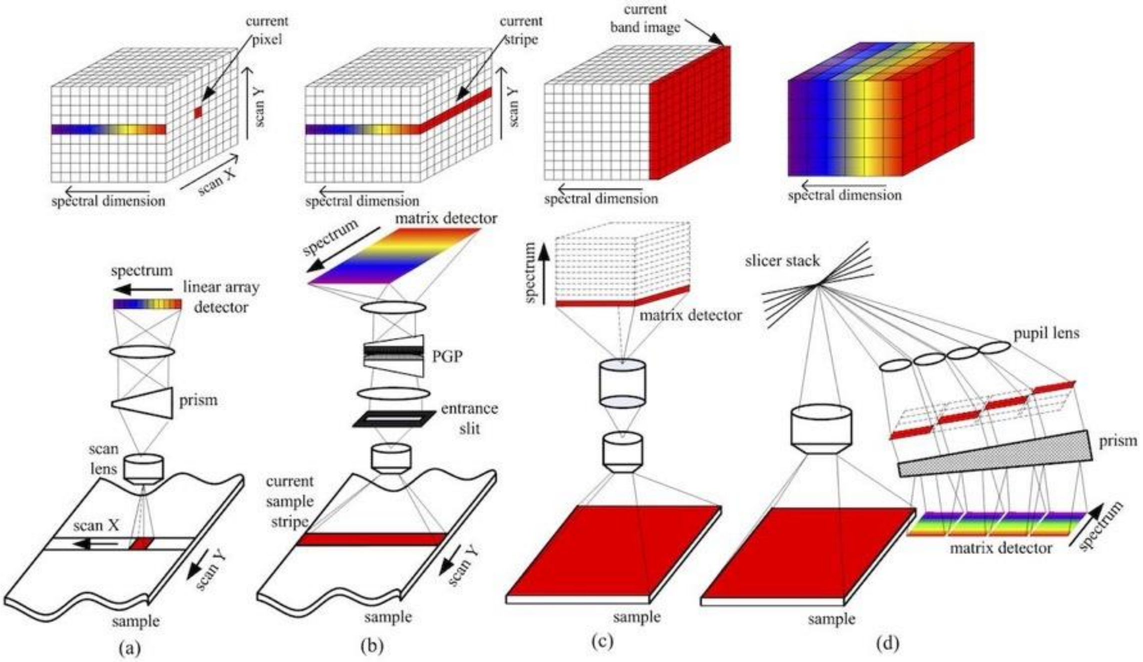

Figure 2.3: Spectral imaging optical methods: a) whiskbroom, b) pushbroom, c) staring and d) snapshot, [29].

The last method is the snapshot technique, which provides a full datacube acquisition in a single shot spreading all the voxels of the datacube on a single imaging sensor (as done in color imaging, but with higher spectral resolution). The advantage is clear but, when projecting all the datacube on the sensor at the same time, the spatial resolution is strongly reduced [29]. Differently from other techniques that do not need of a strong post-processing to reconstruct the datacube, snapshot HSI systems do. The complexity of this post-processing depends strongly on the organization of the datacube on the sensor; in this way, it might sometimes take several minutes to reconstruct a series of images due to the multiplexed and structured illumination technique utilized to encode all datacube information.

Regardless of the kind of spectral imaging technique, those share a basic structure that consists of an illumination system, a spectral filtering mechanism and a detector. In the following sections, some of the different approaches that have been put into practice are pointed out, also providing a panoramic view of several applications.

2.2.1 Light sources and filters

HSI systems can either use broadband or narrowband sources. Conventionally, any of the configurations described above - i.e., whiskbroom, pushbroom, staring, and snapshot methods - include a spectral sampling device together with a broadband source. Broadband sources, such as halogen lamps, mercury lamps or super-continuum lasers, span the spectrum in the VIS or even beyond. Depending on further characteristics such as the temporal and spatial coherence, polarization or power, one can choose the source that better fits for a specific purpose. Systems using broadband sources require a tandem with a filtering device to achieve spectral dimensionality, with a certain spectral resolution. As a specific example, staring systems including a mechanical device for scanning, like a filter wheel in front of the camera with interference filters, were common some years ago. From the interference between dielectric layers, interference filters are able to transmit a spectral band with variable width, ranging from 1 nm to 100 nm. Furthermore, they are cheap. Nevertheless, due to the limited number of spectral bands and therefore, the limited spectral resolution, apart from the inconvenience of including mechanical moving parts in the set-up, they are no longer used.

Alternatively, filters that are capable of selecting dynamically a variable spectral window, as Liquid Crystal Tunable Filters (LCTFs) and Acousto-Optic Tunable Filters (AOTFs), and diffractive elements, as prisms or diffractive gratings, are used nowadays. LCTFs are composed by a series of optical birefringent cells and linear polarizers, which can be spectrally tuned by means of applying a variable voltage to each single cell placed within two plates. In particular, by changing the voltage these filters add a variable phase delay between the extraordinary and the ordinary components of the polarization vector depending on the specific crystal structure of the birefringent material such as quartz, glass etc. Only wavelengths that are in phase are transmitted by a linear polarizer, reaching the next cell. They provide enough transmissivity (from 20% to 50% from 400 nm to 750 nm), robustness to aberrations, and can be used to filter light both in the illumination and in the detection paths, although the last one is the most commonly used configuration [30]. On the other hand, the limitation of this technology is in the spectral scanning speed (ms), so it cannot be used in dynamic recording applications where a high temporal resolution is needed. On the contrary, AOTFs are systems based on the acousto-optic principle, making use of the interaction of light waves with an acoustic wave as it propagates through a vibrating piezoelectric material driven by a radio-frequency signal. The transmitted wavelength is chosen from the conservation of the angular momentum and the energy between the acoustic and the light waves. They can be tuned in wavelength faster than LCTF (in the range of µs). These systems show a good transmission (>90%) and are often used in the illumination path because they have small aperture and can seriously deteriorate image quality.

Besides of the two previous examples, one can also consider the traditional possibility of dispersing light with optical components such as prisms, gratings, or a Fabry-Perot interferometer [27], [31]. These systems exploit their dispersive potential thanks to very basic light effects as refraction, diffraction and interference, respectively. In particular, prisms and diffraction gratings disperse the light so, blocking the light except for a particular angle, it is possible to select the transmitted spectral band. In the case of the Fabry-Perot interferometer, it samples the selected spectral band by changing the distance between two mirrors that compose an optical cavity. The main drawback of such devices is the high cost, which rises up as the precision and the acquisition speed increase. Despite of this, manufacturers can increase the spectral resolution of diffraction gratings up to the order of fractions of a nanometer with modern holographic optical techniques; accordingly, they are considered the best solution when the highest spectral resolution is required.

Back to the description of light sources, there are also those with narrow band emission, among which we can list lasers and LEDs. Spectral imaging systems using these light sources do not generally include filters, as their spectrum is already narrow. Lasers are sources with a very narrow band emission (≈ nm) and spatial and temporal coherence; these types of sources are used for applications in which it is important to have a high power, clean and controlled light source, as in confocal microscopy. Nevertheless, they are poorly used in spectral imaging because of their cost and the narrow band [20]. On the contrary, LEDs are light sources that, in the last few years, caught the attention of scientists and industry thanks to its quality, low cost and durability. A LED is a semiconductor incoherent light source based on a p–n junction diode. When a suitable voltage is applied to the junction, electrons are able to recombine with holes releasing energy in the form of photons. This effect is called electroluminescence, and the color of light (which depends on the energy of the photon) is determined by the energy band gap of the semiconductor material [10], [32]. Like the band gap of a particular material, the emission band and the central wavelength of LEDs depend on several factors such as the temperature and the material pureness. Commonly, they show a Full Width at Half Maximum (FWHM) of 20 nm − 30 nm in the VIS, while in the NIR and InfraRed (IR) regions it is >40 nm, with very different powers that span from ≈ µW to W. Moreover, LEDs can be driven and controlled by an electric signal with a fast response (µs) which, in the context of HSI technology, makes them powerful for sequential acquisition as in the staring techniques. In fact, these sources can be combined and multiplexed in integrative light systems, with an improved stability, acquisition speed and durability compared with common spectral imaging systems based on filters. Their use has also an impact on the overall cost of the apparatus, reducing it significantly. Thus, this lighting technology has already been successfully used in many different systems in a variety of applications: to reproduce CIE (Commission Internationale de l'Eclairage) standard illuminants [10], to improve the diagnosis of skin cancer [26] and for imaging the ocular fundus [14], [15].

2.2.2 Imaging sensors

The choice of the proper imaging sensor is one of the key steps for a good performance of a spectral imaging system and depends strictly on the application it is going to be used for. As a first approximation, the main parameters of an imaging sensor are resolution, Quantum Efficiency (QE), noise levels, frame rate and spectral sensitivity. All of these parameters can change a lot and are often dependent one to the others because of the manufacturing process, materials involved and size. Next, some imaging sensors that can be used in a spectral imaging system from the VIS to the IR are briefly described.

A first classification between imaging sensors can be made among point, 1D and 2D detectors, which are used in different applications depending on the purpose. In particular, point sensors are generally used when a high sensitivity and extreme spectral precision are required. Examples of point detectors are conventional photodiodes, Photo-Multiplier-Tubes (PMT) and Avalanche PhotoDiodes (APD). The two last ones are used for measuring low light levels as they can notably increase the Signal to Noise Ratio (SNR) by performing a large amplification of the signal. The multiplication factor can reach values of 10^8 for modern PMTs, while APDs, besides a good multiplication factor of the order of 10^4–10^5, also have good QE in a broadband part of the spectrum. In general, all these detectors are used in combination with whiskbroom scanning techniques - i.e., those including a conventional scanning spectrometer - that thanks to their spatial scanning process allow obtaining high quality image at the expense of time consumption. However, conventional whiskbroom imagers commonly use 1D detectors - i.e., linear arrays of photodiodes or even linear Charge Couple Device (CCD) cameras - that permit to acquire simultaneously a complete dispersed line from the light collected by a single point (or small area) on the object and, thus, provide a complete spectral scan in one shot.

Regarding the 2D imaging sensors, the most commonly used in the VIS are the CCD, CMOS and Electron Multiplying - CCD (EM-CCD). They cover a spectral sensitivity from 400 nm to almost 1000 nm, with a strong QE dependence on the wavelength that can range from 95% in the VIS to 10% in the NIR. In CCD and EM-CCD sensors, the whole area of pixels collects the incident light, and a restricted number of output nodes, usually one, transfer each charge that is stored in an intermediate memory (register) and convert it into an analogue voltage signal for subsequent elaboration. This readout mode is the principal limitation of this kind of sensor limiting the transfer of the electrons from the pixel to the subsequent electronics passing through the charge register. They are able to expose all the pixel area and are very useful in conditions where the light level is low.

On the other hand, the CMOS technology has the advantage of fast acquisition and low noise level. Moreover, modern CMOS imaging sensor spectral sensitivity goes from 400 nm to 900 nm and can reach up to 82% of QE between 500 nm and 650 nm. To increase the speed and to reduce noise, compared to CCD, CMOS technology bypasses the register and integrates, converts and stores the signal at the same place where the light is collected. In this way, the speed is improved, but the area of light integration of each pixel (fill factor) is reduced. Modern evolution of micro lenses arrays and back illuminated CMOS help to reduce this gap in comparison with the bigger collection area of CCDs, maintaining the speed features of CMOS. This is why CMOS are nowadays replacing CCDs in almost all applications.

During the last few years, the technology in the IR region was quickly developed and many companies started to produce digital IR cameras. These cameras work similarly to CCD and CMOS sensors but using different materials. InGaAs and HgCdTe (Mercury Cadmium Telluride. MCT) cameras are the most commonly used in the NIR and in the Short Wave IR (SWIR). In the earliest attempts, these cameras were prohibitive for their huge cost and issues that used to arise during the fabrication process. However, major technological improvements have been achieved, and they are already being used for specific research purposes. In this sense, although InGaAs and MCT technology is still far from the CCD/CMOS performance, their use is growing fast. In general, they have lower QE, higher noise and lower spatial resolution than VIS cameras. This is because of the material itself, which is difficult to handle, and the small band gap between the conduction and the valence bands. For reasonably expensive InGaAs cameras, comparable to high performance CMOS camera prices, common QE is $60 - 70\%$ from 900 nm to 1700 nm with a frame rate of 66 Hz [33]. Nevertheless, with long exposure times (~ 1 s) the sensor may show a lot of inhomogeneities because of the acquisition noise and errors in the manufacturing process. MCT cameras have the same problem of enhanced noise because of the narrow band gap. As a differential characteristic, they can be tuned to different wavelength ranges depending on the working temperature, reaching the long IR wavelength range in some cases (20 μm).

2.2.3 Biomedical applications of spectral imaging systems

A general overview of some applications of HSI systems in the biological and biomedical fields is provided in this section. The reader can refer to more complete reviews on HSI techniques in [5]–[8], [11], [34].

As a starting point, the description of some systems that make use of the whiskbroom method is given. This technique has already been applied in cancer analysis, measurement of oxygen saturation and fluorescence imaging [35]–[37]. Yu et al. presented a HSI system that uses a xenon arc lamp attached to a fiber to illuminate the sample between 387 nm and 700 nm. The illumination and the collection is achieved with the same multi-fiber cluster, which delivers light over the sample with the internal fiber and collects the reflected light from the outer ones. The light collected is then dispersed by a spectrograph and a CCD. This system allowed for the spectral examination and identification of tissue characteristics ex- and in-vivo, collecting light from a Field Of View (FOV) of 800 µm.

HSI whiskbroom systems have also been combined with confocal microscopes to improve axial sectioning and reduce noise. Two examples of this application are the experiments carried out by Constantinou et al. [36] and Sinclair et al. [37], who developed systems to study autofluorescence of the heart and reflectance of tissue, respectively. In particular, in the system developed by Constantinou and colleagues the detector was a composition of a PMT array with 32 channels that granted the necessary gain and speed to acquire a single voxel in 200 µs from 500 nm to 720 nm. The authors tested this system on the reconstruction of the autofluorescence spectra of heart tissue sections acquiring a 4.0 mm x 5.29 mm x 32 channels datacube in 80 min., with spatial resolution of 2 µm. On the other hand, Sinclair et al. developed a confocal HSI system that simultaneously acquired the spectrum from 500 nm to 800 nm, with 3-nm spectral resolution. Thanks to confocality, this microscope demonstrated very good spatial resolution and permitted to reconstruct the spectrum of different artificial beads (with 8300 spectra per second) using a prism spectrometer coupled with an EM-CCD (Figure 2.4).

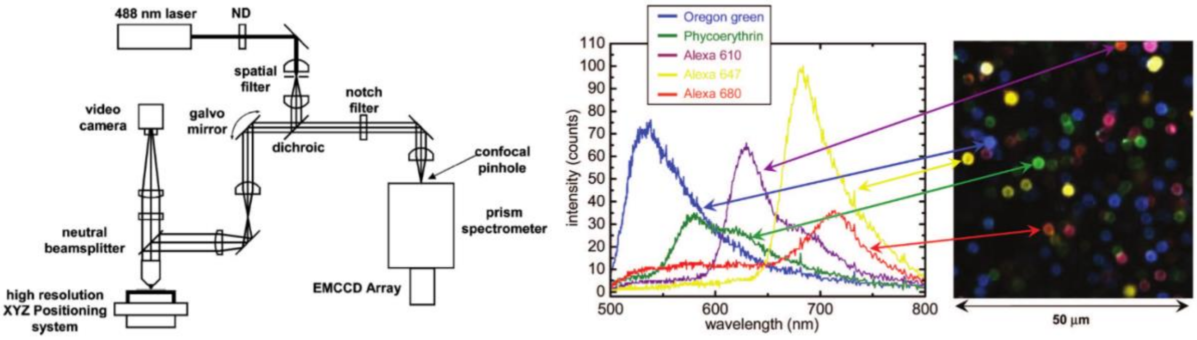

a) b)

Figure 2.4: a) Schematic diagram of the layout of a hyperspectral confocal microscope, b) hyperspectral image of 2.3 µm diameter silica microspheres labeled on their surface with four different fluorescent compounds. The raw emission spectra of the five compounds are shown in the inset, with the arrows indicating the microsphere from which each spectrum was obtained, [37].

In their work, authors proved the possibility of reconstructing the spectrum of several different fluorescent dyes simultaneously. This capability is important in techniques such as fluorescence resonance energy transfer (FRET), where the biological dynamics is tightly bound with the change of fluorescence spectrum of a particular studied protein and, sometimes, the spatial resolution is not enough to resolve it [37].

With the arrival on the market of 2D imaging detectors, many systems using whiskbroom technology were replaced by pushbroom ones. De Beule et al. [38] implemented a pushbroom sensor for Fluorescence Lifetime Imaging Microscopy (FLIM). In this context, spectrally resolved microscopy is commonly used as an alternative tool to fluorescence intensity microscopy as a means of removing artifacts. In FLIM, the main source of contrast is the decay time of fluorescence, but this measurement is usually not enough to analyze tissue autofluorescence; spectral resolution can provide additional contrast. In their study, the authors presented a pushbroom system that acquired in less than 40 s a complete spectral and time resolved 300 µm x 100 µm field of view (FOV) with an EM-CCD (178 frames per second [fps]) with a spectral resolution of 2 nm and a spectral range from 380 nm to 780 nm. This acquisition rate was proven successful in the task of reconstructing different autofluorescent tissue substances, allowing their discrimination with enhanced contrast.

As already detailed, staring imagers can scan the wavelength by means of tunable filters, avoiding mechanical scanning techniques. In this context, Vilaseca et al. [39] evaluated two different staring strategies to image the human iris and obtain color and spectral information: one that made use of a RGB LCTF to acquire color images, and another that included a filter wheel with 7 interference filters. This evaluation was performed on several human irises, prostheses and contact lenses and the RGB LCTF system was shown to provide the necessary information to analyze the colors and reflectance from irises with enough accuracy.

As above-mentioned, in order to improve the robustness and the lighting performance of staring imagers, systems based on LEDs have raised as an alternative to obtain a fast and narrowband scan of the sample. One example is the system by Bouchard et al. [40], who presented a LED-based system capable of collecting high resolution multispectral images at a frame rate of 220 Hz. This system was composed by two LEDs with different wavelengths and synchronized with a CCD camera. This technique enabled simultaneous visualization of brain oxygenation dynamics within a single vessel and the changes of fluorescence with high temporal resolution.

Another example of a staring imager based on LEDs is that by Delpueyo et al. [26], which was used for the improvement of the diagnosis of skin cancer lesions (Figure 2.5). This handheld system used a total amount of 32 LEDs spread in a spectral range between 400 nm and 1000 nm, arranged in a symmetric configuration to guarantee a homogeneous illumination over the sample. Moreover, this system also used two crossed polarizers to remove specular reflection from the skin.

Finally, some examples of snapshot systems are also described in this section. Gao et al. [41], [42], encoded the datacube coordinates of each single voxel on a detector and used strong post-processing to reconstruct it. Those authors developed methods to encode information on an area sensor called Image Mapping Spectrometer (IMS) (Figure 2.6) and Image Slicing Spectrometer (ISS) [42], respectively. ISS and IMS share almost the same principle: the collected light is reflected on an optical component composed by small size mirrors, named imaging mapper, which encodes the position of each single pixel and projects it on a component composed by prisms attached to a CCD camera. In particular, ISS is able to acquire a datacube of 350 x 350 pixels and 46 spectral points in a range from 450 nm to 780 nm with a frame rate of 7.6 Hz, while IMS acquires 285 x 285 pixels and 60 spectral points in the spectral band from 450 nm to 650 nm with 3 nm spectral resolution. These kind of systems have been tested on several applications such as fluorescent imaging, retinal imaging and depth resolved microscopy [43]–[45].

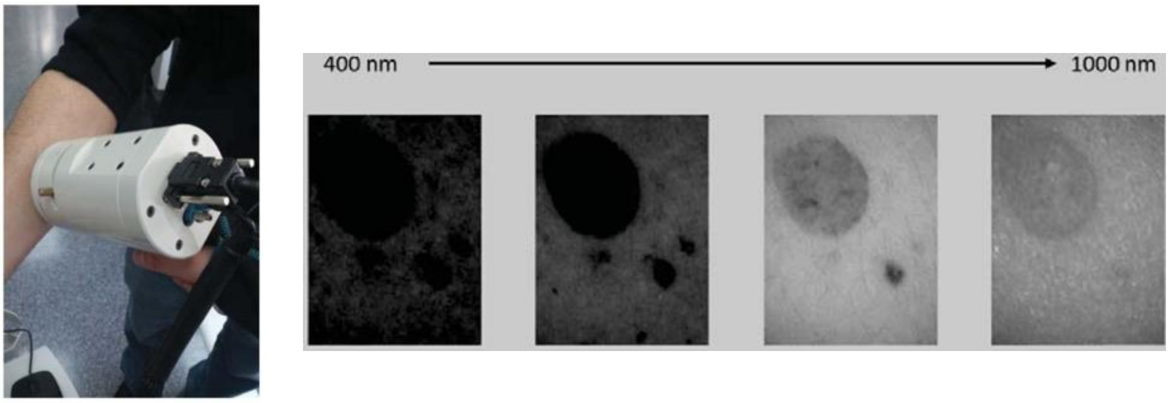

a)

b)

Figure 2.5: a) Handheld HSI system for the analysis of skin cancer lesions and b) 4 spectral images of a benign lesion (common nevus) acquired with the system, adapted from [26].

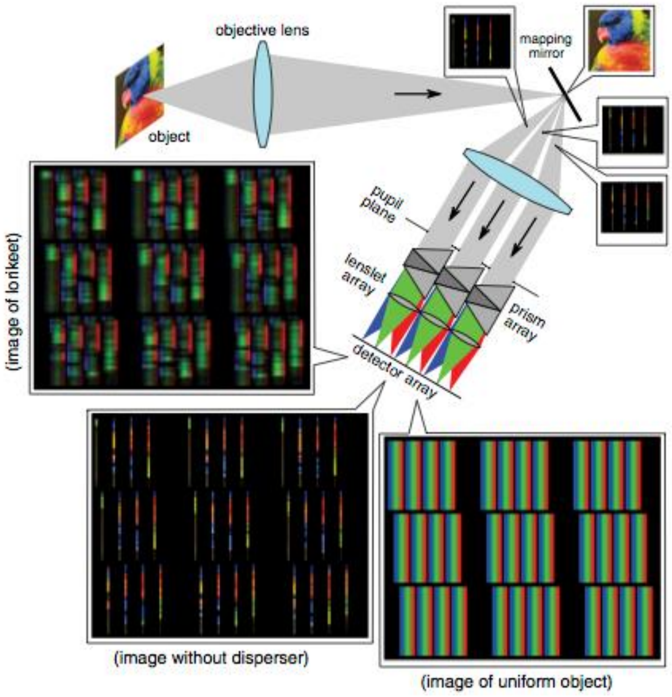

Figure 2.6: a) The Image Mapping Spectrometer (IMS) system layout. Three different raw images are shown corresponding to a set-up in which the lorikeet is being imaged in different manners: through the full system, without the prism, and replacing the lorikeet with a spatially uniform object; adapted from [27].

On the other hand, there are snapshot systems that rely their spectral imaging features to optical filters attached to pixels, as it is usually done in RGB cameras. These systems encode the spectral information in the relative position of the complete image on the detector, preserving the integrity of each spectrally filtered image. The advantage of this technique is clear: the amount of time required for post-processing is strongly reduced. However, since more than 3 channels are needed in hyperspectral configurations, this spatial filtering cannot provide neither the spectral nor the spatial resolution of other spectral imaging cameras [46]. Example of these systems are those presented by Mattews [47], [48], who built a hyperspectral snapshot system based on lenslet arrays placed just in front of a CCD and combined with 18 narrowband filters (with a bandwidth of 10 nm) ranging from 460 nm to 886 nm to simultaneously acquire 18 spectral images of the same scene (Figure 2.7 a). This system was successfully applied on the spectral monitoring of skin wounds providing oxygenation maps (Figure 2.7 b) [48].

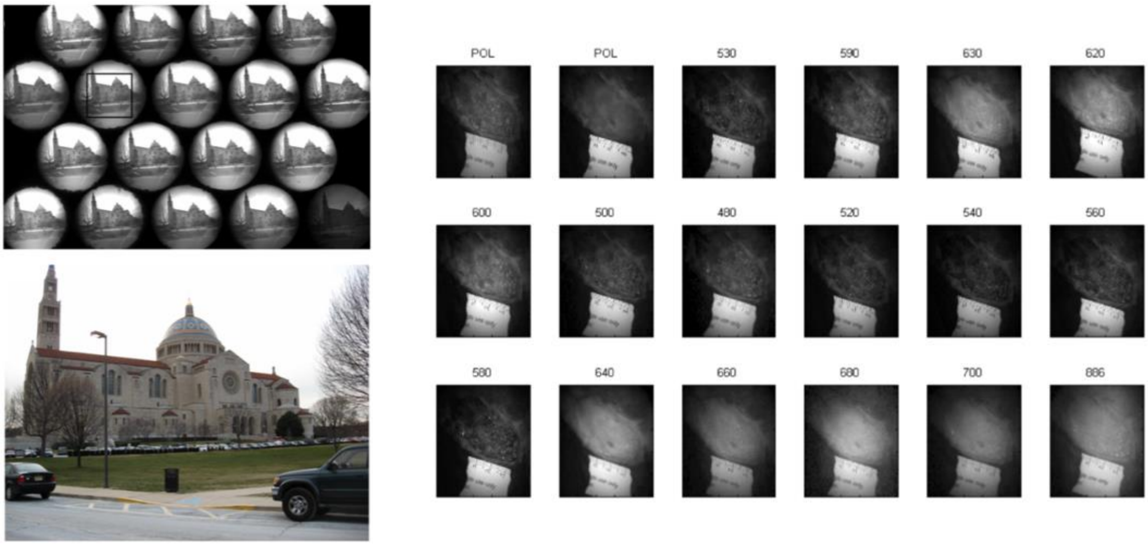

a)

b)

Figure 2.7: a) Image of the optical lens composition (top) used to image 18 copies of the sampled scene (bottom), [47]. b) 18 spectrally resolved images of a skin wound used to analyze the oxygenation levels of the tissue [48].

2.3 Retinal imaging

The first attempts to visualize structures of the retina were performed in 1823 and 1847, respectively, by Johannes Purkinje and Charles Babbage, who developed the first instruments that provided visual access to the posterior part of the eye [1]. However, it was in 1851 when Helmholtz wrote the first article stating the basis of retinal imaging or, equivalently, retinography. Retinal imaging presents some peculiar difficulties considering that the illumination and detection must share a part of the optical path. In this context, one must be aware that back reflected light from preceding eye optical structures, such as the cornea, is much brighter than the retinal reflected light itself. Retina is a minimally reflective surface (2 - 3% in the VIS) and several strategies have been developed during years in order to optimize the collection efficiency and reduce back reflections [49], [50]. In his work, Helmholtz illuminated the retina with a light bulb, split the illumination and detection paths with a 45° tilted semitransparent mirror placed between the lamp and the observer's eye, and observed the image through a 3 mm eyepiece. This configuration, the so-called direct ophthalmoscopy, permitted to isolate the contribution of the retinal reflected light from undesired back reflections and to observe the image of the ocular fundus. Moreover, the observer refraction and accommodation were corrected by moving a lens between the observer's eye and the semitransparent mirror. An evolution of this first ophthalmoscope is still present in common daily routine analysis of ophthalmologists and optometrists, and current hand-held systems are not far from the earlier described optical scheme. Clearly, this simple instrument can only be used for direct inspection of the retina by the clinician, and no objective record is acquired.

Based on this concept, the fundus camera constituted a great advance in retinal imaging, as it was able to image a larger field of view of the ocular fundus and to take photographs of it. In this way, the diagnosis and follow-up of retinal diseases became more objective, as the images taken at different moments could be more carefully analyzed and compared. Another remarkable improvement of fundus investigation arrived with the integration of digital photography in common ophthalmoscopes. As reported by Dobbins [51], the first digital camera invented by S. Sasson at Eastman Kodak in 1975, and the subsequent shift from analog to digital imaging revolutionized the medical records and posed the basis of modern retinography [52]. Nowadays, the use of digital RGB fundus cameras is widespread, and they have become a basic tool in clinical practice, although they cannot be used for some specific purposes, such as monitoring of metabolic substances, large FOV imaging of the retina or the acquisition of high-resolution images, for which custom-made systems are demanded.

Accordingly, a series of developments have been carried out by several researchers, turning towards innovative technologies for the study of the retina, such as OCT, cSLO, and various types of novel retinographs, like large FOV fundus cameras, which allow imaging also the peripheral portion of the retina. In parallel, spectrally resolved fundus cameras in the VIS have also been developed at research level allowing for the study of retinal structures and diseases related to particular substances of the eye [12], [14], [53]. Of remarkable importance in the context of this project is the evolution of fundus reflectometry, which permits to investigate many wavelength-dependent features of the ocular fundus, e.g., oxygenated and de-oxygenated hemoglobin, melanin or lipofuscin concentrations [54], [55].

In the following sections, we will give an overview of the principal modern techniques used in ophthalmoscopy, explaining their main physical principles, advantages and drawbacks. After this, we will focus on fundus cameras and their use for diagnosis for retinal diseases, as well as HSI systems used for retinal imaging.

2.3.1 Modern systems for retinal imaging

One technique that plays a protagonist role in current ophthalmic investigation is OCT (Figure 2.8). The potential of this technique relies on its capability of providing depth resolved imaging in a non-invasive way. Its working principle is based on the low coherence interferometry technique. In a simplified manner, the OCT can be seen as a Michelson interferometer using a broadband spatially coherent source, e.g., superluminescent LEDs. Due to its broadband spectrum, the light source used in OCT has a low temporal coherence, so the interference of the beams of the two arms of the interferometer (probe and reference arms) will only be constructive for phase differences within the small coherence length. Scanning the reference beam phase with a moving mirror inserted in the reference arm of the interferometer makes possible to obtain an axial sectioning of the sample. Moreover, adding a scanning system in the two lateral directions permits OCT to reconstruct 3D tomographic images.

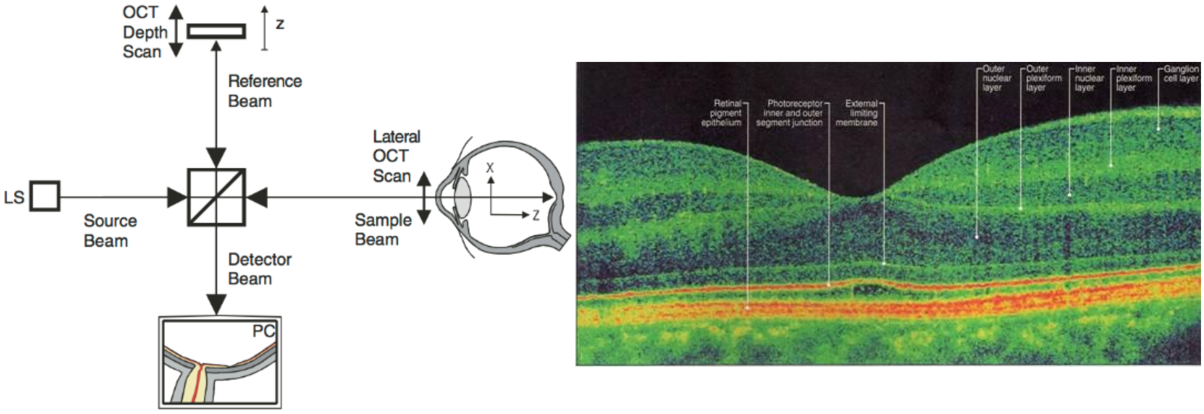

a) b)

Figure 2.8: a) Standard OCT optical layout based on a low time-coherence Michelson interferometer and b) common OCT 2D images of a healthy retina (foveal region) showing its principal layers, adapted from [56].

This OCT system is called Time Domain OCT (TD-OCT), but nowadays there are many different kinds of configurations with increased speed and resolution. One of these is the Fourier Domain OCT (FD-OCT) that, instead of performing a temporal scan, relies its axial sectioning capability on the spectral dispersion of the reflected light. This allows acquiring the entire axial scan simultaneously. The axial resolution basically depends on the spectral bandwidth of the illumination, while the maximum achievable depth depends on the wavelength (NIR light penetrates more into the tissue). For biological samples, it is limited by the absorption of water (very strong over 1300 nm) and scattering of the tissue. Recently, using light sources at 1060 nm, OCT systems have been deployed to image down to the choroid [56], [57].

Common OCTs suffered from two main limitations: the noise given by the speckle, and the required acquisition time. Scanning the focused beam all over the sample, modern OCT systems can produce 2D and 3D images with optimal resolution; however, eye movements during the scan can affect them, compromising their quality. To resolve these constraints, several techniques that combine fast scanning methods, adaptive optics or swept sources have recently been developed. Despite increasing OCT performance, these improvements also rise up the price of the instruments.

Nowadays, for certain diseases, no ophthalmological precise diagnosis can be done without using OCT systems. Even more, the development of OCT technology for the anterior segment imaging has made it not only suitable for studying the retinal layers, but also other ocular structures such as the cornea and the lens. Nevertheless, most of the applications are still for the monitoring and diagnosis of several retinal diseases such as glaucoma, age related macular degeneration (ARMD), diabetic retinopathy and retinitis pigmentosa, among others.

Another scanning technique mainly used in ophthalmologic research but with some early implementations in clinical environments is cSLO [58]. This is a basic technique of microscopy that produces diffraction limited resolution (if combined with adaptive optics) and low noise images. cSLO achieves optical sectioning by means of a confocal pinhole located at a conjugate plane of the focus of the illumination light, cutting out the light coming from out–of-focus layers and axially resolving the sample with increased contrast (Figure 2.9).

The main drawbacks of this technique are the scanning speed and the integration time required for single point detection. In fact, when the pinhole size is reduced, the collected light is cleaned-up but the integration period or the illumination intensity must increase to have enough signal from the sample. Larger integration times can seriously compromise the optical quality due to the eye movements, while increasing light intensity can enhance the damage and the photobleaching rate.

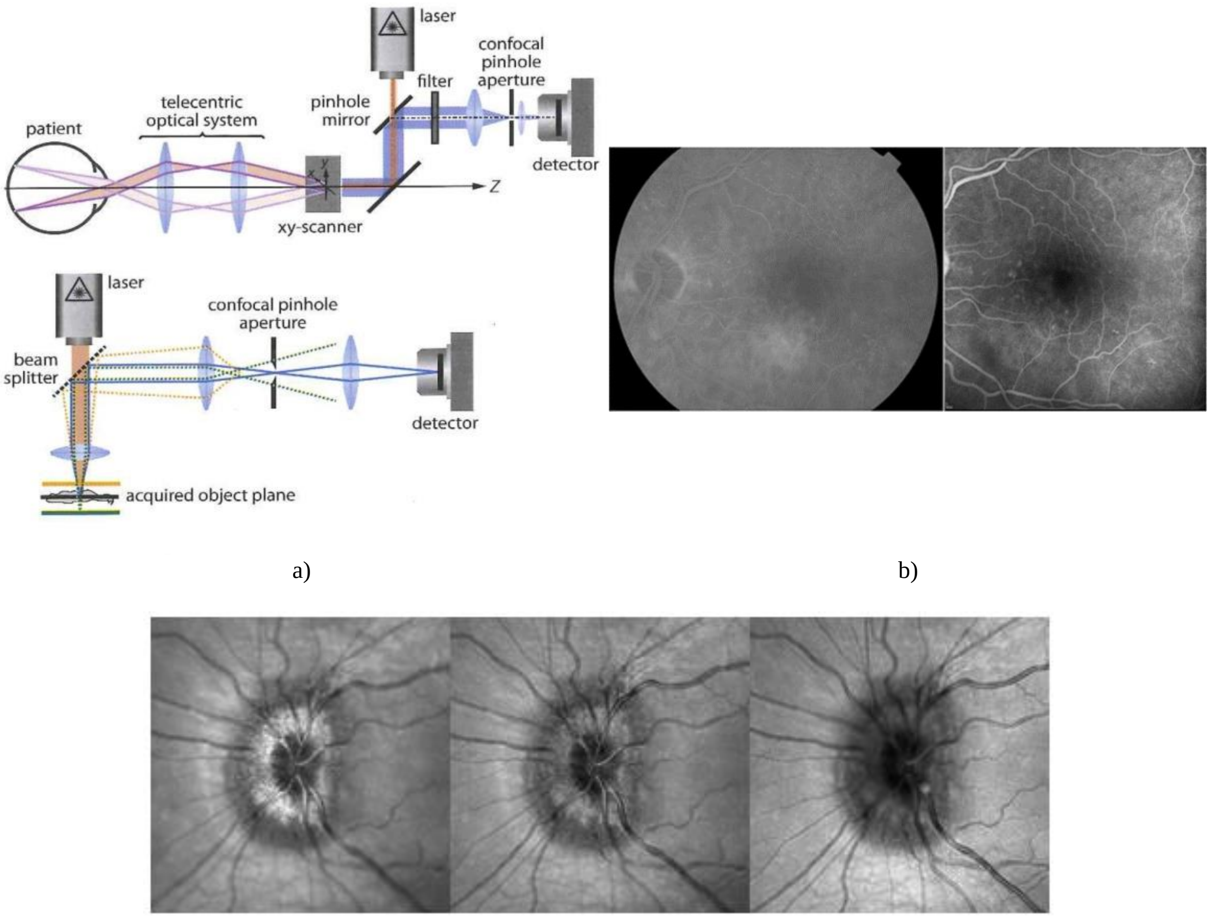

a) b)

c)

Figure 2.9: a) cSLO basic principle and set-up composed by an x-y scanning system, the confocal pinhole, the laser light source and the detector, [1], b) fluorescein angiogram with fundus camera (left) and with cSLO (right), and c) axial optical sectioning effect in the cSLO images. All three images are taken at the same wavelength. Focus is on the elevated optic disk on the left image. Tonality changes as focus is shifted towards the retinal surface, [59].

From the applications of cSLO, we may point out fluorescein and IndoCyanine Green angiography (ICG) to study in detail the vasculature of retinal and choroidal layers, respectively, taking advantage of the contrast given by fluorescence and the axial sectioning. Therefore, cSLO is used for circulatory related diseases such as diabetic retinopathy, as well as to collect lipofuscin autofluorescence information from the retina, where the presence of this protein is a common indicator of photoreceptors losses. In order to increase the image quality of cSLO, but only for small FOV fundus images (Figure 2.10), adaptive optics is also being used. In this way, Roorda et al. [60], [61] were able to identify fine details of the retina, such as the cones and their pigmentation with diffraction limited resolution.

All of these systems exploit very good resolution, image quality and contrast but are usually limited to restricted areas of the retina. A trade-off between the acquisition time, the delivered power and the retinal portion under study must be found to avoid photodamages and/or compromised image quality.

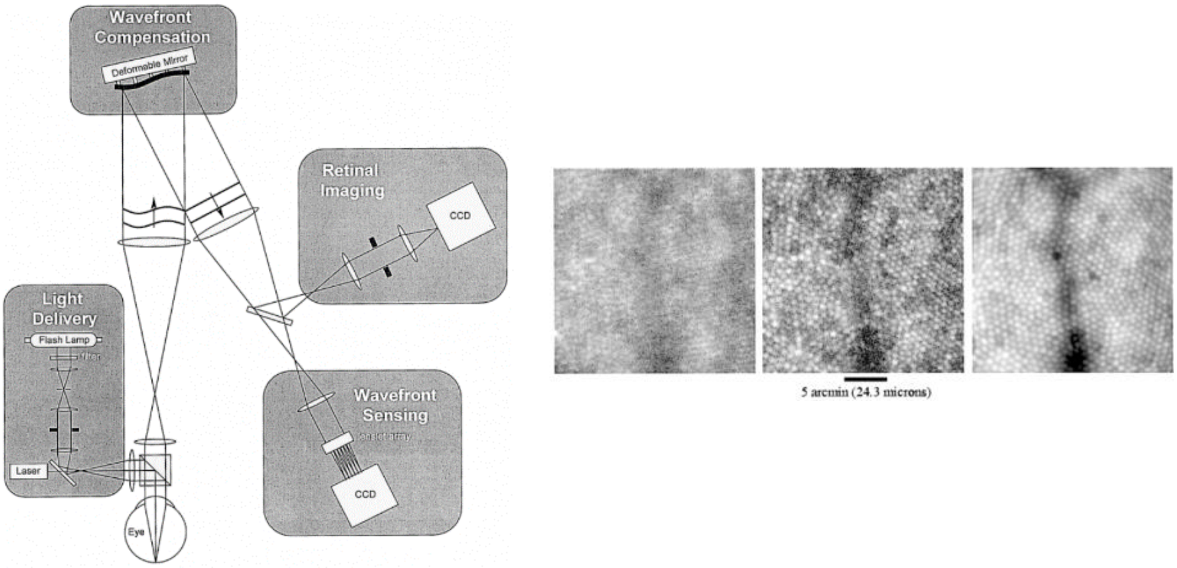

a) b)

Figure 2.10: a) Retinal imaging layout that makes use of adaptive optics in order to correct the ocular wave front and increase the image quality, [61] and b) series of images of the same retinal area without (left) and with adaptive optics (center, right), [60].

2.3.2 Fundus Camera (retinograph)

Besides the two modern systems described above, ophthalmoscopes and retinographs are still the most widely used instruments since they are able to provide a general overview of the retina with fairly good resolution and give a reference for further diagnosis or analysis to the ophthalmologist [62]–[65].

As aforementioned, the Helmholtz approach (direct ophthalmoscope) settled the fundamentals for retinal imaging techniques. Based on an evolution of that original system (the indirect ophthalmoscope), the design and development of the first commercially available fundus camera instrument by the Carl Zeiss Company (1926) was a remarkable step forward in the imaging of the ocular fundus. Later, with the successful integration of CCD digital cameras, faster and improved acquisitions of retinal images were possible. In the subsequent, several developments were made widening the fields of application of such optical technique, combining the fundus camera with stereoscopic imaging, increasing the FOV (up to 220º), and going from monochromatic to color imaging [52], [66], [67].

About monochromatic imaging, of remarkable importance are the techniques that permit to highlight ocular structures and substances by means of filtering or illuminating the retinal layers with selected wavelengths. For instance, red-free fundus photography allows increasing the contrast of blood vessels thanks to the hemoglobin green light strong absorption; blue light illumination permits to highlight the Nerve Fiber Layer (NFL), and spectrally selected excitation sources can be used to excite fluorescence from exogenous or endogenous substances like fluorescein or ICG and lipofuscin, respectively [52], [54], [55], [68]. Nowadays, common fundus cameras are only used in RGB and monochromatic modes with limited spectral resolution. In consequence, they present some problems as metamerism, which masks a lot of interesting information. Due to this, besides continuing searching on optical system strategies to increase the collection and illumination efficiency, research is looking to new hyperspectral solutions in order to improve fundus cameras capabilities.

2.3.2.1 Optical principles of fundus photography

When we take a photo with a common digital camera using the flash, the eyes of any person in the photo often appear as luminescent red spots. This is due to the flash light that, entering inside our open eyes, is back reflected by the ocular fundus, which is a strongly vascularized zone of our body. To avoid this effect, it is sufficient to misalign the camera's sensor from the back reflected light to exclude it from the detection path. This example shows in a simple manner the concept of fundus imaging and provides an insight about the illumination and detection systems that have to be built.

Since the retina must be illuminated and imaged simultaneously through the eye, illumination and detection optical systems in fundus imaging must share a common optical path and elements, at least those corresponding to the eye's optics (cornea, lens, etc.). Considering also that the retina has low reflectivity, this takes to the compulsory need to carefully build the illumination and detection systems so as to avoid undesired back reflections from all the optical surfaces shared by both paths before the retina [49]. This is achieved by accomplishing the geometric pupil separation principle [1], which states that the illumination and observation beam paths must be geometrically separated in all locations where scattering and reflections may occur (Figure 2.11). In this way, proper apertures and blocking elements must be placed in the detection path to cut off the light reflected from the shared ocular elements, collecting the light passing through the portion of the pupil that is not illuminated.

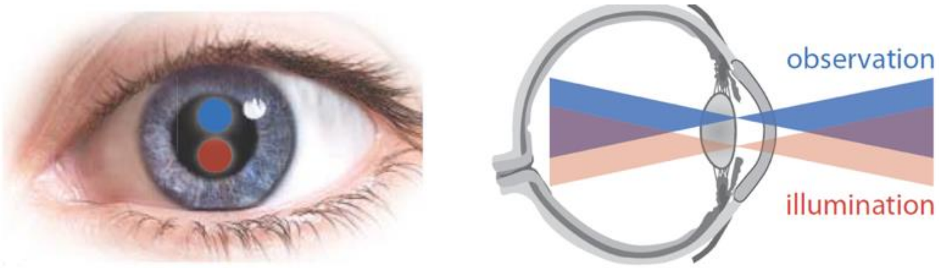

Figure 2.11: Optical principle of geometric pupil separation, [1].

Historically, common strategies used for the illumination of the retina can be divided in two main methods (Figure 2.12) [69]. The oldest, used in the original direct ophthalmoscopes, makes use of an off-axis tilted mirror. Thus, the illumination beam is tilted (Figure 2.12 a), ensuring that the detection and illumination systems have two different optical axes and so, leaving the detection almost free of back reflections from the eye's optical elements. In general, this technique can be used for its simplicity and low cost, but may present irregularities in the illumination distribution on the retina, mainly due to the asymmetry between illumination and detection axes.

Nowadays, the most common illumination strategy is based in the so-called Maxwellian view configuration (Figure 2.12 b) [1]. In this case, the light is focused at the anterior segment of the eye, nearby the subject's pupil plane, and then spreads inside the posterior segment covering a wide retinal area. This method restricts the interaction of the illumination beam with the ocular optical elements only to a focalized region in the anterior segment, which helps in the accomplishment of the geometrical pupil separation principle.

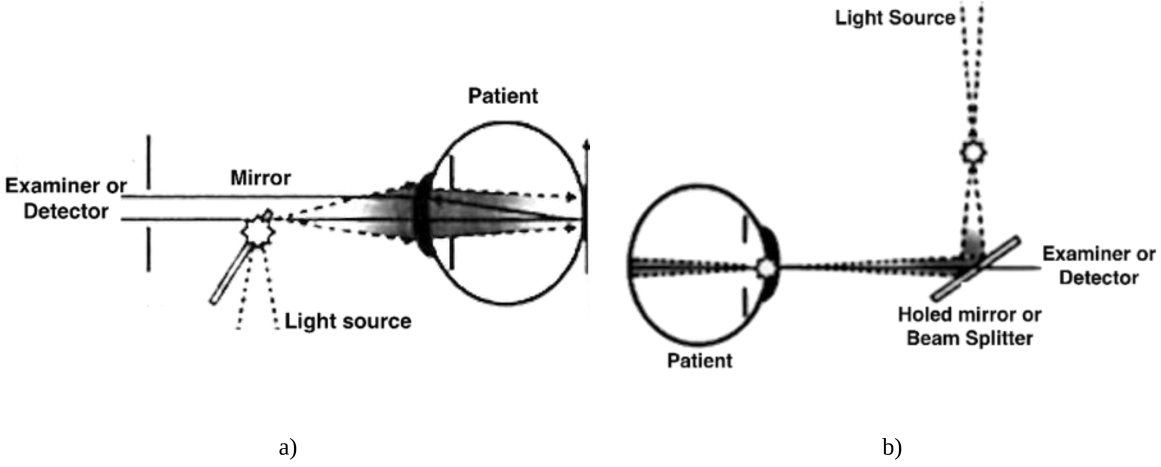

Figure 2.12: Principal strategies used to illuminate the retina. a) The division is achieved with a tilted mirror that decouples the illumination and detection optical axes. b) Maxwellian view: the retina is illuminated with a shaped light beam (generally an annulus) focused at the anterior segment, adapted from [69].

In fundus cameras, this geometrical separation is generally achieved by the use of a ring-shaped illumination beam (Figure 2.13). This ensures a homogeneous illumination of the retina in the entire field of view, leaving the central part of the pupil free to collect the light reflected by the retina. Ideally, in this technique there is only one surface where the illumination and the detection beams are coincident: the retina [1], [50]. The cut-off of the undesired back reflected light is done by inserting a circular aperture in the detection path, placed in a plane conjugated with the subject's pupil.

Apart from the optical elements of the eye, the illumination and detection paths should ideally be completely independent so that no further back reflections could affect the image. This could be achieved in the so-called external illumination configuration of a fundus camera (Figure 2.14 a), according to the nomenclature used by DeHoog et al. [49]. In this configuration, a beamsplitter is placed in front of the subject's eye, combining both paths. The first lens in front of the eye (objective lens) is then placed after the beamsplitter. This allows a better correction of system's aberrations, as its design can be tackled with no limitation in the number of its optical surfaces, i.e., no care must be taken regarding back reflections on those surfaces. The geometric pupil separation is achieved by means of a diaphragm in the detection path in a plane conjugated with the eye's pupil. However, the use of the beamsplitter, introduces inevitable losses both in the illumination and the detection optical paths. For this reason, higher power light sources must be used. It should be also noticed that high FOV are limited by the Numerical Aperture (NA) of the required objective lens. Due to the presence of the beamsplitter, the distance between the objective and the eye (working distance) cannot be reduced, so the only possibility is to use lenses with high apertures. This supposes a considerable increase in the price of the optics, worse integration capabilities, and, in fact, a much harder aberration balance although using several elements on its design.

Due to these limitations, common fundus cameras use the so-called internal illumination configuration (Figure 2.14 b) [49], where the objective lens is placed in front of the cornea and not using a beam splitter. In this way, collection efficiency greatly increases but the surfaces of the objective lens can potentially generate undesired back reflections and precautions must be taken. The separation between the illumination and detection light is generally achieved by means of a holed mirror placed in a plane conjugated with the eye's pupil. On the one hand, the ring-shaped illumination light is focused on the holed mirror, thus being focused at the subject's pupil, and reflected by its external part. On the other hand, the light coming from the retina passes through the hole, which acts as a diaphragm for the detection. Accordingly, this element, besides splitting the two optical paths of the system, ensures the geometrical pupil separation. The main advantage of this approach is the possibility for achieving a wider FOV with more cost-effective objective lenses and with better integration capabilities. Moreover, the light efficiency of the system is greatly increased compared to the use of a beamsplitter, as almost no losses occur in both illumination and detection arms.

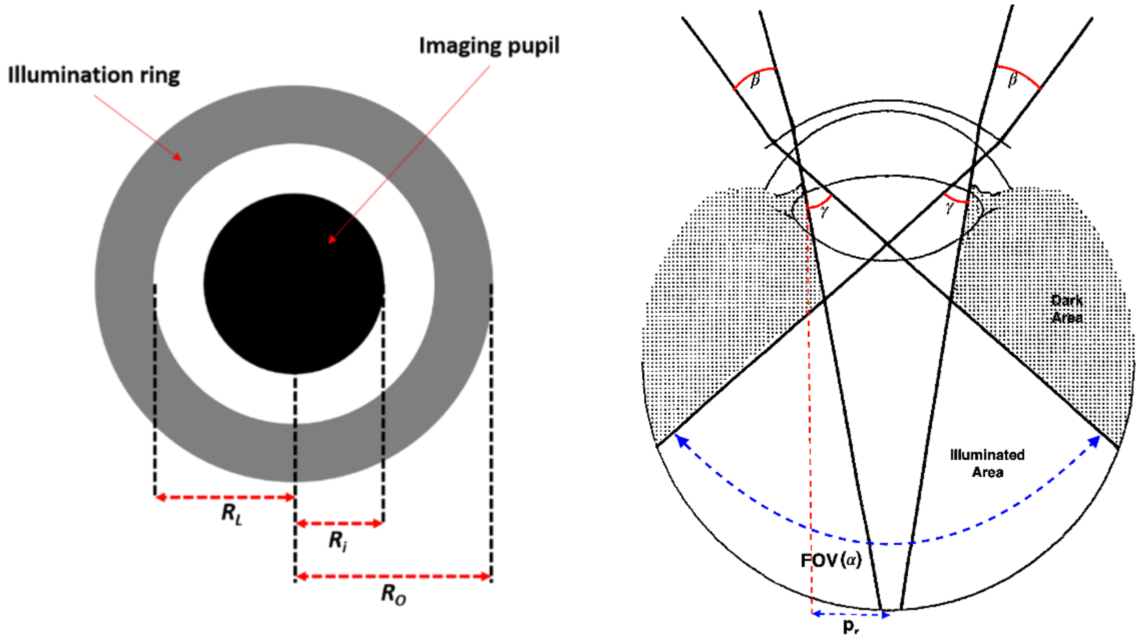

a) b)

Figure 2.13: Schematic representation of the ring shaped illumination and the geometrical separation with the detection at the pupil, from two different views: a) front view at the illumination focus plane at the anterior segment, adapted from [50]; and b) top view, adapted from [70]. Some parameters used to characterize a fundus camera are shown. β: illumination cone angle before the cornea. γ: illumination cone angle after eye optical surfaces. FOV (α): illuminated FOV. R_i, R_L, R_O: imaging pupil radius, internal and external radius of the illumination area, respectively. p_r: pupil radius.

As previously outlined, the use of an objective lens as a shared optical component between the illumination and detection paths may cause undesired back reflections. This imposes important constraints in the design of this lens, especially in regards to the number of surfaces, which should be minimized. Consequently, there might be a poorer aberration balance that must be compensated in the design of the rest of the detection arm. In any case, and although minimizing the number of the surfaces of the objective, some further strategies are required in order to eliminate the produced back reflections. Using antireflection coatings, their intensities can be strongly reduced, being much lower than the corneal reflection, but still higher than the retinal one. In general, the mostly used approach consists of placing some obscurations in the illumination path, which shade the parts of the surfaces of the objective lens that cause those problematic reflections. Nevertheless, those stops can cause illumination inhomogeneities if not placed and designed carefully.

From the literature analysis, the overall performance of the internal configuration is better, despite of the back reflected light and more complex alignment. Therefore, this is the one used nowadays.

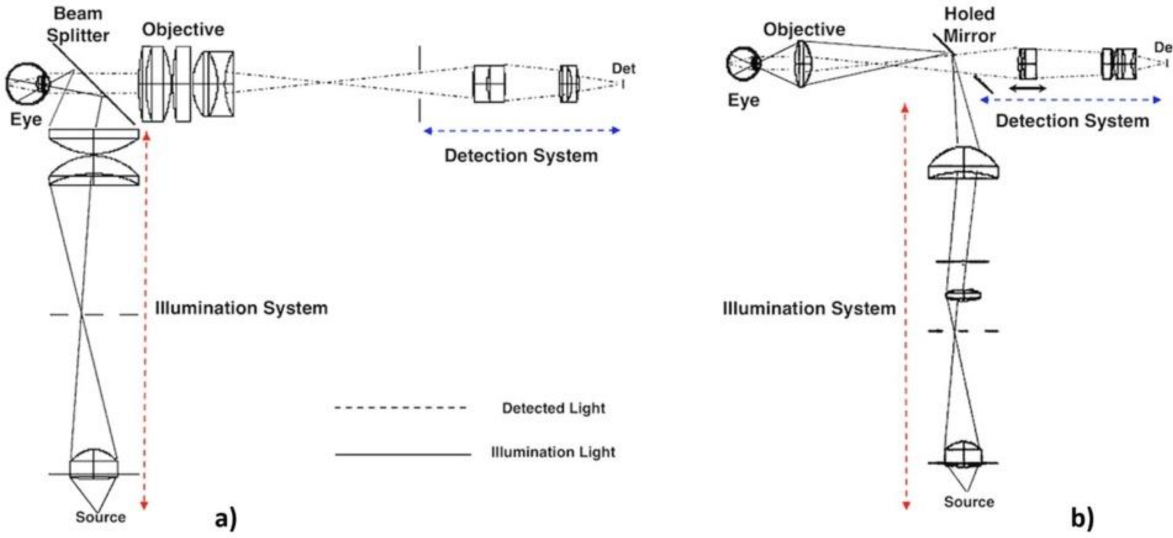

Figure 2.14: a) External and b) internal illumination designs for fundus cameras, adapted from [49].

Avoiding back reflections may be one of the most challenging issues when designing a fundus camera, but not the only one. Apart from this, the illumination arm should guarantee the best possible homogeneity of the retinal illumination, and the detection arm must be designed so as to obtain a sharp image of the ocular fundus all over the FOV. Both arms must also consider the potential refractive errors that the eye may have, so that the fundus camera can properly work for a range of ametropias. As an example of the design of a fundus camera, the scheme of the layout of a commercial device (Carl Zeiss Meditec) is depicted in Figure 2.15 [1], although it should be noticed that other approaches may have been considered in other instruments. In this design, as shown at the bottom left part of the figure, the geometric pupil separation is granted, as aforementioned, by focalizing the ring-shaped illumination (red) at the pupil plane, leaving the central part of the pupil for the collection of light reflected by the retina (yellow).

Regarding the illumination system, a flash lamp is usually used. The fast operation of the flash light mode is required in order to avoid the undesired movements of the eye during the measurement. Some optics are used to condense the light on a mask with a ring aperture, which creates the shape of the illumination. This ring is imaged on the reflective outer surface of the holed mirror by means of a lens (L_{illu}), so that the whole illumination pattern is reflected and then imaged on the eye's pupil by the objective (L_{obj}). As we will explain later on, this mask must be carefully designed in order to have the best light collection efficiency, illumination homogeneity and reflections rejection, considering the eye's pupil dimensions. A series of spectral filters are usually inserted in the illumination path to highlight particular retinal substances and structures, such as hemoglobin or the NFL, which present a higher absorbance or reflectance than the surrounding background at particular wavelengths. A variable field diaphragm is also usually included in the system, which controls the illumination over the FOV. As aforementioned, a set of covering points are placed at the proper planes in order to exclude the back reflections of the surfaces of the objective lens. For a correct illumination performance, additional optical elements, as condensers and diffusers, can be included in the illumination path to provide the required intensity distribution at the retinal plane.

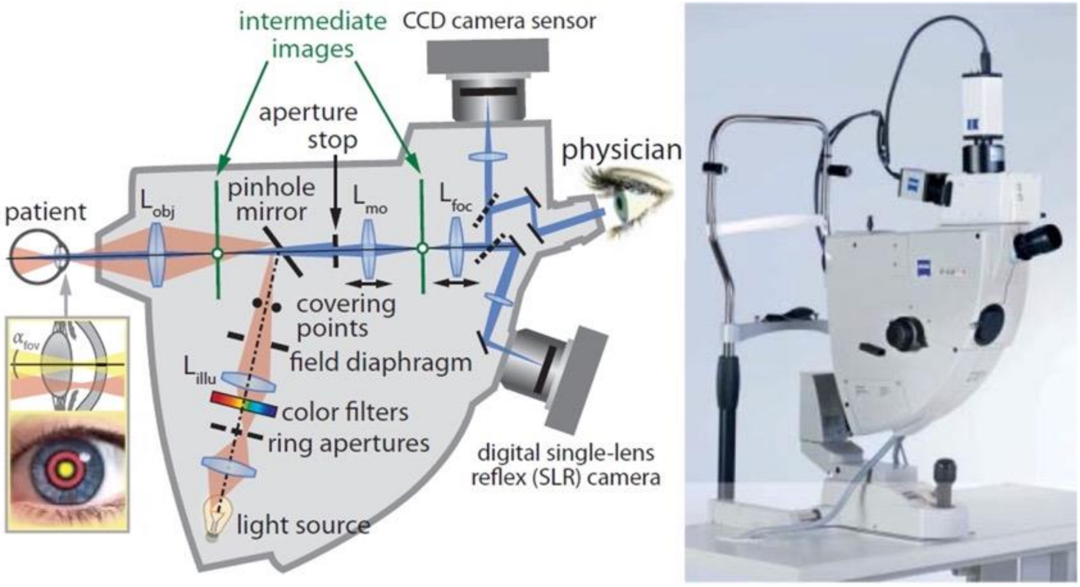

Figure 2.15: Layout of a commercial fundus camera set-up by Carl Zeiss Meditec, [1].

In regards to the detection system, the retinal reflected light exits the eye through the entire pupil. Then, the objective lens forms an intermediate image of the ocular fundus at its focal plane in the case of an emmetropic eye. As explained for the illumination arm, the objective lens conjugates the plane where the holed mirror is placed with the eye's pupil. In this way, only the light that is collected from the central area of the eye's pupil passes through the hole of the mirror, which acts, as the aperture diaphragm of the system. Then, further optics (L_{mo} and L_{foc} in the figure) are inserted to compensate the patient's refraction by axially moving one (or several) of the lenses so as to apply the spherical compensation without changing the final fundus image size. After this correction, the light is collimated and can be split into different optical paths. One of them is dedicated to collect the image from the ocular fundus by means of a detector, generally a RGB CCD or CMOS camera, with enough sensitivity and speed for a proper acquisition of the images. The other subsidiary optical paths are necessary for a proper alignment of the eye and focusing of the retinal image before the capture. They can be used to place a monitoring camera to observe the ocular fundus or even to introduce fixation targets.

Going deeper into the optical design of a fundus camera, it is worth describing the basic parameters that characterize the system's performance, too [50]. The imaging FOV is the very starting point for the design of both the illumination and detection arms, as the performance of the whole system strongly depends on it. The FOV is measured in degrees (α) and modern fundus cameras have angles that span from 20° up to 200°. A FOV of 30° allows imaging the main structures of the retina such as the optic disk, the fovea and the temporal fundus. The angles γ and β (see Figure 2.13 b), which correspond to the angle spanned by the illumination light cone after and before the focus in the anterior segment, have to be matched with the imaging FOV. These angles must be chosen in such a way that the illumination light cone completely fills the FOV with a homogeneous intensity distribution.

Other parameters that influence the resolution, the geometric pupil separation capability, the illumination homogeneity and the collection efficiency are the outer and inner radii of the annular illumination (R_O and R_L), and the radius of the detection pupil (R_i) (see Figure 2.13 a). The upper limit of R_O is limited by the radius of the ocular pupil (p_r). In the so-called mydriatic fundus cameras, wider illumination rings are used, as a wide pupil diameter is guaranteed by the instillation of dilating drops, while non-mydriatic systems must be able to work for very small pupils. On the other hand, the detection radius (R_i) value is given by the system's pupil size, i.e., the size of the image of the pinhole in the holed mirror. Its value determines the light collection efficiency, the resolution and the contribution of back reflections to the final fundus image. A revision of the literature suggests that R_i are around 0.75 mm and 1.5 mm but, in terms of efficiency, homogeneity and image quality, there is minimal benefit to increasing the imaging pupil radius beyond 1 mm [49], [50]. On the other hand, R_L must be set so as to leave some separation between the illumination ring and the detection area, thus ensuring a certain tolerance in the positioning for the removal of reflections.

Finally, other important functional parameters to be considered while designing a fundus camera, are the working distance, the range of spherical refraction compensation and the sensor's and optical resolutions. Of course, the system must also be safe, so the design must guarantee the fulfillment of the regulatory rules that limit the illumination levels delivered to the eye (basically, standards ISO 10940:2009 [71] and ISO 15004-2:2007 [72]). A thorough description of all these parameters and constraints, and their impact on the design, is out of the scope of this basic review, but it can be found in [49], [50], [73].

The system's performance depends on all former parameters but also on functional relationships between them, so a complex compromise must be met in order to achieve the best operation at lower cost. For more information, the reader can refer to several studies that have been carried out in order to study methods to increase the performance of retinographs [49], [50] and to find agreement and reproducibility with experimental data [61], [70].

2.3.2.2 Ocular spectral properties

The transmittance and reflectance (Figure 2.16) of the ocular media were studied in 1962 by Boettner and Wolter, considering also their scattering properties [1], [74]. In this work, the authors showed that the cornea and aqueous humor transmit light from 300 nm to 2000 nm; below and above this range, the light is strongly absorbed and reflected by the characteristics of the ocular media (Figure 2.16 a).

The lens presents a glass-like spectral behavior and is our first defense against ultraviolet (UV) radiation; specifically, it strongly absorbs light between 300 nm and 400 nm, which can seriously damage the retinal layers. Due to the eye's structure, water absorption is especially important when light passes through the vitreous humor, which is 25 mm thick. In fact, the light after the lens is modulated by water absorption, thus light beyond 1350 nm hardly reaches the retina.

Experimental reflectance spectra of the ocular fundus is presented in Figure 2.16 b, which were reported by Elsner et al. [65]. This figure highlights that the spectral characteristics of the ocular fundus depend on the pigmentation of individuals: the dark-pigmented individuals (DP) reflect less light than the light-pigmented (LP) ones and, for both types of subjects, the retinal reflectance increases with the wavelength reaching values of 10% around 800 nm - 900 nm. This is the reason why it appears reddish.

This global reflectance can be explained by the individual reflectance and absorbance characteristics of each structure and layer in the retina [75]. The first retinal reflector is the inner retinal membrane, a narrow film between the vitreous and the retina that serves as another protection against UV light. This structure presents a quite flat spectral reflection and contributes to the final retinal image with both specular and diffuse reflectance [76].

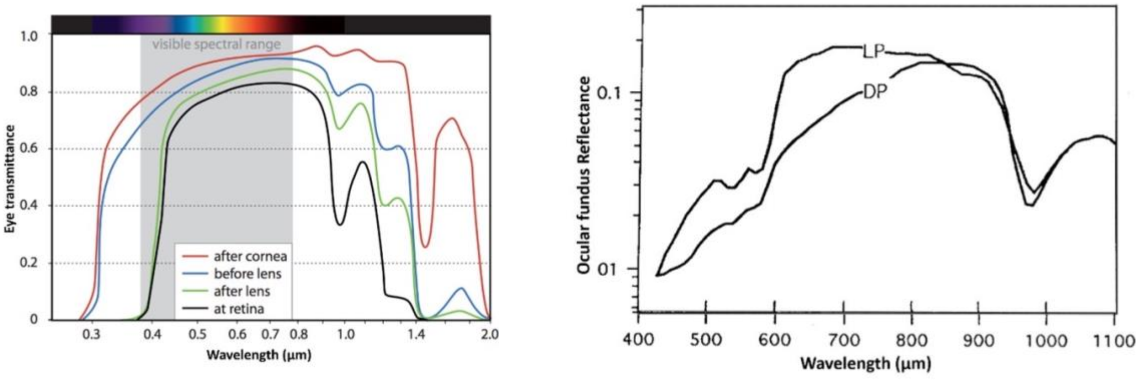

a) b)

Figure 2.16: a) Spectral transmittance of the eye at different axial locations, [1] and b) spectral reflectance of the retina for dark-pigmented (DP) and light-pigmented (LP) subjects (log scale), [65].

After this film, there is the NFL with a reflectance spectrum (Figure 2.17 a) that decreases with λ from 460 nm to 560 nm, with a very slight change between 560 nm and 680 nm [77], [78]. Therefore, the best region to study the NFL is in the blue part of the VIS range, where its reflectance is higher [79] and the light is still not absorbed by the crystalline lens.

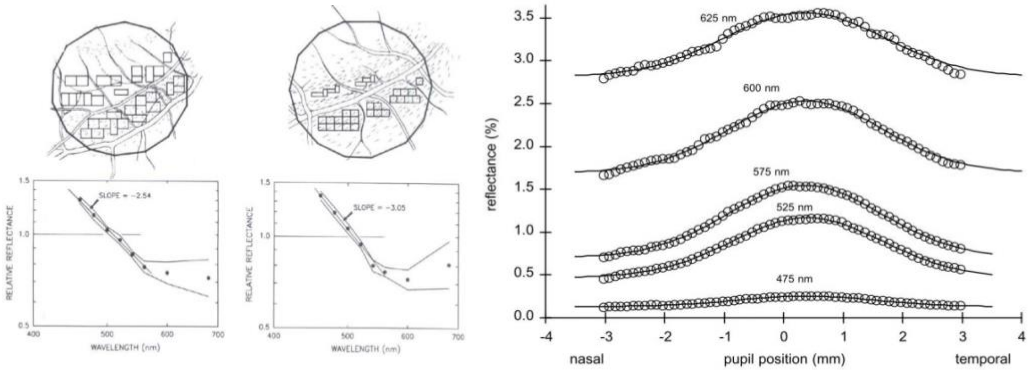

a) b)

Figure 2.17: a) NFL reflectance spectrum based on experimental results from two different sampled zones on the retina, [77]; b) Spatial profiles at five different wavelengths showing the Stiles–Crawford effect. Solid lines depict Gaussian fits [75].

Photoreceptors show a directional and spectral dependency of their response, named Stiles-Crawford effect, which is shown in Figure 2.17 b for different wavelengths and at different positions on the pupil's plane. This effect [80] comes from the light guide behavior and directionality of the outer segments of the cones, which are oriented within the eye in a way that they point towards the pupil center. Due to this, fundus reflectance exhibits a bell-shaped intensity distribution at the pupil plane [81]–[83] and a spectral change in the reflectance due to their ability to capture photons at different wavelengths [84]. Despite of this, the absorption of photoreceptors is neither relevant nor detectable in standard fundus photography due to the high levels of light involved. In fact, more than 99.5% of the visual photopigments present in rods and cones become bleached (saturated) by the flash [54], [85].

Macular pigments (Figure 2.18 a, c) are located in the inner retinal layers and extend over an area of 0.5-2.0° in diameter centered on the fovea. The spectral signature of these pigments, with their maximum absorption in blue, is recognized by the fact that foveal reflectance is lower than the perifoveal one for wavelengths shorter than 520 nm [86].

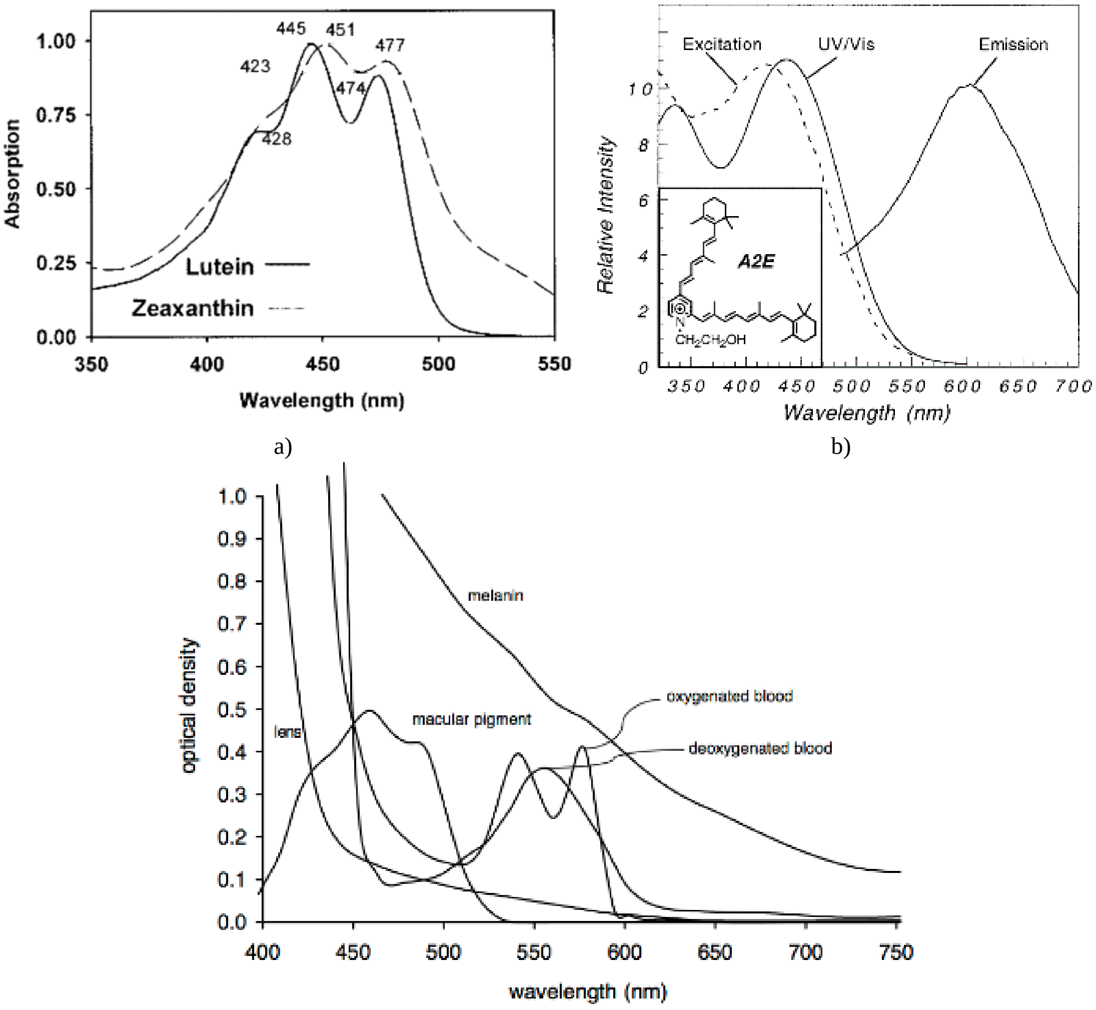

a) b)

c)

Figure 2.18 : a) Spectra of lutein and zeaxanthin in ethanol, which illustrate the characteristic differences in the absorption properties of the two carotenoids, [87]. b) UV/VIS excitation, absorption and emission spectra of A2E (major fluorophore of lipofuscin) in methanol, [88]. c) Absorption spectra of some substances of the ocular fundus, [75].

In particular, macular pigments such as lutein and zeaxanthin act as a yellowish filter absorbing light between 390 nm and 540 nm with a maximum at 460 nm [87], [89] (Figure 2.18 a). The density varies from person to person and a dependency on gender has been reported by Hammond et al. [90]. Macular carotenoids are very effective antioxidants, capable of reducing lipofuscin formation. Nowadays, autofluorescence of lipofuscin and fundus reflectometry allow objective quantification of macula pigment ocular densities, [91].

Between the retina and the choroid there is the Retinal Pigment Epithelium (RPE), a tissue with a high absorbance and dense melanin concentration, forming a dark pigmented wall [92]. The RPE helps in the absorption of scattered light, increasing the quality of the perceived image. This layer absorbs strongly at short wavelengths because of the melanin.

Lipofuscin, the name given to fine yellow-brown pigment granules mainly composed of lipid-containing residues, accumulates as a product of phagocytosis of photoreceptors in the outer segments. It is concentrated in the RPE and has an impact on the retinal spectral reflectance [93]. Its distribution increases from the eye equator and has a dip at the macula [94]. On the other hand, its concentration increases continuously through the entire life and, besides lipids, it can also consist of proteins and fluorescent compounds. The fluorophore with the maximum concentration is AE2, which is a derivative product of vitamin A, and its photoisomers are toxic and can lead to cells death. As it is shown in Figure 2.18 b, AE2 has absorbance peaks at 285 nm and 420 nm, and fluorescence emission around 600 nm [88], [95], [96].

While melanin concentration that resides in the RPE is similar between differently pigmented individuals, dark pigmented subjects have almost twice the amount of choroidal melanin than light pigmented subjects, [97]. The amounts of both choroidal and RPE melanin decrease with age and the spectral absorption decreases monotonically with increasing wavelength (Figure 2.18 c), with a $\lambda^{-4.6}$ trend in the middle of the VIS [98].

Hemoglobin is one of the most interesting sources of information and can be used for direct measurements of the metabolism of the eye. In fact, hemoglobin can be either oxygenated or de-oxygenated. In the VIS range, oxygenated blood shows spectral absorption maxima at 416 nm, 542 nm and 577 nm and minima at 510 nm and 560 nm, whereas de-oxygenated blood shows a local minimum at 470 nm and a local maximum 559 nm. In the NIR range, the spectral absorption curves of de-oxygenated and oxygenated hemoglobin cross around 800 nm. In this way, a study of the retinal oxygenation (VIS range) but also of the choroidal one (NIR-IR range) might be possible with HSI systems including these two spectral ranges, where the reflectance contribution of oxygenated and de-oxygenated hemoglobin are different [98], [99] (Figure 2.19).

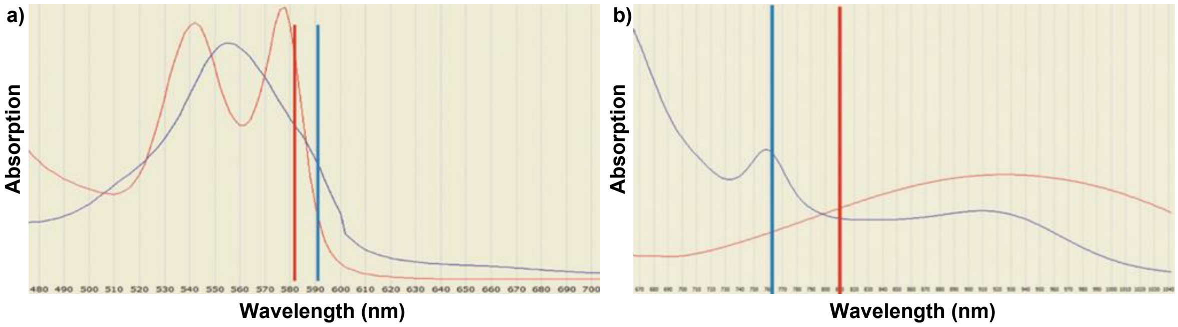

Figure 2.19 : Oxygenated (red) and de-oxygenated (blue) hemoglobin spectral absorption curves from 480 – 700 nm in a), and from 670 – 1040 nm in b). Common wavelengths used to provide oxygenation maps of the ocular fundus are highlighted with red (583 nm in a and 762 nm in b) and blue (590 nm in a and 810 nm in b) vertical lines, adapted from [53].

Finally, the sclera has a reflectance of about 50%. It is one of the most reflective surfaces of the ocular fundus and the last layer. From the literature, in vitro and in vivo measurements with human sclerae showed a slight decrease of reflectance with increasing wavelength, [75].

2.3.2.3 Diagnosis of retinal diseases with fundus cameras

The study of the ocular fundus helps in the investigation and earlier diagnosis of diseases affecting the retina, as different structures and substances can be highlighted and monitored. A detailed description of all diseases is out from the scope of this thesis but some of them are briefly presented below, [100]. For a comprehensive and exhaustive description the reader can refer to current literature [101].

Some of the most frequent diseases are glaucoma, maculopathies, diabetic retinopathy or retinitis pigmentosa. Visual dysfunctions and diseases are generally related with changes in concentration of particular substances, position, morphology and thickness of specific structures of the retina [75]. With age, a decrease in the central visual acuity and foveal light sensitivity may also occur. This might be partially explained by the cones malfunction due to decreased visual pigment density after the age 60.

Glaucoma is a retinal disease that mainly affects the NFL [102], reducing its thickness. It is caused by the progressive dead of several nerve cells due to the increase of intraocular pressure. One of the parameters used to diagnose the glaucoma is the optic disk/cup ratio [103], which can be studied from fundus images (Figure 2.20 a).It shows a wedge shape defect at the center of the optic disk caused by the thinning of the NFL (which is precisely measured with OCT systems, Figure 2.20 b) while the lamina cribrosa is exposed. The changes in reflectance of the NFL with fundus photography (Figure 2.17 a) might additionally help in the early detection of this disease [104]. In fact, by combining OCT technology with fundus cameras, it is possible to correlate the OCT images to pathology landmarks or to make follow-up measurements at later stages at exactly the same location on the retina [1]. Moreover, scientists have also analyzed spectral reflectance of the fundus at different stages of glaucoma. Changes found were attributed to a lack of oxyhemoglobin caused by damaged microcirculation in early open angle glaucoma [105].

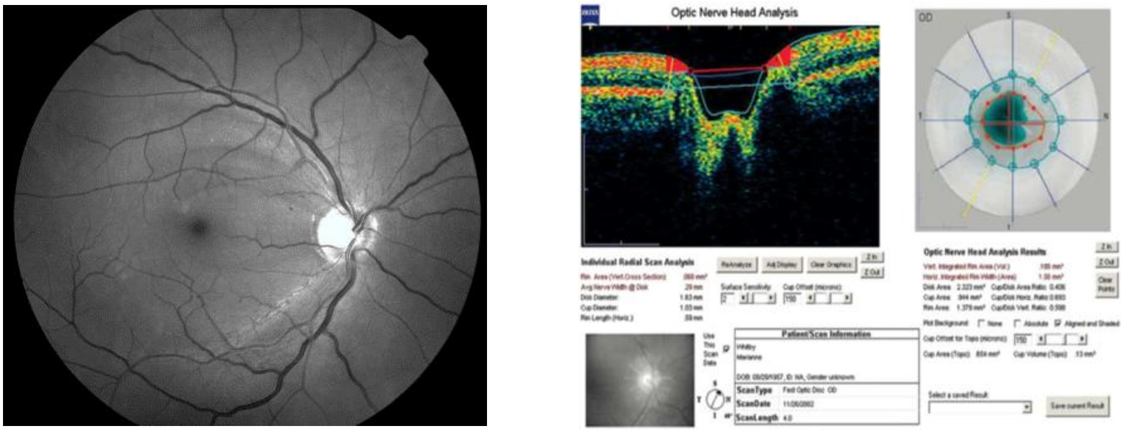

a) b)

Figure 2.20: a) Retinal image of an eye with a wedge-shaped defect in the NFL [105]; b) diagnosis based on OCT and fundus camera optic nerve head analysis. On the left, an individual OCT radial scan and a fundus image acquired with a Carl Zeiss OCT system are shown. On the right, composite diagram of the optic nerve head analysis. The yellow line indicates the position of the selected individual scan, [1].

High levels of lipofuscin in the RPE may contribute to the pathogenesis of macular diseases like Best disease, adult vitelliform macular dystrophy, Stargard disease, and ARMD. In the VIS region, the spectral fingerprint of lipofuscin resembles that of melanin. In this regard, early diagnosis of age related diseases such as ARMD [106], which is a degenerative disease that affects mainly the macula causing a loss of central vision, can be achieved by looking at the accumulation of these autofluorescent pigments generated by the phagocytosis of dead photoreceptors, or by simply studying the reflectance of melanin that prevents the advent of maculopathy and protects healthy photoreceptors from photodamage (Figure 2.21 a) [94], [107].

These accumulations (exudates) of extracellular material are called drusen (Figure 2.21 a), which are generally located between the RPE and the Bruch's membrane, with a color that can vary from white to pale or bright yellow. As drusen revert, they lose their coloration, which could be associated with glistening areas of calcification, areas of RPE atrophy or depigmentation. Drusen themselves may lead to deterioration and atrophy of the retina. Depending on their morphological features, they can be divided into hard and soft drusen. Hard drusen are smaller and have sharp edges while soft drusen are larger (diameter greater than 1000 μm), mound-like elevations with margins that are not clearly defined. They are often found in retinas with ARMD and are the most common early sign of the non-exudative form of this disease (see below). The amount, size, shape, distribution and clinical appearances can lead to different prognoses [108], [109].

ARMD can be divided in two category "dry" and "wet". About 90% of all people with ARMD have dry ARMD, a condition in which layers of the macula (including the photoreceptors and the RPE) get progressively thinner, functioning less and less as they do, which is called atrophy. At early stages of dry ARMD, the pigment or color of the macula changes and tiny drusen appear on the retina. Dry ARMD is also called non-neovascular ARMD or non-exudative ARMD because it does not involve the exuding of fluid from blood vessels. Advanced cases show RPE atrophy, which is the complete depigmentation and degeneration of the RPE. Wet ARMD is also called neovascular ARMD or exudative ARMD because it involves the exudation or leakage of fluid and blood from new blood vessels.

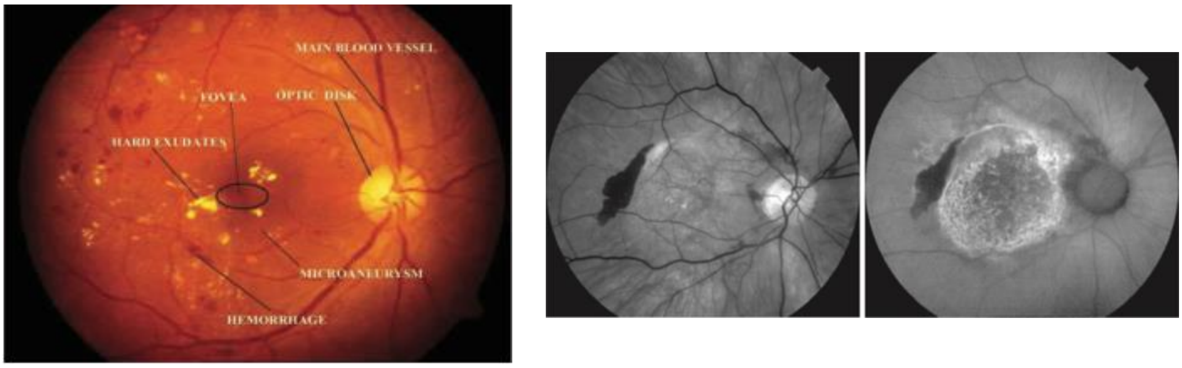

a) b)

Figure 2.21 : a) Fundus image of patient with ARMD (left) and fundus autofluorescence image to identify pigmentary changes and choroidal neovascular formations (right), [68]; b) illustration of various lesions (hemorrhage and drusen (exudates)) on a retina with diabetic retinopathy, [110].

Patients with diabetic retinopathy (Figure 2.21 b) do not present vision loss at early stages but when neovascularization, lesions and hemorrhages appear, it is often too late for a targeted therapy. Nowadays, fundus photography is the standard method for observing and recording this condition. However, the contrast between lesions and healthy surrounding tissue is limited and sometimes a green filter is used to enhance the superficial lesions, vascular abnormalities and associated hemorrhages. The use of these filters excludes completely the red part of the spectrum that also provides important diagnostic information. In this context, HSI in both the VIS and NIR ,allowing imaging of the choroid, could be a valuable tool to increase the contrast of specific structures by a tailored spectral analysis [111]. Using spectral fundus analysis in patients with diabetes, it has been actually shown that, even at early stages, alterations might occur especially in the choroid when they underwent laser photocoagulation as there is an alteration in blood flow, [75], [112]. Additionally, macular edema has been found to be associated with lowered foveal pigment density, decreased directionality of foveal cones and reduced foveal reflectance.

Retinitis pigmentosa is an inherited eye disease that causes loss of vision due to the progressive degeneration of the rod photoreceptor cells in the retina. Its early symptoms start with loss of night vision and FOV. The diagnosis of the ophthalmologist is confirmed by fundus and OCT images when dead cells at the periphery of the retina are observed, where the rods are denser. Once again, HSI systems can be helpful in order to highlight these structures in an earlier degeneration stage. Besides retinitis pigmentosa, retinitis is a general term to identify inflammations of the retinal and choroidal layers that can manifest as symptoms of viral infections related to other diseases such as toxoplasmosis, AIDS, etc. Sometimes, in these cases it is required to have enhanced contrast of the vasculature of the eye to be able to see bleedings and vessels. For this purpose, exogenous fluorescent dyes, such as fluorescein and ICG, are used to highlight retinal and choroidal layers, respectively [68] (Figure 2.22). In this way, fluorescein and ICG angiographies are important tools in the understanding, diagnosis and treatment of retinal disorders. This diagnostic imaging procedure uses a fundus camera or a SLO, after an intravenous injection, to capture a rapid sequence of the retinal vasculature [1]. In order to subtract the background and highlight the fluorescence, fundus cameras are equipped with a matched pair of excitation wavelengths (465 nm − 490 nm for fluorescein and 600 nm − 700 nm for indocyanine green) and detection filters (520 nm − 530 nm for fluorescein and 700 nm − 800 nm for indocyanine) to excite and detect only the fluorescence emission. This technique facilitates the in-vivo study of the retinal and choroidal circulation and is particularly useful in the management and assessment of retinopathies, macular degeneration as well as in the totality of retinal diseases that affect circulation. In rare occasions, fluorescein angiography of the iris and other anterior eye structures may be of value, too.

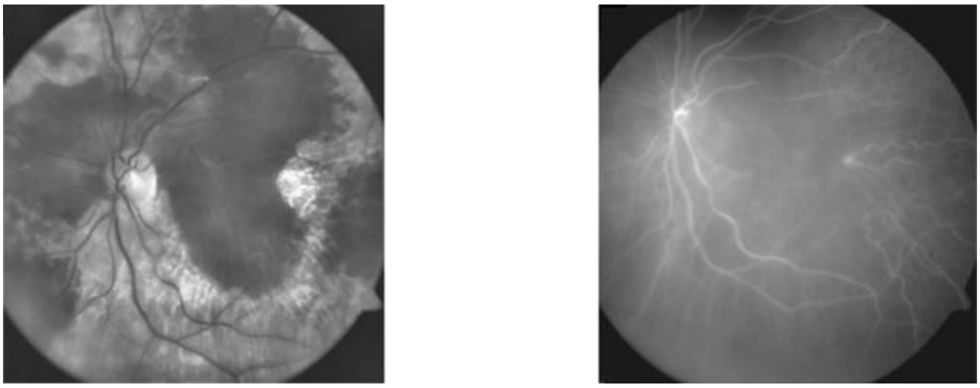
a) b)

Figure 2.22: : ICG images: a) Image acquired with a green filter of an eye with a large sub-retinal hemorrhage, and b) fluorescence image acquired with a NIR filter (835 nm) that reveals a sub-hemorrhage of the choroidal vessels, [68].

Other diseases that can benefit from the use of HSI fundus cameras for their evaluation are those affecting the choroid. This structure can be partially visualized with OCT (central peak wavelength 1060, [113]) or the novel OCT-Angiography [114], although they only provide good qualitative but limited quantitative morphological information (like thickness). However, when imaging the choroid with these conventional techniques, a great part of light is easily lost due to scattering and attenuation from pigment in the RPE and from dense microvasculature in the choriocapillaris [115]. Moreover, some eye disorders can trigger artifacts that degrade the quality of the images obtained from the choroid in conventional OCT methods, and therefore make its visualization difficult, as well as the layers segmentation, providing inaccurate results (Figure 2.23).

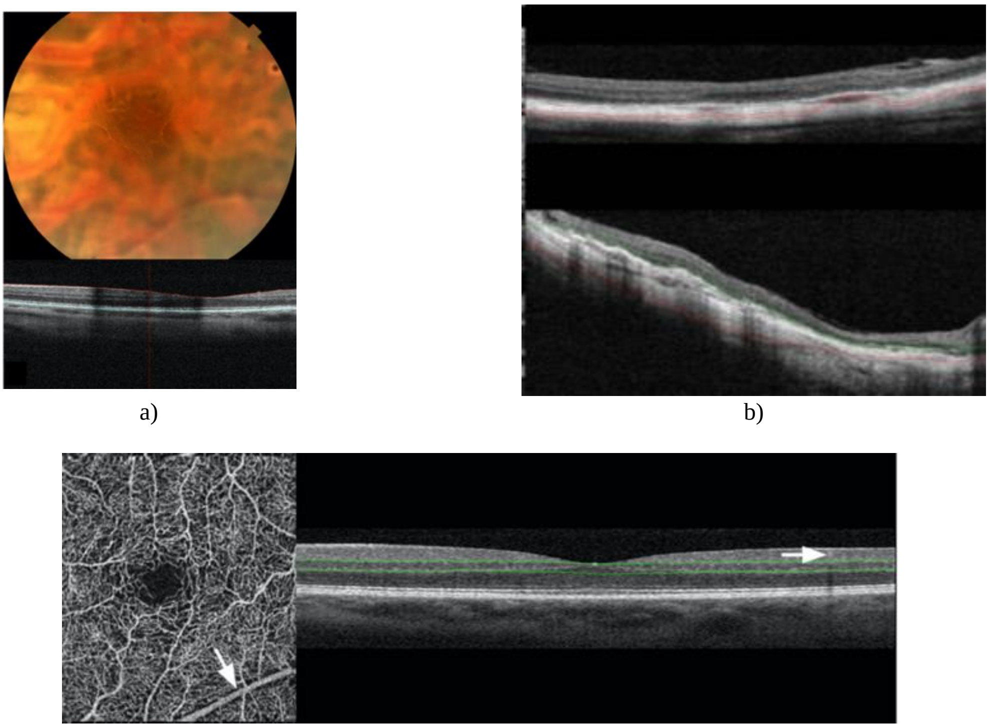

a)

b)

c)

Figure 2.23: Common artifacts in OCT images caused by the intrinsic properties of the eye: a) media opacity causing artifacts, b) blurred layer visualization in highly myopic eyes, which can lead to errors in their segmentation , d) inner retinal vessels causing artifacts (green lines), [115].

The choroid might be affected by different retinal disorders such as ARMD, central serous chorioretinopathy (CSC), diabetes and the Vogt-Koyanagi-Harada disease (VKH), or just become primarily involved in conditions such as polypoidal choroidal vasculopathy (PCV) and choroidal tumors. Besides ARMD, which has already been formerly described, CSC occurs because of a serous detachment of the neurosensory retina due to hyperpermeable choroidal capillaries, which often causes a central vision loss or distortion [116]. In turn, VKH disease is an inflammatory syndrome, which is probably a result of an autoimmune mechanism influenced by genetic factors [117]. On the other hand, PCV causes a serous-sanguineous detachment of the RPE, which is sometimes related with exudative ARMD. Finally, choroid tumors are caused by the abnormal growth of the choroid cells.

In the latter case, as there is a large variety, it is difficult to distinguish among them using only conventional color retinography, since information about the depth and the composition of the tumor is required. Shields et al. [118] analyzed 2514 choroidal nevi, some of them turning out melanomas, and concluded that the factors predicting tumor growth into melanoma included thickness (greater than 2 mm), subretinal fluid existence, symptoms of visual loss, presence of lipofuscin, margin near disk, ultrasonographic hollowness, and absence of halo. A study by Torres et al. [119] demonstrated, by means of OCT, that nevi show a homogenous and medium intensity band with visible choroidal vessels, whereas choroidal melanocytic nevi have a high intensity band at the Bruch's membrane and RPE (Figure 2.24). On the other hand, a band with low intensity in the deep choroid with enlargement of the suprachoroidal space was shown in choroidal metastasis. Therefore, it was concluded that there is a difference between the tumor intensity at IR wavelengths used in OCT imaging (commonly, 1060 nm), depending on its etiology.

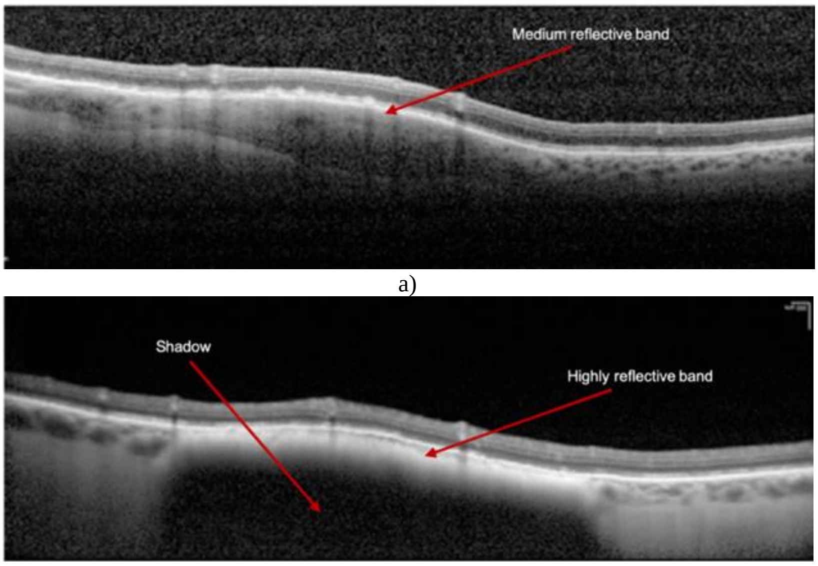

a)

b)

Figure 2.24: a) Amelanotic and b) melanocytic nevus, [119]. Images show that there is a difference in the reflectivity and the shadowing depending on the lesion etiology (a complete table of differences in reflectivity can be found in [119]).

2.3.2.4 HSI fundus cameras

HSI systems can be a powerful and straightforward approach to investigate biological tissues. Due to this potentiality, the spectral study of the retina has developed quickly in the last few years. Several works have been already carried out with the goal of characterizing the retinal and choroidal metabolism, and the composition and shape of the smallest retinal structures, such as vessels, drusen, etc. with the aim of improving the diagnostic tools used by ophthalmologists. One of the earliest attempts to apply HSI to ocular fundus was made by Riva et al. [120], who developed a MSI system with 7 filters integrated in a scanning disk, allowing the measurement of the reflectance from 400 nm to 800 nm. These authors made use of polarizers in order to cut off the back reflected light and register the metabolic changes of hemoglobin. A whiskbroom MSI system was later developed by Delori et al. [54] (Figure 2.25), who measured the averaged reflectance of retinal selected areas in healthy subjects. This was done by means of an adapted commercial fundus camera (Carl Zeiss Meditec) attached to a monochromator, which allowed dispersing light from 450 nm to 800 nm. In particular, the authors analyzed the influence of the age on fundus melanin pigmentation in different parts of the retina.

Hammer et al. [121] developed a fundus reflectometer based on a pushbroom scanner to record the spectrum of an entire retinal horizontal section in one single shot. This system was able to spatially and spectrally resolve 192 points of the retina, arranged on a line, with a spectral resolution of 2 nm and in a range from 400 nm to 710 nm. Thanks to this good spectral resolution, this system allowed highlighting different tissues and substances and discerning among arteries, veins, hemorrhages and exudates (Figure 2.26).

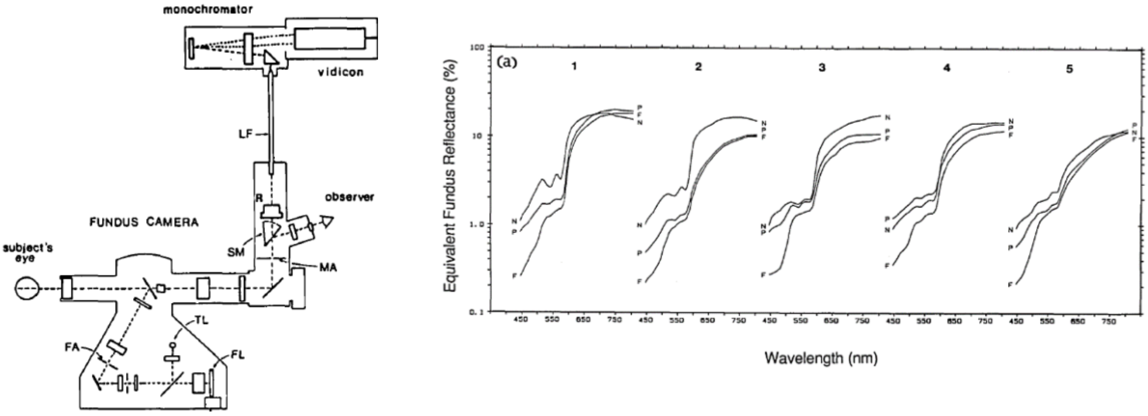

a) b)

Figure 2.25: a) Layout of a whiskbroom system for retinal reflectance measurement, and b) reflectance spectra from the nasal fundus (N), the perifovea (P), and the fovea (F) for five subjects with different degrees of ocular pigmentation. Subjects with blue irises (1,2,3) and green or hazel irises (4,5), adapted from [54].

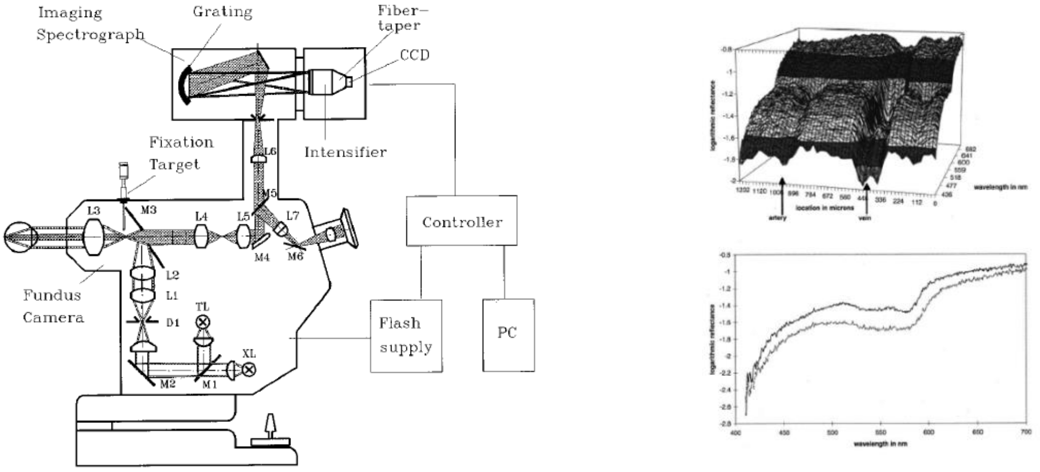

a) b)

Figure 2.26: a) Experimental set-up of the fundus pushbroom reflectometer, and b) local distribution of the reflectance spectra from blood vessels (top) and spectra from an artery (black) and a vein (grey) (bottom), adapted from [121].

In the case of staring imagers, tunable filters were used by Nourrit et al. [13] and [99] for the study of retinal structures in different diseases and retinal oxygenation (Figure 2.27). Both used LCTFs attached to commercial fundus cameras. In particular, Nourrit and colleagues observed the eye fundus at 8 wavelengths from 495 nm to 720 nm. They were able to characterize hemorrhages and the optic disk in patients with diabetic retinopathy and glaucoma. Mordant et al. built oxygenation maps of the vasculature, restricting the analysis from 560 nm to 630 nm.

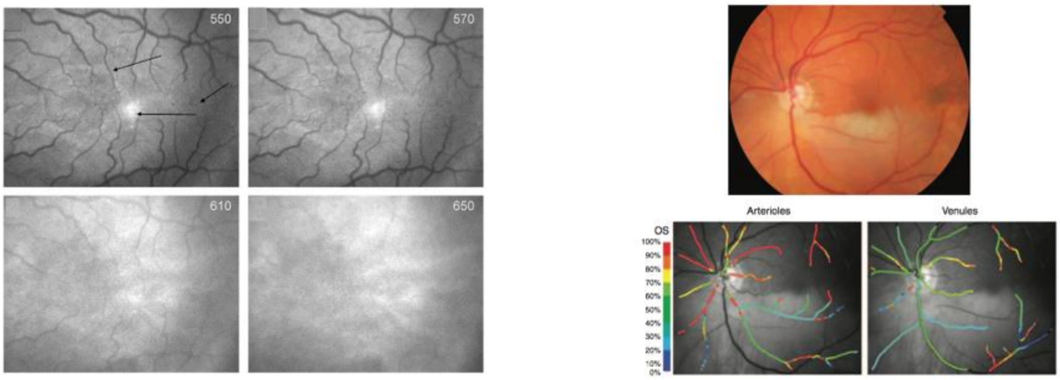

a) b)

Figure 2.27: Hyperspectral images of the ocular fundus acquired with a staring fundus camera: a) image of a retina with diabetic retinopathy, adapted from [13]; and b) oxygenation maps of arteries and veins acquired with a LCTF based HSI system, which reveals an occlusion in the inferotemporal retinal arteriole, adapted from [99].

On the other hand, Everdell et al. [14] and Zimmer et al. [53] used fundus cameras with a LED-based illumination and narrow band filters in order to increase the spectral resolution, proving that this approach is good at reducing artifacts and misalignments caused by the eye movements. Everdell and colleagues coupled the light of 6 LEDS into a fiber and collected the retinal reflected light with an EM-CCD, both attached to a commercial fundus camera. The spectral range covered was from 504 nm to 620 nm with a 4 nm step (Figure 2.28). This system gave a proof of the potentiality of LEDs when applied to HSI system for medical applications, allowing a fast control of the spectral scan when synchronized with the detection system (512 x 512 pixels retinal images were obtained in 0.6 s).

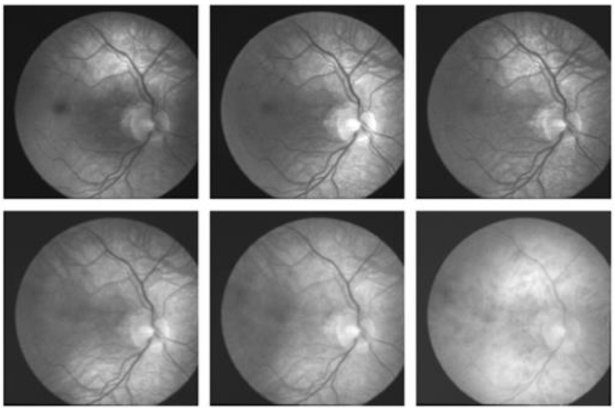

Figure 2.28: Images of the ocular fundus acquired with a LED-based spectral fundus camera. From left to right and top to bottom, the wavelengths are: 504, 525, 557, 582, 600, and 620 nm. It can be observed that the lower absorption coefficient of both hemoglobin and melanin at longer wavelengths is linked to a reduction in contrast, [14].

Similarly, Zimmer and colleagues used LEDs in a broader spectrum (from 550 nm to 850 nm) to study the choroidal structure and its composition. The system was based on a commercialized multispectral fundus camera (Annidis RHA, [53]) that used a LED illumination. Shanshan et al. [122] used the same system for the in-vivo study of retinal transmission function of choroidal layers, thanks to its NIR range imaging capabilities up to 850 nm. Besides the ones already commented, in the last few years several works have been presented showing the potentiality of the Annidis RHA system [15], [106]–[113]. Despite the fact that it includes a silicon-based imaging detector with limited QE in the NIR, it still provides new hints of the retinal and choroidal layers from an unprecedented point of view. In Figure 2.29, a sequence composed of 11 spectral images from 550 nm to 850 nm is shown. As can be noticed, the superficial layers including retinal veins and arteries, the fovea and nerve fibers are well visible at short wavelengths. As the wavelength increases, deeper layers of the ocular fundus come into view, especially the choroid. These studies also reveal that several diseases can be better studied using the spectral information from the NIR, [129]. In particular, the retinal pigment epithelium atrophy, diabetic retinopathy, Stargadt disease and uveitis.

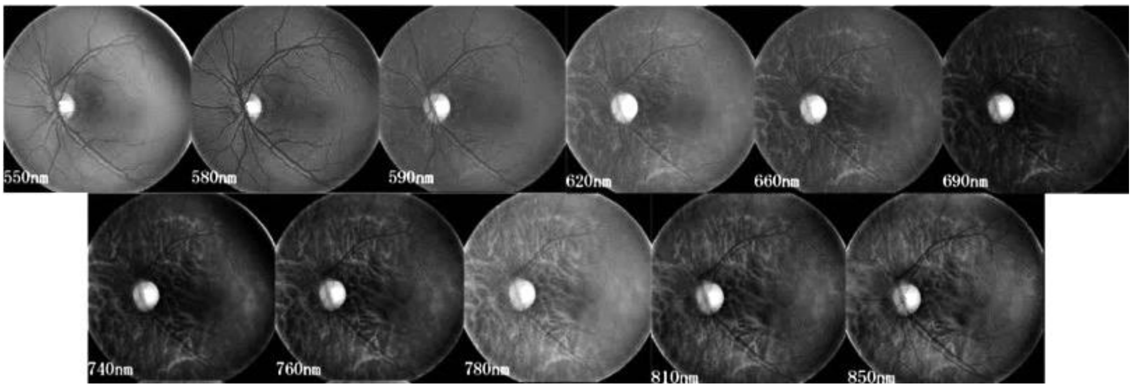

Figure 2.29: Fundus images taken at various wavelengths with the Annidis RHA fundus camera with sensitivity up to the NIR, which permits to highlight the retinal and the choroidal vessels, adapted from [122].

On the other hand, Bartczak et al. [111] used a light source composed of 42 different types of LEDs ranging from 380 nm to 780 nm to enhance the contrast of various retinal features and lesions in fundus images (Figure 2.30). In particular, optimal illuminants for diabetic retinopathy lesions detection were studied. They proved, with an optimization algorithm, that the intensity modulation of different spectral channels led to a mean contrast enhancement of 19% in comparison to red-free images.

Finally, snapshot systems have also been used for retinal imaging, where the speed of acquisition is essential. In this context, Gao et al. [12] presented a snapshot retinal HSI system using the IMS technique. The resulting system was capable of obtaining simultaneously a datacube of 5.880.000 voxels between 470 nm and 650 nm with a frame rate of 5.2 fps and a spatial resolution of 350 x 350 pixels (Figure 2.31a). The authors claimed that the system permitted the imaging of the retina providing spatial and spectral information of the presence of drusen and anomalous vessels and oxygenation maps. Although the system provided fast acquisition, heavy post-processing was required afterwards. The high cost of the image mapper is another drawback of this device.

On the other hand, Firn et al. [98] made use of an optical image splitter component and filters in order to obtain 7 narrow spectral channels of 4 nm width centered at 522 nm, 542 nm, 548 nm, 560 nm, 569 nm, 577 nm, and 586 nm. This system allowed reproducing 7 quasi-perfect copies of the same image and, projecting it on its seven filters, the authors encoded the spectral information on a CCD (Figure 2.31 b). The system was used for the dynamic recording of the oxygen saturation, demonstrating its fast acquisition. Nevertheless, its main drawback, besides the low spatial resolution was that, using specific spectral filters, the system performance was limited to fixed spectral bands.

To conclude, it is to be said that despite of the enormous technological improvements that have been made in the last years, some important limitations have not yet been overcome and HSI has still not shown its full potential in fundus imaging.

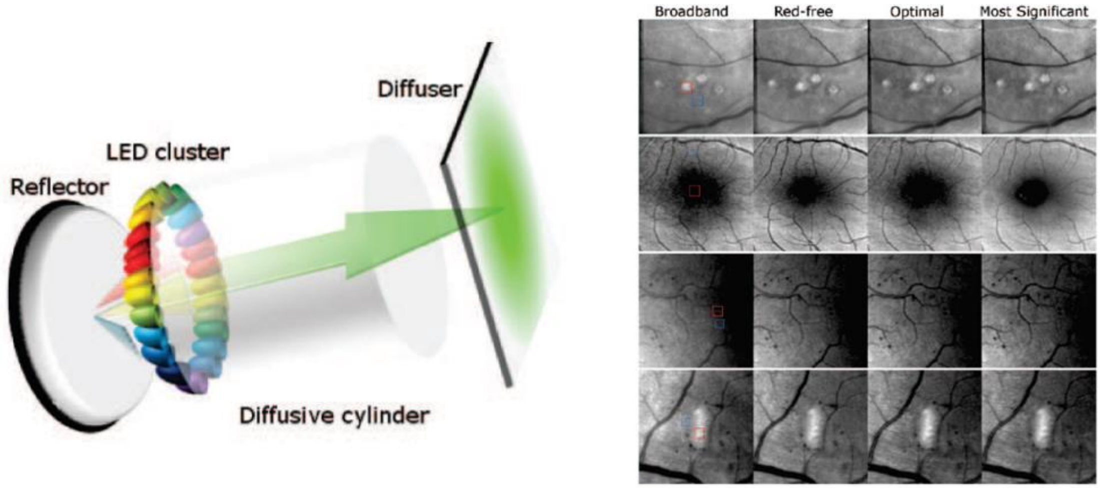

a) b)

Figure 2.30: a) Optical set-up of the LED-based spectrally tunable light source and b) segments from computational images demonstrating contrast-enhancement for the optimized illuminations compared with traditional broadband and red-free illuminations for different lesions caused by diabetic retinopathy, adapted from [111].

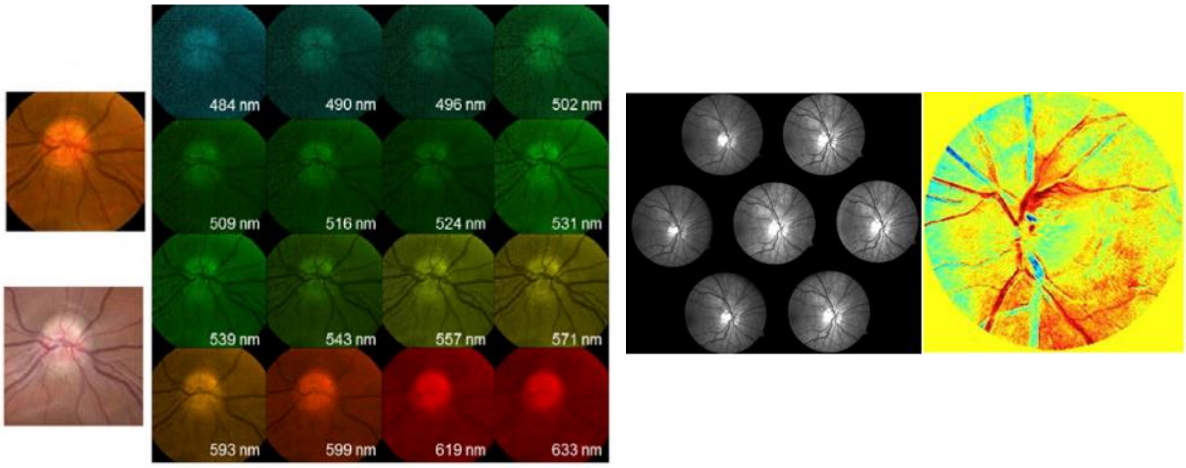

a) b)

Figure 2.31: a) Subset of 16 of 48 spectral images of the retinal optic disk, acquired with a snapshot HSI system, adapted from [12]. b) Monochromatic images corresponding to the seven spectral channels (left) that are used to reconstruct the oxygenation maps of the optic disk (right), adapted from [98].

3 FUNDUS CAMERA PROTOTYPE

The design and the laboratory prototype of the fundus camera developed in this thesis are described in this chapter.

3.1 Optical design

The system was designed according to the main goal of the thesis: to build a hyperspectral fundus camera with the largest possible number of spectral bands and with extended sensitivity in the NIR (400 nm to 1300 nm), to investigate deeper inside the back of the eye than commercially available fundus cameras. To achieve this goal, an internal-configuration retinograph was selected, according to the nomenclature used by DeHoog et al. [49] (see Section 2.3.2.1) , i.e., with optically independent detection and illumination arms, although still sharing the objective lens. In order to cover the desired spectral range, the use of 2 different cameras in the system was required: one based on silicon to cover the VIS and NIR (CMOS) and another camera with an InGaAs sensor to cover the IR range beyond 950 nm. In this way, the detection had to be split into 2 separate arms.

The simulations needed for this optical design process were carried out by means of the Zemax software (Radiant Zemax, USA) and using a Liou-Brennan eye model [131]. Sequential and non-sequential modes were used in order to obtain: (i) a design with a good optical performance of the illumination and detection arms of the system individually, and (ii) to test and optimize the system altogether.

3.1.1 Detection

As commented above, a retinograph with internal-configuration was chosen since it is more efficient than the external-configuration one in terms of illumination and light collection, although it has some additional complexity regarding alignment and removal of back reflections. In this configuration, the geometrical pupil separation between the light reflected by the retina and that reflected on the cornea and the lens is obtained by illuminating the retina with a ring of light focused at the patient’s pupil plane. Additionally, a holed mirror is placed at a plane optically conjugated with the patient’s pupil, allowing the imaging of the retina through the hole and preventing back reflections from the ocular optical elements to enter inside the detection path.

The detection system was designed according to the following premises: the best compromise in terms of resolution, FOV and light collection efficiency, and trying to reduce as much as possible the contribution of back reflections and optical aberrations on the fundus image through the entire spectral range, i.e., from 400 nm to 1300 nm. Our goal was to obtain a FOV of 30° and an optical resolution comparable or lower than the limit imposed by the imaging sensors used (pixel size of 6.5 μm for the CMOS and 20 μm for the InGaAs camera; see Appendix A for further details on the imaging sensors). Moreover, since we wanted to build a non-mydriatic system to avoid using eye dilation drops, we considered a minimum pupil diameter of 3 mm to illuminate and image the retina, as it is a common value found in commercial non-mydriatic fundus cameras. Additionally, all components to be used in the system should be commercially available (off-the-shelf) to keep the cost of the prototype low.

Besides of the optical elements of the eye itself, the holed mirror and the objective are the components shared between the illumination and detection paths, and for this reason the objective was the first component designed. This design consisted of 2 achromatic doublets to reduce as much as possible the spherical and chromatic aberrations (Figure 3.1). The diameters (50 mm and 30 mm) and focal lengths (75 mm and 50 mm, providing an effective focal length of 35 mm for the objective) of these 2 lenses were chosen in order to have the desired FOV of the retina and an eye relief of approximately 25.4 mm (distance between the patient's eye and the first lens of the objective). This configuration is the result of the trade-off between the market availability of lenses, the required FOV (mainly limited by the objective NA) and the minimum feasible eye relief distance that we have considered (19 mm). The use of 2 achromatic doublets has the advantage of keeping the aberrations contribution lower than in a single lens approach but, due to the considerable number of optical interfaces (three for each doublet), it produces more ghost images. As compensating large aberrations in the design of the rest of the detection system might be not feasible with commercial optical components, we decided to assume this constraint so as to assure a good quality of the retinal image on the sensors.

The holed mirror was placed at the plane conjugated with the eye's pupil plane by means of the objective lens (1st Pupil image in Figure 3.1). The light passing through the hole is then collected with an achromatic triplet (50 mm focal length) to keep the chromatic aberrations low throughout the entire spectral range. This triplet was placed so that its object focal plane lied at the pupil image plane. This arrangement corresponds to a telecentric configuration, which assured that the FOV of the system does not change with the refractive error of the eye under examination. Afterwards, a dichroic mirror was placed to split the optical path in two: one for the spectral range between 400 nm and 950 nm (VIS-NIR), and the second for that between 950 nm to 1300 nm (NIR-IR). The subsequent optics of both optical paths are devoted to form the images on the detectors.

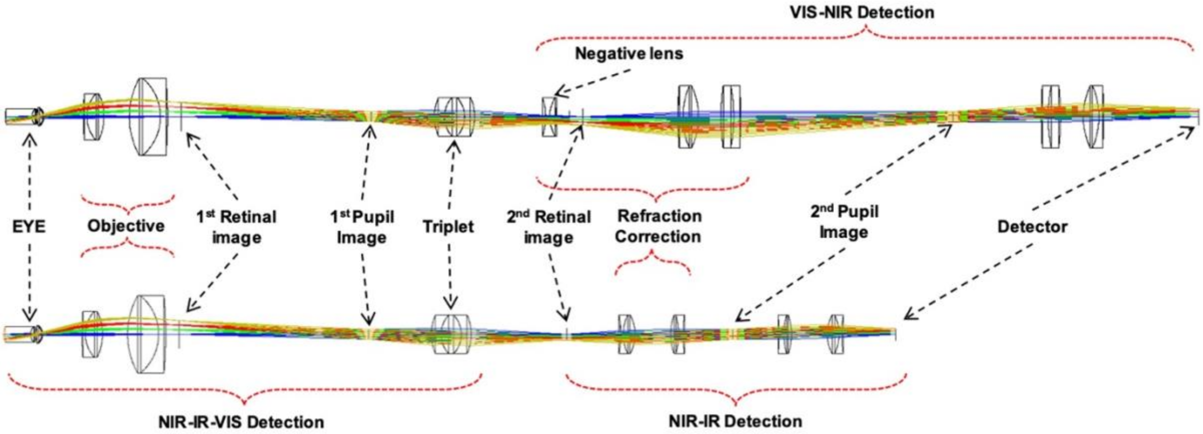

Figure 3.1: Schematic optical layout of the VIS-NIR (top) and NIR-IR (bottom) detection paths.

To form the image on the detector of the VIS-NIR range, we designed a system composed by a negative lens (focal length -50 mm) in order to change the magnification to match the sensor size and to correct for the field curvature, and a 1:1 telescope composed by 2 pairs of achromatic doublets (effective focal length of 75 mm of each pair). For the NIR-IR path, a 1:1 telescope with 2 pairs of achromatic doublets (effective focal length of 50 mm of each pair) was also placed just after the dichroic mirror.

In order to compensate for the patient's refraction, these two optical paths were designed in a way that part of them could be moved along the optical axis of the system (see components noted as Refraction

Correction in Figure 3.1). This ensured a refraction correction of at least ±15 D for both detection arms at the same time and, as previously stated, without changing the magnification (detected FOV) thanks to the telecentric configuration. The chosen design allowed both VIS-NIR and NIR-IR telescopes to be jointly moved with a linear translational stage. Finally, the second pair of achromats of each telescope focused the retinal image on the cameras' sensor planes. The paraxial magnifications (ratio between retinal image and its corresponding size on the retina) - considering Liou-Brennan's eye model - were 1.21 for the VIS-NIR and 0.88 for the NIR-IR ranges. Special care was also taken to minimize the radial distortion, which had a maximum of -1.45% and -1.92% for the VIS-NIR and NIR-IR arms, respectively, at the full FOV (30°).

Field diaphragms were placed at planes conjugated with the retina (noted as 2nd Retinal Image in Figure 3.1) to obtain sharp-edged 30° images and to minimize the effect of straylight. A pair of diaphragms, slightly smaller than the holed mirror pinhole, were additionally placed at pupil conjugated planes (2nd Pupil Image), thus effectively acting as the aperture diaphragms of the system. The best balance between diffraction and aberrations was achieved with a detection pupil diameter of 1.75 mm (R_i = 0.875 mm), similar to the values reported in the literature.

We designed our system to match, as much as possible, the chromatic focus shift with the thickness of the ocular fundus layers, i.e., the best focus position going deeper into the fundus tissue as the wavelength increases. In this way, focused images for long wavelengths can be achieved, in accordance with their larger penetration depth. To characterize this shift at the retina as a function of wavelength, 2 point sources were simulated at the retinal plane: one on-axis and another at 7.5° (0% and 50% of FOV, respectively). The axial position of the sources (retinal depth) was then optimized (best focus on the image plane). These simulations were carried out for an emmetropic eye for both the VIS-NIR and NIR-IR detection arms, covering the entire spectral range of the hyperspectral camera (400 nm to 1300 nm) with a wavelength step of 50 nm. The results are depicted in Figure 3.2, as well as the corresponding depth of field (vertical bars) considering the resolution limit imposed by the pixel sizes of the two sensors.

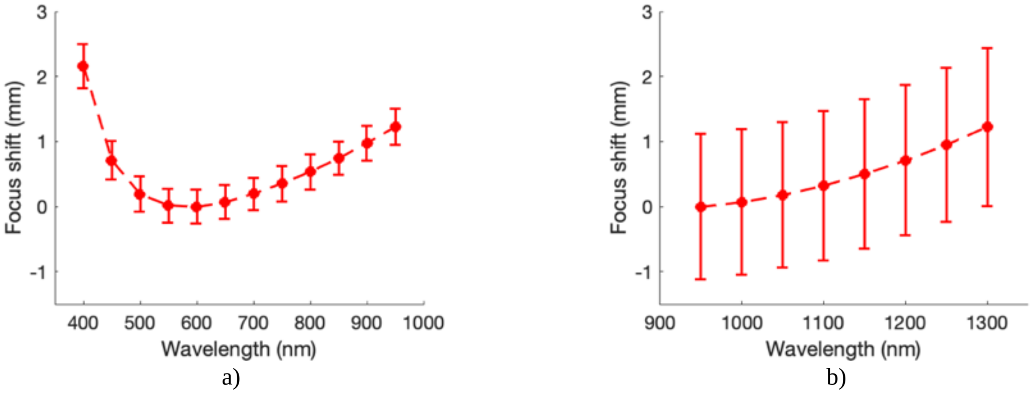

Figure 3.2: Focus shift at the retina vs. wavelength of the system for an emmetropic eye, for both the VIS-NIR (a) and the NIR-IR (b) spectral ranges. The vertical bars are the depth of field for each wavelength considering the resolution limit imposed by the pixel size of the cameras.

As can be seen, despite the careful design for chromatic aberration compensation, the maximum focus shift is larger than the ocular fundus thickness (which is less than 1 mm from the inner limiting membrane to the sclera) for both the VIS-NIR and the NIR-IR arms. However, the effect of this optical defocus is significantly mitigated by the large depth of field given by the pixel size of the cameras. For instance, in the VIS-NIR arm (Figure 3.2 a), the images for all wavelengths above 450 nm could be considered to be in focus (or almost) within their targeted retinal depth range. For deep blue wavelengths, the focus shift has the opposite effect as the one desired (best focus for very deep layers, instead for more superficial ones), so blurred images are expected in those wavelengths. Nevertheless, this limitation was accepted enabling the use of off-the-shelf components, and thus keeping the cost of the system low.

The depth of field magnitude is even more noticeable in the NIR-IR arm (Figure 3.2 b), due to the larger pixel size of the InGaAs sensor (20 μm). In this case, all ocular fundus layers can be considered to be in focus for its entire spectral range (950 nm to 1300 nm). The spatial resolution limitation given by this pixel size would not be critical in practical terms, as the images for these IR wavelengths would be strongly affected by scattering of fundus tissues, as they penetrate more into it, so that only the largest structures would be observable. In order to match the focusing ranges of the two detection arms, we chose to make the minimum focus distance ("0" focus shift in Figure 3.2) coincident for both. That is, when a given plane is optically focused in the VIS-NIR camera for 600 nm, it will be also optically focused in the NIR-IR camera for 900 nm.

Additionally, the optical quality of the system, regardless of the used sensor, was evaluated through the entire spectral range and over the full FOV. To do so, the Strehl ratio of the system was computed (Figure 3.3) changing the retinal depth in each case to match the focus shift, thus simulating the optical performance for different layers of the ocular fundus.

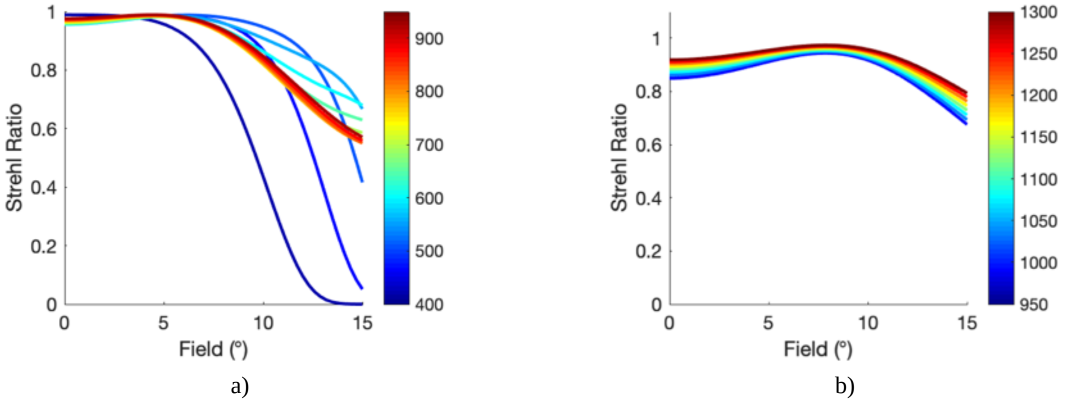

a)
b)

Figure 3.3: Strehl ratio vs. field for various wavelengths (depicted from blueish to reddish as wavelength increases). a) VIS-NIR spectral range. b) NIR-IR spectral range.

The Strehl ratio curves for wavelengths in the spectral range from 450 nm to 1300 nm showed a value above the 0.8 reference (Rayleigh criterion) for radial fields up to 10°, so they can be considered diffraction limited. Furthermore, a Strehl ratio value above 0.6 is maintained over the entire FOV for wavelengths above 500 nm. The worse image quality is obtained for deep blue wavelengths, with an important decrease of the Strehl ratio at the edge of the FOV. This is mainly due to field curvature, which makes the image at the border of the FOV to be out of focus.

For a deeper analysis of the optical performance along the spectral range, the sagittal and tangential Modulation Transfer Functions (MTF) were evaluated at three reference fields: 0°, 7.5° and 15° (Figure

3.4). The observed decrease of the MTF with the wavelength is due to diffraction. Apart from this, the MTF shows that the system preserves optimal optical quality, as expected from the Strehl analysis, without strong aberrations in any direction except the tangential one (15°) and blue wavelengths. In this case, the aberrations are much more significant, in particular the astigmatism and coma, as well as the aforementioned field curvature.

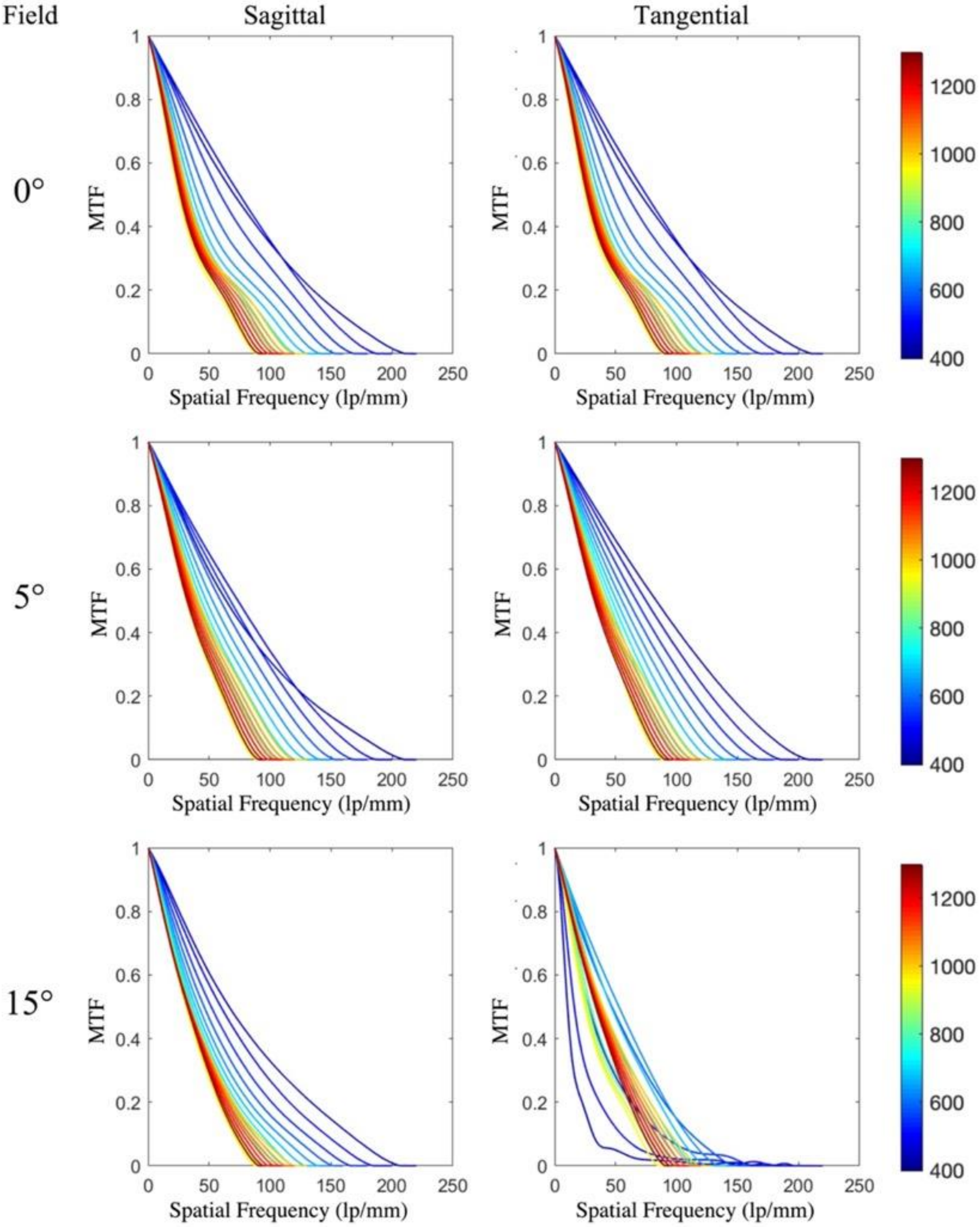

Figure 3.4: Sagittal (left) and tangential (right) MTFs for three positions in the FOV: 0°, 7.5° and 15°, and for wavelengths from 400 nm to 1300 nm (depicted from blueish to reddish as wavelength increases).

From these results, it can be concluded that, despite residual aberrations, which are a consequence of using commercially available optics, the optical quality of the system is good over the entire FOV and spectral range, except for wavelengths below 450 nm. Moreover, the optical resolution is better than the limit imposed by the imaging sensors for both detection arms (76.9 lp/mm and 25 lp/mm for the VIS-NIR and NIR-IR ranges, respectively) for the full FOV, as can be seen in Figure 3.4.

3.1.2 Illumination system

Taking the objective designed for the detection as the starting point, the illumination was designed to grant a good geometrical pupil separation, a homogeneous distribution of light on the retina and maximal illumination efficiency (minimum losses of light emitted by the source). In this context, the designed illumination system can be divided in 3 main subsystems: one that combines the light from several LEDs into one single broadband source, another which creates the ring-shaped illumination, and a third one composed by a 1:1 telescope and the objective lens, which forms the image of the ring on the patient's pupil plane.

Regarding the combination of light from different sources, three main approaches were considered. The first one was a commercial system (Mightex Systems, Canada) that couples the light of several LEDs using dichroic mirrors (Figure 3.5 a) into a single fiber with quasi-perfect superposition at the fiber exit. This system allows a large number of LEDs to be coupled, but it is expensive and hardly customizable.

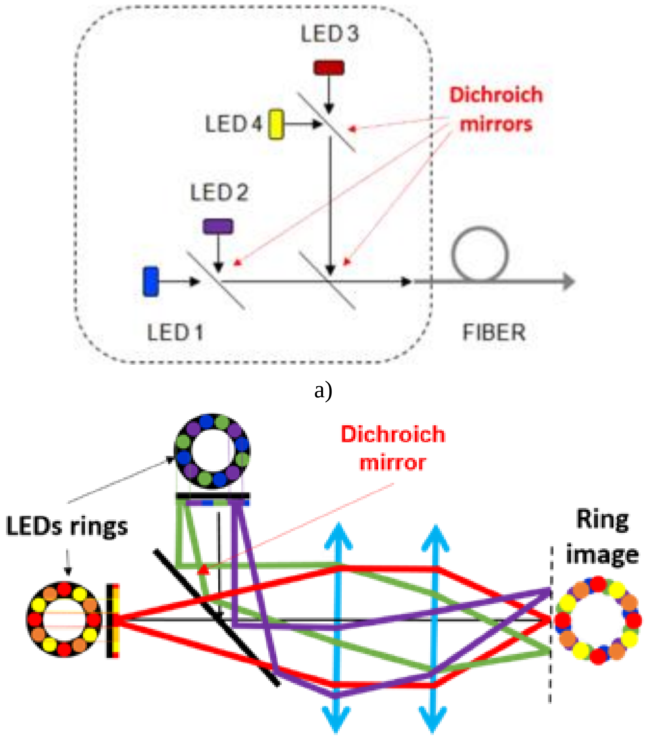

a)

b)

Figure 3.5: a) Layouts of the LEDs coupling system from Mightex Systems and b) custom-made coupling system with LED-based rings.

The second strategy consisted of a custom-made optical system including a set of dichroic mirrors and condensers that collimate the light from different LED sources, combining them into the same optical path. The advantage of this approach is that its cost is lower; but the alignment, coupling efficiency are worse than in the above-mentioned commercial system. Moreover, the space required is bigger.

The third strategy consisted in using custom-made rings (Figure 3.5 b), each including LEDs with different wavelengths welded in a symmetrical configuration to provide the most homogeneous illumination. In contrast to common fundus cameras, the illumination ring for each wavelength is discontinuous (discrete) and composed by the images of the LEDs, which are formed at the patients' pupil plane. This configuration joins the light of different LED rings by means of dichroic mirrors and has the advantage of not requiring any additional optics to create the ring shape. Therefore, the cost of the optics drops considerably down and the efficiency is increased. However, it presents some disadvantages, as the limited number of rings that can be implemented, the number of LEDs inside each ring and the discontinuity of the illumination, which can affect homogeneity of light on the retina. In particular, the number of LED rings is limited by the space required to combine the light from different rings in one single path; the number of LEDs with different wavelengths in each ring is limited by its diameter that, in turn, is limited by the pupil diameter, and the minimum intensity required to illuminate the retina limits the number of LEDs for each wavelength.

As above-mentioned, the latter approach does not require any further strategy to create the ring shape of the illumination. For the other two options (the fiber-based solution or to compose the light from different LEDs using dichroic mirrors and lenses), we designed and simulated 3 configurations to generate the ring illumination pattern at the pupil's plane (Figure 3.6).

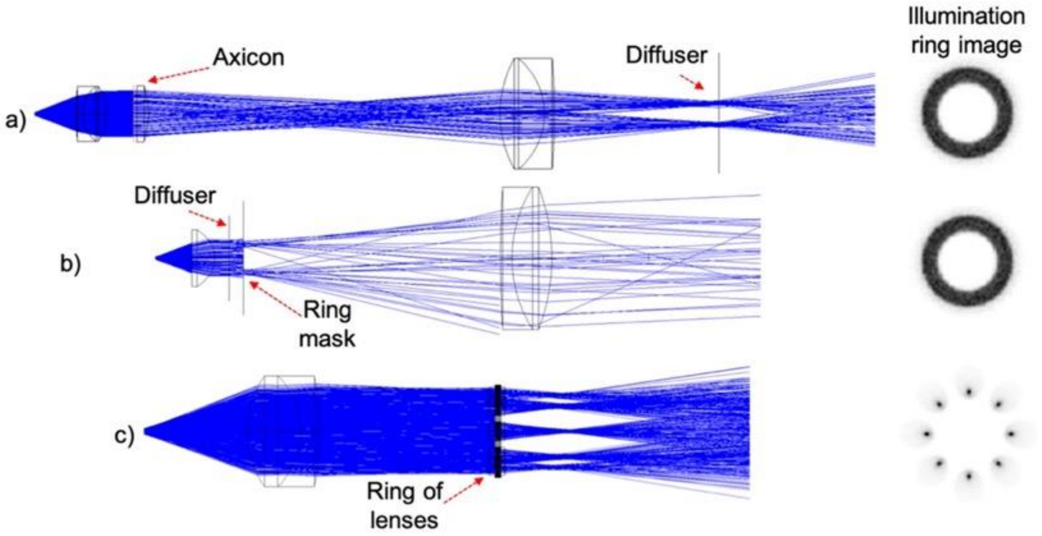

Figure 3.6: Systems used to create a ring-shaped illumination at the pupil plane: a) system that uses an axicon, b) system used in common fundus cameras with a diffuser and a binary mask and c) system that uses an encapsulated ring of lenses to produce a ring-shaped image at the pupil plane.

The first solution (Figure 3.6 a) uses an axicon. This is a conical optical component that forms a cone of light from a collimated beam. Afterwards, a ring-shaped illumination with the proper dimensions can be created choosing the apex angle of the axicon and placing a lens with a suitable focal length. In this case, the resulting illumination is strongly inhomogeneous if a diffuser is not used just after the lens. The advantage of this configuration is that it involves the smallest light losses, despite the use of the diffuser; however, it is the most expensive.

The second option refers to the standard approach traditionally used in fundus cameras (Figure 3.6 b), where a diffuser is used after collimating the light from a lamp or a fiber. Then, a binary mask is inserted, letting the light pass through a ring with precise internal and external radii. This system is the simplest and cheapest one in terms of optical components but it presents the lowest illumination efficiency.

The last method (Figure 3.6 c) makes use of a custom-made ring of lenses encapsulated within a thin cylinder. As in the case of the light combination strategy that uses LED rings, the illumination ring is discontinuous, with one focalized spot of light for each encapsulated lens. Regarding the collection efficiency, this system gathers less light than the axicon; but considering that it does not require a diffuser, the overall illumination efficiency is balanced. Apart from this loss of the light that does not pass through the lenses of the ring, its main disadvantage is the cost of the lenses.

All possible approaches of LEDs light combination and ring shaping strategies were simulated by means of non-sequential ray tracing in Zemax, using available source files from manufactures. A summary of the obtained performance is shown in Table 1.

Table 1: Summary of the characteristics of each simulated illumination strategy. The values of light source powers were found during an exhaustive search among different manufacturers in the designing phase. The collection efficiencies were calculated in the simulations as the ratio between the light reaching the retina and that emitted by the source. Then the resulting power is simply calculated from the former columns. The cost was estimated from optical, LEDs and light sources manufacturers' catalogs.

Light combination	Ring shaping	Source Power		Collection efficiency	Resulting power at the retina (Best Case)	Average cost (in k€)
Fiber based combination	Axicon (Diffuser)	VIS-NIR	1-10 mW	50-60%	6 mW	22
		NIR-IR	0.1-1 mW		0.6 mW	
	Ring mask (Diffuser)	VIS-NIR	1-10 mW	1-10%	1 mW	21
		NIR-IR	0.1-1 mW		0.1 mW	
	Ring of lenses	VIS-NIR	1-10 mW	30-40%	4 mW	22
		NIR-IR	0.1-1 mW		0.4 mW	
Custom LEDs combination	Axicon (Diffuser)	VIS-NIR	100-500 mW	5-6%	25 mW	10.1
		NIR-IR	10-100 mW		2.5 mW	
	Ring mask (Diffuser)	VIS-NIR	100-500 mW	0.1-1%	5 mW	9.1
		NIR-IR	10-100 mW		1 mW	
	Ring of lenses	VIS-NIR	100-500 mW	3-4%	20 mW	4.1
		NIR-IR	10-100 mW		4 mW	
LEDs rings	-	VIS-NIR	100-500 mW (2x)	1%	10 mW	1.1
		NIR-IR	10-100 mW (2x)		2 mW	

In view of the results, the advantage of having a fiber-based solution is clear since the light from the LEDs is well combined into one single source; nevertheless, these approaches are the most expensive ones. On the other hand, the solution based on custom LEDs combination needs custom-made optics to compose the light from different LEDs and this, besides its cost, requires considerable room making the prototype bulky. Instead, the LED ring solution joins the light from different LEDs without the need of any additional shaping system.

After an in-depth search of commercially available components, we finally chose the LED rings solution. This configuration could be easily manufactured in our mechanical and electronic workshops, making this solution easily customizable and cheaper. Furthermore, the cost of the optics and the space required to build this system is substantially smaller than in the others. Despite of the reduced light collection efficiency, the commercial availability of LEDs and the unnecessary use of diffusers allowed us to design 3 LED rings with 15 wavelengths (spectral channels) comprised between 400 nm and 1300 nm. These produced an amount of light reaching the retinal plane higher than the fiber-based techniques and not so different from the best solution (LED combination + axicon). In particular, for each spectral channel, at least 2 identical LEDs were placed symmetrically in one of the rings (Figure 3.7 b). The simulations actually proved that this choice was a good trade-off between the number of spectral bands and the efficiency to illuminate homogeneously the retina (Figure 3.7 c). As required by the detection, the ring size and the magnification of the telescope (1:1, formed by 2 achromatic doublets of 100 mm focal length) was chosen so that the ring image formed at the patient’s pupil plane, composed by all twin pairs of LEDs, had internal and external diameters of 2 mm and 4 mm, respectively (R_L = 1 mm; R_O = 2 mm); the calculated centroid of the image for each LED was1.47 mm far away from the optical axis.

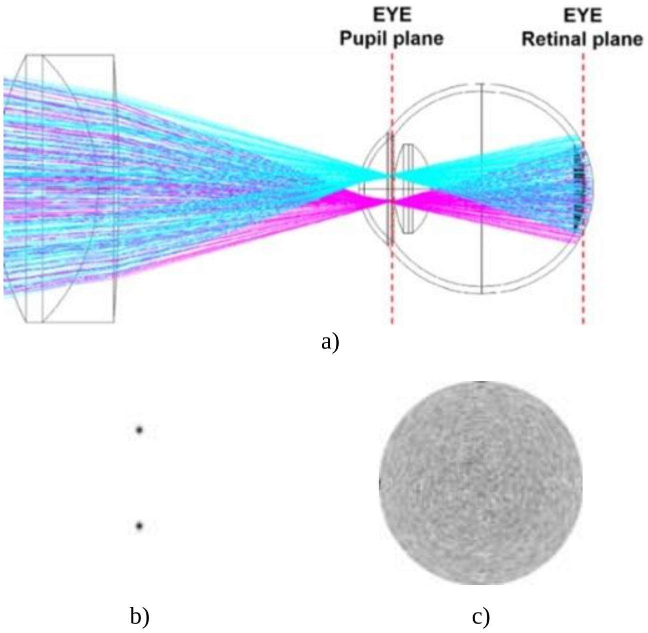

a)

b)

c)

Figure 3.7: Ray tracing simulations with the LED ring configuration with 2 symmetrically arranged LEDs emitting at 850 nm (central wavelength of the considered spectral range). a) Objective and eye model with the pupil and retinal planes labeled. b) Light distribution at the pupil plane and c) at the retina (30° FOV). The contrast of the image in (c) was inverted for visualization purposes: darker regions correspond to zones reached by more rays.

The risk of choosing this strategy is that, due to the differences in shape from pair to pair of LEDs and the discontinuity of the illumination, the images corresponding to each spectral channel might provide a slightly different retinal illumination so that a correction would be necessary.

3.1.3 Simulations on the integrated system and removal of ghost images

Once the optimal design of the illumination and detection systems had been achieved, non-sequential simulations of the entire system were carried out in order to test its performance as a whole. In particular, the non-sequential modality allowed us to test the geometrical pupil separation between the illumination and detection arms by means of the holed mirror placed where the image of the ring is formed, i.e., the 1st Pupil image in Figure 3.1, after the illumination telescope (Figure 3.8). Setting the reflectivity of each surface of the eye model to 100% we ensured that the light reflected from the cornea and the lens formed an image on the external reflective part of the holed mirror, without entering inside the detection path.

Common fundus cameras generally use a single aspheric objective lens and/or customized optics to minimize the number and intensity of ghost images. In our case, due to the use of commercial optical components, and the consequent use of achromatic lenses to reduce as much as possible the chromatic aberration, several ghost images appeared on the detector. Despite choosing achromats with high performance broadband anti-reflective coatings, part of the incident light was still reflected (between 0.5% and 3%), thus reducing but not avoiding the ghost images. In order to get rid of these undesired artifacts, black stops (labeled as covering points in Figure 2.15) were inserted in the middle of the 1:1 telescope at specific positions, as shown in Figure 3.8 a, in order to shade the portion of the objective creating the back reflections.

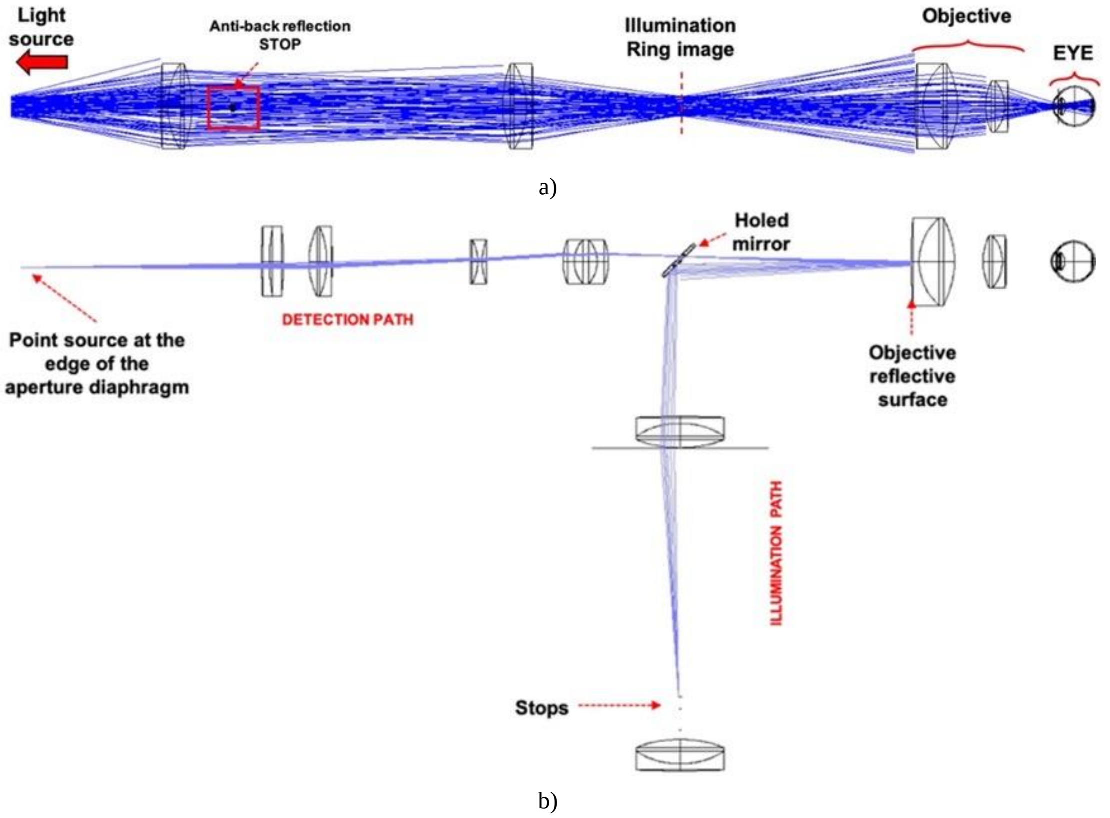

Figure 3.8: a) Simulated illumination path (not folded) and ray tracing simulation showing the position of an axial stop (the dimensions of the stop is not in scale). b) Non-sequential simulation of the fundus camera (illumination + VIS-NIR detection) for the optimization of the removal of ghost images.

The location, number and diameter of those stops were analyzed considering each surface of the objective independently as a perfect mirror, and tracing back towards the illumination arm the light of a point source placed at the edge of the aperture diaphragm of the detection system (Figure 3.8 b). By doing so, we assured a proper shading of the light reflected on the objective's surfaces that would pass through the aperture diaphragm. In accordance with the results of these simulations and for the sake of simplicity, a unique 1.6 mm (radius) stop was finally considered, which, placed at the proper position, avoided the reflections from all surfaces.

This stop, as reported elsewhere and predicted by our simulations, led to some inhomogeneities on the illumination pattern (Figure 3.9). In our design, they are close to the optical axis so its removal is critical. In fact, as the black stop is lighted by a pair of LEDs used for a specific spectral band, a portion of the illumination cone of each LED is shaded. Once the illumination cones are superimposed along the optical path, also the shaded portions are, thus appearing as two symmetrical dark circles (shadows) at the retinal plane. It should be noticed that, if the stop was exactly located at a plane conjugated with the retina (not nearby as it actually is), the shaded portions of the illumination cones would be completely superimposed, and only one completely dark shadow circle would appear, making impossible the extraction of information in that area. In the developed HSI prototype, the removal of these inhomogeneities by means of processing algorithms makes possible to extract information of the whole retina, as described later in this thesis.

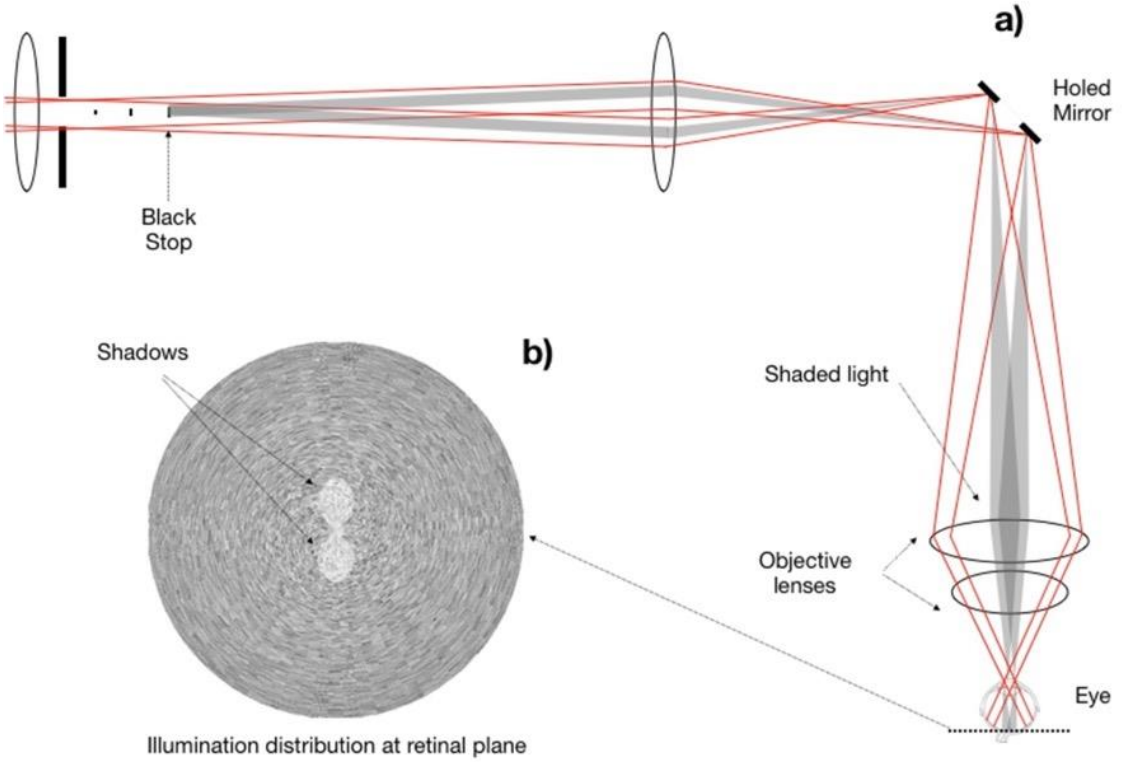

Figure 3.9: a) Schematic layout of the shading effect of the black stop. Red lines indicate the illumination. Gray areas represent the shaded portions caused by the black stop. b) Illumination distribution at the retina. The contrast of the image in b) was inverted for visualization purposes: darker regions correspond to zones reached by more rays.

3.2 Experimental set-up

An experimental set-up to acquire spectral images of the ocular fundus was developed, implementing the optical design explained above. In this section, the built system is described, including the optical and electronic components, as well as the developed software. Internal and external views of the set-up and the corresponding optical scheme are shown in Figure 3.10. Details and references for all used components can be found in Appendix B.

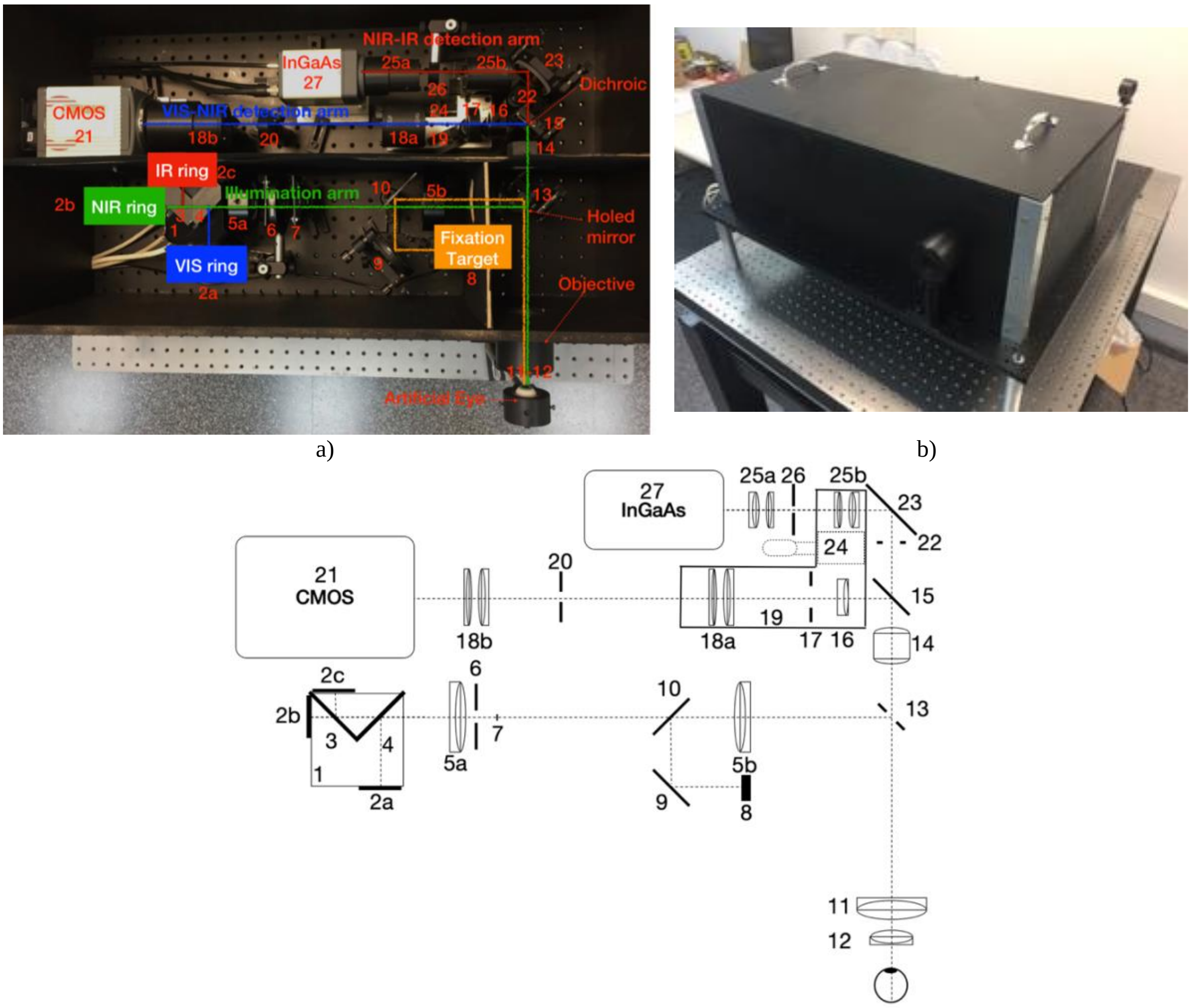

a) b)

c)

Figure 3.10: a) Top internal view of the experimental set-up. b) External view of the experimental set-up. c) Optical scheme of the experimental set-up with labels. Illumination: 1) LED rings cage. 2) a, b, c LED rings VIS, NIR and IR, respectively. 3) NIR-IR dichroic mirror. 4) VIS-NIR dichroic mirror. 5) a, b Illumination telescope's lenses. 6) Retinal conjugated diaphragm. 7) Anti-back reflections stop. 8) Fixation target. 9) Mirror. 10) Methacrylate plate. Detection: 11-12) Objective lenses. 13) Holed mirror. 14) Triplet lens. 15) 950 nm dichroic mirror. VIS-NIR detection path: 16) Divergent lens. 17) Field diaphragm. 18) a, b VIS-NIR telescope's lenses. 19) Refraction correction platform. 20) Aperture diaphragm. 21) CMOS sensor. NIR-IR detection path: 22) Field diaphragm. 23) Gold mirror. 24) Linear translation stage. 25) a, b NIR-IR telescope's lenses. 26) Aperture diaphragm. 27) InGaAs sensor.

3.2.1 Illumination and detection

The optical system of the built set-up is explained here in detail, making emphasis on some aspects of the optical design for a better understanding of the used components and their arrangement.

Thirty-two SMD (Surface Mounted Devices) LEDs were welded in a ring-shaped configuration on three PCBs (Printed Circuits Board) (2a, 2b, 2c in Figure 3.11), and used as light sources. Each ring is responsible for the illumination in a specific spectral band of the whole range of the fundus camera (from 400 nm to 1300 nm). In particular, the VIS ring (2a) consists of LEDs with emission between 400 nm and 700 nm, the NIR ring (2b) of LEDs with emission between 700 nm and 1100 nm, and the IR ring (2c) of LEDs with a peak wavelength at 1200 nm. The 32 LEDs are distributed in this way: 18, organized in 9 twin pairs, belong to the VIS ring; 10, in 5 twin pairs, belong to the NIR ring; and the remaining 4 LEDs fill the third ring.

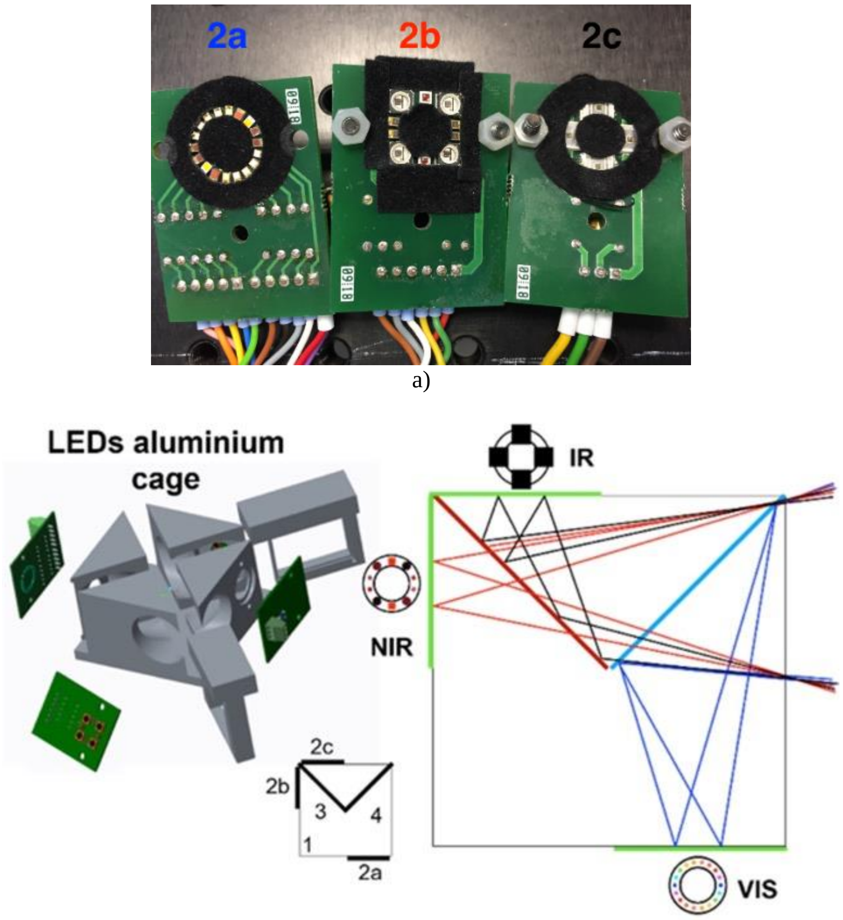

a)

b)

Figure 3.11: a) Picture of the LED rings and b) design of the aluminum cage (left) with its internal optical layout (right).

As explained, all of them conform the spectral bands (channels) of the hyperspectral system through which the spectral sampling of the retina is done. The ring-shaped illumination is created symmetrically arranging these LEDs with the optical center of each unit in a circle of radius 5.2 mm. The light from different rings is combined in a common optical path by means of two dichroic mirrors with cut-off wavelengths at 1150 nm (3) and 700 nm (4). A custom-made aluminum cage (1) was designed to ensure the alignment of the LED rings and mechanical stability. The LEDs PCBs were directly attached to the cage and the distance from the dichroic mirrors were adjusted in a way that all LEDs were equally distant from the cage exit. In this section, we will refer to the LEDs with the nominal peak wavelength declared by the manufacturer.

The wavelengths of the LEDs were chosen in order to obtain as much information as possible from the light absorption of the structures and biological substances of the retina (see Section 2.3.2.2). The LEDs at 415 nm, 450 nm, and 470 nm were selected to investigate the superficial layers of the retina - the NFL reflects more light in the spectral range between 400 nm and 500 nm - and the absorbance and fluorescence properties of the retinal pigments (carotenoids of photoreceptor pigments acting as a yellowish filter in the macula, and lipofuscin that accumulates as a product of phagocytosis of photoreceptors in the outer segments and concentrates in the RPE). Wavelengths within 500 nm and 700 nm - i.e., narrowband LEDs with peaks at 500 nm, 530 nm, 580 nm, 615nm and 660 nm - were chosen to study the macular pigments as well as the retinal layers with vasculature and used to contrast arteries and veins, similarly to what is done in conventional red-free images taken with a green filter and in commercial fundus cameras. These LEDs are expected to differentiate among oxygenated (arteries) and de-oxygenated (veins) blood by means of the spectral differences in the absorption between these two hemoglobin states (Figure 2.19). Additionally, a broadband LED emitting at 590 nm was used to cover wavelengths that were not properly covered by the former ones (530-580 nm) and, thus, to light the retina with a homogeneous spectral sampling. The LEDs at 740 nm and 850 nm, besides penetrating deeper inside the retinal tissue due to the lower absorption of melanin, were expected to provide information about the oxygenation of the deepest retinal vasculature, the superficial choroidal vasculature and the RPE (drusen, atrophies etc.).

The LEDs with longer wavelengths (940 nm, 1050 nm, 1140 nm and 1200 nm) were selected to study the choroid and, since the retina appears progressively more transparent, even projecting light into the sclera, which can be used for imaging congenital hypertrophy, atrophies and degeneration of the RPE, choroidal ruptures, or melanomas [122]. Lipids (drusen) also show absorption peaks in the NIR that exceed water absorption, and therefore images taken at longer wavelengths might be relevant in the study of ARMD [132].

Moreover, LEDs were also chosen considering their physical and optical characteristics such as radiometric power, angle of emission and dimensions, as they were expected to be as much similar as possible. However, the commercial availability was a limiting factor. Table 2 shows information of the spectral, optical and physical characteristics of the LEDs taken from the manufacturer datasheets. The justification for their choice is also given.

The light from the LEDs (red path in Figure 3.12) goes to the retina through the designed illumination optical system, composed by a set of lenses and mirrors (elements 1-12). The image of the LEDs is formed at the focal plane of the second lens of a telescope (5) composed by two achromatic doublets (5a, 5b: focal length 100 mm and diameter 50 mm). In particular, the first lens of the telescope permits to collimate the light collected from the LED rings cage while the second forms the image of the LED rings on the holed mirror. In the middle of the telescope, there is a black stop (7) and a diaphragm (6). As aforementioned, the stop prevents the back reflected light from the objective optical surfaces entering inside the detection optical path whereas the diaphragm, placed at the retinal conjugate plane, blocks part of the parasite light and isolates the light necessary to homogenously illuminate the FOV.

Table 2: Optical and physical characteristics of the chosen LEDs. The manufacturer references and the justification for their choice are provided. For the LEDs used to study the blood oxygenation, the absorption relation between Oxygenated (Ox) and de-Oxygenated (de-Ox) hemoglobin is indicated. Abbreviations are used: Superficial (Sup), Intermediate (Int.).

Peak Wavelength (Typ.) (nm)	FWHM (Typ.) (nm)	Nominal power (mW)/ Luminous flux (lm)	LED Code (Vendor)	Angle of emission (°)	Dimensions (L x W x H) (mm)	Choice justification
415	20	1255 mW	LHUV-0410 (Lumileds)	125	0.65x0.65x0.56	NFL, macular pigments, fluorescence
450	20	500 mW	LXZ1-PR01 (Lumileds)	125	0.65x0.65x0.56	NFL, macular pigments, fluorescence
470	20	24 lm	LXZ1-PB01 (Lumileds)	125	0.65x0.65x0.56	NFL, macular pigments, fluorescence
500	20	82 lm	LXZ1-PE01 (Lumileds)	125	0.65x0.65x0.56	Macular pigments, Sup. retinal vasculature, oxygenation (de-Ox<Ox)
530	20	118 lm	LXZ1-PM01 (Lumileds)	125	0.65x0.65x0.56	Macular pigments, Retinal layers, Oxygenation (de-Ox=Ox),(red-free)
580	20	56 lm	LXZ1-PL01 (Lumileds)	125	0.65x0.65x0.56	Macular pigments, Retinal layers, Oxygenation (de-Ox<Ox)
590	80	52 lm	LXZ1-PL02 (Lumileds)	125	0.65x0.65x0.56	Int. broad band LED
615	20	82 lm	LXZ1-PD01 (Lumileds)	145	0.65x0.65x0.56	Retinal layers, Oxygenation (de-Ox>Ox)
660	20	315 lm	LXZ1-PA01 (Lumileds)	145	0.65x0.65x0.56	Deep retinal layers, RPE
740	20	230 lm	L1C1-FRD1000 (Lumileds)	162	1x1x1.35	Sup. choroid, Oxygenation (de-Ox>Ox), RPE
850	35	1050 mW	L1IZ-0850 (Lumileds)	150	0.67x0.67x1.35	Int. choroid, Oxygenation (de-Ox<Ox)
940	50	1150 mW	L1IZ-940 (Lumileds)	150	0.67x0.67x1.35	Deep choroid
1050	50	40 mW	FL-LED-1050 (FutureLED)	120	3.8x3.8x1.0	Deep choroid, Sclera
1140	65	42 mW	FL-LED-1140 (FutureLED)	120	3.8x3.8x1.0	Deep choroid, Sclera
1200	68	35 mW	SMBB1200-1100 (USHIO)	120	5.2x5.2x1.0	Lipid absorption, Sclera

As can be seen in Figure 3.12 (green path), a fixation target (8) is placed at a retinal conjugate plane and the light emitted is reflected by a mirror tilted 45° (9) and a methacrylate plate (10). Due to the high transmittance and low reflectance properties of the methacrylate, it allows redirecting a small part of the light from the fixation target to the patient while transmitting most of the light used for illumination of the retina. This fixation target is composed by two red LEDs (LXZ1-PA01, see Table 2) separated by a distance of 6 mm, allowing for the correct alignment of the retinal image while the patient is fixating at the target (at one LED for the left eye and at the other for the right eye), thus ensuring a proper imaging of the main retinal structures (fovea and optic disk).

After the telescope, the LED rings are imaged on a 45° custom-made holed mirror (13) (UAB ALTECHNA, Lithuania) that reflects the light towards the objective. As aforementioned, this mirror is a crucial component of the system: it permits to isolate the light reflected by the retina from the back reflections of the cornea and the crystalline lens (geometric pupil separation). For this purpose, it is placed at the focal plane of the illumination telescope and at a conjugate plane of the patient's pupil plane. The hole of the mirror has an elliptical shape that, once tilted at 45°, conforms a circle with a diameter of 6.4 mm. Finally, the LED rings are imaged by the objective, composed by two achromatic doublets (11, focal length 75 mm, diameter 50 mm; and 12, focal length 50 mm, diameter 30 mm), at the patient's pupil plane, de-magnified by a factor of 3.25. Finally, the light spreads inside the eyeball and illuminates the retina, while the fixation target is imaged on the patient's fovea.

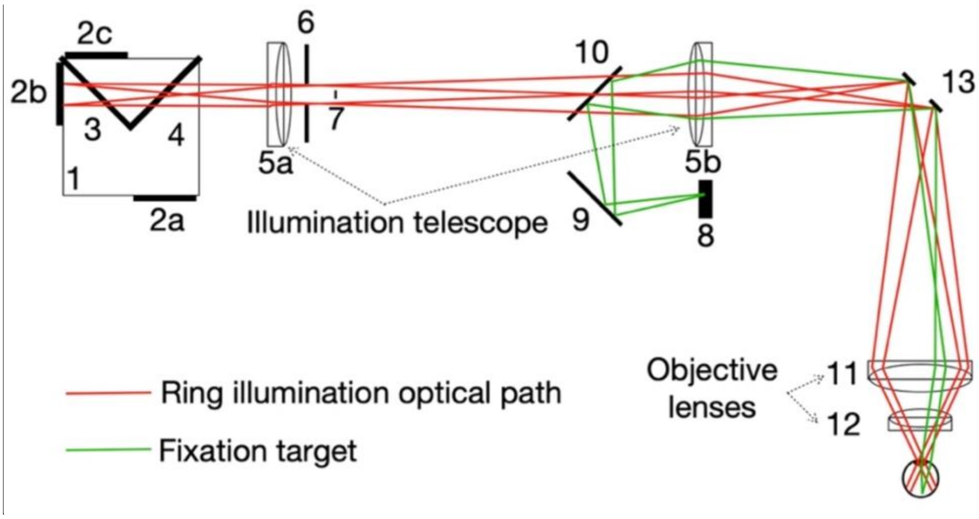

Figure 3.12: Layout of the illumination system. In red, the light emitted by the NIR ring. In green, light from the fixation target.

In regards of the detection (Figure 3.13), the back reflected light from the retina (green path) is collected by the eye's lens and cornea. For an emmetropic eye, the light exiting the eye is collimated, so a first retinal image is formed at the back focal plane of the objective.

Afterwards, the retinal light is separated from the back reflected light of the cornea and the crystalline lens by means of the aperture of the holed mirror and enters inside the detection optical paths not shared with the illumination. Those are composed of a series of lenses (14, 16, 18 in the VIS-NIR path, 14, 25 in the NIR-IR path) that permit to form the retinal images on the sensor of the cameras, as well as to correct eye's ametropia. The first component, common to both detection paths, is an achromatic triplet (14, focal length 50 mm, diameter 25 mm), which minimizes chromatic and spherical aberrations.

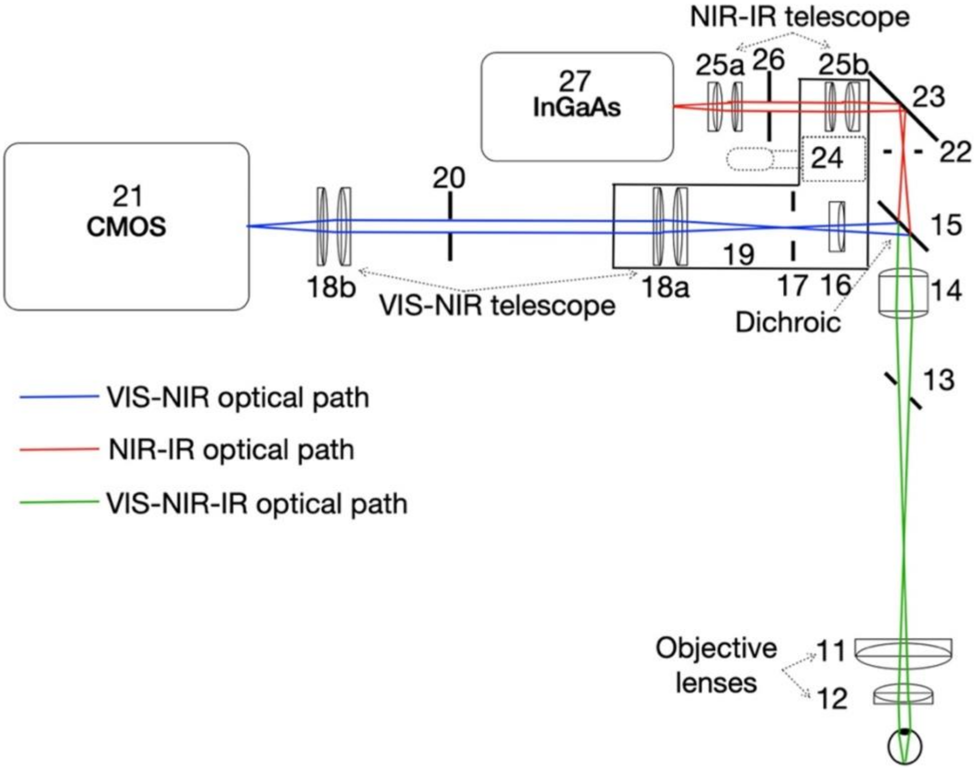

Figure 3.13: Layout of the detection system. In green, the common optical path shared for the whole spectral range. In red, the NIR-IR optical path. In blue, the VIS-NIR optical path.

Then, to split the VIS-NIR (blue path) and the NIR-IR (red path) optical paths, a dichroic mirror (15) with a cut-off wavelength at 950 nm is inserted after the triplet. Its cut-off wavelength was chosen considering the spectral sensitivity of the InGaAs camera, which permits to collect light from 960 nm to 1700 nm. The VIS-NIR detection path is composed by: a divergent lens (16, focal length 50 mm, diameter 25 mm), that corrects for some field curvature and adjusts the magnification, and a telescope (18), that forms the retinal image at the sensor plane. This telescope, composed by two equal compounds of achromatic doublets (18a, 18b; each one formed by two doublets with 40 mm diameter and a focal length of 250 mm and 100 mm, respectively), firstly collimates the light and then re-focalizes it on the CMOS sensor (21). Two diaphragms are used after the divergent lens (17) and in the middle of the telescope (20), at conjugated planes of the retina and pupil, respectively. Accordingly, the first one limits the optical field while the second acts as the aperture stop of the VIS-NIR detection system. In regards of the NIR-IR optical path, a 45° gold mirror (23) redirects the light into a telescope (25) that resembles the retinal image on the InGaAs sensor (27). As in the case of the VIS-NIR detection path, the telescope is composed by two groups of achromatic doublets optimized for NIR-IR light (25a, 25b; each one formed by two doublets with 25.4 mm diameter and a focal length of 125 mm and 75 mm, respectively). Field (22) and aperture (26) diaphragms were also placed at retinal and pupil conjugated planes.

The divergent lens (16) and the first lenses of the telescopes of both detection arms were directly attached to an aluminum platform (19) that, in turn, was attached to a linear translation stage (24). This allows the possibility for correcting the patient's refraction. In fact, when the patient's eye is not emmetropic, the light coming from the retina is not collimated and thus, re-collimation is required to obtain a focused image on the camera.

To re-collimate the light, the entire platform can be linearly moved along the optical axis for a range of refraction corrections of ± 15 D. This platform was designed in a way that moving the two detection parts together, the refraction can be corrected simultaneously for both optical paths. As explained in the design section, the focal length and position of the achromatic triplet (14) were selected in order to be arranged in a telecentric configuration along with the objective. In this way, no change in magnification (change in the FOV) is produced when correcting patient's refractive error.

In the VIS-NIR range, a 16-bit CMOS detector (Orca Flash 4.0, C11440-22C, Hamamatsu, Japan) that provides enough sensitivity from 400 nm to 950 nm, a maximum frame rate of 100 fps and a variable exposure time between 1 ms and 10 s, was selected to acquire the retinal images. For the NIR-IR path, the sensor used was a 12-bit InGaAs camera (C12741-03, Hamamatsu, Japan) with response from 960 nm to 1700 nm, maximum frame rate of 62.7 fps and a variable exposure between 16.7 ms and 3 s. The choice of the sensors was done according to their sensitivity, frame rate etc., as well as the acquisition modality, described in the next section. Complete sensors specifications are given in Appendix A.

All optical components of the system were carefully selected so that their working spectral range (design wavelengths and antireflective coatings) matched the working spectral range of the arm they are part of, in order to minimize undesired reflections and maximize the transmittance. The complete list of the optical components is available in Appendix B.

The whole set-up was covered with a black case in order to avoid the interference of the ambient light on the measurements, as well as to protect the internal components (Figure 3.14). As the patient must be properly aligned with the system before the spectral images acquisition, a chin-rest was placed in front of the objective lens directly attached to the optical bench. The base of this chin rest can be moved a few centimeters in the three directions of the space allowing proper alignment while the patient is looking at the target.

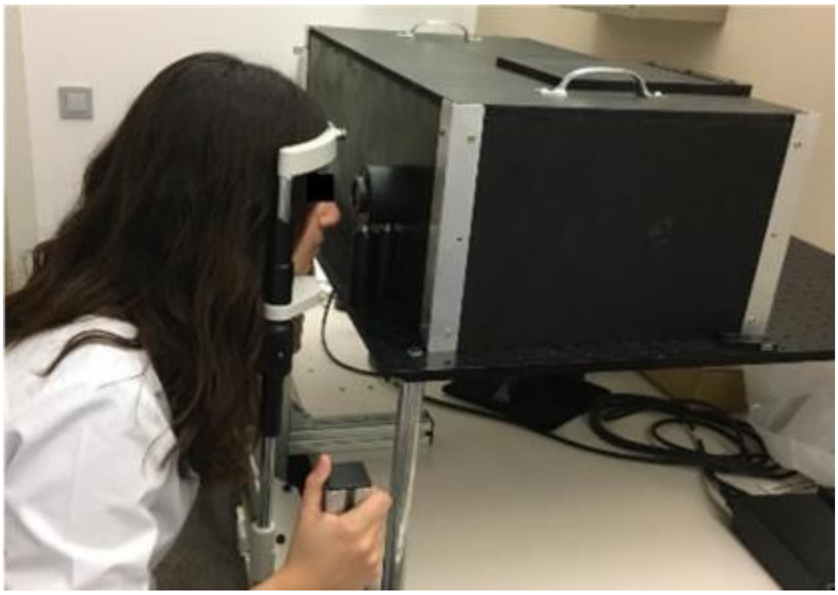

Figure 3.14: Picture of a patient during the alignment of the system.

3.2.2 System control: Electronics and software

One of the most important parts of the prototype is the software and the electronics architecture, responsible for the synchronization of all detection components and image acquisition as well as the LEDs control. In fact, the LEDs and camera settings, synchronization of the illumination and image acquisition are entirely controlled by the electronics communication among components, as shown in Figure 3.15.

In particular, the LEDs emission is controlled with a custom-made Electronic Principal Board (EPB) that, in turn, is directly connected to the LEDs boards, the computer, and the CMOS and InGaAs cameras. The EPB was designed to control up to 20 different groups of LEDs. Of them, 15 were used to control the LEDs of the ring-shaped illumination, 2 to control the LEDs of the left and right eye fixation targets, and the last three are still available for future improvements of the system. The entire hyperspectral stream acquisition is done turning on and off the LEDs sequentially for each frame acquired with the cameras, i.e., emitting only the LEDs corresponding to one spectral band at a time, using a Pulse-Width Modulated (PWM) signal. Each LED emission follows the oscillation of the PWM, a train of squared pulses of very short period (≈10 μs), which, by changing its duty cycle, makes possible to control the time averaged power emitted by the LED. The PWM is active during the camera sensor exposure time (t_{on}). After each t_{on}, the PWM is turned off and, because of the necessary readout time required for image digitization, a rest time (t_{off}) over which the LED does not emit is additionally required. The next group of LEDs is turned on right afterwards, repeating the sequence for all the spectral bands. The duration of t_{on} and t_{off} can be set independently for each band by the operator, which communicates with the EPB by means of an USB serial port. Besides t_{on} and t_{off}, the operator can control several parameters of the illumination such as the order of the illumination sequence, the number of sequence repetitions, the emitted power and the start and stop signals of the entire LEDs activation. Specifically, the maximum number of repetitions of a single sequence in one activation is 99.

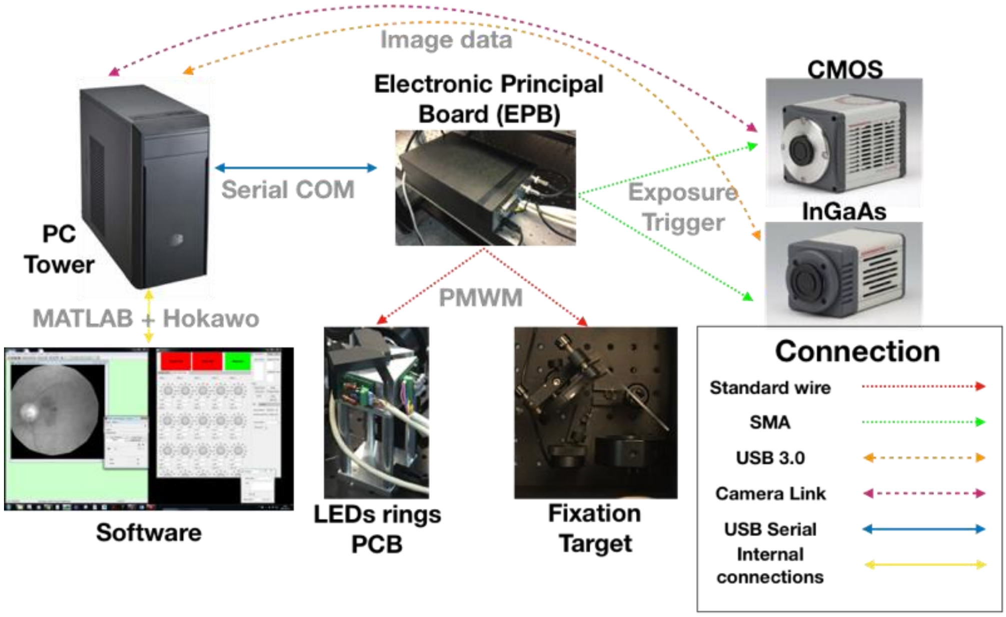

Figure 3.15: Electronics and software scheme to control the camera acquisition, LEDs illumination and synchronization among components.

The EPB is also responsible for triggering the cameras acquisition and its synchronization with the LEDs emission. This is done using a square wave perfectly synchronized with the LEDs excitation signal. This signal oscillates between 3.3 V (High state) and 0 V (Low state), maintaining the High and Low state voltages during t_{on} and t_{off}, respectively. Connecting this signal to the external trigger input of the cameras, the acquisition starts once it changes from Low to High state. The camera acquires until the signal changes back from High to Low. This trigger modality is called External Level (EL) trigger mode. Moreover, sending the right activation command to the EPB, the trigger signal can activate for both cameras or only for one.

The synchronization was experimentally tested using an oscilloscope (Figure 3.16).

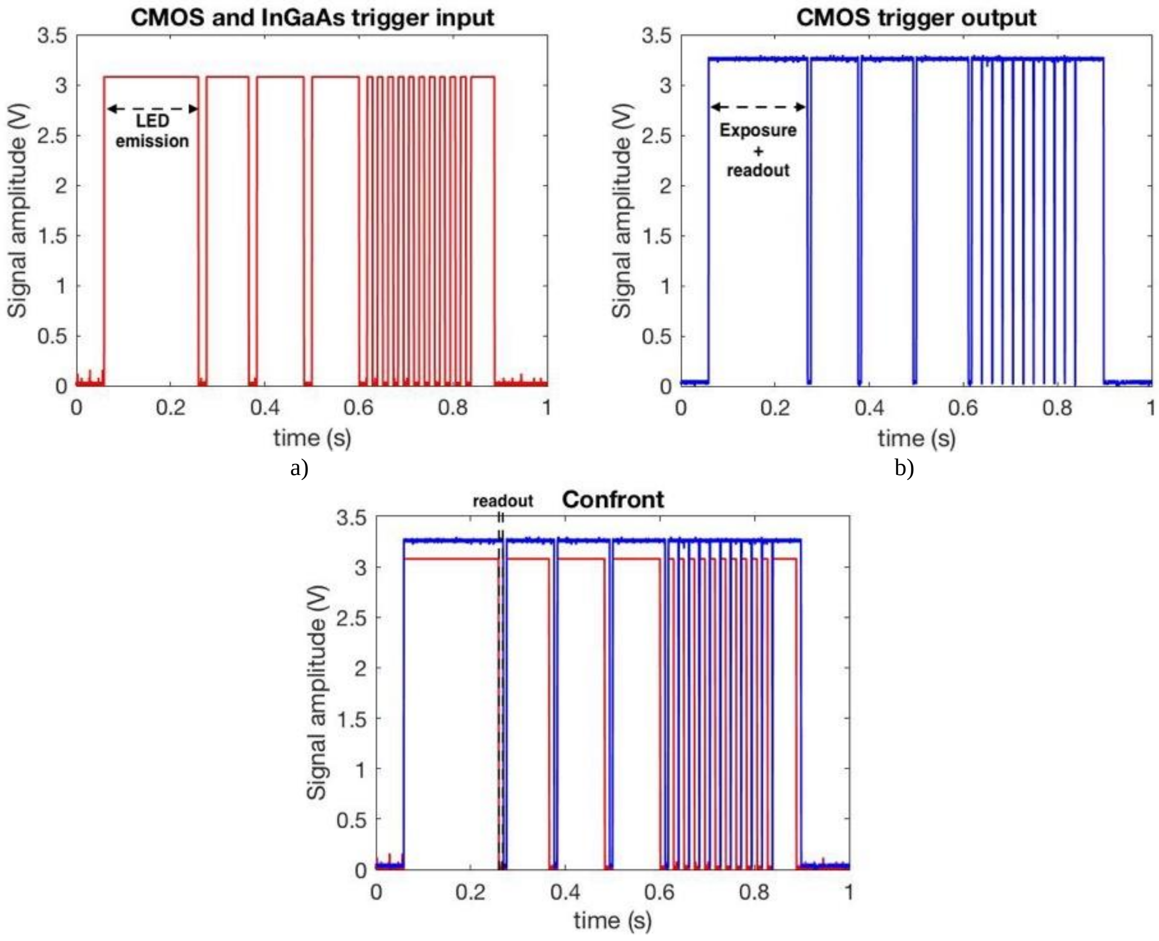

a)

b)

c)

Figure 3.16: Signals measured with an oscilloscope: a) EPB signal synchronized with the LED emission and connected to the external trigger input of the cameras. b) Trigger output signal of the CMOS camera. c) Comparison of the two signals.

During these measurements, the oscilloscope received three signals: 2 trigger signals from the EPB and the trigger output signal generated by the CMOS. This latter signal changes the state from Low to High every time the acquisition starts, and from High to Low when the readout is finished and the camera is ready for another acquisition. Unfortunately, the InGaAs camera does not provide a trigger output; nevertheless, this is sufficient to confirm the synchronization with the CMOS because the manufacturer and the EL trigger modality is the same for both cameras.

As can be seen in Figure 3.16, the trigger output signal generated by the CMOS camera follows faithfully the signal generated by the EPB. Moreover, the only difference between the external trigger signal and the output signal of the CMOS camera is the time needed to finish the readout. The EL trigger modality is the best to avoid contamination between spectral channels.

For both cameras, the maximum frame rate is limited by the minimum pulse width of the external trigger (equal to the minimum exposure time) and the readout time of the camera itself. In these regards, the InGaAs camera maximum frame rate is 30 fps, with a minimum exposure time of 16.7 ms, and a readout time of 16.7 ms; whereas the CMOS maximum frame rate is 90 fps, with an exposure time of 1.05 ms, and a readout time of 10 ms.

The difference in terms of minimum trigger pulse width between the two cameras allows tailoring the external trigger in a way that both acquire at their maximum speed. Owing to the differences in terms of retinal reflectivity, LED powers and QEs of the two cameras, the exposure time for each spectral band was properly adjusted (Table 3) in order to have the best compromise between fast acquisition and SNR. The total acquisition time was 613 ms, 220 ms corresponding to the VIS-NIR spectral bands and 393 ms to the NIR-IR ones. In particular, to avoid the effect of eye movements due to the glare caused by the bright illumination, the IR wavelengths were established as the first ones in the sequence.

Table 3: Exposure times used to acquire fundus images for each spectral channel (LED peak wavelength) of the system.

LED peak wav. (nm)	415	450	470	500	530	580	590	615	660	740	850	940	1050	1140	1200
Exposure time (ms)	11	11	11	11	11	11	11	11	11	11	11	11	100	120	100

To control this acquisition, Hamamatsu provides a tailored computer and software (Hokawo) to acquire complete streams of data from both detectors at the same time in the Random Access Memory (RAM). Figure 3.17 (left) shows the Hokawo acquisition software, which allows setting the cameras acquisition modes and parameters, mainly used for acquisition and extraction of data. Additionally, Figure 3.17 (right) shows the interface built in MATLAB using the AppDesigner tool that allows changing the parameters of LEDs emission and synchronization and communicating them to the EPB.

This interface is divided in two main panels: the measure panel and the single-LED (spectral channel) control panel. The first one is composed by three buttons: two (red) that are used to choose between right or left eye, and one (green) that is used to start the hyperspectral measurement. By clicking on one of the red buttons, the system charges the settings to activate the fixation target phase. During this phase, a sequence of 3 groups of LEDs is activated: the fixation target (right LED for the left eye and left LED for the right eye) to help the patient fixating at the target while keeping the eye aligned with the system, and two groups of LEDs to image the retina during alignment. The two groups used for this purpose are those of spectral bands 1050 nm and 1140 nm (FL-LED-1050 and FL-LED-1140). Since they emit IR light, they do not change the patient's pupil size. The trigger signal is only sent to the InGaAs camera, so the images are acquired only by this one.

Once the patient is correctly positioned and aligned, the operator can press the measure button to proceed with the measure phase. The program loads the measurement parameters and the EPB sends the trigger and PWM signals to the cameras and the LEDs clusters, respectively. In this phase, the hyperspectral sequence is acquired sequentially, channel by channel, following the previously described process.

Finally, the single-LED control panel permits the operator to control the different spectral channels of the system individually, building custom on/off sequences and changing the emitted power and the exposure time of LEDs. This is particularly useful for the alignment of the system, its characterization and preliminary check of operation.

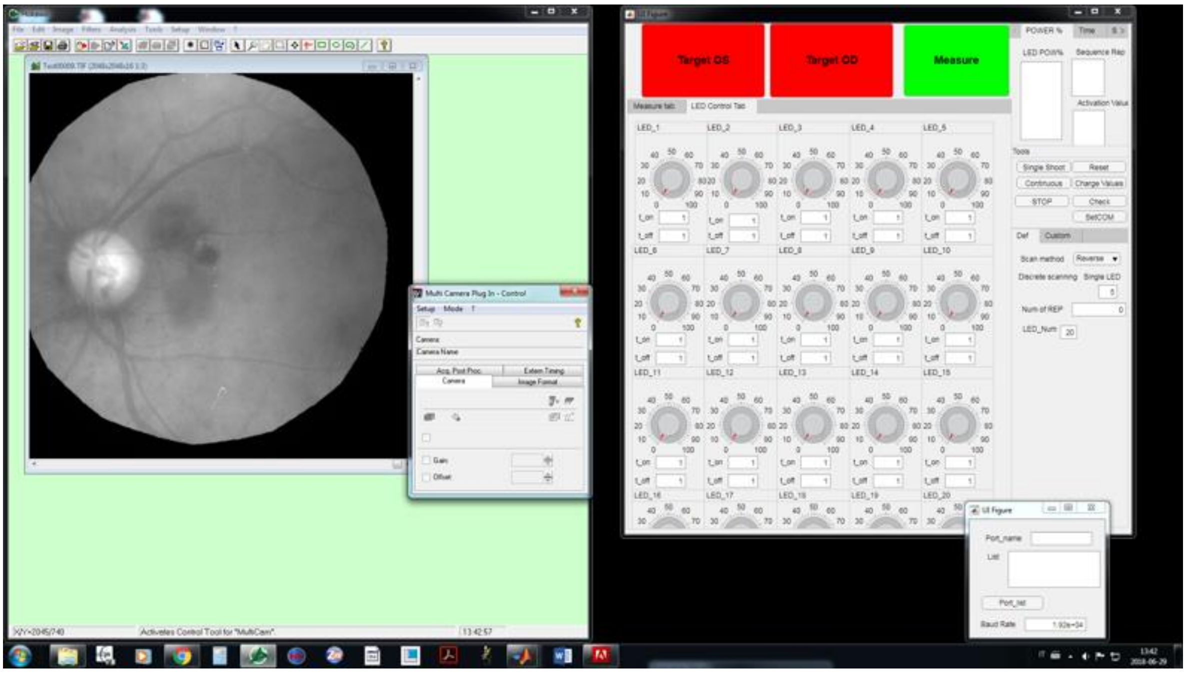

Figure 3.17: Screen shot of the acquisition software. On the left, a retinal image is shown using the Hokawo software. On the right, the MATLAB interface to control single LEDs emission, the fixation target and to perform the hyperspectral measurement (LED_1: 415 nm, LED_2: 450 nm, LED_3: 470 nm, LED_4: 500 nm, LED_5: 530 nm, LED_6: 580 nm, LED_7: 590 nm, LED_8: 615 nm, LED_9: 660 nm, LED_10: 740 nm, LED_11: 850 nm, LED_12: 940 nm, LED_13: 1050 nm, LED_14: 1140 nm, LED_15: empty channel, LED_16: 1200 nm, LED_17: left fixation target, LED_18: right fixation target).

3.3 System characterization

The optical and radiometric characterization of the system is presented in this section. They were carried out following the ISO standards for fundus cameras and ophthalmic instruments ISO 10940:2009 “Ophthalmic instruments -- Fundus cameras” [71] and ISO 15004-2:2007 “Ophthalmic instruments -- Fundamental requirements and test methods -- Part 2: Light hazard protection” [72], respectively. Both standards specify requirements and test methods for fundus cameras operating for observing, photographing or recording electronic images of the fundus of the human eye in order to provide the image information for diagnosis.

3.3.1 Optical characterization

Firstly, we carried out the optical characterization of the system following the guides given by the ISO 10940, which describes the requirements of both the illumination and detection systems such as resolution, FOV and magnification of fundus cameras (Table 4).

In this standard, the following definitions are given:

- **Resolving power of the fundus camera optics on the fundus:** minimum separation allowing recognition of two adjacent lines on the fundus, expressed as number of line pairs per millimeter (lp/mm).
- **Angular field of view (FOV):** maximum image size displayed on the image plane, expressed as the angle subtended at the exit pupil of the eye by its maximum dimension $2r$ (Figure 3.18). In this characterization, $2r$ is the diameter of a circular FOV.
- **Magnification of the image (M):** ratio of the size of the image of an object at the center of the image plane to that of the fundus, assuming that the eye is emmetropic and that it has a focal length of 17 mm in air.
- **Pixel pitch in the fundus (pixel step) (P):** distance between two pixels (from center to center) of a digital image sensor theoretically projected at the ocular fundus, expressed in microns (μm), assuming that the eye is emmetropic and that the focal distance in the air is 17 mm.

As stated in the standard, the resolving power of the fundus camera optics on the fundus, FOV, M and P of the system must be measured by means of a target placed in front of the system at a distance of 1 m (in the formulas indicated as L). This distance should be measured with an uncertainty of ± 5 mm. The light source used to illuminate the target can be the illumination of the fundus camera itself or an external light source. The peak wavelength of the light used must be within 520 nm and 560 nm, and 790 nm and 890 nm, for VIS and NIR applications, respectively. The FWHM of the source spectrum cannot be broader than 80 nm and 120 nm, for VIS and NIR evaluations, respectively. These indications refer to standard fundus camera systems and can be fulfilled only with the CMOS camera. For a complete characterization of the system, a specific and adapted evaluation for the NIR-IR arm has been carried out.

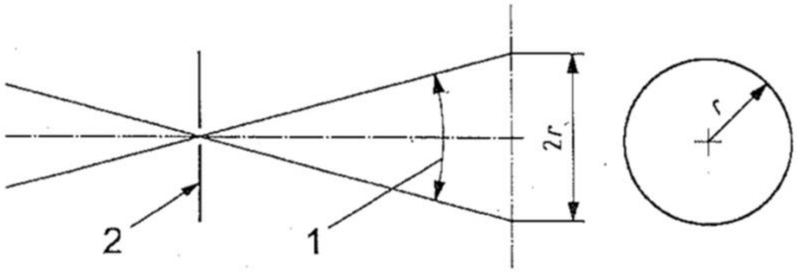

Figure 3.18: Meaning of dimension r for a circular FOV. In the figure, the FOV (1) and the eye exit pupil (2) are indicated (taken from Appendix A of the ISO 10940).

In order to perform the optical characterization, we used the LEDs purchased for the experimental set-up that, placed in front of the system's objective, allowed for a homogeneous illumination of the target. It is important to state here that, regardless of the nominal peak wavelengths given in Table 3.1, the actual peak wavelengths measured experimentally were the following ones: 416, 450, 471, 494, 525, 595, 598, 624, 660, 732, 865, 955, 1025, 1096, 1213 nm. Therefore, from now on these will be the wavelengths used to identify the LEDs of the spectral bands of the system.

Table 4: Optical requirements for fundus cameras.

Criteria		Requirements	
Resolving power of the fundus camera optics on the fundus	FOV ≤ 30°	Center	$\geq 80\ \mathrm{lp/mm}$
		Medium (r/2)	$\geq 60\ \mathrm{lp/mm}$
		Periphery (r)	$\geq 40\ \mathrm{lp/mm}$
	FOV ≥ 30°	Center	$\geq 60\ \mathrm{lp/mm}$
		Medium (r/2)	$\geq 40\ \mathrm{lp/mm}$
		Periphery (r)	$\geq 20\ \mathrm{lp/mm}$
Tolerance on FOV		±5% on the measure	
Tolerance on the magnification of image		±7% on the measure	
Tolerance on pixel step at ocular fundus		±7% on the measure	
Range of patients’ refraction correction		±15 D	

In order to accomplish with the standard requirements, we used the CMOS camera to acquire images and the LEDs of peak wavelengths of 525 nm and 865 nm (FWHM of 33 nm and 37 nm, respectively) to illuminate the target. Additionally, images of the targets were also acquired with the InGaAs camera using the LED with a peak wavelength of 955 nm (FWHM 58 nm).

We evaluated the FOV of the system by means of a series of three printed rulers (ruler length: 25 cm) stacked together and placed at 1 m from the entrance pupil of the system. Thus, the total length of the FOV target was 75 cm. This target was placed perpendicular to the optical axis and centered in the FOV according to Figure 3.18. The distance r from the center to the periphery of the FOV could then be assessed from images such as the one shown in Figure 3.19.

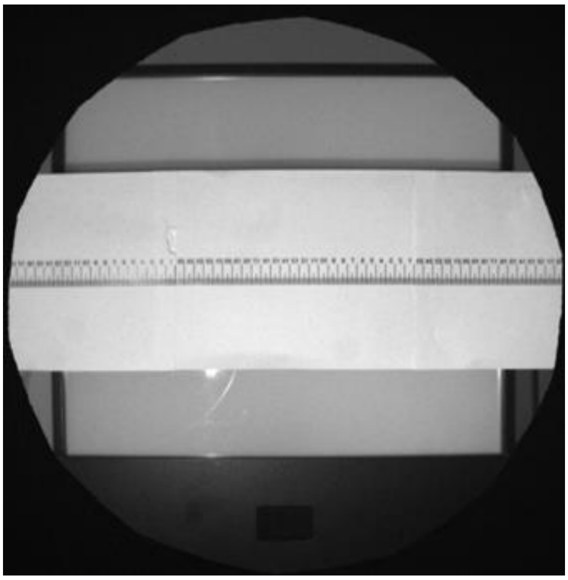

Figure 3.19: Image of the target (stacked rulers) used in the evaluation of the FOV.

The FOV can be then computed as follows:

$$FOV = 2 \cdot arctan\left(\frac{r}{L}\right) \qquad 3.1$$

being its uncertainty:

$$\Delta FOV = \mathrm{FOV} \cdot \frac{1}{1 + \left(\frac{r}{L}\right)^2} \cdot \sqrt{\left(\frac{\Delta r}{r}\right)^2 + \left(\frac{\Delta L}{L}\right)^2} \qquad 3.2$$

where Δr and ΔL are the smallest resolvable divisions of the ruler in the image of the target (1 mm for the CMOS and 2.5 mm for the InGaAs) and the standard deviation on the measured values of L, respectively.

In order to calculate the magnification of the system, we used a 100 mm length portion of the FOV target at its center. The size in millimeters of this portion on the image (*l*), can be determined by measuring the corresponding number of pixels and multiplying it by the pixel size. The magnification can be then calculated as follows:

$$M = l/1{,}7 \qquad 3.3$$

with an uncertainty ΔM given by:

$$\Delta M = M \cdot \frac{\Delta l}{l} \qquad 3.4$$

where Δl is again the smallest resolvable division in the image of the target.

Table 5 summarizes the results obtained for the FOV and M. These results are in accordance with the values expected from the simulations performed in the optical design phase.

Table 5: Results of FOV and M.

LED peak wavelength (Sensor)	r ± Δr (mm)	L ± ΔL (mm)	FOV ± ΔFOV (°)	l ± Δl (mm)	M ± ΔM
525 nm (CMOS)	273 ± 1	1000 ± 3	30.5 ± 0.2	2.04± 0.02	1.20 ± 0.01
865 nm (CMOS)	270 ± 1	1000 ± 3	30.3 ± 0.2	2.04± 0.04	1.20 ± 0.02
955 nm (InGaAs)	278 ± 2.5	1000 ± 3	31.1 ± 0.3	1.47 ± 0.09	0.88 ± 0.05

To evaluate the resolving power of the optics of the system on the fundus, the standard recommends using a target with vertical and horizontal black lines on a white background. The width of the white space must be equal to the width of the black lines. The length of the lines must be 5 times the width, and the reflectivity of the background must be at least 1.4 times the reflectivity of the black lines. The patterns for central, periphery and medium FOV must be in the same image and the achieved resolving power must be the one specified in Table 4 for any of the three areas.

The ISO also states that, for the NIR-IR range (i.e., above 770 nm), the resolution values indicated in *lp/mm* must be divided by 1.6 due to the change of the minimum resolution obtainable with IR light. Furthermore, to evaluate the resolution of the NIR-IR optical path, the target cannot be more than 25 *lp/mm* because this is the maximum resolution that can be achieved with a sensor whose pixel side is of 20 μm. Figure 3.20 shows a portion of the images with the resolution patterns printed on white sheets of paper and distributed along the FOV.

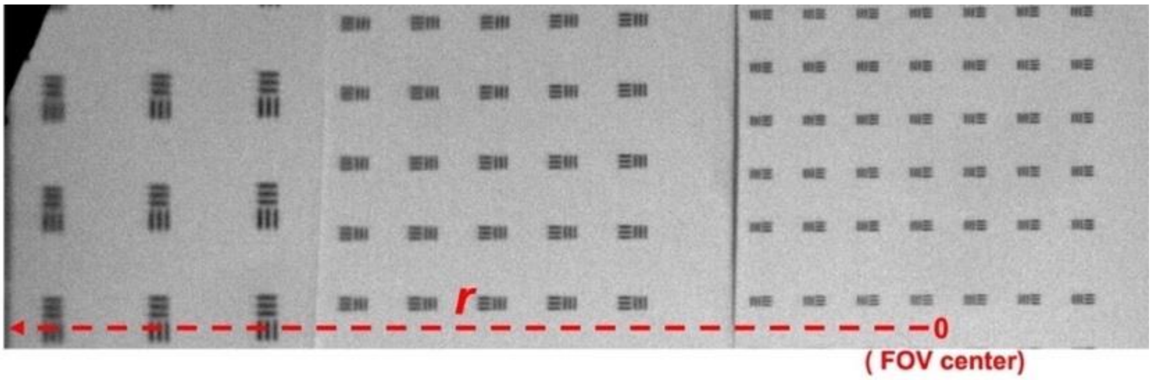

Figure 3.20: Image acquired for the evaluation of resolution. The three sheets of paper with the different resolution patterns are centered at different distances from the center of the FOV (0). In particular, the pattern on the left side is centered at a distance *r* from the center of the FOV, the sheet in the center at *r*/2, and the sheet on the right is at the center.

Using this target, we acquired images for the three light sources and the two cameras, and we evaluated the Michelson contrast (C):

$$C = \frac{(Max - Min)}{(Max + Min)} \tag{3.5}$$

where Max and Min are the maximum and the minimum values in terms of digital levels of the curve obtained from averaging the pixels of row/columns of a single pattern along the dimension perpendicular to these lines (vertical/horizontal). The procedure was repeated for three identical vertical patterns, centered at three distances from the center of the FOV (center, medium (*r/2*), periphery (*r*)), both for the vertical and horizontal lines. The results are shown in Table 6.

Table 6: Results of resolving power on the fundus.

LED peak wavelength (Sensor)	FOV position	Target (lp/mm)	$C \pm \Delta C$ (Vertical lines)	$C \pm \Delta C$ (Horizontal lines)
525 nm (CMOS)	center	60	0.12 ± 0.01	0.14 ± 0.01
	r/2	40	0.12 ± 0.02	0.14 ± 0.02
	r	25	0.20 ± 0.01	0.17 ± 0.02
865 nm (CMOS)	center	40	0.13 ± 0.02	0.10 ± 0.02
	r/2	25	0.27 ± 0.03	0.16 ± 0.02
	r	13	0.38 ± 0.01	0.40 ± 0.04
955 nm (InGaAs)	center	25	0.13 ± 0.04	0.13 ± 0.03
	r/2	25	0.11 ± 0.03	0.10 ± 0.04
	r	13	0.34 ± 0.14	0.28 ± 0.06

Finally, the pixel pitch at the fundus P can be determined using the calculated M values, the sensor pixel size (P_s) and the formula below.

$$P = \frac{P_s}{M} \tag{3.6}$$

The uncertainty of this measure is given by:

$$\Delta P = P \cdot \sqrt{\left(\frac{\Delta P_s}{P_s}\right)^2 + \left(\frac{\Delta M}{M}\right)^2} \tag{3.7}$$

where ΔP_s is the error of the length of the pixel side given by the manufacturer. The results obtained are presented in the table below:

Table 7: Results of pixel pitch at the fundus P.

LED peak wavelength (Sensor)	Ps ± Δ Ps (µm)	P ± Δ P (µm)
525 nm (CMOS)	6.5 ± 0.1	5.4 ± 0.1
865 nm (CMOS)	6.5 ± 0.1	5.4 ± 0.1
955 nm (InGaAs)	20 ± 1	23 ± 3

Besides the former measurements, the knowledge of the area of the LEDs used as illumination sources at the patient's pupil plane is also needed for the light hazard evaluation, as indicated in the ISO 15004-2:2007 "Ophthalmic instruments – Fundamental requirements and test methods – Part 2: light hazard protection" [72]. Accordingly, these areas were determined as an additional step of the optical characterization as follows. In order to obtain an image of each LED ring, we used a CMOS imaging camera with enhanced sensitivity in the NIR (UI-1240LE-NIR-GL, Imaging Development Systems GmbH, Germany). This camera was placed at the patient's pupil plane, where the LED rings images are formed. In particular, because of the differences between shape and thickness of LEDs, an analysis of the different focus positions was carried out and, as a trade-off, the focal plane of the LEDs emitting at 732 nm was chosen as the imaging plane for all rings. To acquire the images without saturating or under-exposing the camera sensor, adjustments in the camera exposure time and LEDs power were needed. Figure 3.21 shows the images of the three LED rings.

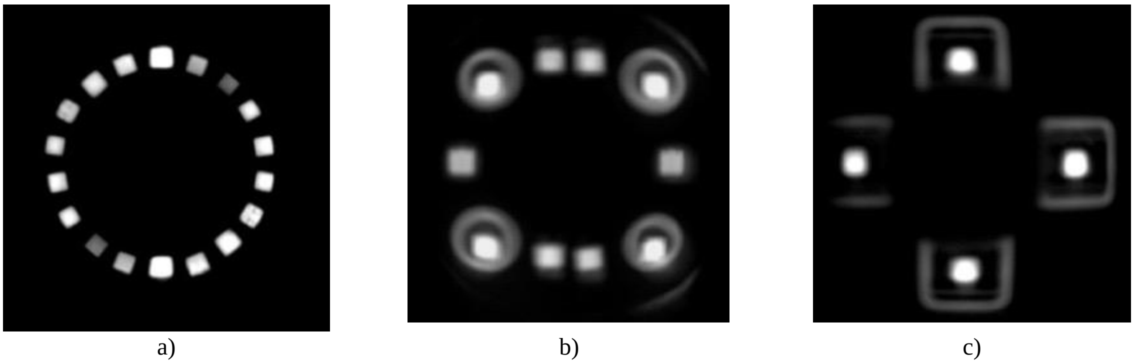
a) b) c)

Figure 3.21: Images of the three LED rings at the patient's pupil plane: a) VIS ring, b) NIR ring, c) IR ring.

From these images, we measured the side length (T) of each LED in pixels and then, using the pixel size from the datasheet of the camera manufacturer, we obtained the length in mm. As shown in Figure 3.22, to estimate the length of the side of each LED, we considered the pixels with digital values above 10% of its central maximum value. Five sections of each LED were considered (blue lines in Figure 3.22).

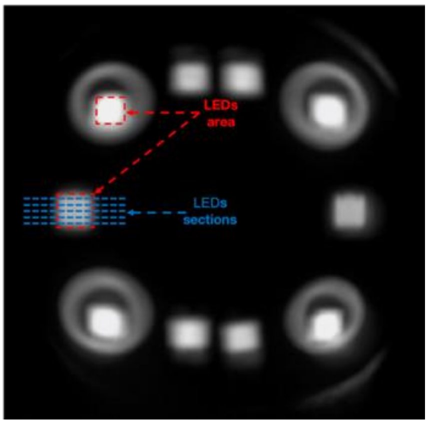

Figure 3.22: Method used for the evaluation of the LEDs area. The LED area, calculated as that with digital levels per pixel above 10% of the maximum central value, is marked in red. The area sections considered for the side length estimation are indicated in blue.

As the standard deviation calculated on this measure was smaller than the length of a single pixel, we took this value as the corresponding uncertainty (ΔD). In Table 8, the LEDs areas are provided as $S = T^2$, a$\Delta S = 2T\Delta$T indicating the corresponding uncertainty.

Table 8: Area covered by the LEDs at the patient's pupil plane.

LED peak wavelength	T ± ΔT (mm)	S ± ΔS (mm^2)
416 nm	0.329 ± 0.005	0.108 ± 0.003
450 nm	0.291 ± 0.005	0.085 ± 0.003
471 nm	0.275 ± 0.005	0.076 ± 0.003
494 nm	0.297 ± 0.005	0.088 ± 0.003
525 nm	0.323 ± 0.005	0.104 ± 0.003
595 nm	0.286 ± 0.005	0.082 ± 0.003
598 nm	0.329 ± 0.005	0.108 ± 0.003
624 nm	0.302 ± 0.005	0.091 ± 0.003
660 nm	0.302 ± 0.005	0.091 ± 0.003
732 nm	0.429 ± 0.005	0.184 ± 0.004
865 nm	0.339 ± 0.005	0.115 ± 0.003
955 nm	0.323 ± 0.005	0.105 ± 0.003
1025 nm	0.355 ± 0.005	0.126 ± 0.003
1096 nm	0.373 ± 0.005	0.137 ± 0.004
1213 nm	0.382 ± 0.005	0.146 ± 0.004

It is important to note that, as mentioned above, only the area that contains pixels with digital levels above 10% of the maximum value were considered in these results. In the safety evaluation, we assume that the 100% of the radiometric power is focused inside this area. This, besides of a simplification in the computation of the area, grants the evaluation of the worst-case scenario for light hazard: the greater the light focused in a smaller area, the bigger is the hazard.

Finally, the required movement of the platform for patient's refraction correction was also characterized to ensure a good performance of the fundus camera at the clinics. The theoretical curve relating the refractive error (Rx) in diopters (D) and the platform shift was obtained by simulating through Zemax different ametropias in the eye model and finding the best platform position in each case. The obtained values are depicted in Figure 3.23, which have been fitted using a second order polynomial to obtain a compensation curve for any patient's refraction.

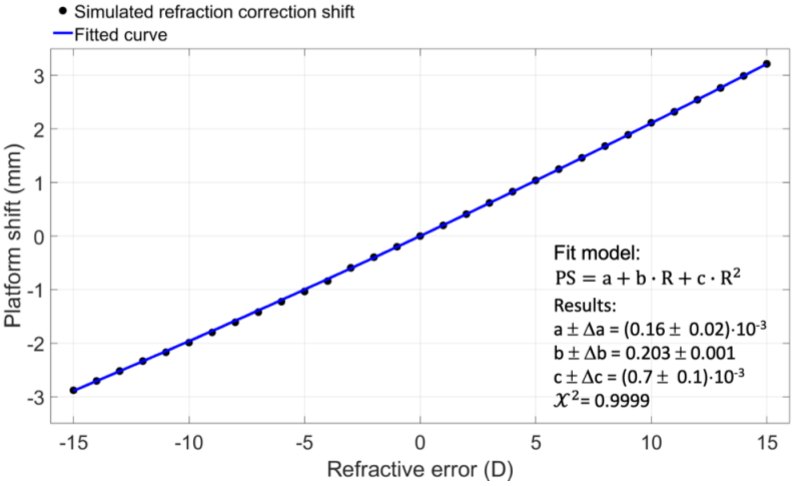

Figure 3.23: Platform shift (PS) in millimeters vs. Refractive error (R) in Diopters with the corresponding fit in the range between -15D and +15 D. The letters a, b, c are the parameters of the fit, and $\mathcal{X}^2$ is its Chi-squared value.

According to all results shown in this section, it was concluded that the developed prototype permits the imaging of the human retina with good optical performance as established in the international ISO standard for fundus cameras through the whole spectral range considered.

3.3.2 Spectral and radiometric characterization

In order to characterize our system in terms of emitted radiation, we carried out measurements of radiometric power (W) and irradiance (W/m^2), as well as of the relative spectral emission of each LED at the pupil plane, where the illumination light is focused. A power meter PM100D (Thorlabs Inc., United States) equipped with a photodiode-based sensor S120C (Thorlabs Inc., United States) with sensitivity between 400 nm and 1100 nm was used to perform measurements of absolute radiometric power (W). A scanning spectrometer Spectro 320 (Instrument Systems GmbH, Germany) with sensitivity between 370 nm and 1700 nm and with the accessory EOP-146 attached allowed spectral irradiance measurements of the light incident to the module. For an estimation of the absolute power (W) of the LEDs emitting in the spectral region beyond the spectral sensitivity range of the power meter (>1100 nm), the readings from both systems were combined in order to find a specific conversion factor between them. This factor was estimated by using the records of the LEDs emitting within the spectral range where the two instruments had sensitivity, i.e., from 400 nm to 1100 nm, allowing for a direct conversion from spectral irradiance values (W/m^2) to radiometric power values (W) along all wavelengths, also those longer than 1100 nm. It should be noted that to compute the absolute radiometric power (W) from the irradiance readings of the spectrometer, one must assume that there is a homogeneous illumination over the area of the EOP-146 sensor (spectrometer), which is not our case (see Figure 3.21). Therefore, only a relative measure in terms of irradiance was possible with the spectrometer as the LEDs illumination did not cover the whole area of the sensor (the homogeneous field of illumination is achieved only on the retina, after light passing through the optics of the eye). To reproduce the same conditions in both measurements, the two sensors were positioned at the focused image of the same LED (peak wavelength at 732 nm, formerly used in the optical characterization, too).

Furthermore, since the spectrometer is a scanning instrument with a moveable internal diffraction grating to scan all wavelengths, it lasts certain time to carry out a single measurement. Accordingly, the LED under analysis needs to be switched on for a relatively large period of time if a complete measure is to be obtained. Nevertheless, the LEDs of the developed fundus camera cannot be maintained for a long time working at their maximum current (100%) without risking serious damage, due to the increase in temperature (there is not a heat dissipation system). For this reason, the measurements for the estimation of the conversion factor were carried out with the LEDs working at 12.5% current. The sampling speed of the Spectro 320 was chosen as 22 ms/nm, for both the VIS and IR spectral ranges. This value corresponds to the minimum value of an entire LED emission period (t_{on}+ t_{off}) in real conditions (t_{on}=11 ms and t_{off} =11 ms). In this way, the Spectro 320 integrates the same amount of light during each LED activation along the whole sequence. In addition, even if the program can be set in a way that activates continuously the LEDs signal at the maximum number of sequence repetitions (99 repetitions for each activation signal, see Section 3.2.2), the time between the end of one activation and the subsequent produce some discontinuities to appear in the measurements (Figure 3.24 a). Due to this, the total irradiance was finally calculated by performing an interpolation of the raw spectral irradiance distribution for each LED, excluding the discontinuities and then, calculating the area under the interpolated curve (Figure 3.24 b).

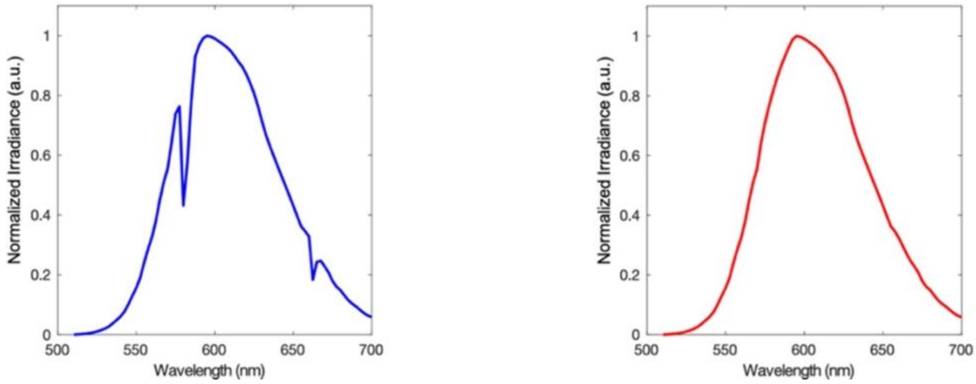

a) b)

Figure 3.24: Normalized spectral irradiance distribution for the LED with peak wavelength at 595 nm. a) Raw data before the removal of the discontinuities. b) Interpolated distribution used to calculate the total irradiance.

The temporal characteristics of LEDs emission (t_{on}=11 ms and t_{off} =11 ms and 99 repetitions) were kept constant along measurements with both instruments (power meter and spectrometer). The average and the standard deviation of radiometric power were obtained by averaging the measurements of the power meter over 1 s (approximately 1000 records). In the case of irradiance measurements, the average and the standard deviation were obtained from 3 measurements, as these last longer. The obtained results are shown in Figure 3.25.

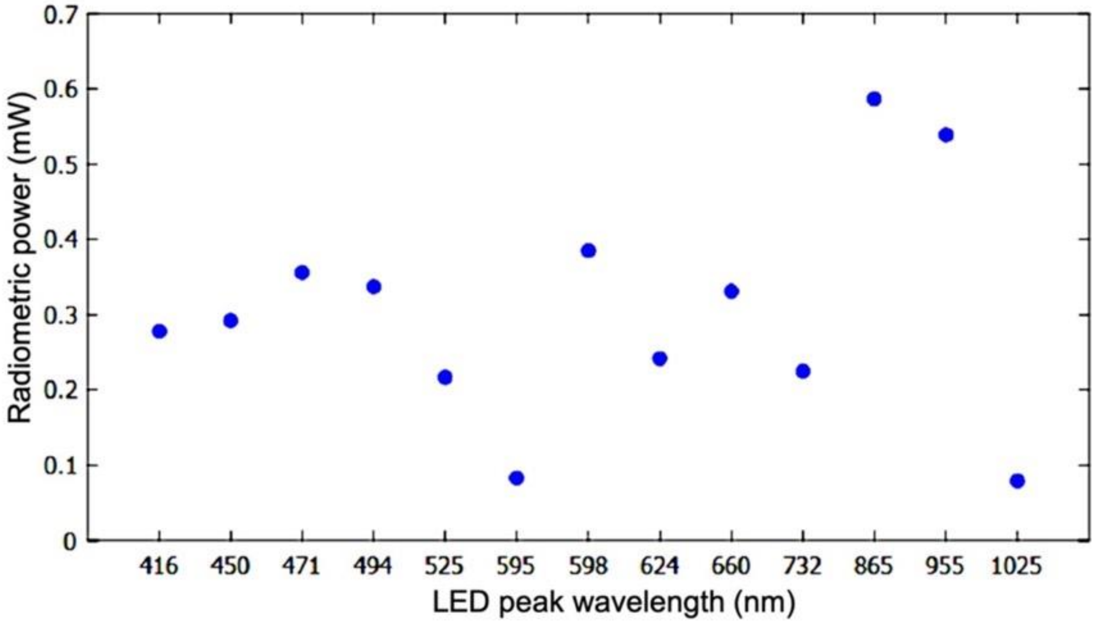

a)

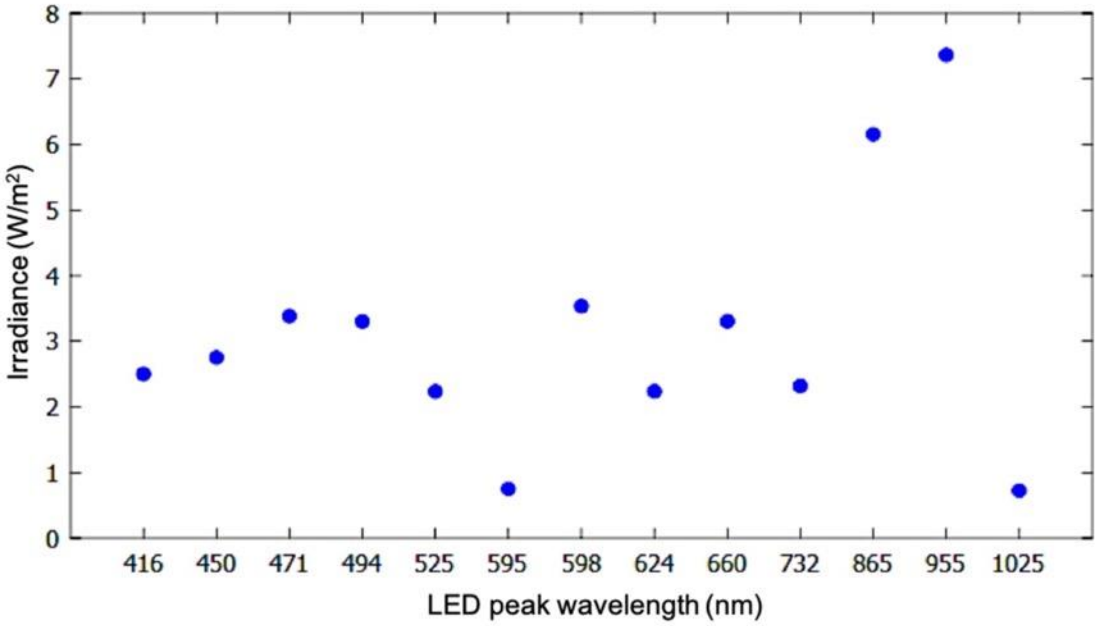

b)

Figure 3.25: a) Radiometric power and b) integrated irradiance, of the LEDs working at 12,5% of their maximum current. The standard deviations are not displayed since they are negligible.

By dividing the radiometric power values by the irradiance ones for each LED, we were able to find the conversion factor (K) between both measurements. Its uncertainty (ΔK) was computed as follows (Figure 3.26):

$$\Delta K = K \cdot \sqrt{\left(\frac{\Delta RP}{RP}\right)^2 + \left(\frac{\Delta I}{I}\right)^2} \qquad 3.8$$

where RP is the radiometric power, I is the irradiance, and ΔRP and ΔI are the corresponding standard deviations.

As can be seen, the values of the conversion factors calculated for different LEDs are distributed around an average value of K = 0.104 with a standard deviation of ΔK = 0.006, except for the LED emitting at 955 nm.The deviation from the mean of this LED is probably due to the responsivity curve of the power meter (Figure 3.27 a) and the broader spectral distribution of the LEDs at longer wavelengths (Figure 3.27 b). In fact, whereas in the linear part of sensitivity curve of the power meter the values around the peak wavelength of each LED are weighted symmetrically due to the Gaussian-like shape of their emission, between 900 nm and 1000 nm the spectral response of the power meter is not linear and the values around the peak wavelength are not weighted properly. Reasonably, the mean value and the standard deviation of the conversion factor can be calculated as the mean of the conversion factors of all LEDs, except for the one with a peak wavelength at 955 nm.

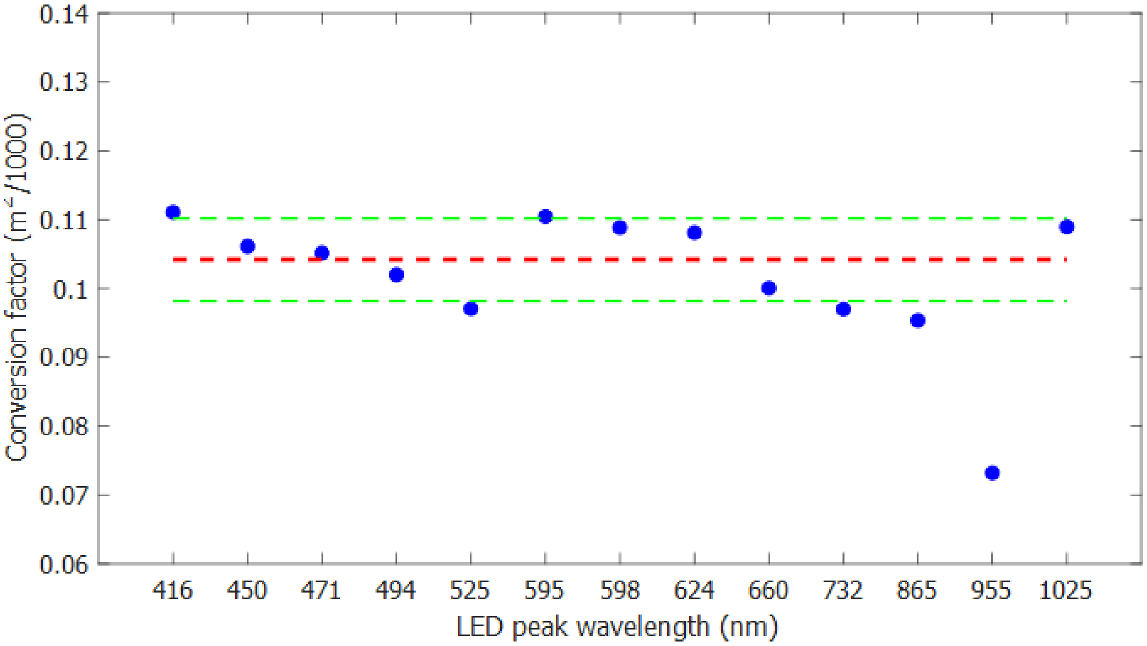

Figure 3.26: Conversion factor (K) for each LED. Red line indicates the mean value for all LEDs. Green lines represent the standard deviation interval (i.e., K ± ΔK). The standard deviations for individual LEDs are not displayed since they are negligible.

In addition, the results show that although the irradiance measurements are dependent on the illuminated area and, as stated above, the LEDs have different shapes at the measurement plane, this dependency is rather negligible. In fact, the deviation from the mean is almost the same through the entire spectral range regardless of the LEDs sizes (see Table 8).

According to all this, we were able to calculate the radiometric power values of LEDs with wavelengths 1096 nm and 1213 nm from the irradiance values measured with the spectrometer Spectro 320.

Finally, the total radiometric power ($RP_{100\%}$) of the LEDs between 400 nm and 1100 nm working at 100% (except for the one emitting at 955 nm) was measured with the power meter, whereas for LEDs 1096 nm and 1213 nm powers were estimated from the irradiance ($I_{100\%}$) measured with the Spectro 320. For the 955 nm - LED, its radiometric power was calculated multiplying the irradiance by the ratio between the mean conversion factor and the conversion factor calculated for this LED, to avoid the photodiode responsivity issue.

To obtain the effective radiometric power, the values obtained using the power meter must be finally multiplied by 2, as LEDs emit for half of the period of the applied signal (see Section 3.2.2).

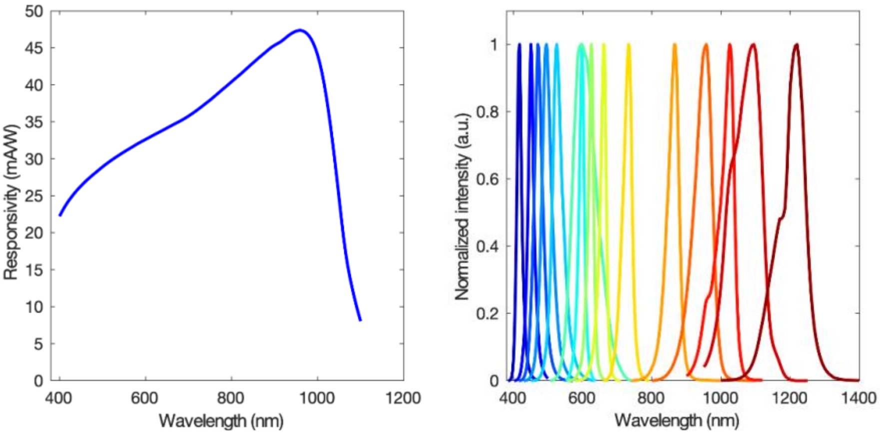

a) b)

Figure 3.27: a) Responsivity curve of the photodiode-based sensor S120C, used with the power meter PM100D [133]. Normalized spectral emission of the LEDs.

The spectral and integrated radiometric power of each LED at the patient’s pupil and the corresponding peak wavelength and FWHM are shown in Figure 3.28 and Table 9.

The mean FWHM and its standard deviation (ΔFWHM) were calculated from the three measurements carried out for each LED. The standard deviation ($\Delta RP_{100\%}$) for the radiometric power of the LEDs within 400 nm and 1100 nm, except for 955 nm, was provided by the power meter itself from the average of 1000 readings. In regards to the LEDs with peak wavelengths at 955 nm, 1096 nm and 1213 nm, the uncertainty on $RP_{100\%}$ values were calculated with the formula:

$$\Delta RP_{100\%} = RP_{100\%} \cdot \sqrt{\left(\frac{\Delta \mathrm{K}}{\mathrm{K}}\right)^2 + \left(\frac{\Delta I_{100\%}}{I_{100\%}}\right)^2} \qquad 3.9$$

where $\Delta I_{100\%}$ stands for the uncertainty of the irradiance.

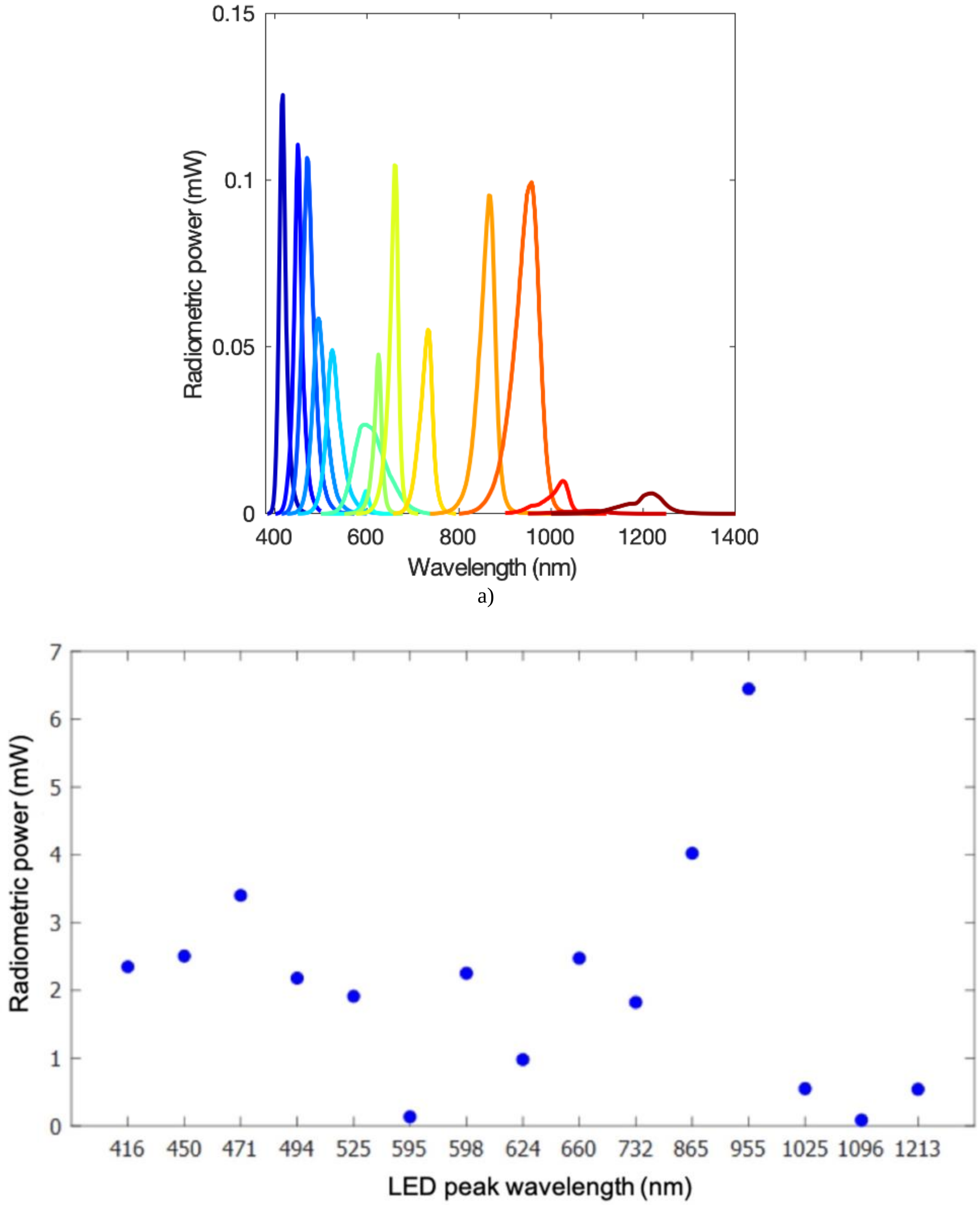

a)

b)

Figure 3.28: a) Spectral radiometric power distribution. b) Integrated radiometric power of the LEDs at the patient's pupil plane.

Table 9: Measured peak wavelength, FWHM and radiometric power (RP) of the LEDs at the patient's pupil plane.

LEDs peak wavelength (nm)	FWHM ± ΔFWHM (nm)	$RP_{100\%} \pm \Delta RP_{100\%}$ (mW)
416	16 ± 2	2.35 ± 0.04
450	18 ± 2	2.5 ± 0.2
471	27 ± 3	3.40 ± 0.07
494	31 ± 3	2.18 ± 0.09
525	33 ± 3	1.91 ± 0.03
595	17 ± 2	0.13 ± 0.01
598	76 ± 5	2.25 ± 0.02
624	17 ± 2	0.98 ± 0.06
660	19 ± 2	2.47 ± 0.07
732	29 ± 3	1.82 ± 0.04
865	37 ± 3	4.0 ± 0.3
955	58 ± 4	6.4 ± 0.5
1025	44 ± 4	0.55 ± 0.01
1096	97 ± 5	0.086 ± 0.005
1213	77 ± 5	0.54 ± 0.03

3.3.3 System repeatability

Once the hyperspectral fundus camera was built, several tests were carried out to ensure its correct operation. The stability of the system was firstly evaluated by means of an analysis of repeatability. In particular, the repeatability of the system was tested by performing the same measurement along different days (mid-term repeatability) and taking measurements consecutively (short-term repeatability). We used an artificial eye (OEMI-7, Ocular instrument Inc., United States) to perform the measurements, thus avoiding the instability given by the patient.

For each measurement, two streams of images were acquired, one with the LED at the 100% of its maximum emission and another with the LED at 0%. This is necessary to ensure a good background subtraction and to keep the measure independent from the ambient light. For the mid-term repeatability, we took a total of 10 measurements in 5 consecutive days (early in the morning and late in the afternoon). In order to have a repeatability estimation, the averaged intensity on the same portion of the image and its standard deviation were calculated for all wavelengths and for all measurements. Once we finished with the mid-term repeatability, the short-term repeatability was analyzed. Specifically, we acquired 10 consecutive complete streams of images. The images were then analyzed as in the mid-term study. The percentage of variability was calculated dividing the standard deviation by the averaged intensity value obtained in each case, resulting in the values shown in Figure 3.29 and Table 10.

As can be seen, the percentage of variation of both the mid- and the short-term analysis were lower than 2.98 % and 1.98 %, respectively. Therefore, the system could be considered very stable. Of course, to ensure a good performance over much longer periods of time, when extracting spectroscopic information from the images recorded with the system, periodical calibrations are required.

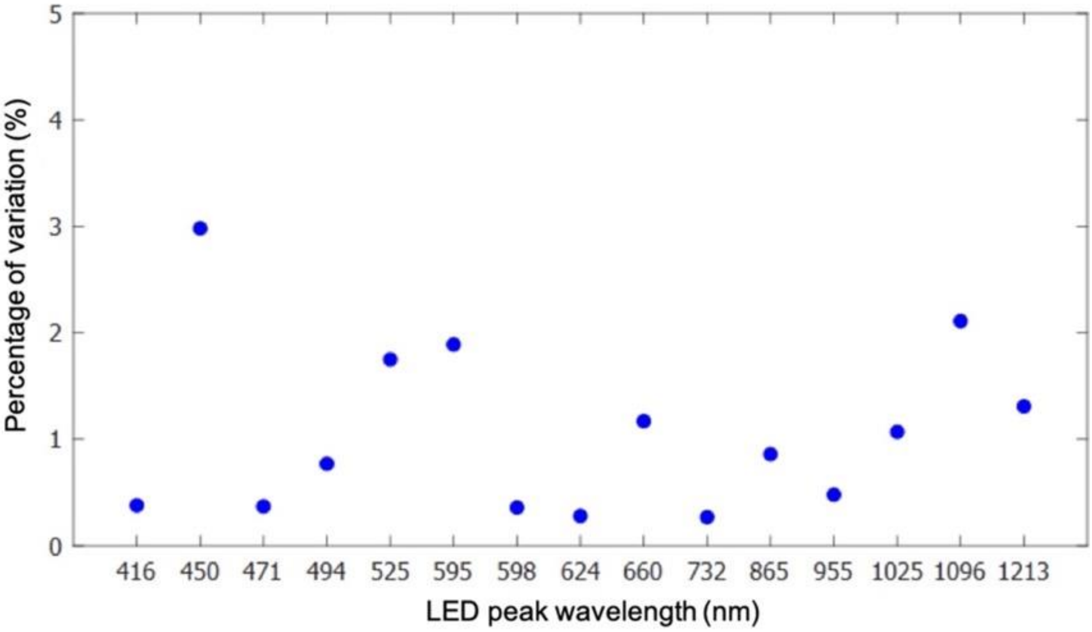

a)

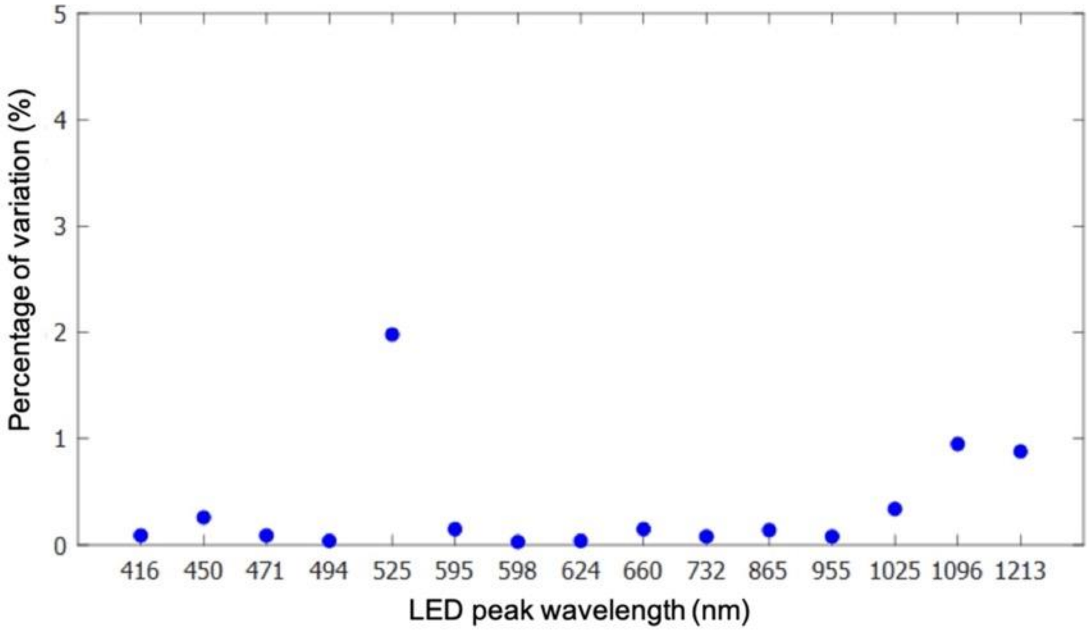

b)

Figure 3.29: Mid-term a) and short-term b) repeatability.

Table 10: Mid-term and short-term repeatability (percentage of variation) calculated dividing the standard deviation by the average intensity value of the same portion of the image.

LEDs Peak wavelength (nm)	Mid-term percentage of variation (%)	Short-term percentage of variation (%)
416	0.38	0.09
450	2.98	0.26
471	0.37	0.09
494	0.77	0.04
525	1.75	1.98
595	1.89	0.15
598	0.36	0.03
624	0.28	0.04
660	1.17	0.15
732	0.27	0.08
865	0.86	0.14
955	0.48	0.08
1025	1.07	0.34
1096	2.11	0.95
1213	1.31	0.88

3.4 Safety evaluation

The evaluation of the light hazard protection follows the Appendix A of the ISO 10940 [71], which is a guide for the measurements and the calculations of the relative values for the light hazard for fundus camera systems. This standard refers to the more generic one ISO 15004-2:2007 [72], which is also considered here and includes recommendations for ophthalmic instruments in general. This standard classifies ophthalmic instruments into either Group 1 or Group 2 in order to distinguish instruments that are non-hazardous from those that are potentially hazardous. For this classification, the systems are considered to include a continuous wave (CW) radiation source (if it delivers a continuous output for a time greater than 0.25 s), or a pulsed light source (if the light source delivers energy in the form of a single pulse or a train of pulses where each pulse has a duration of less than 0.25 s).

For the hyperspectral fundus camera developed in this thesis, the limits established for a pulsed light source will be of applicability in the measure phase (i.e., when acquiring the spectral fundus images) whereas those for CW must be used during the fixation target phase (while aligning the patient with the fundus camera). This is because, during alignment, patients can stand for more than 20 s in front of the system. The ISO states that the limits to be considered for safeness evaluation in the case of an exposition above 20 s are the ones of the continuous sources, even for a pulsed one.

The ISOs provide a step-by-step procedure to carry out the evaluation of a fundus camera:

- Measurement or estimation of the illuminated area at the corneal plane.
- Measurement or estimation of the illuminated area A on the retina (see Figure 3.30).
- Determination of the time width of the pulses of the light source.

- Measurement of the radiation irradiance E_λ, or of the radiant exposure H_λ (J/cm^2), as a function of the wavelength.
- Estimation of the radiant exposure H_{xx} (J/cm^2) in the corresponding spectral band, eye surface and condition (UV, VIS and IR, and aphakic). The values of H_{xx} are calculated as the sum of irradiance E_{xx} weighted by the functions S(λ) (UV radiation hazard weighting function), R(λ) (VIS and IR radiation thermal hazard weighting function) and A(λ) (aphakic photochemical hazard weighting function) [72]. The irradiances E_{xx} are obtained by dividing the radiometric power by the illuminated area on the retina and the cornea in the case of limits that correspond to the retinal or anterior segment optical planes, respectively.
- Determination of the number of pulses that the light source can emit during a time of 20 s.

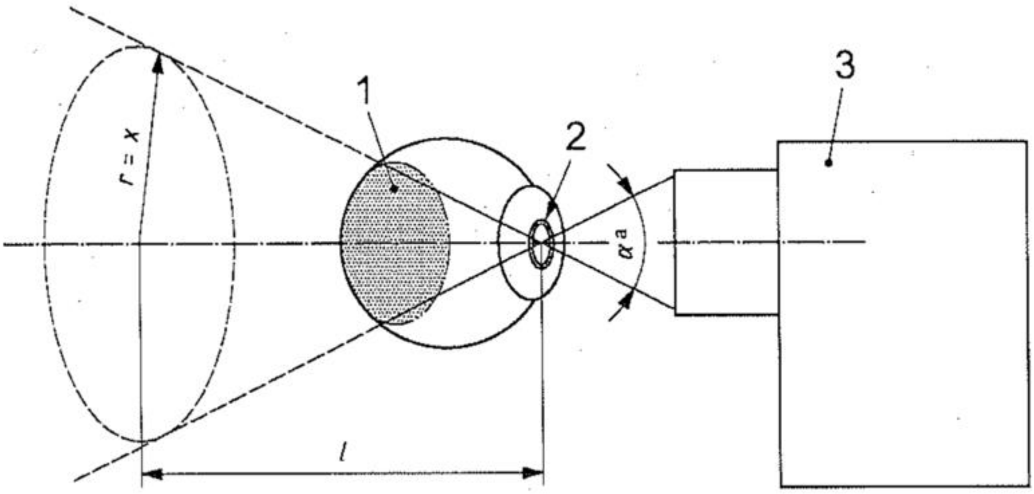

Figure 3.30: Description of the Maxwellian illumination conditions from Appendix A of the ISO 10940 [71]. The numbers and letters of the images refer to the illuminated retinal Area *A* (1), image of the light source in the pupil (2), fundus camera (3), full angular cone of illumination (α^a), distance between the pupil plane and the plane in which the measure to obtain the angular cone is performed (l), and the radius of the illumination field in that plane ($r = x$).

The ISO can be followed except for the calculation of the area covered by the illumination ring. In fact, in common fundus cameras the illumination forms a focused ring at the patient's pupil plane whereas in our system each single pair of LEDs only covers part of the ring. Therefore, the source can be considered multiple and the area that must be considered for each spectral channel at the patient's pupil plane is the portion of the area illuminated by each pair of LEDs, and not the complete illumination ring. In this regard, we measured the area covered by each LED at the patient's pupil plane as described in section 3.3.1. Considering that for each spectral channel of the system there are two LEDs of the same type, the total illuminated area for each spectral channel is twice the area (S) of that in Table 8.

In regards of the estimation of the retinal area illuminated by the system, and to remain in the worst-case scenario, we used the smallest measured values of the FOV presented in Table 5 as a measure of the complete angular cone (α). The illuminated retinal area A can then be calculated as follows:

$$A = (1.7cm^2)\omega = (1.7cm)^2 4\pi sin^2(\frac{\alpha}{4}) \qquad 3.10$$

The uncertainty ΔA is given by:

$$\Delta A = \Delta\alpha \cdot \frac{1}{2} \cdot cot(\frac{\alpha}{4}) \qquad 3.11$$

where the factor 1.7 cm^2 considers the distance from the retina to the patient's pupil and ω is the solid angle of the illumination cone.

The calculated value for the area A (±ΔA) from the complete angular cone was 0.631± 0.002 cm^2.

Due to the differences in retinal reflectance and radiometric power between LEDs of different spectral channels, the exposure times necessary to acquire fundus images were also different (Table 3). To remain in the worst-case scenario, we considered the maximum exposure times that permit the retinal imaging through all spectral channels without incurring in artifacts created by eye movements or pupil constriction. Thanks to the synchronization of the LEDs emission with the EL trigger signal of the EPB (see Section 3.2.2), an experimental measure of the pulse width was not necessary because the time length of a pulse is exactly the exposure time.

E_{xx} and H_{xx} can be calculated from the radiometric power values given in Table 9. The quantities that must be evaluated in our case are:

For the hyperspectral measurement (pulsed light source):

- H_{VIR-R}: R(λ) weighted retinal visible and infrared radiation radiant exposure
- H_{IR-CL}: unweighted corneal and lenticular infrared radiation radiant exposure
- H_{VIR-AS}: unweighted anterior segment visible and infrared radiation radiant exposure

During the fixation target phase (CW light source):

- E_{VIR-R}: R(λ) weighted retinal visible and infrared radiation thermal irradiance
- E_{IR-CL}: unweighted corneal and lenticular infrared radiation irradiance
- E_{VIR-AS}: unweighted anterior segment visible and infrared radiation irradiance

In Table 11, the formulas to calculate these quantities are given, as well as the corresponding safety limits.

In the case of the quantities with subscripts -CL and -AS, the irradiance must be calculated dividing the radiometric power of each spectral channel by the illuminated area at the cornea, while for those with subscript -R, the illuminated area to be considered is the one at the retina A. In addition, for the quantity with subscript VIR-R, the spectral band to be considered is between 400 nm and 1300 nm, for VIR-AS between 380 nm and 1200 nm, and for IR-CL between 700 nm and 2500 nm.

As already commented, our light source can be considered as a multiple light source and thus, an estimation of the safety of each single pair of LEDs is required. To fulfill the safety rules, the ratio between each quantity for each channel and the corresponding limit must be smaller than 1. Moreover, it must be additionally proven that the sum of all ratios is smaller than 1 (Section 5.4.3 of the ISO 15004-2:2007 [72]).

Table 11: Quantities, formulas and limits for the group 1 continuous and pulsed ophthalmic instruments evaluation. Δt is the pulse width, $\Delta\lambda$ indicates spectral summation interval and Δt is the exposure time for a particular radiation.

Quantity	Formula	Limit
H_{VIR-R}	$H_{VIR-R} = \sum_{380}^{1400} (E_\lambda \times \Delta t \times R(\lambda) \times \Delta\lambda)$	$6t^{3/4}$ J/cm^2
H_{IR-CL}	$H_{IR-CL} = \sum_{770}^{2500} (H_\lambda \times \Delta\lambda)$	$1.8t^{1/4}$ J/cm^2
H_{VIR-AS}	$H_{VIR-AS} = \sum_{380}^{1200} (H_\lambda \times \Delta\lambda)$	$25t^{1/4}$ J/cm^2
E_{VIR-R}	$H_{VIR-R} = \sum_{380}^{1400} (E_\lambda \times R(\lambda) \times \Delta\lambda)$	0.7 W/cm^2
E_{IR-CL}	$E_{IR-CL} = \sum_{770}^{2500} (E_\lambda \times \Delta\lambda)$	0.02 W/cm^2
E_{VIR-AS}	$E_{VIR-AS} = \sum_{380}^{1200} (E_\lambda \times \Delta\lambda)$	4 W/cm^2

To remain in the worst-case scenario again, the radiometric power that was considered in the computations is the sum of the mean value plus twice the standard deviation of the measure (Table 9). By doing so, there is 96,3% of probability to be below the considered radiometric power value.

Table 12, Table 13 and Table 14 show the safety evaluation for each spectral channel as well as for the entire hyperspectral acquisition. In view of the results, the pulsed hyperspectral fundus camera classifies as Group 1. Regarding the evaluation of the system over 20 seconds, it is not necessary because the system electronics and software permits only one measure in 20 s, regardless of being pulsed.

Table 12: Safety evaluation of R(λ) weighted retinal visible and infrared radiation radiant exposure during hyperspectral acquisition.

H_{VIR-R}: Retinal visible and infrared radiation radiant exposure (Spectral range 380 nm – 1400 nm)						
LED peak wavelength	Δt (s)	Area (cm^2)	Weighted (R(λ)) LED power (mW)	Value (J/cm^2)	Limit (J/cm^2)	Ratio
416 nm	0.011	0.63	1.75	3.05E-05	0.20	1.53E-04
450 nm	0.011	0.63	2.50	4.36E-05	0.20	2.18E-04
471 nm	0.011	0.63	3.40	5.93E-05	0.20	2.96E-04
494 nm	0.011	0.63	2.18	3.80E-05	0.20	1.90E-04
525 nm	0.011	0.63	1.91	3.33E-05	0.20	1.66E-04
595 nm	0.011	0.63	0.13	2.34E-06	0.20	1.17E-05
598 nm	0.011	0.63	2.25	3.92E-05	0.20	1.96E-04
624 nm	0.011	0.63	0.98	1.71E-05	0.20	8.53E-05
660 nm	0.011	0.63	2.47	4.31E-05	0.20	2.15E-04
732 nm	0.011	0.63	1.61	2.81E-05	0.20	1.40E-04
865 nm	0.011	0.63	1.95	3.40E-05	0.20	1.70E-04
955 nm	0.011	0.63	2.13	3.71E-05	0.20	1.85E-04
1025 nm	0.100	0.63	0.14	1.08E-05	0.63	1.73E-05
1096 nm	0.120	0.63	0.02	2.85E-06	1.07	2.73E-06
1213 nm	0.100	0.63	0.11	2.57E-05	1.45	1.81E-05
	TOTAL					2.06E-03

Table 13: Safety evaluation of unweighted anterior segment visible and infrared radiation radiant exposure during the hyperspectral acquisition.

H_{IR-AS}: Unweighted anterior segment visible and infrared radiation radiant exposure (Spectral range 380 nm – 1200 nm)						
LED peak wavelength	Δt (s)	Area (cm^2)	LED power (mW)	Value (J/cm^2)	Limit (J/cm^2)	Ratio
416 nm	0.011	2.16E-03	2.43	1.24E-02	8.10	1.53E-03
450 nm	0.011	1.70E-03	2.9	1.88E-02	8.10	2.32E-03
471 nm	0.011	1.52E-03	3.54	2.56E-02	8.10	3.17E-03
494 nm	0.011	1.76E-03	2.36	1.47E-02	8.10	1.82E-03
525 nm	0.011	2.09E-03	1.97	1.04E-02	8.10	1.28E-03
595 nm	0.011	1.64E-03	0.15	1.01E-03	8.10	1.24E-04
598 nm	0.011	2.16E-03	2.29	1.17E-02	8.10	1.44E-03
624 nm	0.011	1.83E-03	1.1	6.63E-03	8.10	8.19E-04
660 nm	0.011	1.83E-03	2.61	1.57E-02	8.10	1.94E-03
732 nm	0.011	3.69E-03	1.9	5.67E-03	8.10	7.00E-04
865 nm	0.011	2.30E-03	4.6	2.20E-02	8.10	2.72E-03
955 nm	0.011	2.09E-03	7.2	3.79E-02	8.10	4.68E-03
1025 nm	0.4100	2.52E-03	0.57	1.13E-02	11.8	9.56E-04
1096 nm	0.120	2.75E-03	0.096	3.49E-03	14.1	2.48E-04
1213 nm	0.100	2.91E-03	0.6	3.09E-02	15.6	1.99E-03
	TOTAL					2.57E-02

Table 14: Safety evaluation of unweighted corneal and lenticular infrared radiation radiant exposure during hyperspectral images acquisition.

H_{IR-CL}: Unweighted corneal and lenticular infrared radiation radiant exposure (Spectral range 770 nm - 2500 nm)						
LED peak wavelength	Δt (s)	Area (cm^2)	LED power (mW)	Value (J/cm^2)	Limit (J/cm^2)	Ratio
865 nm	0.011	2.30E-03	4.6	2.20E-02	0.583	3.77E-02
955 nm	0.011	2.09E-03	7.2	3.79E-02	0.583	6.50E-02
1025 nm	0.100	2.52E-03	0.57	1.13E-02	0.851	1.33E-02
1096 nm	0.120	2.75E-03	0.096	3.49E-03	1.01	3.45E-03
1213 nm	0.100	2.91E-03	0.6	3.09E-02	1.12	2.76E-02
	TOTAL					0.147

The CW analysis of the fixation target phase is required because, as commented previously, this procedure can last more than 20 s. This part includes the evaluation of LEDs used to align the system (1025 nm and 1096 nm) as well as those of the fixation target (660 nm). During the fixation target sequence, the LEDs are turned on and off sequentially and each one emits for a short period of time but, we considered a continuous exposure of the eye to all LEDs as being turned on simultaneously as the worst-case scenario. The entire sequence of the fixation target lasts for 0.1 s and the radiometric power of each LEDs is weighted considering their emission period. In particular, the 1025 nm and 1096 nm LEDs are turned on for 33 ms at 30% and 90% of their maximum emission power, respectively, and the fixation target at 1% for 5 ms, during the refractory time of the InGaAs camera.

In the following tables (Table 15, Table 16 and Table 17), the limits for the fixation phase are listed. In view of these results, the light source used in the fixation target phase also classifies as Group 1, as the values measured are below the limits established by the standards.

Table 15: Safety evaluation of R(λ) weighted retinal visible and infrared radiation thermal irradiance during the fixation target phase.

E_{VIR-R}: Retinal visible and infrared radiation thermal irradiance (Spectral range 380 nm – 1400 nm)					
LEDs peak wavelength	Area (cm^2)	Weighted (R(λ)) LED power (mW)	TOTAL Irradiance (mW/cm^2)	Limit (mW/cm^2)	Ratio
660 nm	2.85E-03	1E-06	1.85.6E-02	700	2.59E-05
1025 nm	0.63	5.6E-03			
1096nm	0.63	5.6E-03			

Table 16: Safety evaluation of unweighted corneal and lenticular infrared radiation irradiance during the fixation target phase.

E_{IR-CL}: Unweighted corneal and lenticular infrared radiation irradiance (Spectral range 770 nm- 2500 nm)					
LEDs peak wavelength	Area (cm^2)	LED power (mW)	TOTAL Irradiance (mW/cm^2)	Limit (mW/cm^2)	Ratio
660 nm	2.5E-02	1E-06	8.02	20	0.401
1025 nm	2.52E-03	1E-02			
1096 nm	2.75E-03	1E-02			

Table 17: Safety rules evaluation of unweighted anterior segment visible and infrared radiation irradiance during the fixation target phase.

E_{VIR-AS}: Unweighted anterior segment visible and infrared radiation irradiance (Spectral range 380 nm – 1200 nm)					
LED peak wavelength	Area (cm^2)	LED power (mW)	TOTAL Irradiance (mW/cm^2)	Limit (mW/cm^2)	Ratio
660 nm	2.5E-02	1E-06	8.02	4000	2.01E-03
1025 nm	2.52E-03	1E-02			
1096 nm	2.75E-03	1E-02			

4 CLINICAL STUDY, IMAGE PROCESSING AND SPECTRAL ANALYSIS

4.1 Clinical study

A clinical study using the HSI fundus camera was conducted at the Instituto de Microcirugía Ocular (IMO) in Barcelona (Spain) and at the University Vision Center (CUV) of the Universitat Politècnica de Catalunya (UPC) in Terrassa (Spain) under the supervision of an ophthalmologist (C. M.). The objective was to validate the hyperspectral retinograph and analyze its usefulness in the detection of fundus structures and diseases. The starting hypothesis was that from the spectral images at specific wavelengths, especially the IR ones, it would be possible to obtain information that is hidden in color fundus images, which might be relevant for clinical diagnosis. To this end, measurements were carried out in healthy patients and with various retinal diseases (retinopathies, glaucoma, ARMD, etc.).

The target population of the study met the following inclusion criteria:

- Healthy eyes (control group).
- Eyes with a retinal pathology.
- Subjective spherical refraction comprised between ± 15 D and astigmatism < 3 D. The spherical refraction is limited by the prototype correction range. A low astigmatism value is needed to obtain acceptable images without high distortion, as it cannot be corrected by the system.

Age was not a restrictive parameter.

Exclusion criteria were the diagnosis of any other ocular or systemic disease affecting the eye different from the previous ones (retinal pathologies), especially those that notably alter the transparency of the ocular media such as mature cataracts. Nevertheless, healthy or eyes with a retinal disease that had undergone cataract surgery with implantation of an intraocular lens (IOL) were accepted to take part in the study, as well as with early/moderate cataracts.

All patients provided written informed consent before any examination and after receiving a written and verbal explanation on the nature of the study, and ethical committee approval was obtained (the written informed consent form can be found in Appendix C). The study complied with the tenets of the 1975 Declaration of Helsinki (Tokyo revision, 2004).

Firstly, some information of each patient was collected from his/her clinical history including age, gender, subjective manifest refraction, best-corrected visual acuity (BCVA), intraocular pressure (IOP) and the ophthalmologist's diagnosis: previous pathologies, presence of cataracts, intraocular lenses implanted, etc.

Conventional color retinography and OCT were performed either with a 3D OCT-1 Maestro (Topcon Corporation, Japan) at CUV or with a mydriatic color fundus camera TRC-50DX (Topcon Corporation, Japan) and CIRRUS HD-OCT (Carl Zeiss Meditec, Germany) at IMO, and when the patient's pupil was not dilated, an Optomap SLO fundus camera (Optos, Scotland) was used instead. OCT images were acquired for some of the patients or, alternatively, were collected from the database if available.

Finally, the recordings with the HSI prototype were carried out. The instructions to the patient when executing the measurements, taken by 4 trained optometrists (N. S., L. R., E. B. and N. M.), were very straightforward:

1. To place the chin and forehead on a chinrest to keep the head still during measurements.

2. To look at the fixation target that appeared when aligned with the instrument. In case that the ocular pathology impaired the patient's vision severely, thus avoiding the target perception, the patient was asked to look straight trying to keep the eyes still.

3. Stop blinking while acquiring the spectral images (during 613 ms).

The measurement protocol was as follows; one eye was measured at a time and the duration of the complete evaluation (including both eyes and two repetitions for each eye) lasted about 10 minutes. The patient's refraction was corrected with the system (spherical equivalent) before any measurement. A background image was acquired just after each measure to remove artifacts such as residual back reflections and ambient light. First of all, the patient was aligned with the fundus camera with the help of the live acquisition mode and the fixation target. This step was crucial for the correct acquisition of the retinal hyperspectral sequence as it allowed the corneal and crystalline back reflections to be avoided. The fixation targets were changed depending on the measured eye (left/right) using the MATLAB routine described in Section 3.2.2. This allowed stabilizing and visualizing the optic disk and the macula inside the same FOV. If a relevant anomaly located at the peripheral retina was observed, the patient was asked to look additionally at another direction in order to allow its acquisition.

A total of 100 patients (200 eyes) with retinal diseases (at least in one eye) were measured as well as 72 eyes from 36 healthy patients (control group). Due to artifacts in the images that could not be removed, obstacles such as mature cataracts and other limitations (too large spherical or astigmatic refraction, etc.), the final spectral analysis was restricted to 60 diseased and 61 healthy eyes. Table 18 shows the corresponding patient demographics. Table 19 shows the number of eyes with IOLs and early/moderate cataracts, as well as the subjective refraction, BCVA and intraocular pressure of all eyes included in the analysis.

Table 18: Patient demographics for the control group and patients with retinal diseases.

<table>
<tr><td></td><td colspan="2">Control group</td><td colspan="2">Patients with retinal diseases</td></tr>
<tr><td>Number of patients</td><td colspan="2">31</td><td colspan="2">30</td></tr>
<tr><td>Number of eyes</td><td colspan="2">61</td><td colspan="2">60</td></tr>
<tr><td>Gender</td><td>14 M (45 %)</td><td>17 F (55 %)</td><td>9 M (30 %)</td><td>21 F (70 %)</td></tr>
<tr><td>Mean age ± SD (min, max) (years)</td><td colspan="2">45.4 ± 17.04 (19, 74)</td><td colspan="2">67.6 ± 15.3 (19, 91)</td></tr>
</table>

Table 19: Eyes of the control group and with retinal diseases with implanted IOLs and with early/moderate cataracts. Subjective manifest refraction (sphere and cylinder) in Diopters (D), BCVA and intraocular pressure (IOP, in mmHg). Except for the number of eyes, the mean ± SD (min, max) are given.

	Control group	Patients with retinal diseases
Number of eyes with IOL (%)	5 (8%)	21 (35 %)
Number of eyes with cataract	-	20 (33 %)
Sphere (D)	-0.38 ± 1.86 (-5.00, 3.25)	0.04 ± 2.44 (-10.50, 4.50)
Cylinder (D)	-0.64 ± 0.64 (-2.00, 0.00)	-0.87 ± 0.70 (-2.75, 0.00)
BCVA	0.98±0.10 (0.6, 1.2)	0,64 ± 0,30 (0.01, 1.00)
IOP (mmHg)	15.0 ± 4.0 (7.0, 24.0)	15.7 ± 4.1 (6.0, 28.0)

The following diagnosis and conditions/treatments were found in the 60 eyes with retinal diseases: dry ARMD (13 eyes), wet ARMD (6 eyes), thrombosis (1 eye), maculopathy (1 eye), glaucoma (3 eyes), Retinal Angiomatous Proliferation (RAP) (1 eye), drusen (11 eyes, 2 of them in the optic disk), choroidal nevus (3 eyes), amblyopia (1 eye), edema (2 eyes), atrophy (5 eyes), RPE degeneration (8 eyes), diabetic retinopathy (1 eye), scars (2 eyes), macular hole (2 eyes), photocoagulation (1 eye), hemorrhage (10 eyes) and retinal inflammation (1 eye). Some patients had more than one diagnosis/condition and thus, they were considered in more than one category simultaneously.

4.2 Image processing

A self-standing software application (Figure 4.1) was developed to remove inhomogeneities, back reflections and artifacts in the retinal images (Figure 4.2). In fact, despite the simulations carried out and the precise alignment, some back reflections from optical components still remain in some cases, as well as artifacts caused by involuntary eye movements and residual inhomogeneities (bright areas) at the borders or at the center of the retinal images due to non-uniformities of the illumination.

The same software was also used to compensate for the spectral response of the system - which is different in each spectral band due to differences in the QE of the cameras and power of the LEDs - so that spectroscopic information useful for diagnosis could be derived from the hyperspectral sequence of images, as described later.

To perform all these corrections, the following steps were carried out. Four complete hyperspectral sequences were acquired for each patient: one for each eye (retinal sequences) and 2 for the background acquisition (background sequences). Considering the one-shot nature of the HSI fundus camera and the high power of the LEDs, a slight change of emission due to LED heating can reduce the effectiveness of the background subtraction producing some artifacts in the images. Therefore, 2 acquisitions of the background were necessary (one for each eye) with exactly the same exposure times and powers used in the retinal sequences. The background sequences were acquired without any eye in front of the system and using a highly absorptive black sheet placed in front of the objective lens and at the furthest position still containing the entire LED illumination, [75]. To reduce as much as possible other error sources, the ambient light was minimized during acquisitions.

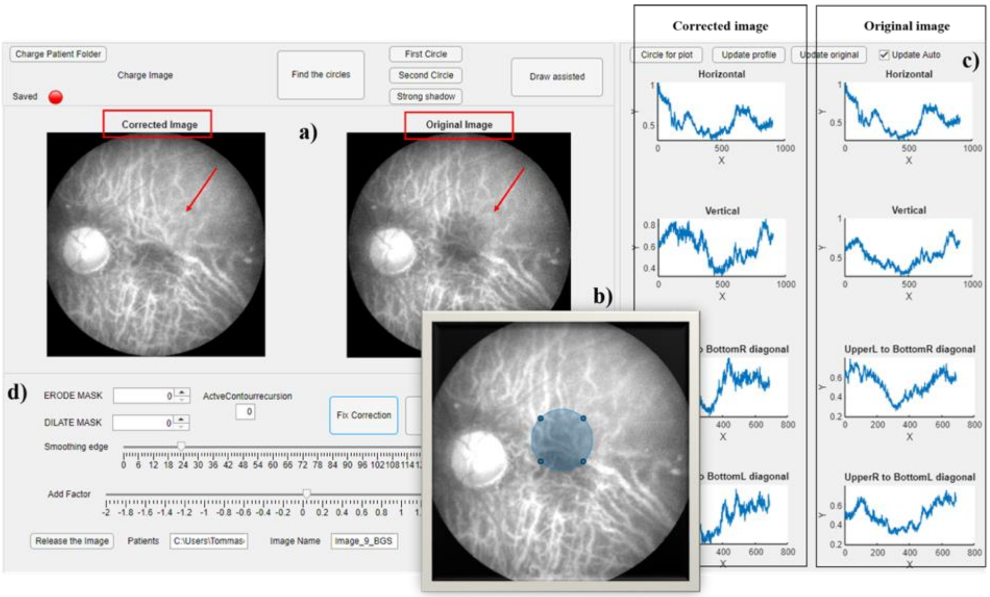

ERODE MASK 0
DILATE MASK 0
ActveContourrecursion 0
Patients C:\Users\Tommas
Image Name Image_9_BGS

Figure 4.1: Software application used to process the spectral images. a) Two images of the retina are shown: the right one corresponds to an unprocessed image; the left one corresponds to the image in which the corrections are applied. Red arrows indicate the area that is being processed. b) Image displayed to draw the segmentations of shadows (in blue). c) Profiles of the digital levels of the pixels of the image before (right) and after (left) shadow correction, in four different directions. d) Eligible values of the parameters that provide the modifications on the shape of the mask and digital levels for the correction. Further explanation later on in this chapter.

Each sequence (retinal or background) consisted of 30 images: the first 15 contained the images taken with the LEDs turned on while the last 15 were acquired automatically and immediately after the first ones, but with the LEDs switched off. These were used as dark-images and were meant to correct for inhomogeneities caused by camera noise, especially of the InGaAs sensor, since it has artifacts due to the manufacturing process that might depend on the exposure time used. Twelve of the 15 images were acquired with the CMOS camera while the other 3 were acquired with the InGaAs. It is worth noting that, to match the two different sensors sizes and resolutions, all the following processing steps were performed considering the corresponding size and resolution so that all images could be considered independent of the sensor. In other words, no rescaling or resizing of the acquired images was done during the processing steps while operations such as the filtering were properly adapted (rescaled) considering the spatial frequencies of the image under analysis and its original resolution.

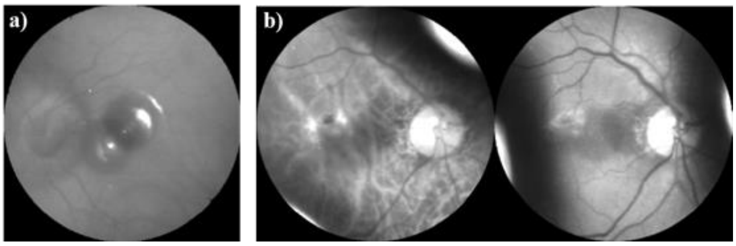

Figure 4.2: Fundus images with bright artifacts caused by: a) back reflections from the objective and b) back reflections due to misalignments between the system and the eye (at the borders).

The first step of processing was the dark-image subtraction (taken with the LEDs off) from both the background and retinal sequences (acquired with the LEDs on), that is, the removal of the last 15 images from the 15 first ones in each sequence. Therefore, any hyperspectral sequence (retinal or background) was actually combined and reduced into 15 dark-subtracted images. A second step was meant to reduce any possible back reflections caused by the radiation of LEDs reflected by the optical surfaces of the system, which would be present in both the retinal and background images when the LEDs are switch on. This was accomplished by subtracting the dark-subtracted background images from the dark-subtracted raw retinal images, providing 15 cleaned images, where the impact of the ambient light, inhomogeneities of the sensors and back reflections were minimal (Figure 4.3 a).

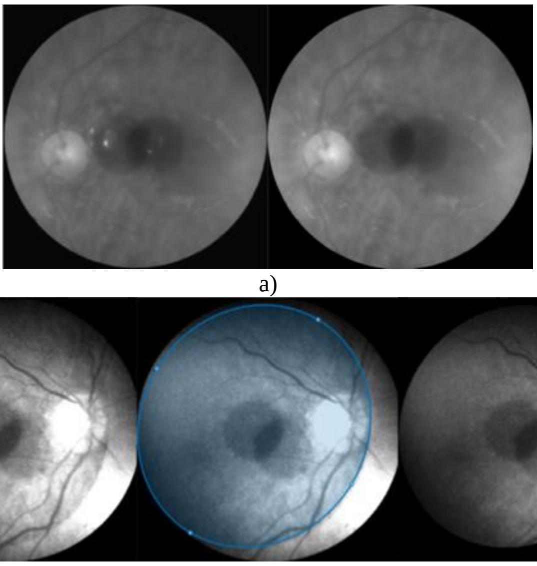
a)

b)

Figure 4.3: a) Uncorrected (left) and corrected (right) retinal image, where the impact of the ambient light, inhomogeneities of the sensor and back reflections have been reduced. b) From left to right, example of a cropping process using an ellipse-shape mask.

Then, a circle-shaped binary mask was applied to all images by default (third step). This mask was created considering the FOV imposed by the diaphragms placed at retinal conjugate planes in the VIS-NIR and NIR-IR detection arms. In some cases, and due to eye misalignments, bright zones at the borders of the fundus image appeared and images were cropped to exclude them by means of a customized ellipse-shaped mask (Figure 4.3 b). To achieve this, the software enabled the user to visualize a montage of the whole sequence (15 images) organized in only one figure, and the image in which the artifacts were more notorious was then selected; the user then drew an ellipse (mask) on it, which was applied for cropping all of the 15 images, thus ensuring the correct selection of the FOV without bright inhomogeneities.

A fourth step allowed correcting the inhomogeneities produced by the black stop used to shadow the back reflections from the objective, which appeared in the images as expected from the optical design (see section 3.1.3). The shadows were located at different positions in each of the 15 images (Figure 4.4 a) since each pair of LEDs was illuminating the retina from different angles depending on their location on the ring. Furthermore, due the patient’s refraction, the shadows could be nearer or farther to each other. All this prevented from performing general strategies to process the images and, as a consequence, customized corrections for each of the images were needed. These corrections included the creation of a segmented mask with the shape of the shadow, which was later multiplied by the original image after some adjustments on the segmented area. In particular, the mask was an image with resolution equal to the image to be corrected, with 1's for the segmented area and 0's elsewhere. As the black stop has a circular shape, the software enabled the user to segment the artifact's zones in 2 circles (one for each LED shadow), using a circle-shaped tool. However, a draw-assisted tool could also be used to carry out a customized shape in order to better segment the artifact when the circular one was not accurate enough. Further details are referred to any segmentation-shape. Once the two masks had been generated (one for each shadow), the software enabled choosing a multiplying factor for each one (by which the values of the pixels inside the segmented area were multiplied) and a smoothing factor that regulates the width of a Gaussian filter applied only at the edges of the mask. Finally, the resulting masks were added to an image filled with 1's. In this way, in the product of this mask image times the original one, only the values different from 1 were changed (i.e., only those inside the corrective masks).

By means of these corrections, the digital levels of the shaded area are increased until the shadowed region appears as continuous with respect to the surrounding area. All these parameters can be adjusted in the software (Figure 4.1 d), including wise dilation and erosion of the segmentation-shape for a fine adjustment at the border of the shadow.

All described modifications were applied and displayed in real time so the user was able to evaluate the correction process and set the parameters adequately. Additionally, a fine evaluation of the correction of artifacts can be done by comparing the profiles of the digital values of the original (raw) image and the corrected one (Figure 4.1 c). The profiles are referenced from the center of the artifacts to 4 different directions in the image (vertical, horizontal and 2 diagonals) to detect the main differences, which are expected to be minimal when comparing the original and the final processed image (Figure 4.4 b).

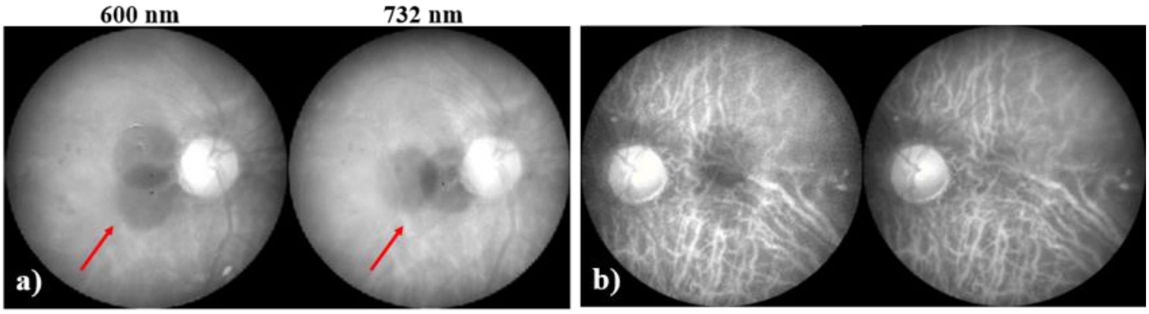

Figure 4.4: a) Example of two retinal images acquired at 600 nm and 732 nm. Red arrows point the shadows, which appear at different positions depending on the wavelength (LEDs pair). b) Spectral fundus image with shadows (left) and corrected (right).

Next, in order to compensate for the spectral response of the fundus camera, which is different in each spectral band due to differences in QE of the cameras and power of the LEDs, we acquired images of a calibrated reference white (BN-R98-SQC, Gigahertz-Optik GmbH, Germany) placed 1 m far from the pupil plane of the system, [75]. The spectral retinal images were then corrected as follows:

$$\mathrm{Ic}_{\lambda n}(\mathrm{i},\mathrm{j}) = \mathrm{Refl}_{\mathrm{ref}_{\lambda n}} \cdot \frac{\mathrm{I}_{\lambda n}(\mathrm{i},\mathrm{j})}{\mathrm{I}_{\mathrm{ref}_{\lambda n}}(\mathrm{i},\mathrm{j})} \qquad 4.1$$

where $Ic_{\lambda n}(i,j)$ is the corrected intensity of the spectral image of the fundus at wavelength λ_n in arbitrary units, $I_{\lambda n}(i,j)$ is the intensity of the processed image of the fundus (using the processing described in the preceding paragraphs), $I_{ref_{\lambda n}}(i,j)$ is the intensity of the image of the calibrated reference white, and $Refl_{ref_{\lambda n}}$ is the calibrated reflectance of the reference white given by the manufacturer.

Although $Ic_{\lambda n}(i,j)$ should correspond to the fundus spectral reflectance, it is noteworthy that it also includes the transmission of the ocular media (cornea, lens, aqueous humor and vitreous) besides the reflectance of the retina itself. Therefore, an absolute comparison of this term among individuals might not be convenient and, in general, relative comparisons within the same fundus image are used for a proper spectroscopic analysis, as it will be described in the following section.

In order to correct for residual inhomogeneities of illumination still affecting the image, an additional (sixth) correction was used with the MATLAB function *imflatfield* (Figure 4.5). This function applies a Gaussian smoothing filter over the whole FOV, filtering out the higher spatial frequencies. Thus, a background correction image with only the lower spatial frequencies is created and, dividing the original fundus image by the filtered one, the inhomogeneities over the FOV are compensated without affecting the fundus structures if the appropriate width of the Gaussian filter is chosen. To do so, this parameter was set according to the dimensions of the biggest structure of the retina that should be preserved after the correcting process: the optic disk. In particular, we considered an average radius of 3° for this structure plus 0.5°, thus ensuring that the filtering process did not affect the relative mean intensity of higher spatial frequencies. The mean value of the created *flatfield* mask was normalized to the unity so the mask could change locally the intensity values of the image but did not change its mean value. The filter was rescaled considering the image resolutions and magnifications, keeping the relative intensities of the same optical frequencies among different spectral bands (channels) unchanged, even if acquired with different sensors.

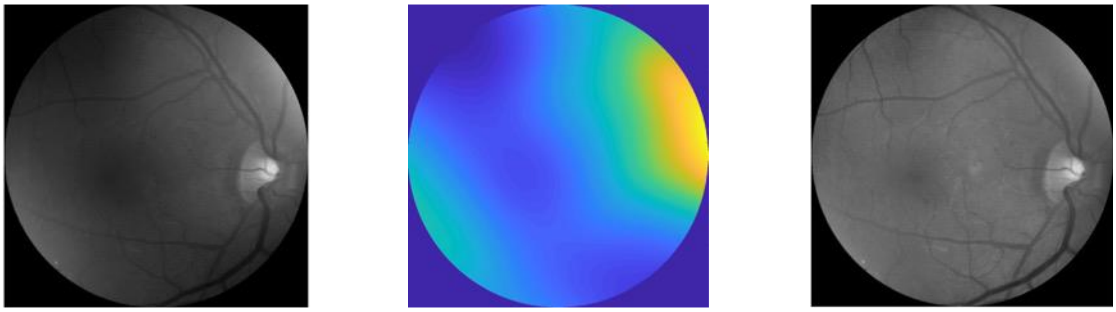
a) b) c)

Figure 4.5: Example of the digital flat field processing: a) uncorrected image, b) filter mask, c) flat-fielded image.

An intensity normalization of the flat-fielded image was required only for visualization purposes. Due to the transmittance of the ocular media, images at different wavelengths might actually have very different mean intensities. Accordingly, a normalization was performed dividing each image by its averaged digital level (calculated only at the non-zero values) and then multiplying this result by the half of the dynamic range used for visualization (8-bits). In this way, all images had the same mean value and details could be better appreciated with the naked eye. As stated formerly, this normalization was only applied for a qualitative analysis of the fundus images as it actually changes the overall intensity of the image and completely biases the corresponding spectral information, which is indeed useful in a quantitative spectral analysis. Additionally, the contrast of the 8-bit image used for visualization was always adjusted to take advantage of the bit depth of the two detectors used (16-bit for the CMOS and 14-bit for the InGaAs) and better appreciate details in the images.

Finally, in order to be able to compare the same Region Of Interest (ROI) in the CMOS and InGaAs sensors, a cross correlation between pairs of images was carried out considering 5 to 10 equivalent points manually selected on both, which allowed to compute a mapping vector to transform the pixel coordinates of the ROI from the first to the second image, or vice versa.

Although the software developed for correcting the spectral images acquired with the prototype was shown to be very useful, some limitations arose during its development. Regarding artifacts caused by misalignments of the eye and the system itself, their exclusion was achieved by means of the proper FOV selection, i.e., avoiding illumination inhomogeneities. These artifacts usually appeared at the borders of the retinal image. Nevertheless, in some cases large areas of the FOV were affected and thus, the image cropping process based on a customized ellipse-shape mask caused their loss. In other cases, the area with bright zones was so big that the ellipse-shape cropping notably reduced the FOV, making the complete image sequence useless. These cases corresponded to measurements where eye movements and poor fixation were notorious during the acquisition process due to the advanced age of many of the patients included in the study. Moreover, 70% of the examined eyes had implanted IOLs or cataracts, especially mature, causing back reflections and/or strong scattering, especially at shorter wavelengths (Figure 4.6 a and b), besides the intrinsic dependency of water transmission over the wavelengths in the NIR, which was also manifested in the spectral sequence. Sometimes, the correction process produced some additional artifacts, most of them at the edges of the segmented areas (shadows) (Figure 4.6 c). If this happened, the operator avoided performing spectral analysis on that part of the image.

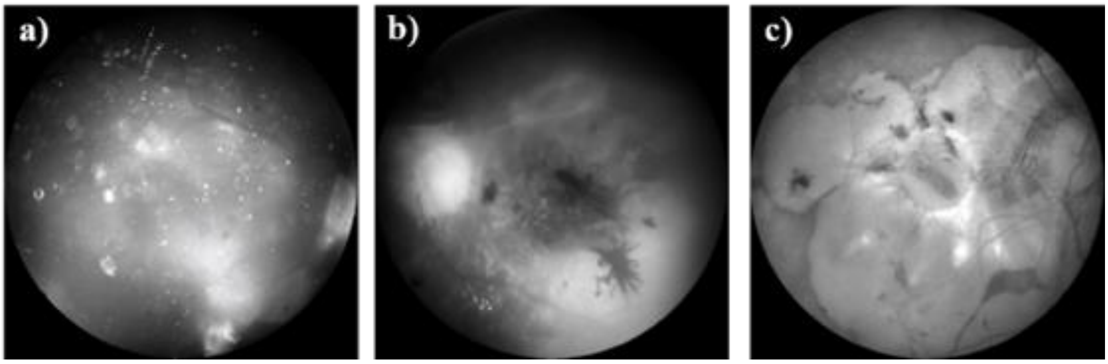

Figure 4.6: Examples of retinal images containing inhomogeneities and artifacts that could not be corrected with the software. a) Back reflections caused by the presence of an IOL, b) blurred and distorted image due to the presence of a cataract, and c) imperfect shadow correction with additional artifacts around the segmented area.

This processing was applied to all retinal spectral images acquired for healthy and diseased eyes included in the clinical study. As an example, Figure 4.7 depicts three retinal sequences at different levels of processing.

It can be seen that the shadows cannot be perceived in the corrected images. The flat field correction makes the images uniform and the artifacts due to residual back reflections and misalignments are eliminated, permitting a good visualization of the fundus. It is worth noticing that images at 416 nm and 1213 nm (border wavelengths of the prototype) are of much poorer quality than the rest. This is mainly due to the higher absorption of the lens and water at 416 and 1213 nm, respectively, and the worse optical quality of the detection system for those wavelengths, as described in the design section.

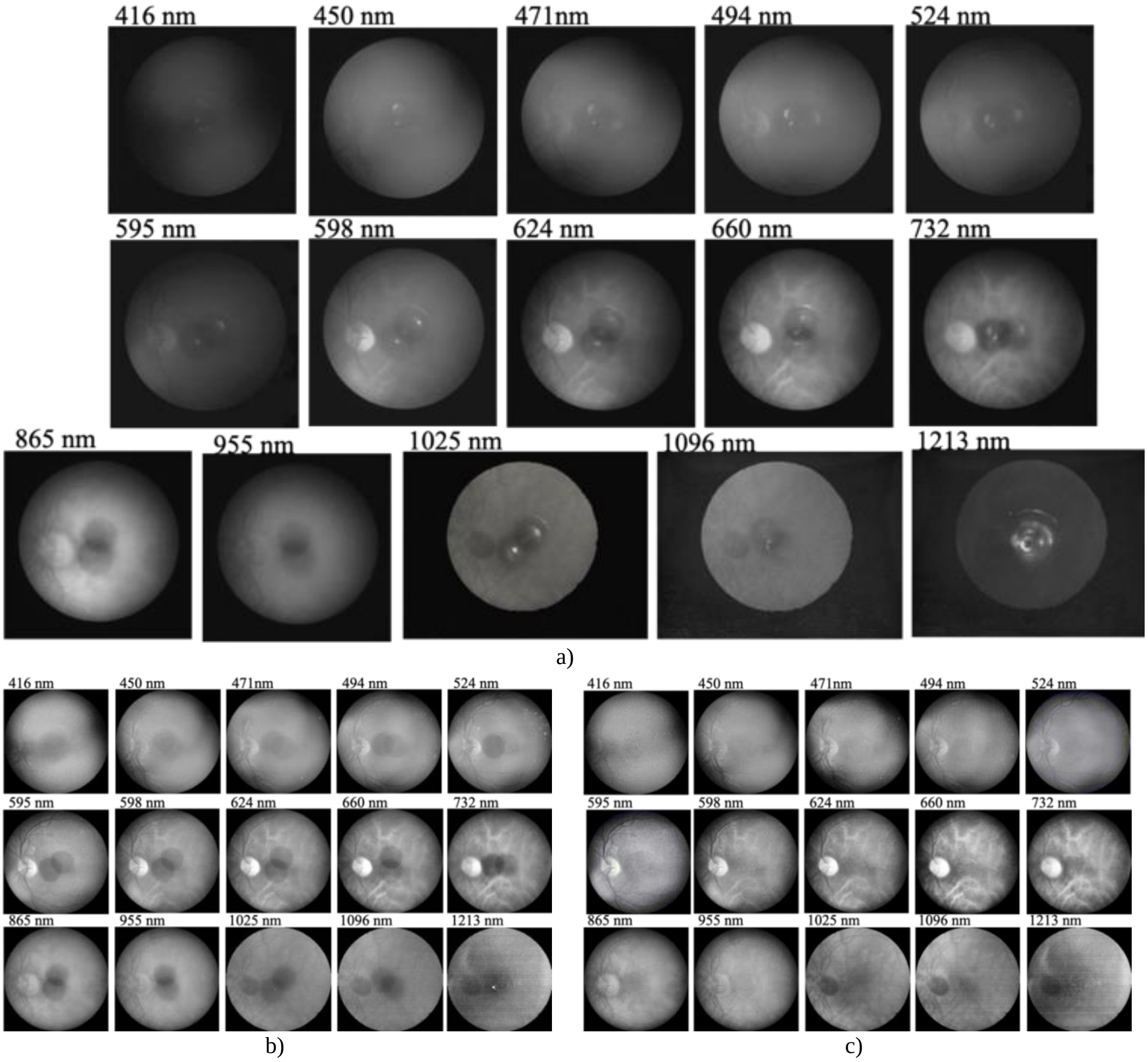

Figure 4.7: Sequence of retinal spectral images: a) raw images, b) images without the correction of shadows (only the dark- and background-subtraction have been applied, i.e., steps 1 to 4), and c) final corrected images including all processing steps.

4.3 Spectral analysis

In common clinical practice, the ophthalmologist's interpretation of retinal images is usually done by qualitatively comparing the color between degenerated and healthy areas of the ocular fundus. Due to this, the diagnosis strongly depends on his/her experience and the quality of the images acquired. This comparison can be extended with the developed spectral fundus camera, as every pixel contains spectral information rather than only color values, thus allowing for a spectroscopic analysis. Nevertheless, some additional post-processing steps are still necessary if a precise quantitative study of the ocular fundus is to be conducted.

As previously stated, $Ic_{\lambda n}(i, j)$ (the intensity of the processed images at each pixel) also includes the transmission of the preceding ocular media (cornea, lens, aqueous humor and vitreous) besides the reflectance of the retina itself. Therefore, an absolute comparison among individuals might be biased if they have, for instance, cataracts (especially if they are mature). In general, relative comparisons within the same fundus image are more appropriate for a spectroscopic analysis. In order to overcome this, three additional methods to compute contrast were defined, allowing for a comparison among different ocular fundus structures.

In the first method, named Global Contrast (GC), two spectral intensity curves are computed from a given fundus and used for comparison (Figure 4.8). Firstly, the region of the ocular fundus to be analyzed is selected by the operator by considering a ROI of a specific size, and the spectral intensity curve is calculated by averaging the pixels inside the ROI (*I*) for each spectral channel. Secondly, the mean intensity value is calculated over the entire FOV (I_{FOV}) and the GC contrast is computed as follows:

$$\mathrm{GC} = \frac{\mathrm{I}}{\mathrm{I_{FOV}}} \tag{4.2}$$

In the second method, named Local Contrast (LC), a more local quantification is carried out (Figure 4.9). In this case, two data sets are extracted: for instance, one being the average of the intensity values within a specific ROI at a given retinal/choroidal structure (*x*), and a second one corresponding to a second ROI in the near surrounding of the first one (*y*) (Eq. 4.3). This evaluation is particularly helpful for the quantitative analysis and comparison of small lesions of the retina with the near healthy tissue, or to compare two nearby structures, such an artery and a vein. By doing so, the contribution of residual illumination inhomogeneities is also minimized and a more robust estimation than with the GC analysis can be afforded.

$$\mathrm{LC} = \frac{\mathrm{I_x}}{\mathrm{I_y}} \tag{4.3}$$

where LC is the contrast between a fundus structure (*x*) and another one (*y*), and I_x and I_y are the intensities of the ROIs corresponding to x and y, respectively.

For each eye and for both contrast methods, several intensity curves from different ROIs over the images were selected on specific retinal and choroidal structures.

Figure 4.8 b shows the values of intensity averaged on the overall FOV (blue) and only in the fovea. As can be seen, the two intensity curves are dominated by the transmittance of the ocular media (see section 2.3.2.2 for ocular spectral properties), preventing from a clear discrimination between structures. The use of contrast values reduces this contribution and highlights spectral differences between them. In particular, the strong foveal absorption around 600 nm is enhanced in terms of GC (see Figure 4.8 c).

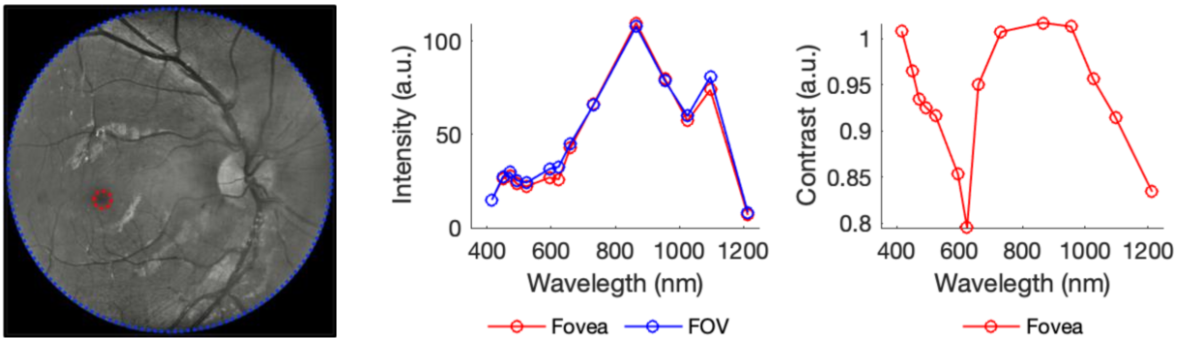

a) b) c)

Figure 4.8: Example of GC analysis of a retinal image. a) Foveal ROI of 0.5° (in red) and whole FOV (in blue); b) Spectral intensity curves of the fovea and the whole FOV; c) Global Contrast, GC: fovea vs. whole FOV.

Similarly, Figure 4.9 depicts the spectroscopic information in terms of LC of a retinal artery (red) and a vein (blue). In this case, two areas subtending an angle of 0.05° were selected at the center of each vessel. Whereas the spectral differences between the artery and vein are not evident in terms of intensity (Figure 4.9 b), they are in terms of LC contrast. In particular, differences in absorbance caused by de- and oxyhemoglobin (see Figure 2.19, section 2.3.2.2) can be easily recognized in the VIS range, especially between 500 nm and 600 nm (Figure 4.9 c).

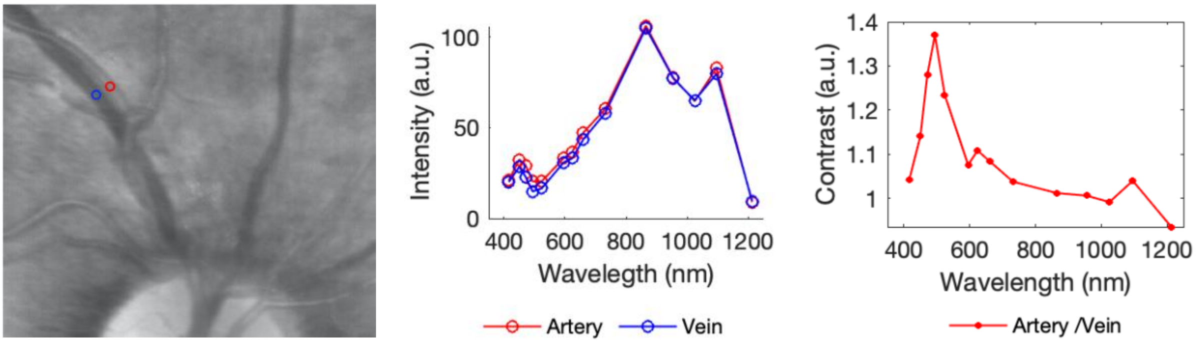

a) b) c)

Figure 4.9: Example of LC analysis of a retinal image. a) ROIs of 0.05º corresponding to a vein (in blue) and an artery (in red); b) Spectral intensity curves of the vein and the artery; c) Local Contrast, LC: artery vs. vein.

In the analysis of diseased eyes, the ratio between two intensity curves that correspond to two far and different structures on the same eye (e.g., atrophied tissue, drusen of different ethology, etc.) is sometimes also used, in order to compare their spectroscopic features. We will refer to this ratio as Specific Contrast (SC) (third method).

It is to be noted that in the subsequent quantitative spectral analysis (Chapter 5), only 14 of the 15 channels available in the system are included in order to preserve the homogeneity of the spectral sampling (the LED emitting at 598 nm was not considered because of its broader emission in comparison with the other LEDs in the VIS spectral region). Nevertheless, the images acquired at this spectral channel are still shown as they allow for a better qualitative analysis.

5 RESULTS

In this chapter, we carry out a qualitative and quantitative analysis of the spectral images acquired with the developed hyperspectral fundus camera over a population of healthy and unhealthy eyes. In the first section, the results of the control group are analyzed, including spectral images as well as spectroscopic information corresponding to several fundus locations such as the fovea, optic disk, vessels, etc. Then, the analysis of the eyes with anomalous fundus is carried out and the outcomes are compared with those found in healthy ones. Additional records such as OCT registers, RGB images, etc. are also used to perform an in-depth analysis.

5.1 Analysis of healthy eyes

Figure 5.1 depicts the RGB and the sequence of spectral images corresponding to a healthy eye. As shown, our system is able to perform fast imaging of the retina in the VIS and NIR regions (400 nm to 1300 nm) through a considerable number of spectral bands (15) and with great spatial resolution.

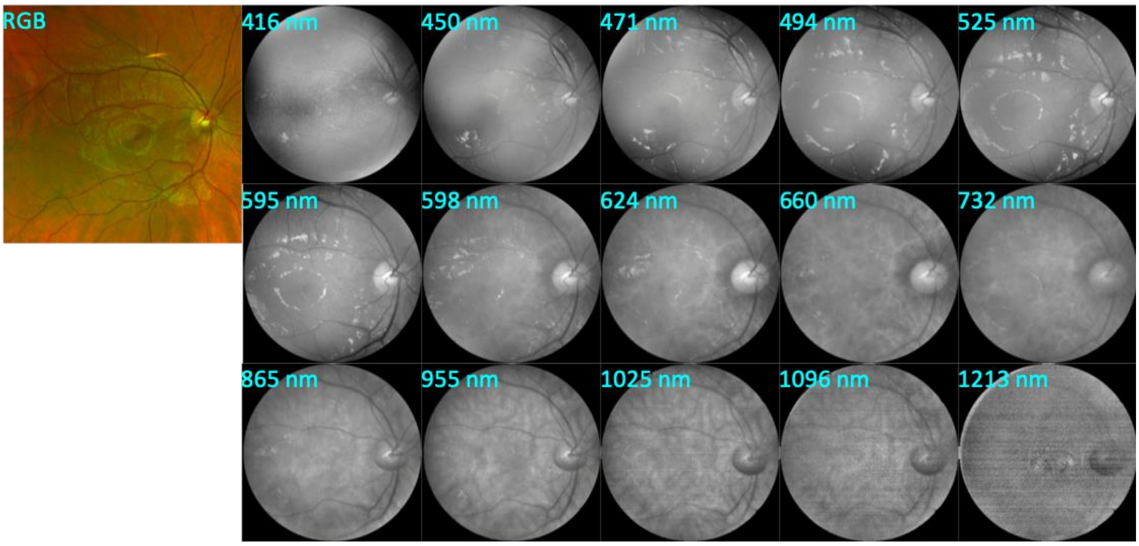

Figure 5.1: RGB color fundus image (left) and complete sequence of spectral images of a healthy eye acquired with the hyperspectral fundus camera (right).

These results represent a significant improvement on what has been previously obtained by means of MSI/HSI systems, mostly consisting of modified traditional fundus cameras whose original illumination or detection systems were replaced. As commented in Chapter 2, these are often linked to limited spectral sensitivity (only one fundus camera performs measurements beyond the VIS, up to 850 nm [122]), low number of spectral bands or, alternatively, low spatial resolution.

It is to be highlighted that acquisition of images beyond 1300 nm was not possible due to high absorption of the preceding ocular media and low QE of the InGaAs camera. Notably, the image at 416 nm is of poorer quality, mainly due to the higher lens absorption and poorer optical quality of the fundus camera.

Moreover, small residual artifacts appear at the center of the image acquired at 1213 nm because of spurious back reflections that could not be completely removed in the processing. This may happen when the acquired retinal signal is similar to that of the back reflected light.

Figure 5.2 depicts the hyperspectral sequence of another healthy eye with a zoomed ROI of some selected channels. In spectral images recorded at short wavelengths, light is reflected and backscattered more superficially, thus making the observation of structures such as the optic disk and nerve fibers (NF) easier. In images from 500 nm to 700 nm, differences in spectral absorption of oxygenated and deoxygenated hemoglobin result in changes of contrast between retinal veins and arteries and the surrounding fundus. For wavelengths in the NIR range, especially those longer than 950 nm, information from layers beyond the retina such as the choroid and its vasculature is available without the use of invasive fluorescent dyes thanks to the reduced absorption of tissue chromophores and the subsequent deeper penetration of light. Specifically, a large amount of backscattered light coming from the sclera forms the image at 1213 nm.

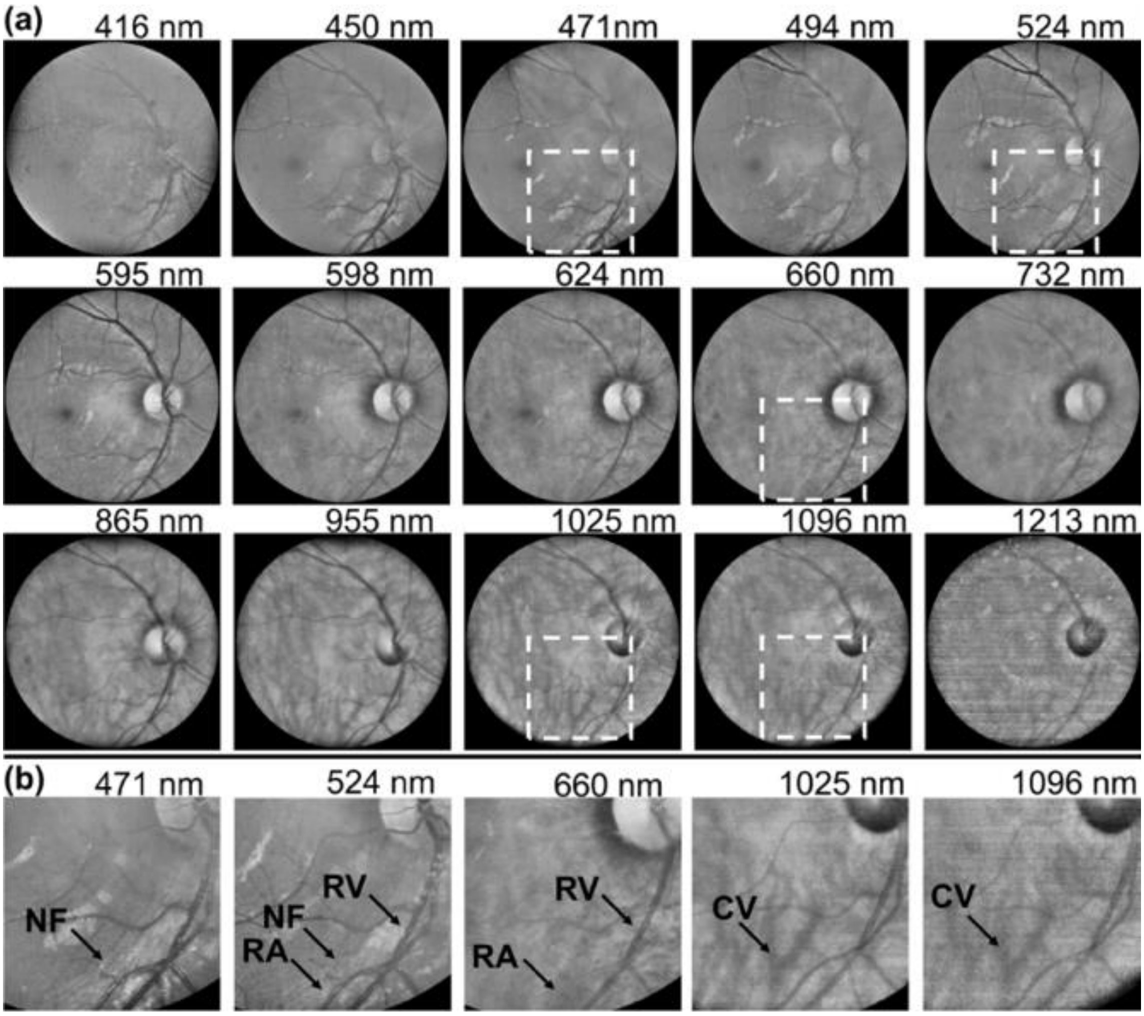

Figure 5.2: a) Complete sequence of spectral images of a healthy eye acquired with the fundus camera. b) Zoomed images of the areas framed with a white box in (a). Labels: nerve fibers (NF), retinal arteries (RA), retinal veins (RV) and choroidal vasculature (CV).

In the literature, quantitative spectroscopic information of the ocular fundus outside the spectral range comprised between 400 nm and 700 nm (VIS) is not available due to the limited sensitivity of spectral fundus cameras used so far. As shown, our system permits to carry out this analysis not only in the VIS range but also in the NIR, especially in the unexplored range from 900 nm to 1300 nm, often called the second NIR window, which is of current interest for biologists [134].

In this context, Figure 5.3 depicts the averaged spectral intensity curves over the entire FOV for the 61 healthy eyes included in the study (the corresponding mean and standard error are also shown). From the plots, it is obvious that eyes have strong differences in terms of fundus intensity, caused by differences in the reflectance of the retina itself and/or the transmission of the ocular media (different thickness of the media, presence of cataracts, IOL implants, etc.). The dominance of the water-like absorbance is evident, which can be clearly seen if they are compared with the transmittance of the ocular media obtained by other authors [1], [65], [74], as shown in Figure 2.16 a.

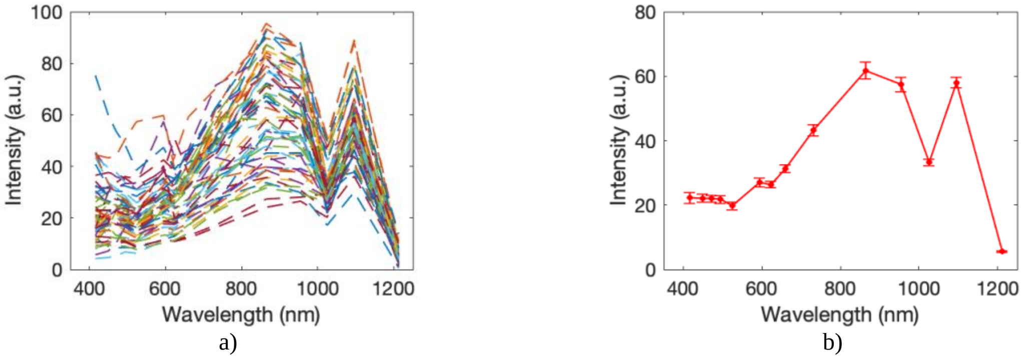

Figure 5.3: Spectral analysis of the overall ocular fundus (whole FOV) of the 61 healthy eyes. a) Intensity values (61 curves). b) Mean and standard error calculated from a).

The intensity curves have an overall monotone increase up to 850 nm, decreasing beyond as the water absorbance increases. In particular, it is worth noting the intensity valley found at 1025 nm, as water has an absorbance peak at this wavelength, and the maximum recorded at 1096 nm, which corresponds to a reduction of water absorption (between 1000 nm and 1150 nm approx.). In fact, in OCTs the selected wavelength used to image both the anterior and the posterior segments of the eye is about this wavelength, as it permits a very good transmissivity through the whole eye ball and a good penetration depth in the fundus tissue. In the mean intensity curve, a small local minimum is also recorded at 524 nm. This lower reflectance could be explained by the combined effect of macular retinal pigments and hemoglobin (both de- and oxygenated), with high absorption in this range.

Variability among patients in terms of intensity was already expected, especially in the range between 600 nm and 900 nm, as previously reported by other authors [65] (see Figure 2.16 b). This variability can be associated to differences in melanin concentration, so choroidal layers and structures below the RPE can be seen to a greater or lesser extent depending on the melanin amount that each patient has.

In regards of this, images of two spectral sequences recorded from two healthy individuals with high and low melanin concentrations are shown in Figure 5.4. Differences between the sequences are significant: for shorter wavelengths, structures below the RPE are only evident in the eye with less melanin. In contrast, at longer wavelengths, melanin absorption is strongly reduced and the choroidal vessels can be seen in both cases.

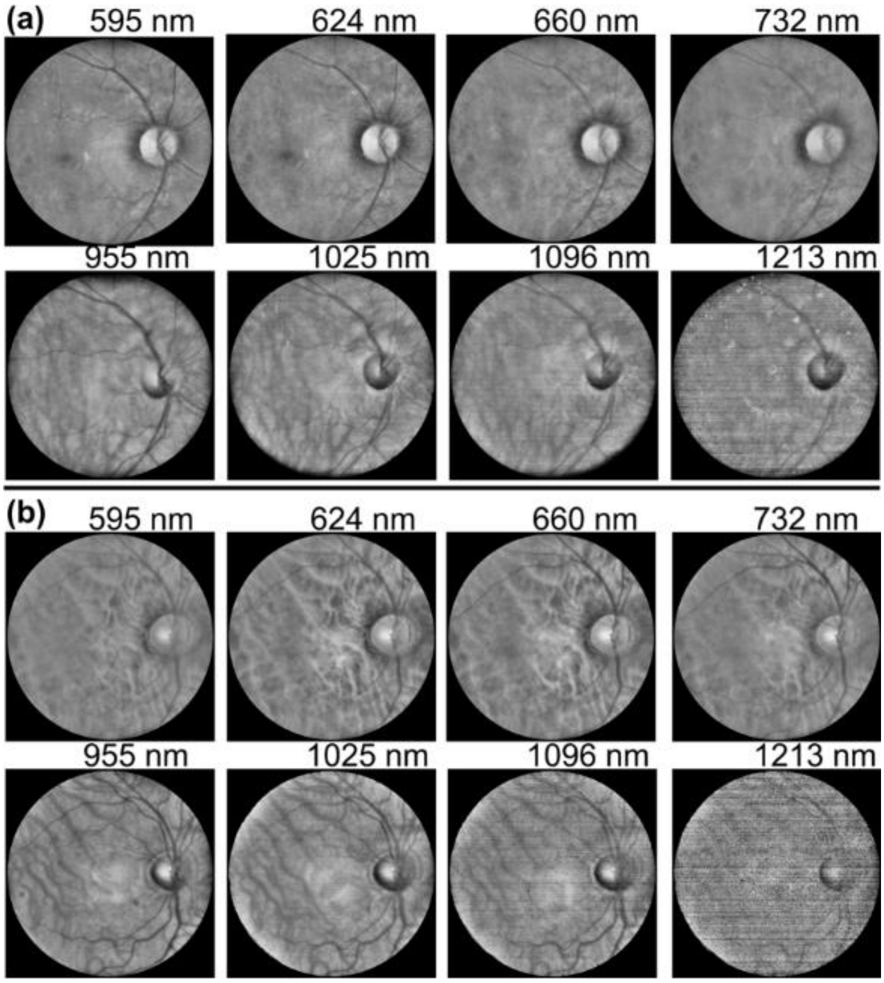

Figure 5.4: Spectral images of two healthy eyes of individuals with high (a) and low (a) melanin concentration.

5.1.1 Analysis of healthy ocular fundus structures

In Figure 5.5, zoomed retinal ROIs of a healthy fundus with and without choroidal vessels are shown. From here on, we will refer to the background as the areas of the fundus where neither retinal structures such as arteries, veins, fovea, etc. nor choroidal vessels are present. On the other hand, we will refer to choroid as the areas where choroidal vessels are clearly visible. Again, the choroidal layers cannot be seen at shorter wavelengths due to the strong absorption of melanin whereas NFs are well contrasted. As the wavelength increases, especially beyond 598 nm, the melanin absorption decreases and the choroidal vessels can be better distinguished.

The spectral curves corresponding to the background and the choroid are depicted in Figure 5.6 for all healthy eyes analyzed (61). In particular, 40 ROIs were selected in each eye for the analysis, 20 corresponding to the background and 20 to areas with choroidal vessels.

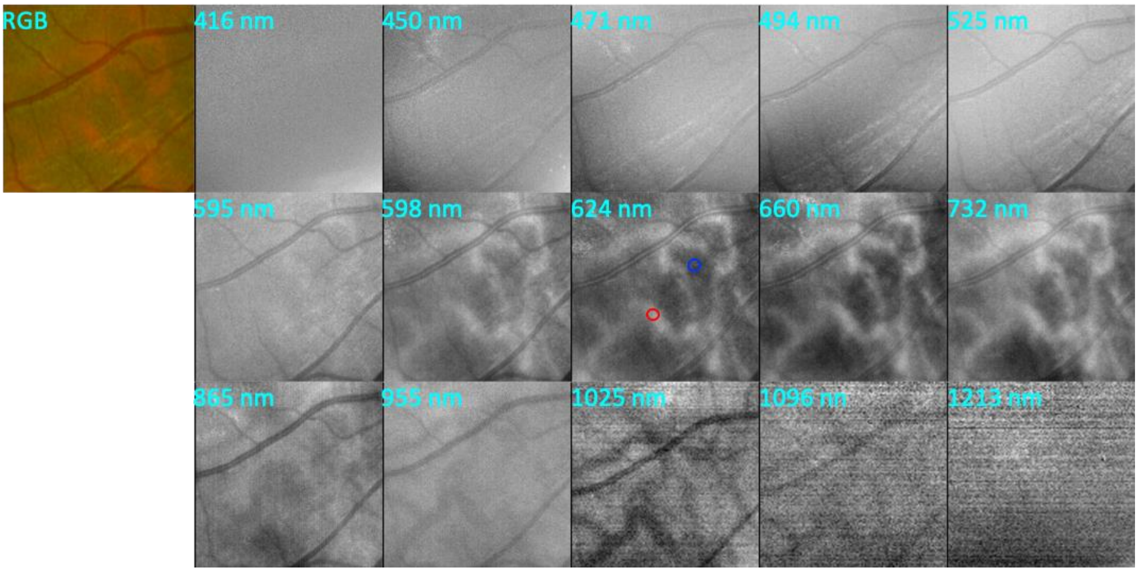

Figure 5.5: Zoomed detail of a color fundus image (left) and corresponding complete sequence of spectral images (right) of a healthy eye. Red and blue circles correspond to ROIs centered on a choroidal vessel and the background, respectively.

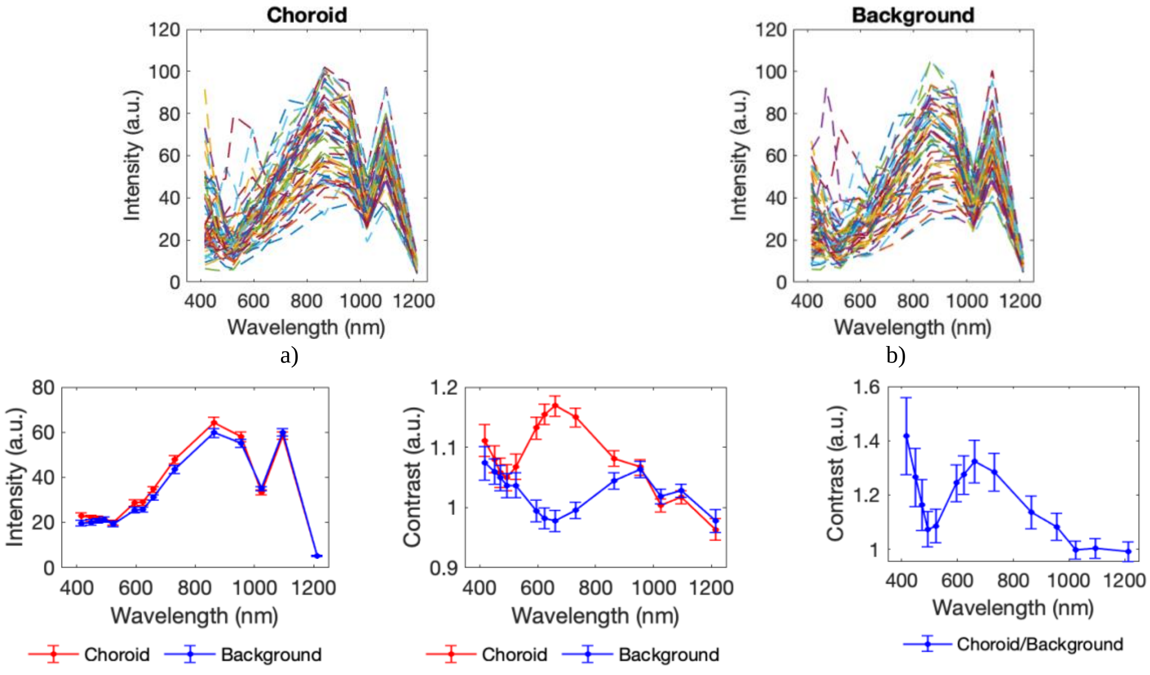

a) b)

c) d) e)

Figure 5.6: Spectral analysis of choroidal vessels (red curves) and fundus background (blue curves). a, b) Intensity values. c) Mean and standard error calculated from a) and b). d) Mean GC contrast curves. e) Mean LC contrast curve. In a) and b), 61 curves are plotted calculated as the average of 20 ROIs for the background and 20 ROIs for the choroid (diameter 0.2°) of each eye.

As can be noticed from the intensity and contrast plots (both in terms of GC and LC analysis), the choroidal vessels are brighter than the background within the range between 500 nm and 950 nm approximately, whereas they are similar or slightly darker at longer wavelengths. As commented, contrasts of choroidal vessels and the background change from patient to patient, mainly due to the differences in melanin concentration at the RPE and the choroid. Therefore, shorter wavelengths are absorbed while longer ones, less sensitive to melanin absorption, penetrate deeper inside the tissue and are reflected back at the sclera. In turn, the choroidal vessels appear darker in images taken at NIR wavelengths because they shade the portion of the back reflected light from the sclera passing through them (LC contrast values above 1000 nm in Figure 5.6 e are about 0.95). These curves as well as the image sequences in Figure 5.4 show how powerful the NIR imaging can be to diagnose disorders that might affect deep layers of the fundus. The peak that can be observed at short wavelengths is a consequence of the worse quality and presence of inhomogeneities in some of these images.

In Figure 5.7, zoomed spectral images of a healthy fovea are shown.

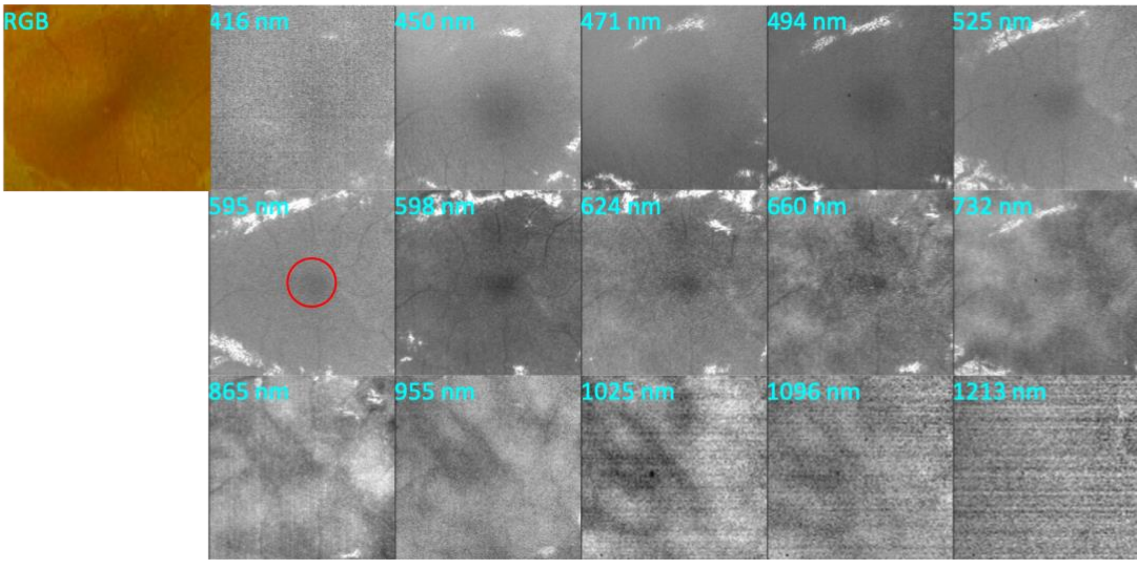

Figure 5.7: Zoomed detail of a color fundus image (left) and corresponding complete sequence of spectral images (right) of a healthy eye. The red circle corresponds to a ROI centered on the fovea.

The foveal pit is well visible as it acts as a yellowish filter (absorber), so that it is perceived dark at short and mid wavelengths. At longer ones, and once surpassed the RPE, there are no observable spectroscopic differences between the fovea and the surrounding tissue. The absorption of the fovea is well known and, as reported elsewhere, it is more prominent in the VIS range [54]. The quantitative spectral analysis of the fovea is depicted in Figure 5.8.

Foveal curves show higher absorption (lower intensity values) than the whole FOV in the range below 600 nm. This is caused by the presence of macular pigments (mainly lutein, maximum absorption around 400 and 500 nm with a peak at 450 nm approx., see Figure 2.18). Moreover, the foveal capillaries could also partially explain the reduced reflectance between 500 nm and 600 nm, as hemoglobin absorbance is maximal here. Between 700 nm and 900 nm, the contrast curve shows slightly higher values of the fovea with respect to the whole FOV. This is probably because the retina is thinner in the fovea so the amount of light reaching the sclera and back reflected is larger. Beyond this wavelength, the differences between the fovea and the peripheral retinal tissue, both in terms of intensity and contrast values, are minimal (contrast near 1).

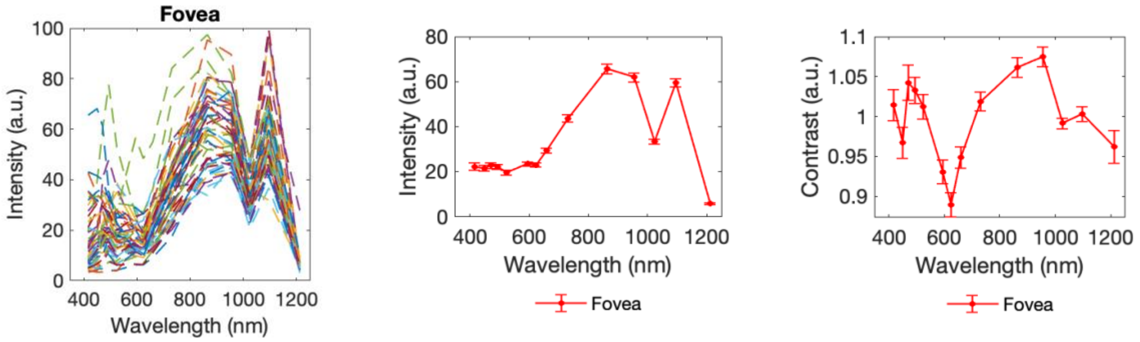

a) b) c)

Figure 5.8: Spectral analysis of the fovea. a) Intensity values. b) Mean and standard error calculated from a). c) Mean GC contrast curve. In a) and b), 61 curves are plotted calculated as the average of 1 circular ROI (diameter 0.5°) centered on the fovea of each eye.

In Figure 5.9, zoomed spectral images of a ROI centered on some NFs are shown. It can be seen that they are better contrasted at short wavelengths as they reflect more light at this range. In turn, Figure 5.10 shows the corresponding quantitative spectroscopic analysis.

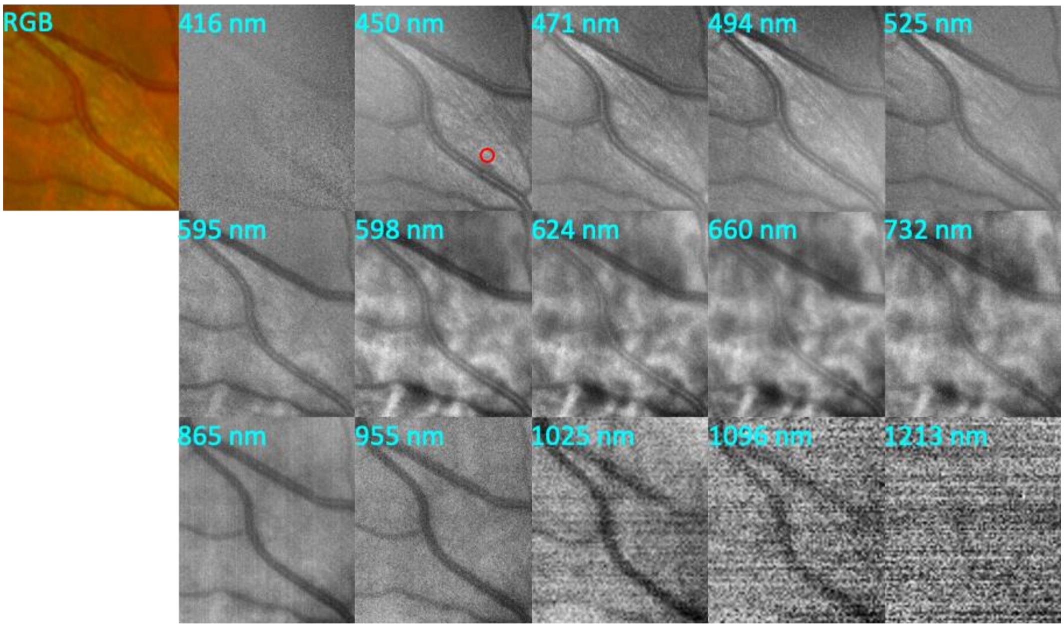

Figure 5.9: Zoomed detail of a color fundus image (left) and corresponding complete sequence of spectral images (right) of a healthy eye. The red circle corresponds to a ROI centered on a NF.

The contrast curve (Figure 5.10 c) presents a monotone descendent behavior besides of a small valley around 500 nm, probably due to the absorbance at this wavelength of capillaries (with hemoglobin) above or below the NFs (unlike cSLO, light coming from different depths can be recorded simultaneously in HSI systems). These results are in accordance with others previously published [54], in which reflectance of NFs was found to have a monotone descendent behavior between 400 nm ant 700 nm [77].

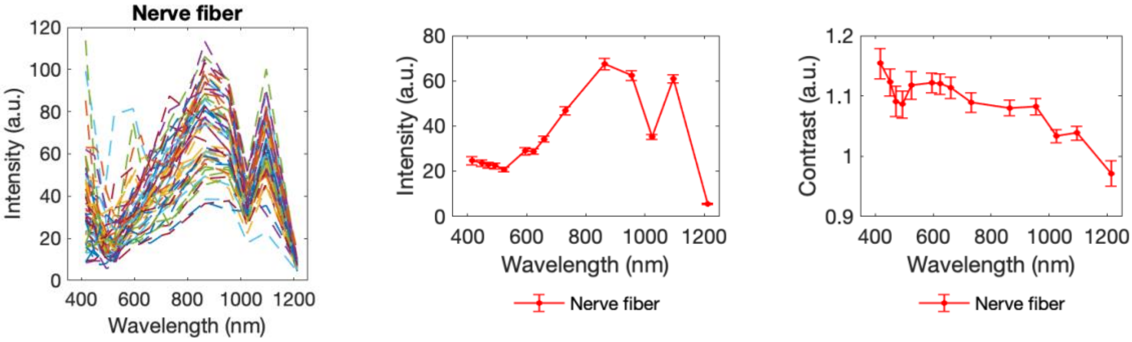

a) b) c)

Figure 5.10: Spectral analysis of the nerve fibers. a) Intensity values. b) Mean and standard error calculated from a. c) Mean GC contrast curve. In a), 61 curves are plotted calculated as the average of 10 ROIs (diameter 0.05°) centered on a nerve fiber of each eye.

On the other hand, the optic disk is a bundle of nerves that, entering inside the skull, transport the information from the photoreceptors to the visual processing zones in the brain. Figure 5.11 and Figure 5.12 depict the complete sequence of spectral images centered on an optic disk and the corresponding quantitative analysis.

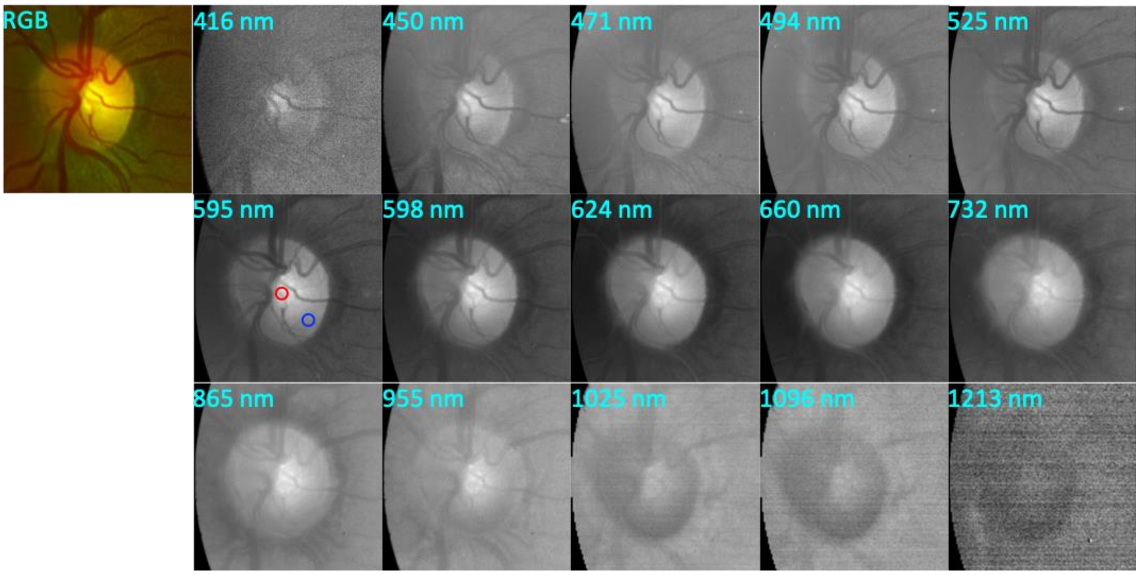

Figure 5.11: Zoomed detail of a color fundus image (left) and corresponding complete sequence of spectral images (right) of a healthy eye. Red and blue circles correspond to ROIs centered on the central region of the optic disk and its periphery, respectively.

According to the literature [77], the highest levels of reflected signals in the optic disk are in the wavelength range between 450 nm and 600 nm. As presented in section 2.3.2.3, the optic disk is often divided in two separated regions (especially for diagnosis of glaucoma): the periphery and the cup.

From the images, two facts can be noticed: firstly, the center of the optic disk (cup) is the brightest and most reflective structure of the fundus at short and mid wavelengths whereas beyond 1000 nm, it gets darker as the wavelength increases; secondly, the periphery of the optic disk behaves similarly although it is darker than the center. These two results are consequences of three effects: the reflectivity of chemical substances, such as the myelin, present in the axons of the ganglion cells once surpassed the lamina cribrosa scleralis [102], the conformation of the pit of the optic disk that, differently from other regions of the retina that lie on the sclera, presents an excavation that penetrates inside the skull, and the visibility of the lamina cribrosa [135].

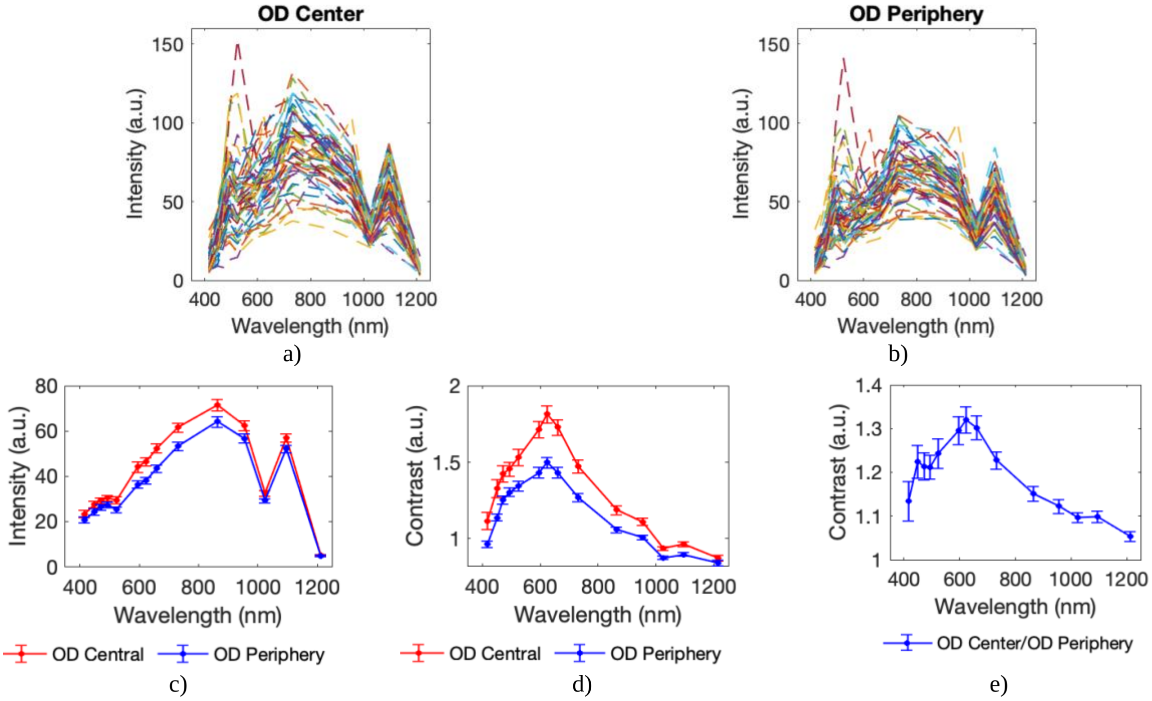

a) b)

c) d) e)

Figure 5.12: Spectral analysis of the center (red curves) and periphery (blue curves) of the optic disk. a, b) Intensity values. c) Mean and standard error calculated from a) and b). d) Mean GC contrast curve. e) Mean LC contrast curve. In a), 61 curves are plotted calculated as the average of 1 ROI (diameter 0.2°) centered on the center of the optic disk of each eye. In b), 61 curves are plotted calculated as the average of 3 ROIs (diameter 0.2°) located at the periphery of the optic disk of each eye.

The lamina cribrosa is a mesh-like structure formed by a multilayered network of collagen fibers and NFs that penetrates into the scleral canal wall. In the cup, and after the excavation, the fibers are placed vertically inside the optic nerve (perpendicular to those of the rest of the fundus [103]). The differences between the cup and the periphery of the optic disk can be understood by looking at the OCT image in Figure 5.13. Due to the morphology of the retina, the absorbed and back reflected light is different in the optic disk and outside. Elsewhere in the retina, the light is partially reflected at the NF layer. The fraction that is not absorbed penetrates deeper into several layers, where it is absorbed again, and finally, the amount reaching the sclera is reflected back. In the optic disk cup, the light is highly reflected because of two main reasons: after the excavation, there is a dense bundle of myelinated fibers conforming the optic nerve, which have higher reflectivity; then, the conformation of the pit makes the lamina cribrosa available and due to its structure reflects the light that is not absorbed by the retinal stratification. This explains why the center of the optic disk is the brightest structure in the ocular fundus up to 1000 nm.

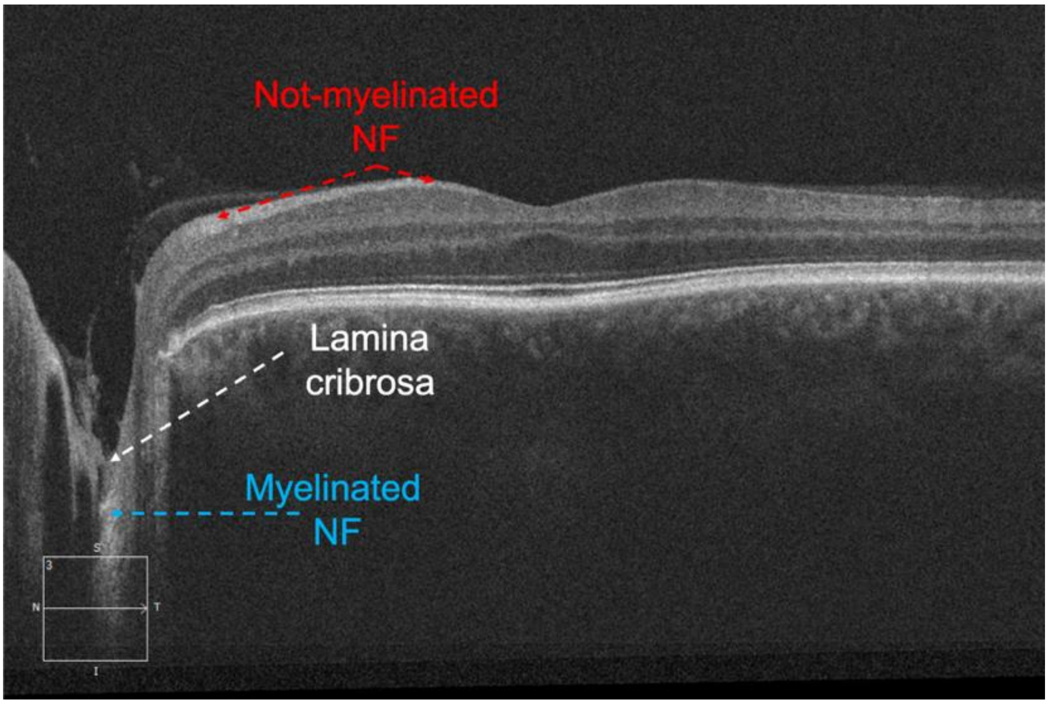

Figure 5.13: OCT image showing the section of a healthy retina as well as the excavation of the optic disk. Red arrows indicate the not-myelinated NFs, blue arrow indicates the myelinated NFs that penetrate inside the skull and the white arrow indicates the lamina cribrosa.

In the NIR, our system shows that the very last layers of the ocular fundus and the sclera are the most reflective structures. In fact, most of the collected light in this case comes from the sclera. Due to this, in the fundus areas where the sclera is homogeneous, the reflected signal is very homogeneous, too; except for the region of the optic disk, which is the darkest structure of the ocular fundus beyond 1000 nm.

According to these results, the intensity values of the reflected signal from the overall optic disk, as well as the LC contrast values between the center and the periphery, could be useful as estimates of the amount of NFs and the thickness of the bundle of nerves. Again, it is well known from the literature that a correlation exists between concentration of NFs and degeneration, such as glaucoma [136]. Additionally, the longest wavelengths recorded with our system (NIR) provide more information on the deepest retinal layers and, accordingly, this could be used to compute more accurate optic disk-cup ratios than traditional color-based fundus cameras [137].

Finally, to conclude the analysis of healthy patients, retinal vessels are studied. In Figure 5.14, a complete sequence of zoomed spectral images with an artery and a vein are shown.

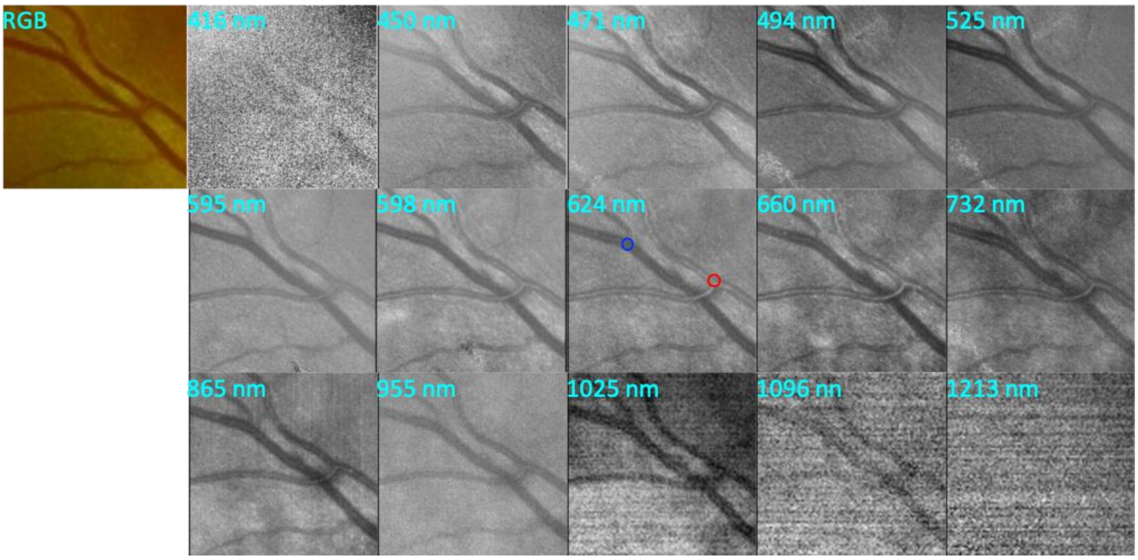

Figure 5.14: Zoomed detail of a color fundus image (left) and corresponding complete sequence of spectral images (right) of a healthy eye. Red and blue circles correspond to ROIs centered on an artery and a vein, respectively.

As described elsewhere (see section 2.3.2.2), the oxygenated and de-oxygenated hemoglobin in the blood stream present differences in their absorbance curves. The arteries become transparent (lighter) as the wavelength increases in the VIS range whereas the veins absorbance remains high for longer wavelengths.

The wavelength range below 600 nm corresponds to that where red-free fundus imaging is usually done in clinics, as the contrast of vessels is maximized with respect to the surrounding tissue. This is due to the fact that both oxygenated and de-oxygenated hemoglobin have (similar) absorption peaks. In fact, the GC contrast of arteries and veins at wavelengths shorter than 550 nm approx. is minimal (see Figure 5.15 d). Nevertheless, it is evident from the LC analysis (Figure 5.15 e) that the larger differences between these two structures lay in the spectral range between 550 nm and 900 nm; below and above this range their absorbances are almost the same (LC contrast value of 1).

The difference in absorption between de- and oxygenated blood in the spectral range comprised between 700 nm and 900 nm has been successfully used in applications to measure oxygen saturation, i.e., pulseoximetry [138], by means of transmittance measurements (for instance through a finger). In this regard, it is known that an isosbestic point exists around 800 nm, where the absorbances of de- and oxygenated blood switch. Other authors have also used reflectance measurements from fundus images acquired at VIS wavelengths to assess oxygen saturation. However, to perform this analysis a thorough preliminary calibration must be carried out [139]. For example, a precise fit to a linear combination of reference curves obtained from fully saturated and desaturated red cells suspensions has been used for this purpose [98].

In our system, regardless that arteries and veins can be well recognized and identified due to spectral differences, the corresponding intensity curves do not show the isosbestic point switch at 800 nm because of the lack of calibration. Thus, no conclusion about the oxygen saturation can be drawn. However, the use of a proper calibration (out of the scope of this thesis) might open the possibility of video recording the retinal oxygenation in the NIR spectral range, where the light does not disturb the patient under examination.

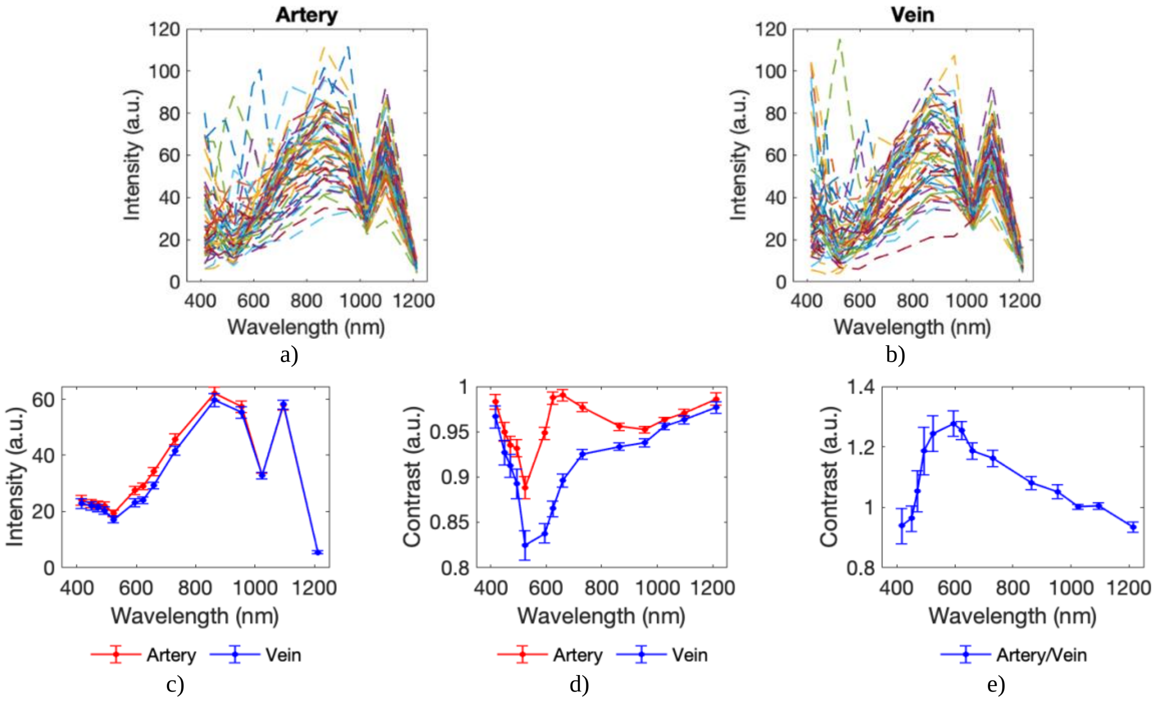

Figure 5.15: Spectral analysis of the retinal arteries (red curves) and veins (blue curves). a, b) Intensity values. c) Mean and standard error calculated from a) and b). d) Mean GC contrast curve. e) Mean LC contrast curve. In a) and b), 61 curves are plotted calculated as the average of 10 ROIs (diameter 0.05°) centered on an artery and a vein of each eye, respectively.

5.1.2 Summary

Figure 5.16 depicts all spectroscopic results obtained for healthy eyes, allowing for an easier comparison among fundus structures. From the intensity curves (Figure 5.16 a), it is clear that the optic disk (center and periphery) are the regions which differ the most. The other retinal structures are linked to similar curves due to the predominant water-like absorption of the eye.

The use of the GC analysis, which allows comparing each structure with the whole FOV, is a good reference in order to mitigate the common spectral properties of the ocular media. Contrast values that correspond to areas where no particular structures are present (as the background) are close to 1. As it can be inferred from Figure 5.16 b, the differences between the optic disk and other structures in terms of this type of contrast are more evident than in terms of intensity. Particular structures such as the fovea and vessels can be well differentiated in this analysis due to their particular spectral absorption peaks linked to specific chemical components (chromophores).

On the one hand, this new spectroscopic information might be useful to improve the analysis of retinal structures that remain hidden in conventional color imaging as it allows obtaining information on their composition, which in turn can be used for ocular diagnosis of certain diseases. On the other hand, the spectral images and information recorded with the system might be useful for other applications; for instance, to increase the performance of artificial intelligence algorithms used for automatic fundus diagnosis, which nowadays are only applied to RGB images [140]. In fact, these algorithms rely on their capacity of discerning among tissues by means of differences in terms of digital levels, so the extra spectroscopic information might be relevant.

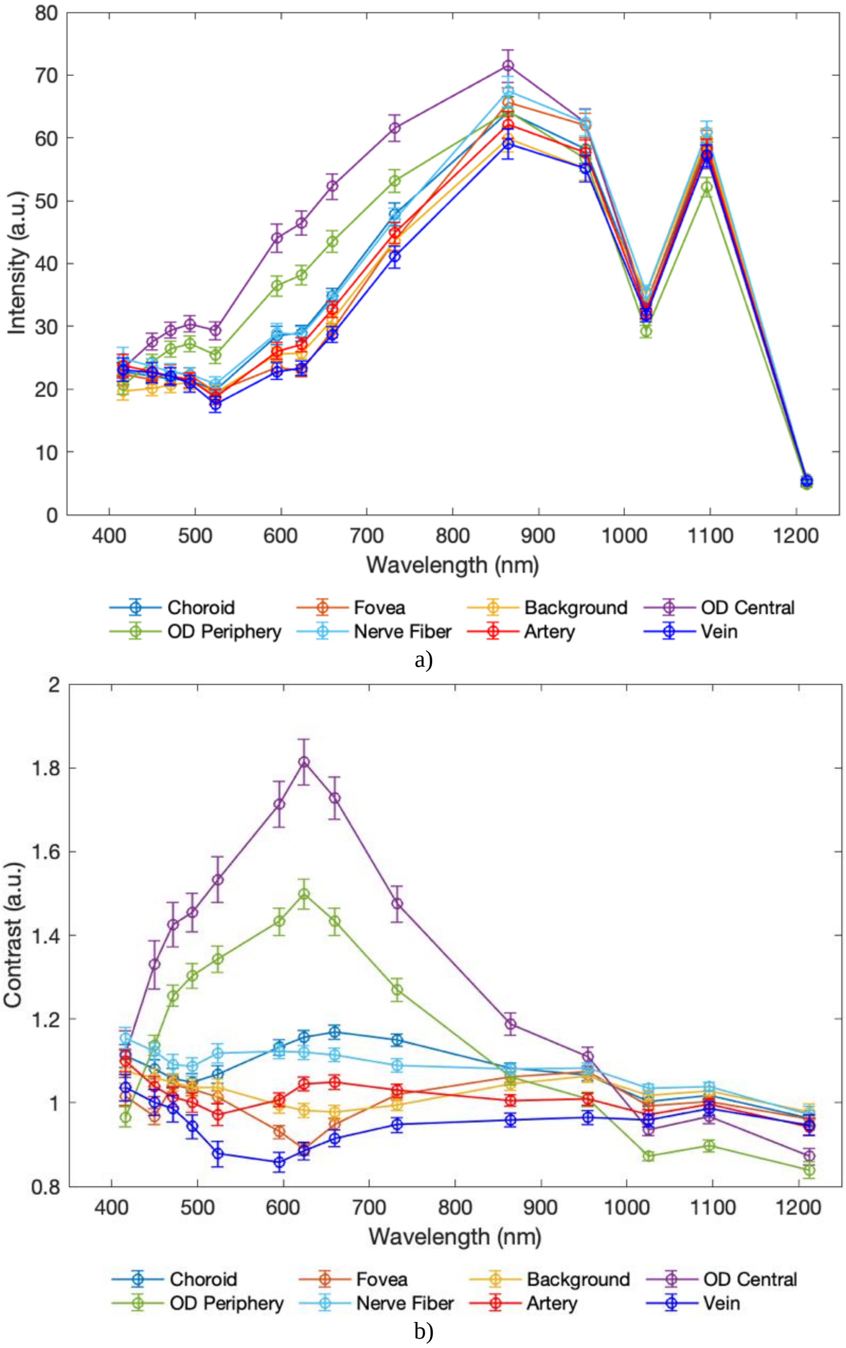

a)

b)

Figure 5.16: a) Averaged intensity curves and b) GC contrast curves from all fundus structures analyzed for healthy eyes.

In the case of the NIR part of the spectrum, especially beyond 850 nm, it is worth to carry out an additional analysis, as it has never been explored. In Figure 5.17, the GC contrasts of several fundus structures are shown for this spectral range.

The differences between the optic disk and the rest of structures are again evident in this specific spectral range. Besides, subtle changes of contrast among the other structures can be recognized. Of special interest is the crossing point (at 950 nm approx.) of the spectral curve of the choroid and that of the background. Therefore, it can be concluded that spectral differences in the NIR are minimal apart from the optic disk and regions where very large choroidal vessels are present.

This information might be still of remarkable value when comparing fundus of healthy and unhealthy eyes with lesions affecting the RPE or even deeper layers, which can give rise to anomalous fundus spectral reflectance. In fact, light collected at wavelengths beyond 1000 nm mainly come from the sclera, where it is reflected, and, if there is a localized damage at the RPE level, an absorption reduction is to be expected because of depigmentation. Thus, the intensity levels recorded will be higher. Consequently, a deviation of intensity from healthy reflectance at these wavelengths will stand out immediately and can be a warning sign of clinical complications. This will be further analyzed in the next section.

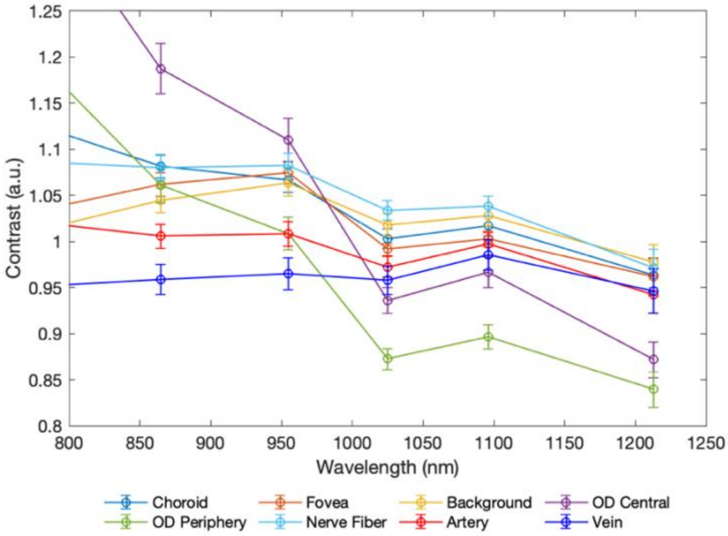

Figure 5.17: Zoom of Figure 5.16 b in the NIR-IR range.

5.2 Analysis of diseased eyes

In this section, eyes with several retinal and choroidal diseases are analyzed. At first, a qualitative analysis is carried out for particular clinical cases using images taken with the hyperspectral retinograph and other records obtained with standard diagnostic tools such as OCTs and color fundus cameras (when available). For OCT, both the sections of the ocular fundus and the en-face view (automatically retrieved image by means of internal segmentation algorithms) are given.

In parallel to the qualitative analysis, a preliminary quantitative spectroscopic analysis focusing on specific abnormal fundus structures, substances or injured tissue, such as drusen and scars, is also conducted to find out differences between these and healthy areas. A descriptive statistical analysis as in the case of healthy patients is carried out (whenever possible), providing the average intensity curves as well as GC, LC and SC contrasts. In the case of the LC analysis, the curves presented in this section are calculated as the ratio between the intensity values of a specific structure (e.g., a lesion) and those collected from areas in its Healthy Near Surrounding (HNS), thus mitigating the impact of residual illumination inhomogeneities on the results. The ratio between two intensity curves that correspond to two far and different structures on the same eye (e.g., atrophied tissue, drusen of different ethology, etc.) is sometimes also used, in order to compare their spectroscopic features (see SC contrast in section 4.3).

Since part of the spectral range (NIR) was studied for the first time in this thesis, no specific targets were declared in terms of retinal diseases in the clinical study. A detailed statistical analysis of specific diseases was neither carried out. Alternatively, we focus on giving some new insights and future research lines, especially for some retinal diseases and related clinical signs, that show the potential of the developed system.

5.2.1 ARMD and other maculopathies

As stated in Section 2.3.2.3, one of the leading causes of blindness in the developed countries is ARMD. In eyes with ARMD, the earliest morphologic feature is the abnormal accumulation of extracellular material at the level of the RPE. These deposits are composed of granular material, which is a cluster of proteins and lipids (e.g., lipofuscin) that do not degrade completely, and can cause retinal dysfunction in later stages of the disease. The localized accumulation of these damaged cells or deposits leads to the development of soft drusen, the first clinical sign of ARMD, which is seen as pigmentary mottling. In color fundus imaging, they appear as round yellow lesions with poorly demarcated boundaries, located under the RPE. Histologically, soft drusen correspond to the abnormal thickening of the inner aspect of Bruch’s membrane, which, together with the RPE, can separate from the rest of the Bruch’s membrane and represent a localized RPE detachment, directly related to visual loss. These drusen can also collaborate in the development of choroidal neovascularization. Other kinds of drusen have also been described, including hard or calcified. Hard drusen are localized and sharply demarcated structures composed of hyaline material that appear to be a consequence of material extrusion from RPE cells. They are usually associated to RPE atrophy and depigmentation. Eyes with hard drusen are less likely to progress to atrophy and choroidal neovascularization in comparison to eyes with soft drusen.

Several changes of the RPE can be seen as another non-neovascular feature of ARMD, including depigmentation, cellular hyperplasia, and RPE atrophy, with frequent disruption of the choriocapillaris, a layer of capillaries that is immediately adjacent to Bruch's membrane in the choroid. These are the second major feature of the disease. In the atrophied areas, a loss of about 90% of RPE cells as well as some photoreceptors has been shown, which is observed as a thinning of the macular layers. All these changes are caused because of a decrease of nutrients and a larger accumulation of extracellular material. These non-vascular changes are typical in dry or non-exudative form of ARMD, but their presence increases the likelihood of choroidal neovascularization to develop. The number of photoreceptors is also lower and hemorrhages might also be present.

Once vascularization involves the fovea, visual outcomes are poor. Neovascular tissue and scars are both features of the exudative or wet form of ARMD. Choroidal neovascular membranes made of RPE cells and choroidal capillaries can also appear at early stages, which can evolve with time to arteries and veins. They have also fibrous tissue that may proliferate within the Bruch’s membrane, as a result of the existence of new vessels from the choroid. This neovascularization may leak fluid or bleed and lead to a hemorrhagic RPE detachment. This bleeding leads to scars, the fourth major feature of ARMD and the last stage of the exudative form.

5.2.1.1 Case reports

As a first approach to the spectroscopic study of all these features, some case reports from specific individuals are included in this subsection. In particular, Figure 5.18, Figure 5.19, Figure 5.20, Figure 5.21 show records of patients with exudative (wet) ARMD.

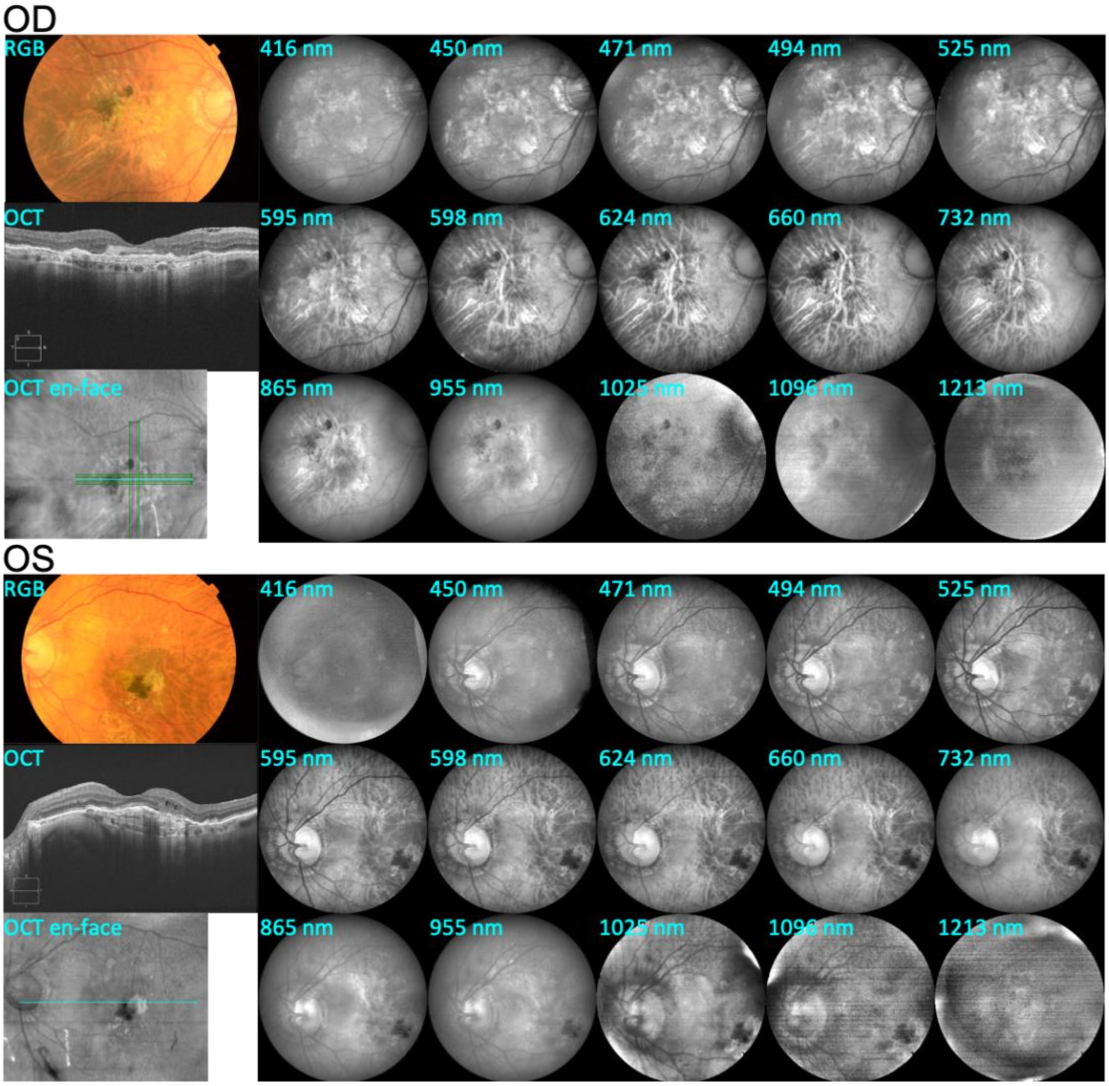

Figure 5.18: Right (OD, top panel) and left (OS, bottom panel) eyes of a patient with exudative ARMD. Left, from top to bottom: Color fundus image, OCT section and en-face image. Right: Complete spectral sequence obtained with the HSI fundus camera.

Despite the bad quality of the images acquired at 416 and 1213 nm in Figure 5.18, especially for the left eye, several lesions of different nature, such as drusen (hard and soft), RPE atrophy and scars can be seen.

Figure 5.19 includes zoomed regions of both eyes shown in Figure 5.18 to highlight some of these interesting structures.

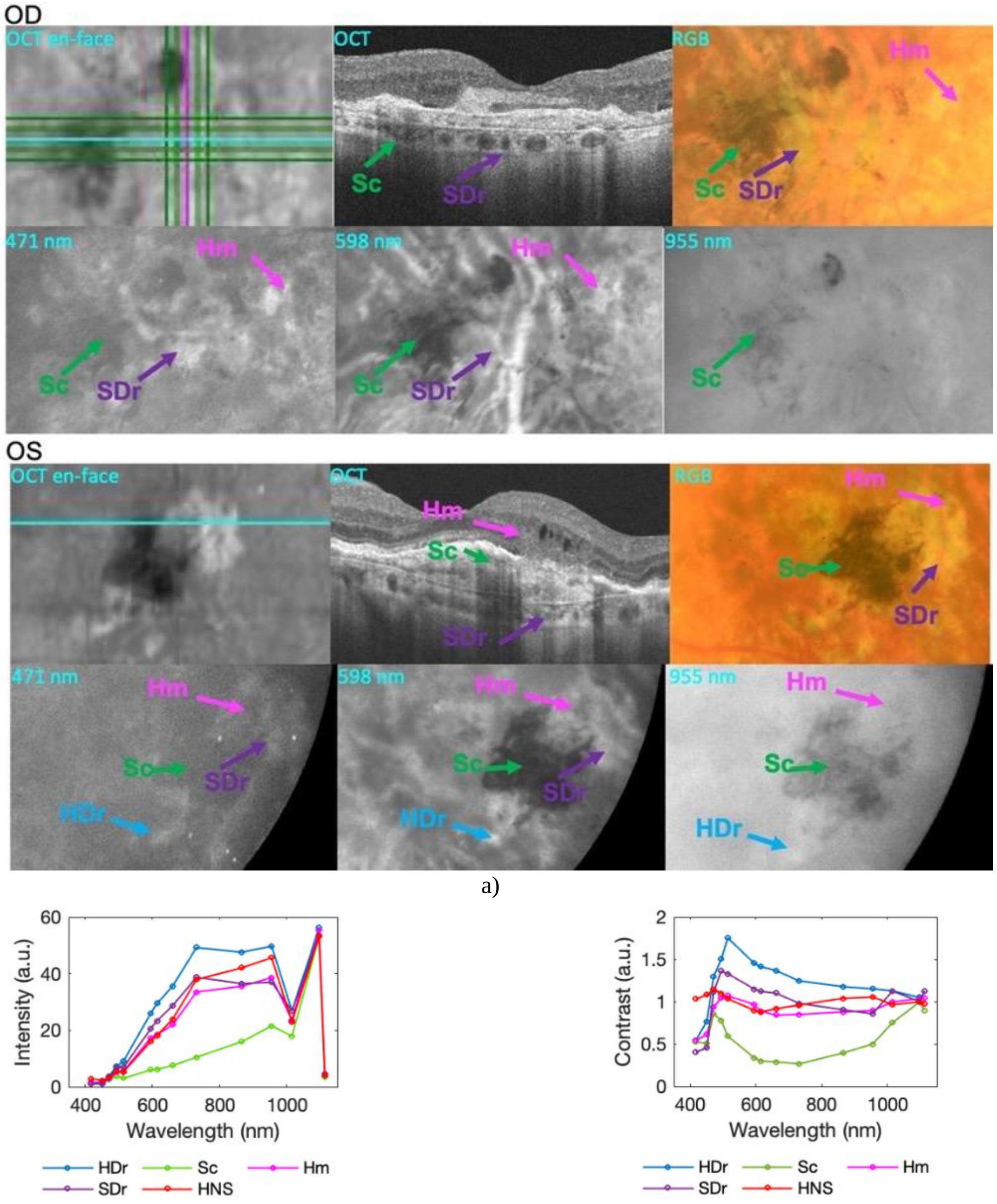

a)

b)

c)

Figure 5.19: a) Zoomed ROIs centered on regions with several structures of the right (OD, top panel) and left (OS, bottom panel) eyes with exudative ARMD shown in Figure 5.18. Top rows from left to right: OCT en-face image, OCT section and color fundus image. Bottom rows from left to right: selected spectral images acquired with the HSI fundus camera. b) Intensity curves of the indicated areas. c) GC curves of the indicated areas. Labels: HDr (Hard Drusen), Sc (Scar), Hm (Hemorrhage), SDr (Soft Drusen), HNS (Healthy tissue of the Near Surrounding).

Additionally, a preliminary analysis of the spectral intensity and GC curves of the left eye is also provided (Figure 5.19 b, c). The macular scars are the most prominent abnormalities in both eyes, also observable in the color fundus images, which implies that this patient is at an advanced stage of an exudative form of ARMD. In the color image and in the VIS spectral range, scars appear as black, with poorly demarcated contours because of their higher absorption and fibrotic nature, increasing scattering and degrading image quality, [65].

From the spectral analysis presented in Figure 5.19 b and c, the higher absorption of the scar in the spectral range between 500 nm and 1000 nm is evident. Scars are blurrier in the VIS spectral range and have better demarcated contours at longer wavelengths (955 and 1025 nm), meaning that they affect deep layers of the fundus, as OCT sections confirm. In fact, the exudation mainly accumulates in the RPE and thus the scar is formed around this depth.

In the OS, soft drusen can be clearly recognized in the color images, whereas in the OD they are hardly visible, probably due to the metamerism of such structures with the surrounding fundus. Nevertheless, they can be clearly seen in images corresponding to short wavelengths (416nm - 525nm) of the hyperspectral sequence on both eyes. They look as hyperreflective areas, which implies a higher intensity signal from this extracellular material.

Spectroscopic differences among drusen or abnormal material released in retinal diseases are mainly caused by differences in their nature and maturity, which affect their chemical composition over time [132], [141]. Higher signal of drusen at short wavelengths might be correlated with autofluorescent emission of specific substances (e.g., lipofuscin). As the wavelength increases, soft drusen are less contrasted and the reflectance signal is lower. On the contrary, hard drusen show higher intensity values at longer wavelengths, which could be attributed to a decrease in melanin absorption since they are usually associated to RPE loss of cells, that is, depigmentation.

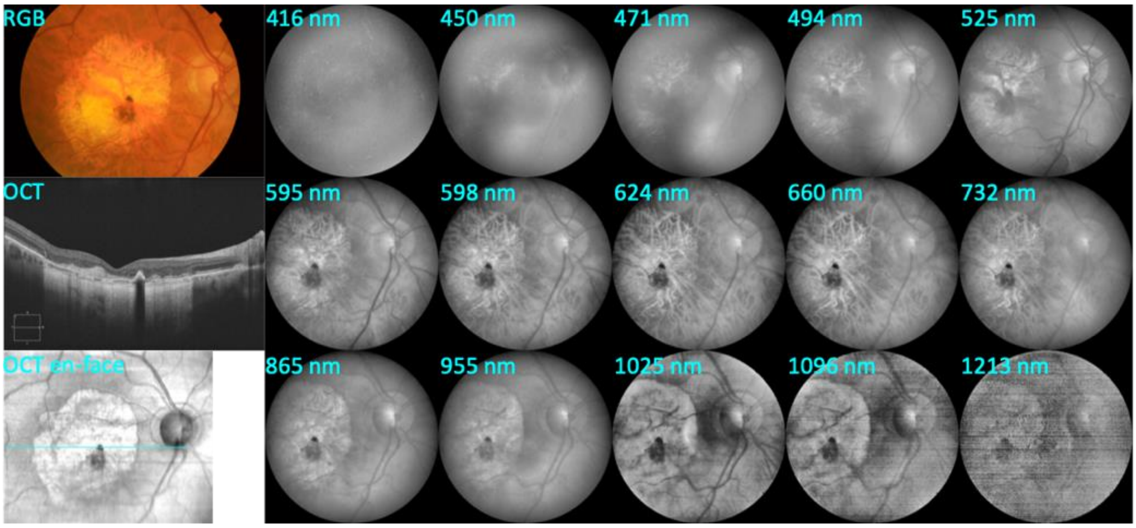

Figure 5.20: Eye with exudative ARMD. Left, from top to bottom: Color fundus image, OCT section and en-face image. Right: Complete spectral sequence obtained with the HSI fundus camera.

Whereas the drusen location (depth) in the ocular fundus is rather specific - they are placed in the Bruch's membrane - other fluids might lay at more superficial or deeper layers (e.g., blood or other fluids from blood vessels). Accordingly, hemorrhages are also labeled in the zoomed images. They present higher absorption in the VIS spectral range, especially from 600 nm up to 850 nm, which is characteristic of coagulated (non-oxygenated) blood, [142]. As hemorrhages are not as compact as fibrotic scars, they gradually disappear at longer wavelengths while the scar contrast remains below 1 up to 1213 nm. With aging, drusen form aggregations that can pierce and decolorate the RPE (leading at the end to the atrophy of the tissue), creating regions with higher intensity than the surrounding healthy tissue at long wavelengths. This can be clearly seen in Figure 5.20 and Figure 5.21.

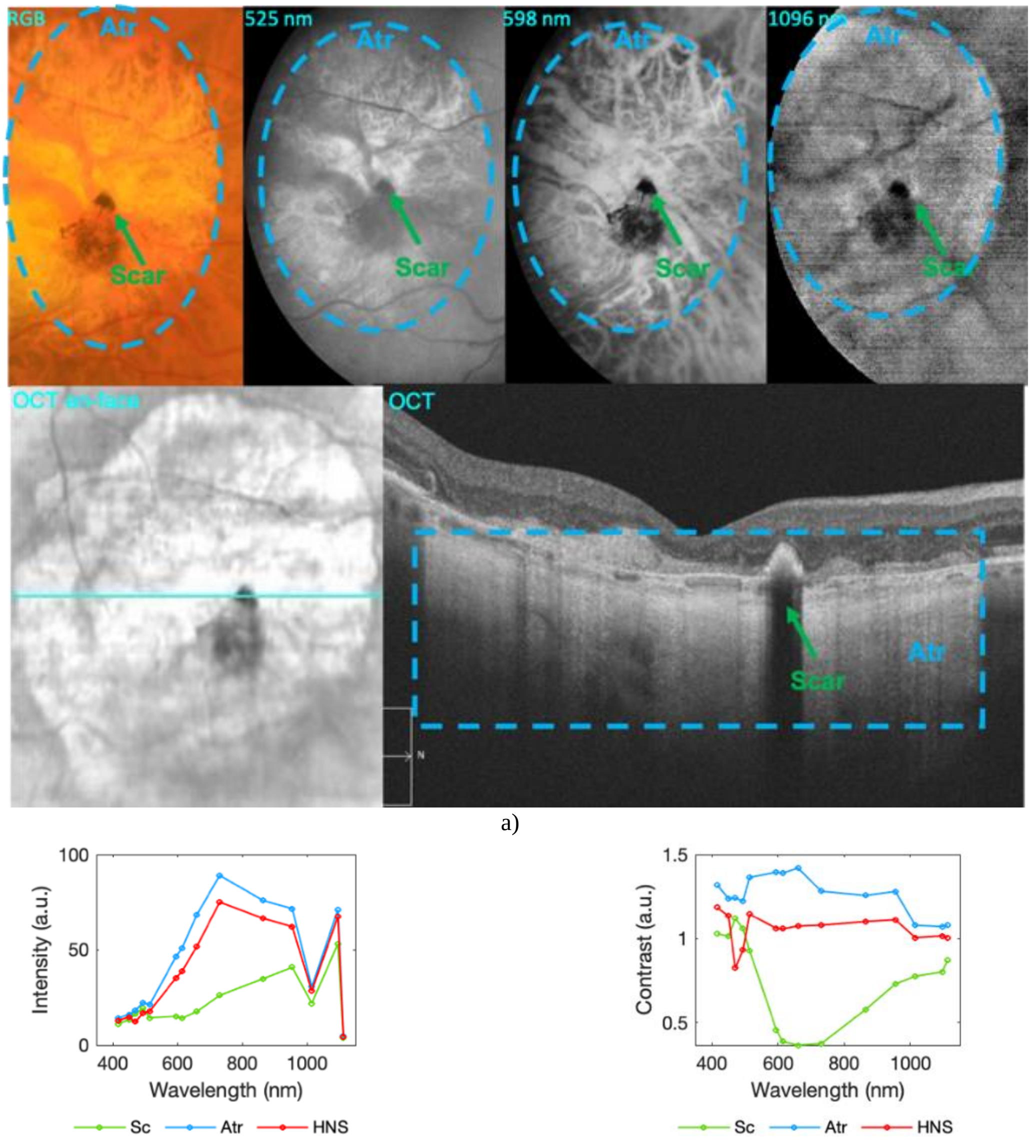

a)

b)

c)

Figure 5.21: a) Zoomed ROI centered on a region with several lesions of the eye with exudative ARMD shown in Figure 5.20. Top row from left to right: color fundus image and selected spectral images acquired with the HSI fundus camera. Bottom row from left to right: OCT en-face image and section. b) Intensity curves of the indicated areas. c) GC curves of the indicated areas. Labels: Atr (RPE Atrophy), Sc (Scar), HNS (Healthy tissue of the Near Surrounding).

In areas without melanin due to RPE decoloration, the choroid vasculature is more evident due to the fact that VIS wavelengths can penetrate deeper into the fundus tissue in this case. In fact, the choroidal vessels can be very well observed in both color and spectral images. This is in line with what was reported in Figure 5.4, about melanin concentration for healthy individuals.

It can also be noticed (see the zoomed images shown in Figure 5.21 a) that images taken at red and NIR wavelengths allow for a better differenciation of attrophied tissue than those acquired at VIS ones (and thus with the RGB image). This can be explained because changes of the tissue occur below the RPE underlying the central macula or nearby, and not at more superficial layers. OCT also shows the real extent of the lesion under the retinal layers (see hyperreflective areas at the bottom of the section); but with less details because of the poor performance of the used system (CIRRUS HD-OCT) at the choroidal level (optimized for more superficial layers, [143]). OCTs that use longer wavelengths can penetrate deeper inside the choroid but at the expense of axial and lateral resolution, [144].

The preliminary spectral analysis depicted in Figure 5.21 b and c corroborates what was said about the higher reflectance signal over the entire spectral range for atrophied tissue, where melanin concentration is strongly reduced.

Figure 5.22 shows the spectral images of an eye with clear signs of dry ARMD. Differently from the exudative form, there are no vascular signs of the disease (such as scars or hemorrhages). Only hard drusen and RPE degeneration, which is hardly visible in the color image, are clearly noticeable in images corresponding to mid-long wavelengths (red box in Figure 5.22) at which light penetrates deeper into the tissue [145].

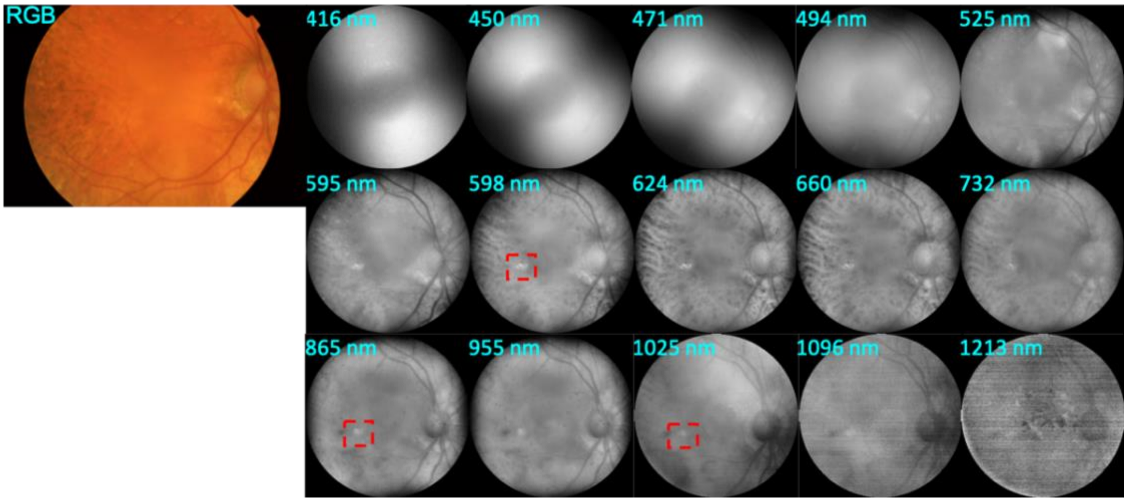

Figure 5.22: Eye with dry ARMD. Left: color fundus image. Right: Complete spectral sequence obtained with the HSI fundus camera. The red box highlights a region of interest where drusen and atrophy are present.

In Figure 5.23, details of some hard drusen and the RPE degeneration are shown. There are relevant differences between the atrophied and the surrounding tissue in terms of spectral intensity, in particular in the red-NIR wavelengths. On the contrary, the atrophy is hardly visible in the color image, in which an analogue analysis in terms of digital levels provided very similar RGB values for the degenerated RPE region (236, 106, 27) and the surrounding healthy tissue (231, 101, 27), as expected. Again, the atrophied tissue is linked to higher signals beyond red wavelengths with respect to the healthy surrounding and even hard drusen, which still preserve fundus pigmentation.

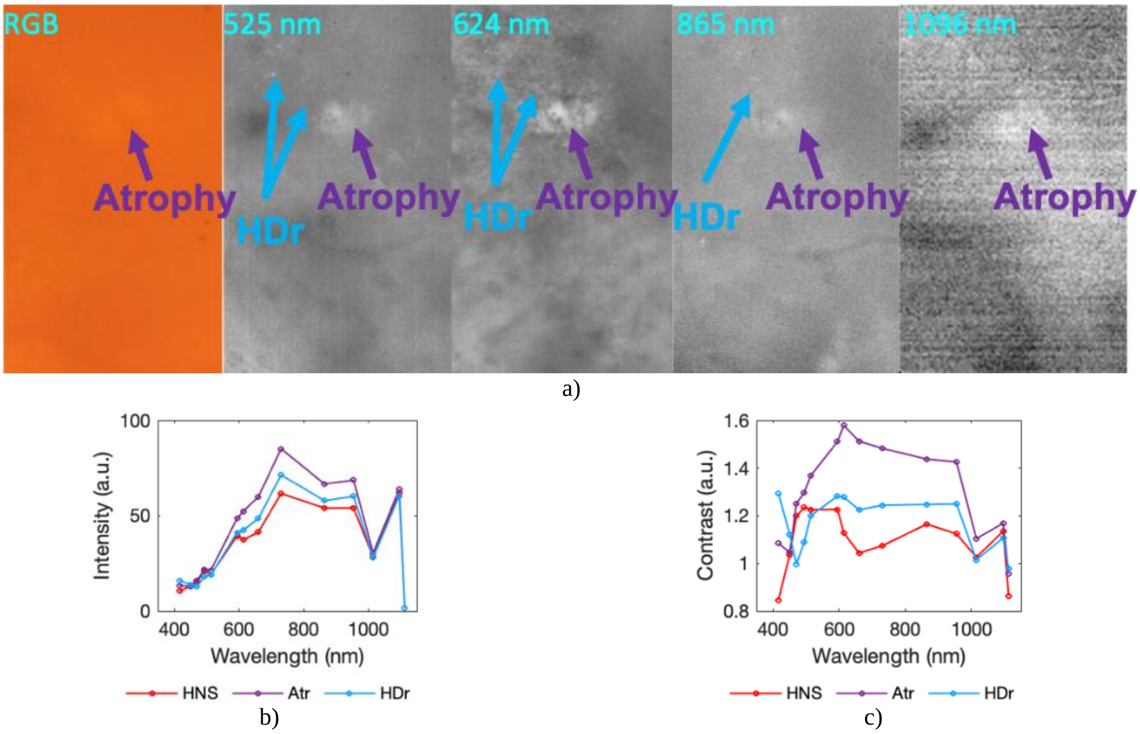

a)

b)

c)

Figure 5.23: a) Zoomed ROI centered on a region with several lesions of the eye with dry ARMD shown Figure 5.22. Top row from right to left: color fundus image and selected spectral images acquired with the HSI fundus camera. b) Intensity curves of the indicated areas. c) GC curves of the indicated areas. Labels: Atr (RPE atrophy), HDr (Hard Drusen), HNS (Healthy tissue of the Near Surrounding).

As an evident example of hard drusen at different stages in the central macula, Figure 5.24 shows images of an eye with dry ARMD. This patient had serious problems in fixating the target and thus, the spectral sequence is not centered as the color image is (this was acquired with the TOPCON fundus camera that is equipped with a rotative and translating stage allowing for a better centration regardless patient's fixation).

In the macular region, groups of well contoured drusen can be seen, which can be classified as hard. In fact, their contours are well localized and do not present the characteristic poorly demarcated round shape of soft drusen. Moreover, they show higher intensity beyond mid wavelengths and no particular changes in reflectance at short ones, which is in accordance with previous findings, [146]. In fact, hard drusen have much more calcification and less autofluorescent compounds than soft drusen. Calcification is crystalline and represents an end-stage drusen in the macula.

The detailed analysis using zoomed images (Figure 5.25) shows that the contrast of these drusen is small or null at short wavelengths while it is higher at mid-long ones. In particular, two different drusen that show different reflectivity behaviors can be distinguished (HDr1 and HDr2). HDr1 contrast is null at short wavelengths and rises up above green and red ones. HDr2 contrast shows more intensity at short wavelengths and disappears around 700 nm. This could be explained by differences in the ageing and degree of calcification: HDr1 would correspond to an aged calcified lesion that has started to pierce the

RPE leading to a reduced pigmentation, which is translated into higher levels of reflected light (especially in the red-NIR region), whereas HDr2 might be probably younger, still preserving some autofluorescent compounds.

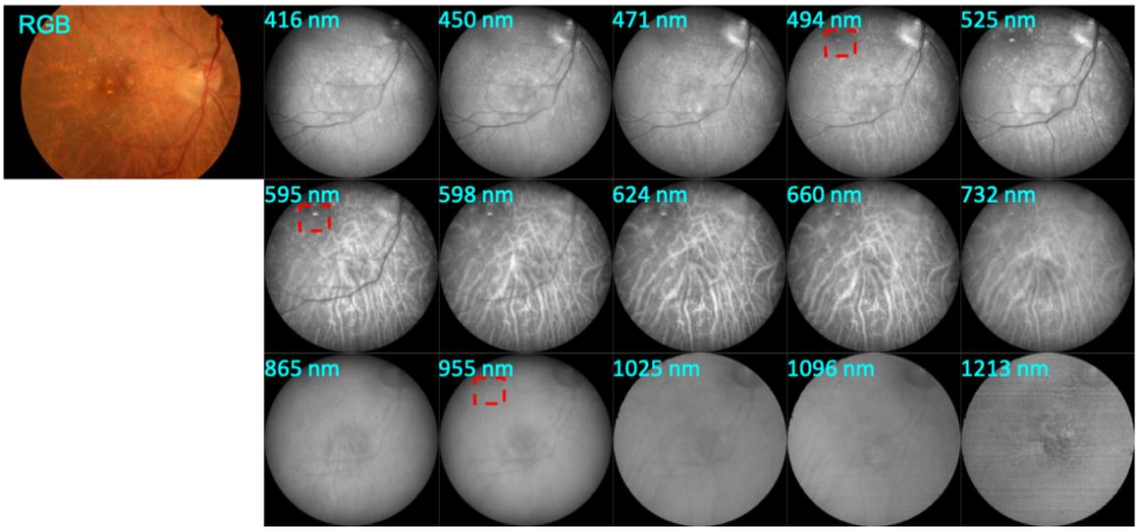

Figure 5.24: Eye with dry ARMD. Left: color fundus image. Right: Complete spectral sequence obtained with the HSI fundus camera. The red box highlights a region of interest where drusen are located.

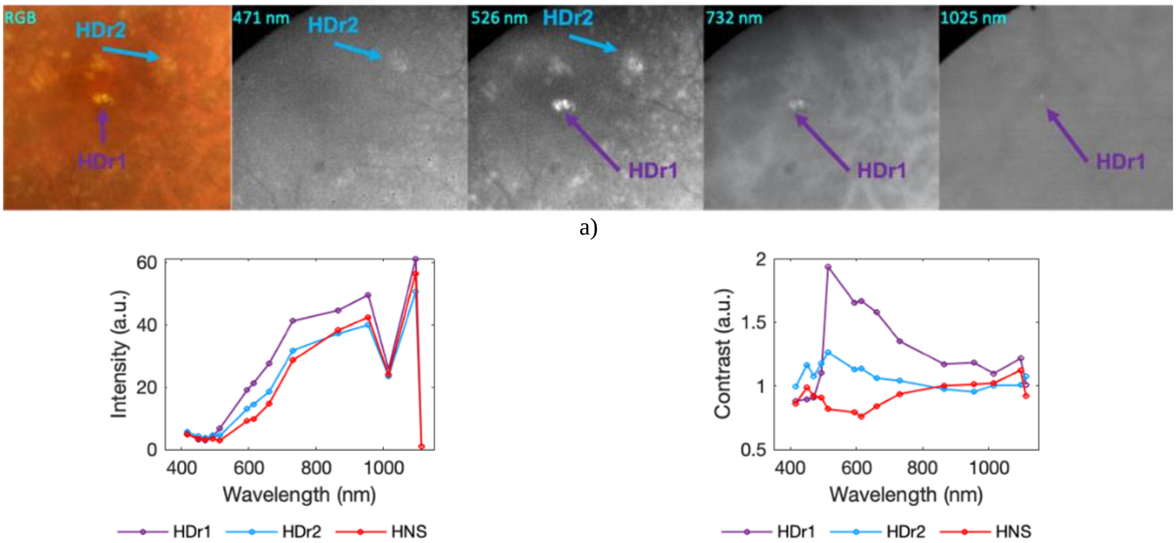

a)

b)

c)

Figure 5.25: a) Zoomed ROI centered on a region with several hard drusen of the eye with dry ARMD shown in Figure 5.24. Top row from left to right: color fundus image and selected spectral images acquired with the HSI fundus camera. b) Intensity curves of the indicated areas. c) GC curves of the indicated areas. Labels: HDr (Hard Drusen), HNS (Healthy tissue of the Near Surrounding).

Figure 5.26 shows images from an eye for which the ophthalmologist’s diagnostic refers to numerous drusen and an epiretinal membrane caused by the growth of atrophied tissue on the inner surface of the macula. The images reveal numerous isolated and aggregated drusen that can be easily identified.

Because of their different nature, different spectral and color properties can be recognized in the spectral images.

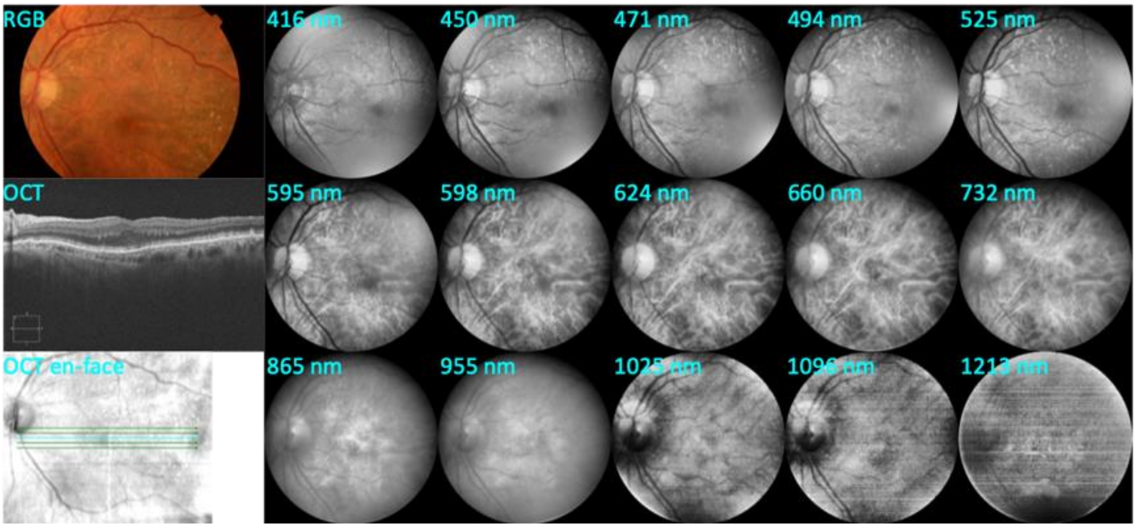

Figure 5.26: Eye with drusen. Left, from top to bottom: Color fundus image, OCT section and en-face image. Right: Complete spectral sequence obtained with the HSI fundus camera.

In particular, several peripherical soft drusen in the superior arch are well contrasted at short wavelengths, with higher intensity values (zoomed in Figure 5.27 a). Therefore, they can be catalogued as soft drusen (semitransparent, autofluorescent, yellowish and non-defined contours). Due to metamerism, these drusen are less distinguishable in the color fundus image.

In the bottom panel of Figure 5.27 a, the spectral images reveal smaller drusen that are barely observed in the color image, located in the peripheral macula. These lesions are classified as hard drusen, as they have defined and localized contours.

Again, the preliminary spectral analysis shows that the intensity levels and contrasts are higher at short wavelengths for soft drusen whereas hard drusen are hyperreflective at long wavelengths. As formerly explained, lipofuscin and autofluorescent compounds present in extracellular material might play a role on this, [93] as well as the local degree of RPE degeneration. The accumulation of lipofuscin is actually one of the most characteristic features of ageing observed in the RPE and drusen. Therefore, it can be concluded that the differences in the reflection pattern at short wavelengths (especially from 400 nm to 550 nm) corresponding to both kinds of drusen is related to the autofluorescence emission of this extracellular material. One should bear in mind that the HSI system excites lipofuscin fluorescence with blue LEDs and that light collected in these spectral bands includes both the reflected and the fluorescence signal in one single frame (see Figure 5.27 b and c). A detailed analysis on this is carried out later in this section.

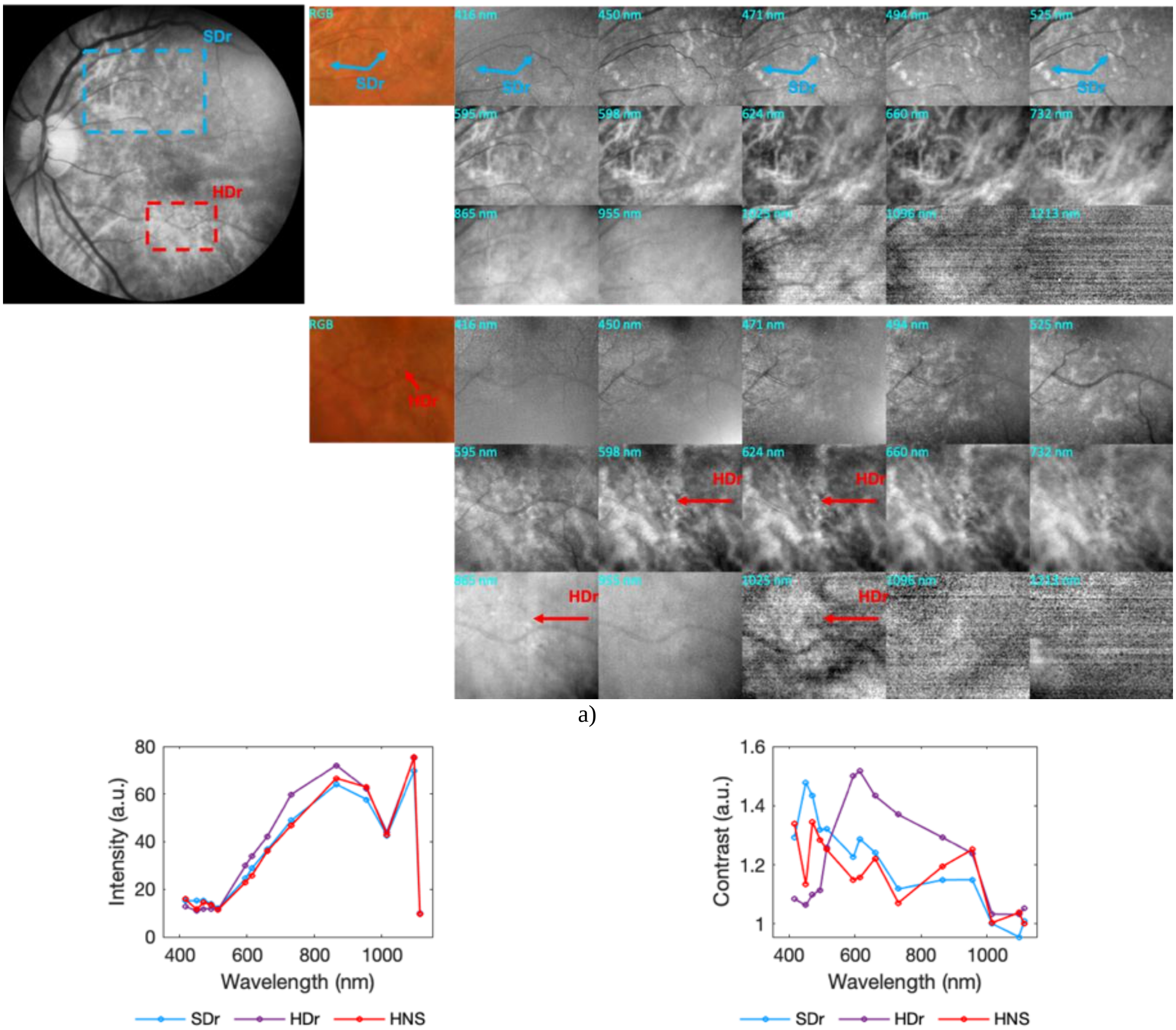

a)

b)

c)

Figure 5.27: a) Zoomed ROIs centered on regions with several drusen of the eye shown in Figure 5.26. Top panel: color fundus image and complete spectral sequence obtained with the HSI fundus camera, showing a ROI centered in a region with several soft drusen. Bottom panel: color fundus image and complete spectral sequence obtained with the HSI fundus camera, showing a ROI centered in a region with several hard drusen. b) Intensity curves of the indicated areas. c) GC curves of the indicated areas. Labels: SDr (Soft Drusen), HDr (Hard Drusen), HNS (Healthy tissue of the Near Surrounding).

In Figure 5.28, fundus records of another patient with dry ARMD are depicted, for who an autofluorescence image was also available. It is to be reminded that when lipofuscin accumulations are present in an eye fundus, autofluorescence images are often taken in the clinic to highlight the region of the RPE that is at risk of progressing to atrophy, [93], [147]. Therefore, autofluorescence provides qualitative information of lipofuscin concentration, which is in turn related with the degeneration state of the RPE. Unfortunately, quantitative information of autofluorescence is poor as it does not give an estimation of the actual state of the RPE.

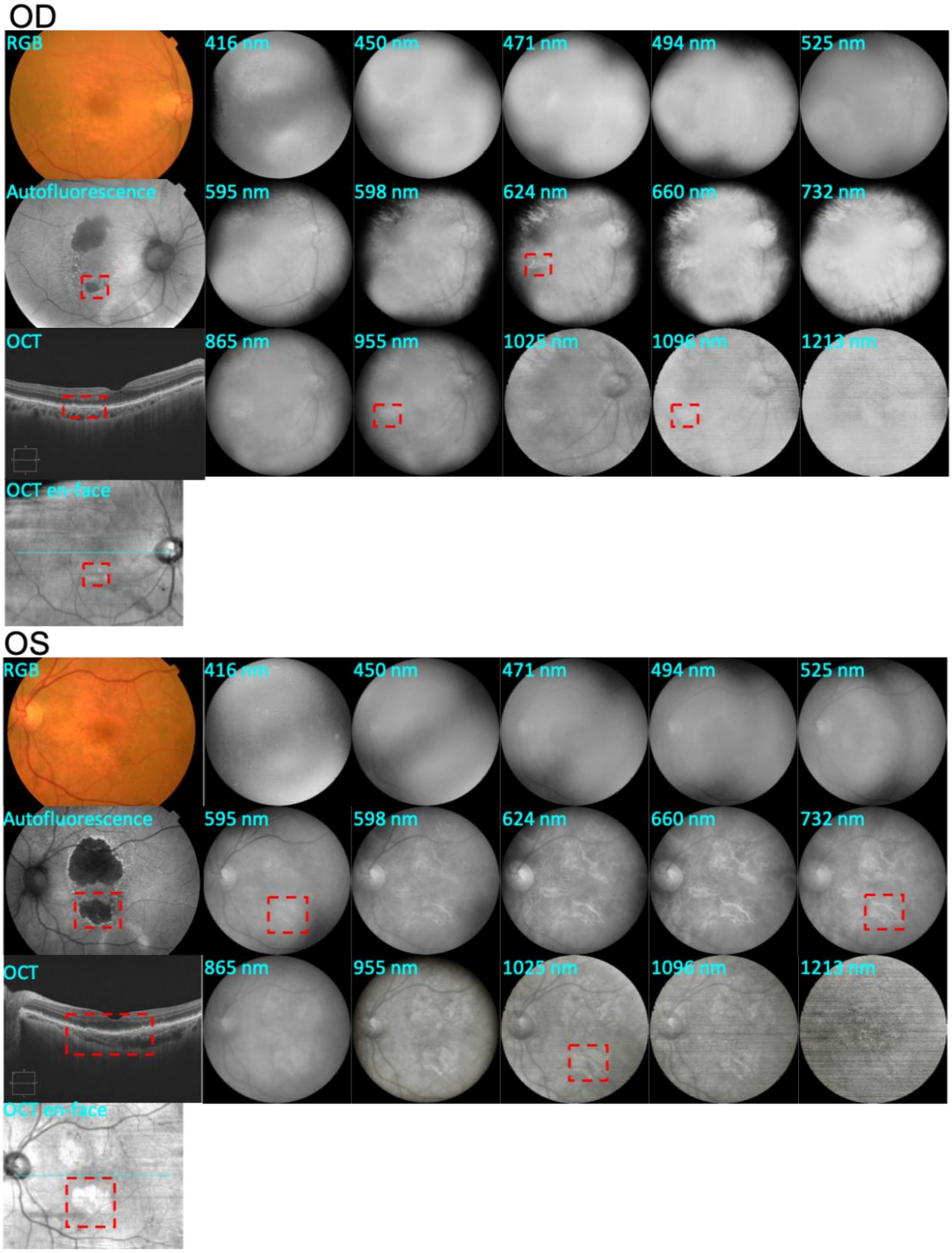

Figure 5.28: Right (OD, top panel) and left (OS, bottom panel) eyes of a patient with dry ARMD. Left, from top to bottom: Color fundus image, autofluorescence image, OCT section and en-face image. Right: Complete spectral sequence obtained with the HSI fundus camera. The red boxes in both eyes highlight areas with atrophied tissue.

In the retina of this patient there is a region corresponding to atrophied tissue due to RPE degeneration with clearly differentiated reflectivity in the spectral sequence where it has a positive contrast (it is brighter in the NIR spectral range). This region can also be identified in the OCT and autofluorescence images, in which it appears as black (with less fluorescence). Nevertheless, it has not defined contours and is less contrasted in the color image. As the decoloration of the RPE progresses due to degeneration, it becomes less absortptive and allows more light to be back reflected. Looking at the autofluorescence image, tissue that will undergo to RPE atrophy can be recognized as it is brighter due to the presence of lipofuscin.

Figure 5.29 depicts zoomed images of the right eye presented in Figure 5.28. Again, the RPE atrophy is neither clearly contrasted in the color image nor along the VIS spectral range in the hyperspectral sequence. As we move forward to longer wavelengths, the lesion is positively contrasted with respect to healthy tissue.

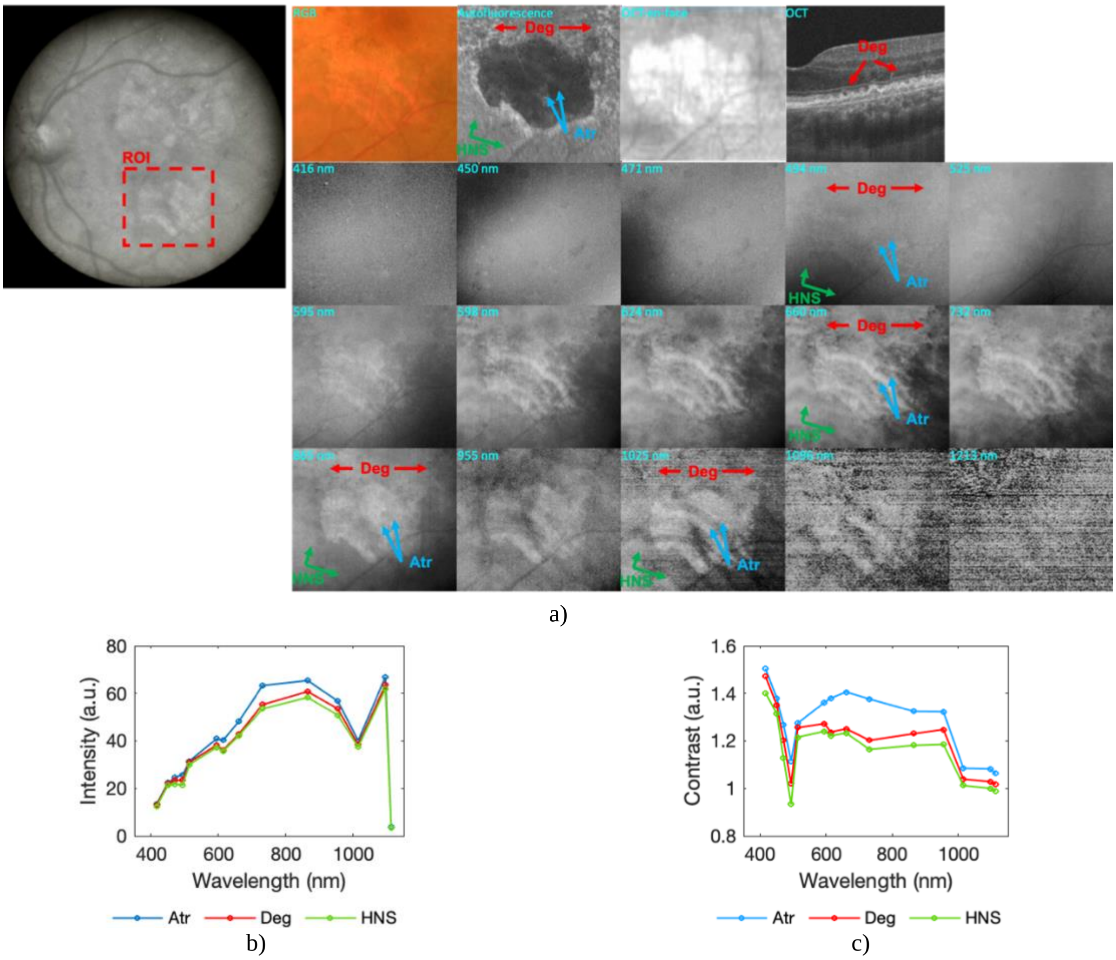

a)

b)

c)

Figure 5.29: a) Zoomed ROI centered on a region with degenerated tissue of the eye with dry ARMD shown in Figure 5.28. Top row from left to right: color fundus image, autofluorescence image, OCT en-face image and section. Bottom rows: complete spectral sequence obtained with the HSI fundus camera. b) Intensity curves of the indicated areas. c) GC spectral curves of the indicated areas. Labels: Atr (RPE Atrophy), Deg (Degenerating), HNS (Healthy tissue of the Near Surrounding).

Partial hyperreflectivity can be recognized in the near surrounding of the lesion corresponding to bright regions of the autofluorescence image where lipofuscin is present, too. This reveals that this tissue is degenerating and that will be the next experiencing damage. Differences in intensity in the spectral curves between healthy and dead tissue were already expected. Intermediate degrees of intensity between these two states where the autofluorescence is slightly higher than in normal tissue would give, thus, information on the progression of the RPE degeneration. Neither the RGB images nor the OCT can retrieve this information. Autofluorescence can be used as a raw estimator of the concentration of chemicals, but without a proper spectral sampling of the autofluorescent emission, the information is poor.

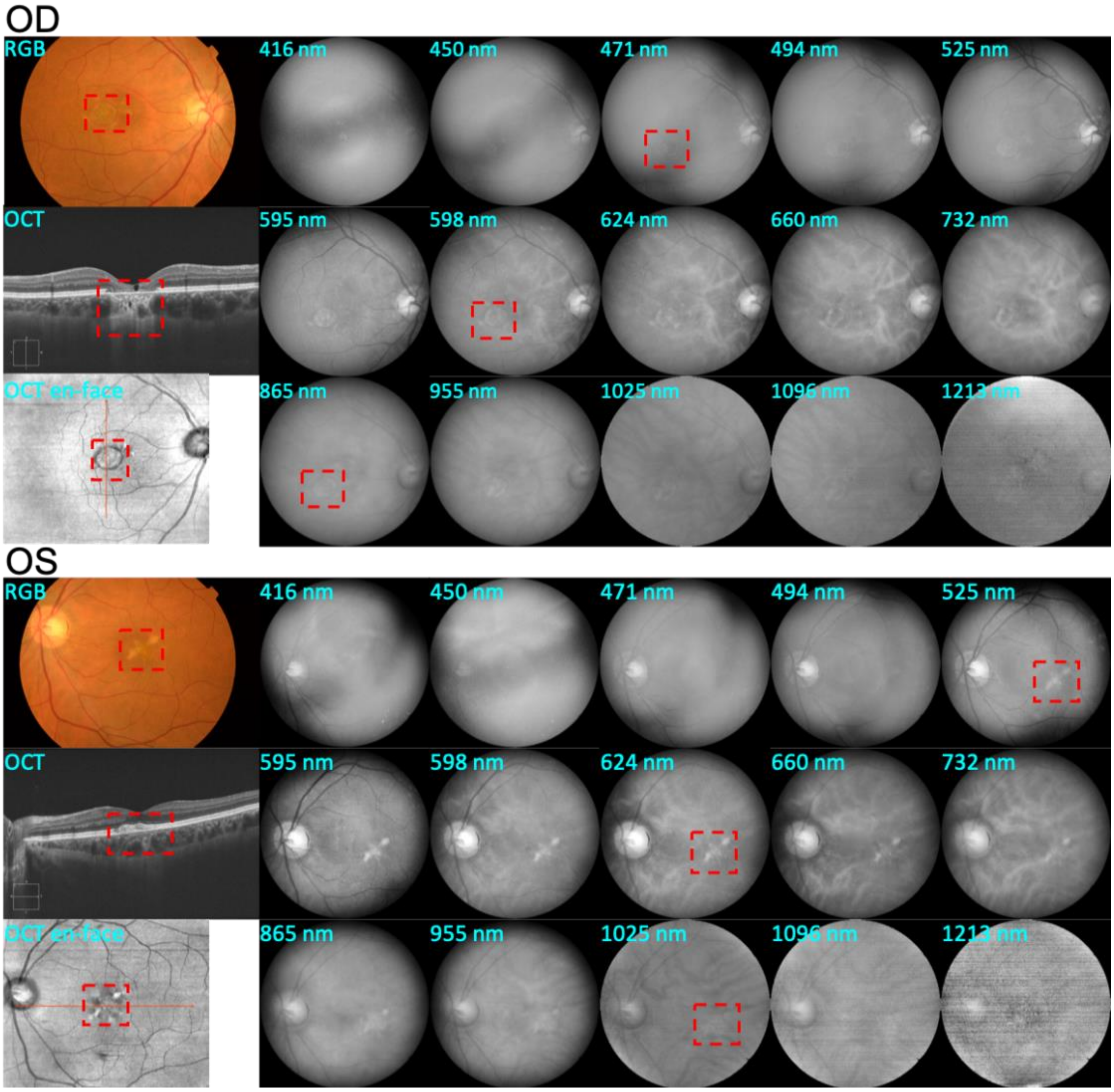

Figure 5.30: Right (OD, top panel) and left (OS, bottom panel) eyes of a patient with pattern dystrophies: vitelliform dystrophy (OD) and butterfly wings (OS). Left, from top to bottom: Color fundus image, OCT section and en-face image. Right: Complete spectral sequence obtained with the HSI fundus camera. The red boxes highlight the regions of interest with dystrophies.

Finally, the fundus images in Figure 5.30 belong to a patient whose diagnosis refers to pattern dystrophies in the central macula. In particular, two different kinds of lesion can be seen: a vitelliform dystrophy in the right eye, and the characteristic form of a butterfly wings-shaped dystrophy in the left one. Pattern dystrophies is an umbrella term for a group of retinal conditions in which a build-up of waste material causes damage to tissue. Different dystrophies are linked to different patterns, which might look like egg yolks, butterfly wings or knotted fishing nets. People will usually have symptoms in both eyes, and may have a different pattern of damage in each. Similarly to ARMD, pattern dystrophies are a group of autosomal dominant macular diseases (caused by gene mutations) characterized by various patterns of pigment deposition within the macula (in the form of the, well known, lipofuscin, [148]), although in general, their symptoms tend to be less severe.

Zoomed images in Figure 5.31 reveal slighlty different patterns of the two conditions.

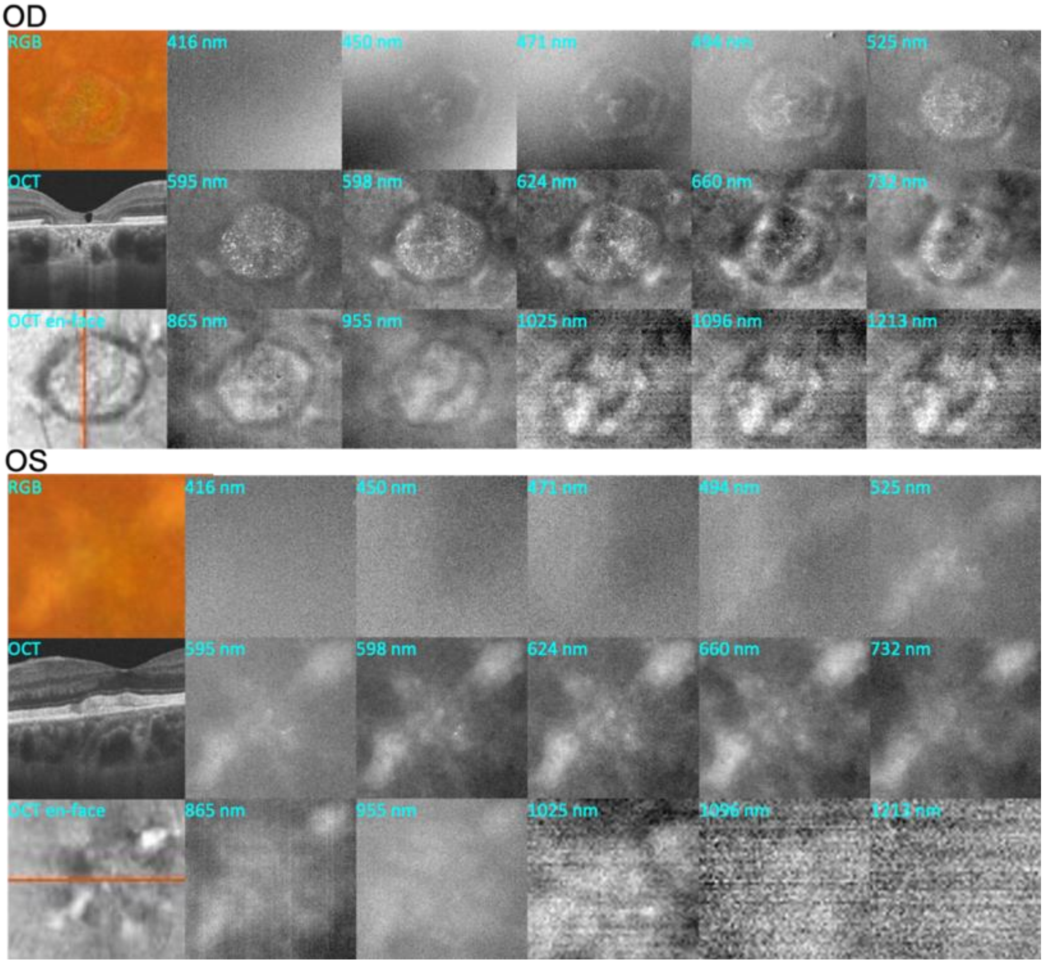

Figure 5.31: Zoomed ROIs centered on regions with pattern dystrophies of the right (OD, top panel) and left (OS, bottom panel) eyes shown in Figure 5.30: vitelliform dystrophy (OD) and butterfly wings (OS). Right columns from top to bottom: color fundus image, OCT section and en-face image. Left columns: complete spectral sequence obtained with the HSI fundus camera.

The butterfly wings-shaped lesion starts to be observable at 494 nm (until 1025 nm) while the vitelliform lesion is well contrasted from 450 nm to the end of the whole spectral range of the HSI system. Additionally, the vitelliform distrophy shows a dotted texture with brighter and darker spots inside while the butterfly wing is more homogeneous. This behavior is in line with what was previously discussed, [148]: butterfly wings do not show autofluorescent emission (high intensity values at short wavelengths), while the vitelliform dystrophy does. This autofluorescent emission creates regions with differentiated reflectivity within the vitelliform lesion as autofluorescent compounds are generally not homogenous on the retinal carpet.

An extended spectral characterization performed on the two lesions is shown in Figure 5.32. In the case of the vitelliform lesion, the RPE is damaged leading to higher values of intensity at longer wavelengths,. On the contrary, in the butterfly wings melanin is still present and the light absorption is higher.

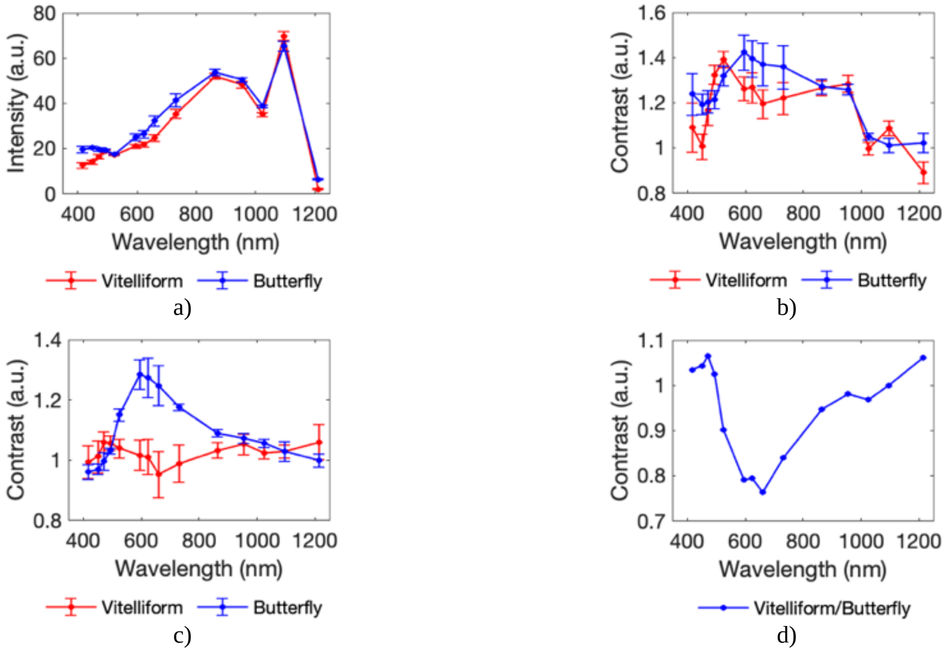

a)

b)

c)

d)

Figure 5.32: a, b, c) Intensity, GC and LC curves collected on the vitelliform (red) and butterfly (blue) dystrophies. d) Specific contrast (SC) computed as the LC ratio of the vitelliform and butterfly curves. The standard deviations correspond to 5 ROIs collected of the same eye.

It is worth to clarify the differencies between the GC and the LC analysis that might take to some confusion. In fact, GC and LC show opposite patterns below 500 nm. As the GC is computed dividing the intensity collected from a single ROI with the mean intensity value of the whole FOV, it is not biased by differences of the ocular media trasmission but residual illumination inhomogeneities can importantly affect it. To solve this, the LC and SC can be computed instead, allowing for the observation of higher contrast levels at shorter wavelengths in the vitelliform lesion and thus enforcing its relationship with autofluorescence.

5.2.1.2 Quantitative analysis of abnormal structures

As in the case of healthy eyes, a throrough quantitative spectroscopic analysis of the abnormal structures found in eyes with ARMD and other maculopathies is carried out here. In the figures below, the intensity curves corresponding to each analyzed eye are plotted as well as the average and the standard error. GC, LC and SC contrasts are also used when required.

Firstly, the analysis of RPE degeneration leading to tissue atrophy is presented (Figure 5.33). According to our former qualitative discussion, the occurrence of an atrophy enhances the intensity values of the ocular fundus from 525 nm to longer wavelengths. This trend is also observable in the GC and LC analysis (Figure 5.33b and c). Accordingly, it can be stated that the reflectivity of the healthy fundus, due to the presence of melanin, is always lower than that of atrophied tissue.

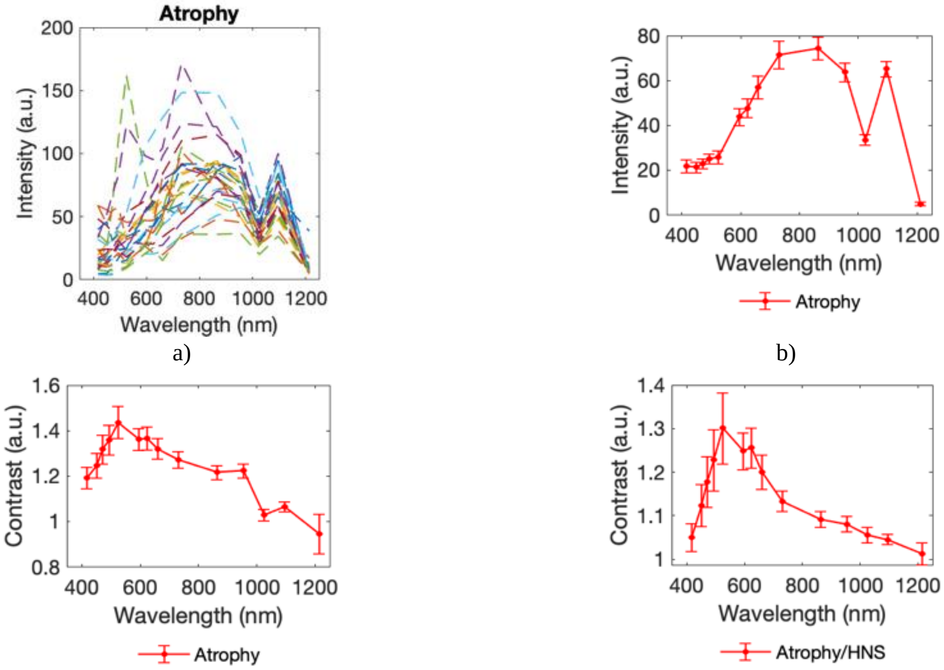

a) b)

c) d)

Figure 5.33: Spectral analysis of atrophies carried out over a population of 27 eyes. a) Intensity curves calculated as the average of all atrophies found in each eye. b) Mean intensity curve. c) GC contrast curve. d) LC contrast curve. In b) and c) the mean and standard error were calculated from 491 ROIs (diameter 0.2°) centered on different atrophies collected from all eyes. In d) the mean and standard error were calculated from 173 ROIs (diameter 0.2°) centered on different atrophies collected from all eyes. In this case, 4 additional ROIs of diameter 0.2° in the HNS were collected, averaged and used to calculate LC.

In Figure 5.34, the spectral analysis of scars is presented. In this case, the analysis in terms of LC was not possible due to the fact that the healthy surrounding of scars was also partly affected. As previously commented, scars show higher absorption in the spectral range between 500 nm and 1000 nm (which is translated into contrast values below 1) because they consist of coagulated blood and fibrotic tissue located at the interface between the retina and the choroid, [65].

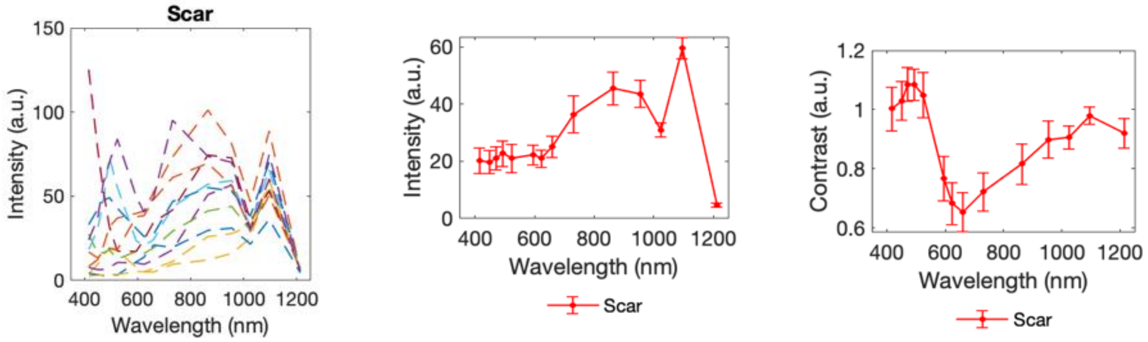

a) b) c)

Figure 5.34: Spectral analysis of retinal scars performed over a population of 11 eyes. a) Intensity curves calculated as the average of all the scars found in each eye. b) Mean intensity curve. c) GC contrast curve. In b) and c) the mean and standard error were calculated from 142 ROIs (diameter 0.2°) centered on different scars collected from all eyes.

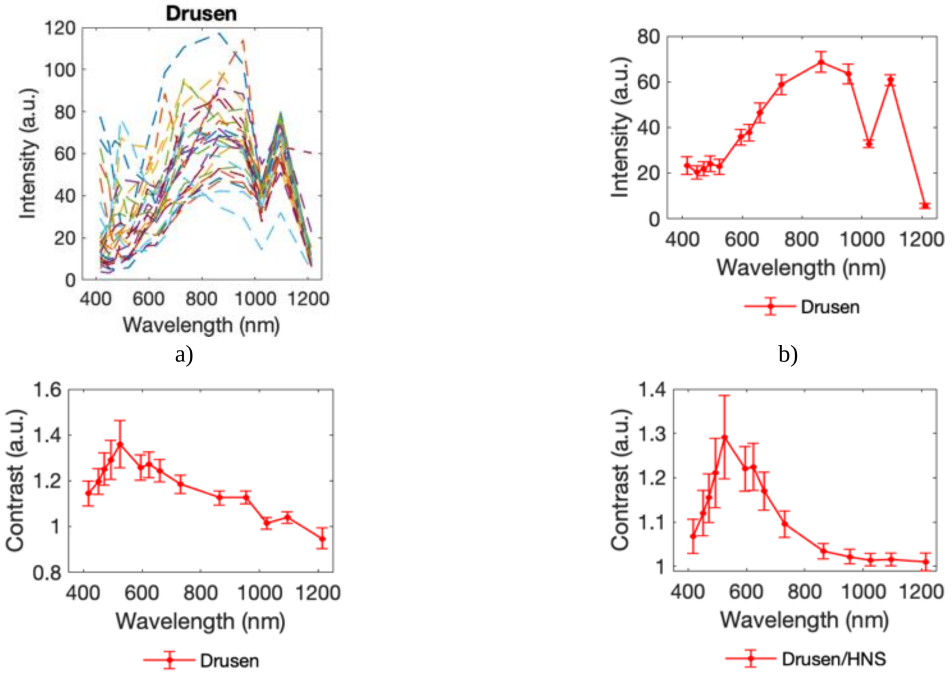

a) b) c) d)

Figure 5.35: Spectral analysis of drusen performed over a population of 25 eyes. a) Intensity curves calculated as the averaged of all drusen found in each eye. b) Mean intensity curve. c) GC contrast curve. d) LC contrast curve. In b) and c) the mean and standard error were calculated from 491 ROIs (diameter 0.2°) centered on different drusen collected from all eyes. In d) the mean and standard error were calculated from 219 ROIs (diameter 0.2°) centered on different drusen collected from all eyes. In this case, 4 additional ROIs of diameter 0.2° in the HNS of the drusen were collected, averaged and used to calculate LC.

In Figure 5.35, the overall analysis of drusen is shown, without discerning between soft and hard. In general, drusen are linked to intensity and contrast values higher than the healthy background at wavelengths shorter than 850 nm approx. This could be caused by two factors: (i) the RPE degeneration, involving depigmentation, and (ii) the lipofuscin fluorescence. As previously commented, drusen appears between the RPE and the Bruch's membrane with a color that can vary from white to pale or bright yellow depending on their nature. As they progress, they lose their coloration leaving glistening areas of calcification and can cause local progression of RPE degeneration. As in atrophied RPE, the early depigmentation reduces melanin absorption and, consequently, the reflected light in the red-NIR range increases. Differently from atrophied tissue, drusen do not show high values of reflectance in the NIR spectral range, and this is due to incomplete RPE degeneration. According to the literature, GC and LC analysis (Figure 5.35 c and d) show the characteristic peak around 500 nm - 600 nm, [12], [149]

An analysis between different types of drusen (hard and soft) is carried out next (Figure 5.36).

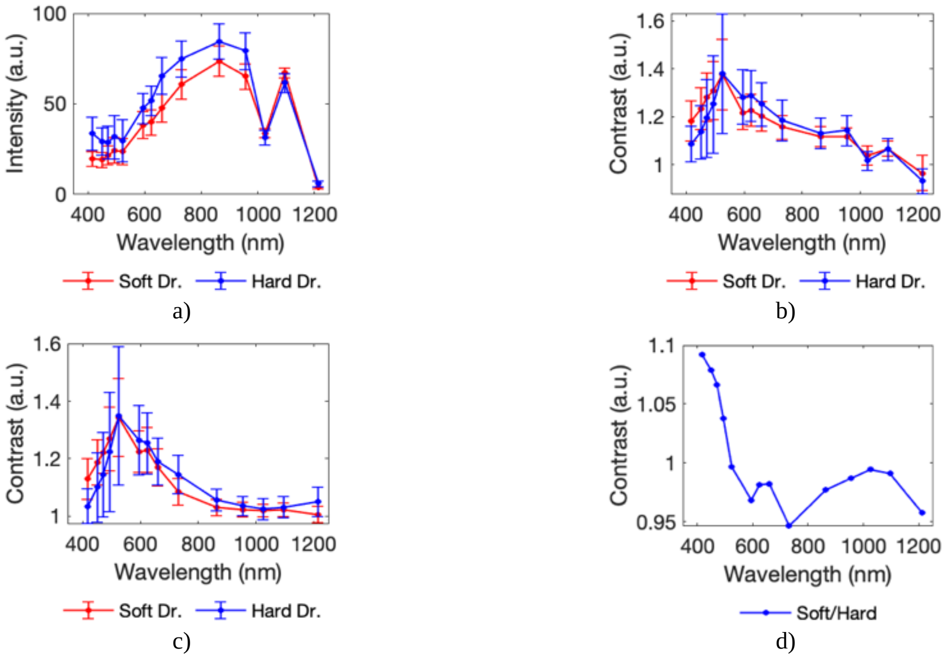

Figure 5.36: Spectral analysis of soft drusen (Soft Dr.) and hard drusen (Hard Dr.) carried out over populations of 10 and 15 eyes, respectively. a) Intensity curves. b) GC curves. c) LC curves. In a, b, c the average and standard error were calculated from 99 ROIs and 224 ROIs (diameter 0.1°) on soft and hard drusen, respectively. In this case, 4 ROIs of diameter 0.1° in the HNS of the drusen were collected, averaged and used to calculate LC. d) SC contrast between soft and hard drusen.

Soft drusen reveal higher mean values of intensity at short wavelengths, probably indicating an increase in autofluorescence emission. On the other hand, hard drusen are linked to higher mean intensities at long wavelengths, probably due to a higher degree of depigmentation. The GC, LC and SC plots support that soft and hard drusen have different spectral features.

Finally, the spectral analysis of hemorrhages is presented (Figure 5.37). As in the case of arteries and veins (see Figure 5.15), the spectral signature of the blood is distinctive. GC and LC analyses show a smooth decrease between 500 nm and 600 nm, where de-oxy and oxygenated hemoglobin have absorption peaks, with a minimum reflectance around 600 nm. Despite being a leakage of blood, these values are in accordance with the absorbance of hemoglobin presented in Figure 5.15: as the wavelength increases, the hemorrhage absorbs less and the contrast becomes closer to 1. Differently from scars, which have contrast values below 1 for the entire spectral range, the blood leakage is still fluidic and do not present a compact fibrotic structure. In this way, the degree of absorption of the lesion in the NIR can be important to evaluate the progression of the degeneration and to promptly intervene to reduce the risk of scars formation.

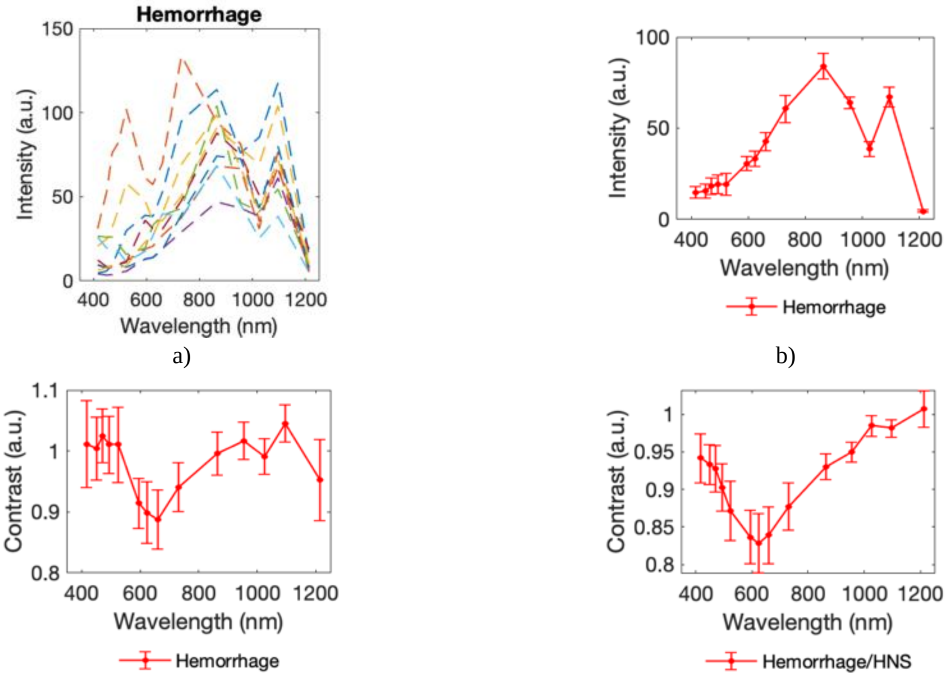

a) b)

c) d)

Figure 5.37: Spectral analysis of hemorrhages performed over a population of 10 eyes. a) Intensity curves calculated as the average of all hemorrhages found in each eye. b) Mean intensity curve. c) GC contrast curve. d) LC contrast curve. In b) and c) the mean and standard error were calculated from 65 ROIs (diameter 0.2°) centered on different hemorrhages collected from all eyes. In d) the mean and standard error were calculated from 46 ROIs (diameter 0.2°) centered on different hemorrhages collected from all eyes. In this case, 4 ROIs of diameter 0.2° in the HNS of the hemorrhage were collected, averaged and used to calculate LC.

5.2.2 Optic disk drusen

Some eyes have optic disk (or papillary) drusen, which are extracellular bodies composed of hyaline proteinaceous material that become calcified with advancing age, and that form anterior to the lamina cribrosa. This kind of drusen are congenital and commonly located ahead the cribriform plate. Its pathogenesis remains unknown but the most accepted theories suggest a blocking of the axonal transport of ganglion cells: they are thought to be the remnants of the axonal transport system of degenerated retinal ganglion cells. Although they are asymptomatic in most cases, sometimes they have been associated with retinitis pigmentosa, angioid streaks, and other eye syndromes causing severe visual impairment, especially if they are at the deepest layers of the nerve head [150], [151], [152]. They are generally bilateral and asymmetrical and may also lead to a loss of visual field or, in rare cases, central visual acuity or anterior ischemic optic neuropathy.

Optic disk drusen can be seen as round, white/yellow refractile bodies on the surface of the nerve or buried beneath it. They produce bright hyper-autofluorescent foci in the disk, understood to be the calcium salts, lipofuscin and mitochondrial porphyrins [153], [154], and often cause an abnormally elevated, small, optic disk with indistinct and irregular disk margins. In children, they are usually buried and undetectable by conventional retinography except for a mild or moderate elevation of the optic disk. With age, the overlying axons become atrophied and the drusen become exposed and more visible. Optic disk drusen can compress and eventually compromise the vasculature and nerve fibers [155].

Figure 5.38 shows images from both eyes of a patient with papillary drusen included in our study.

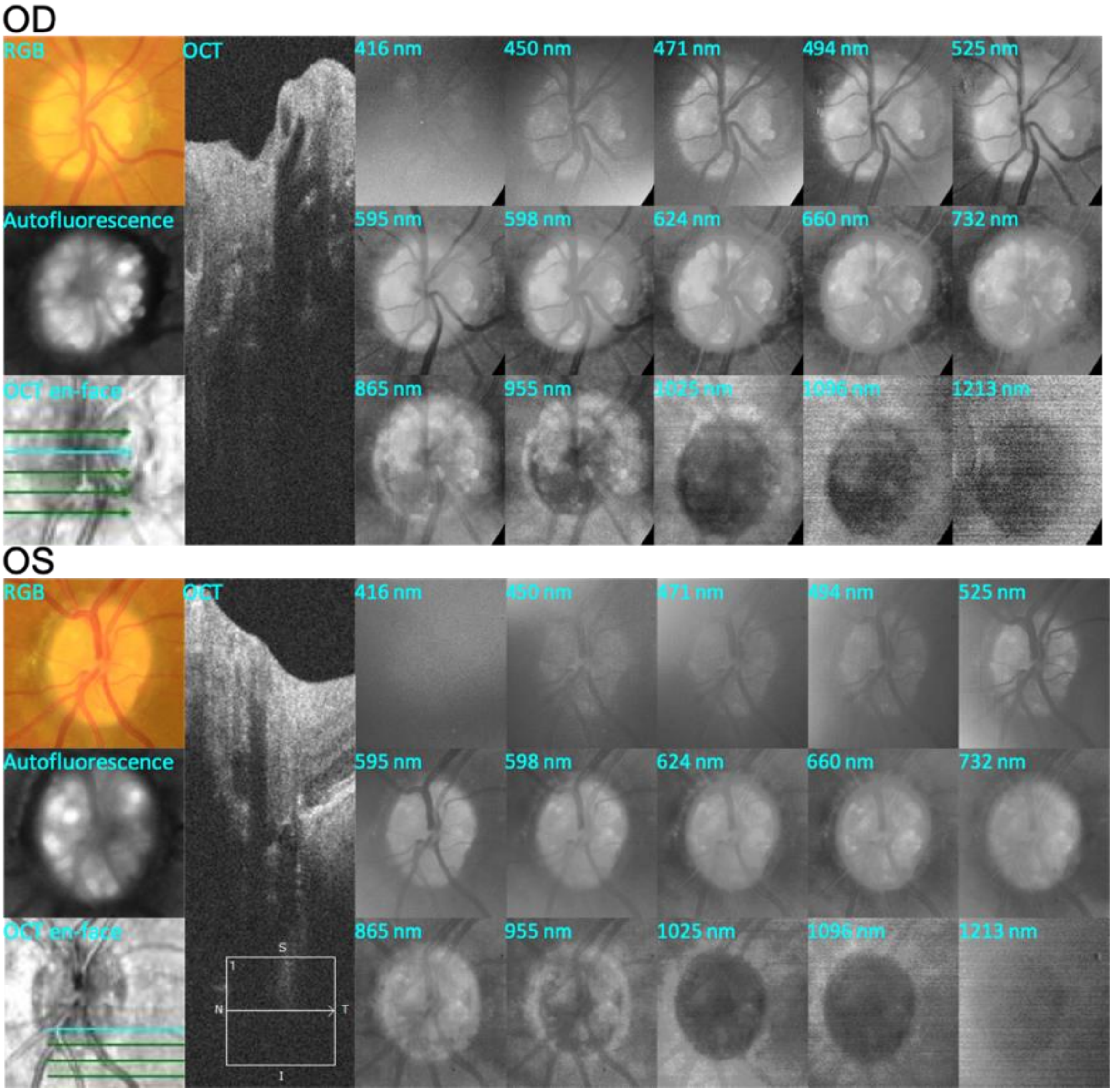

Figure 5.38: Zoomed ROIs centered on the optic disk of the right (OD, top panel) and left (OS, bottom panel) eyes of a patient with optic disk drusen. Left panel from top to bottom: Color fundus image, autofluorescence image and OCT en-face image. Middle panel: OCT section. Right: Complete spectral sequence obtained with the HSI fundus camera.

On the one hand, the drusen bodies are revealed in both the autofluorescence images, as hyperfluorescent extended bodies, and in the spectral sequence, where they appear with different shapes and contrasts depending on the wavelength. In fact, they are highly contrasted and delimited at wavelengths comprised between 595 nm and 955 nm, which might have its origin in that drusen are not placed at the surface of the optic disk but beneath. On the other hand, they are hardly observable in the color images.

As formerly explained, it is actually known that the depth of drusen may vary depending on the progression and stage of the disease, as they grow ascending through the optic nerve, evolving dynamically in the adulthood [156], [157]. This is something that can be analyzed using spectral imaging technology - since images taken at several wavelengths (and thus different penetration in tissue) are available - whereas in standard autofluorescence images, acquired with conventional fundus cameras, there is not any kind of axial optical sectioning, which leads to blurred images, mainly if the fluorescence is originated from an extended volume. Only using advanced cSLO, the contours of the drusen could be distinguished in autofluorescence images.

In Figure 5.39, some zoomed spectral images of the optic disk depicted in Figure 5.38 (OD) are shown. In the autofluorescence image and at images taken at short wavelengths (<525 nm), drusen appear very close one to each other and cannot be well distinguished. On the contrary, they have more delimited contours in the spectral images acquired at red-NIR wavelengths. This might indicate the deeper location of drusen inside the optic disk. OCT correlates with the hyperspectral sequence but as it is optimized for retinal layers and the drusen at superior layers create shadows, the image quality at this depth is poor.

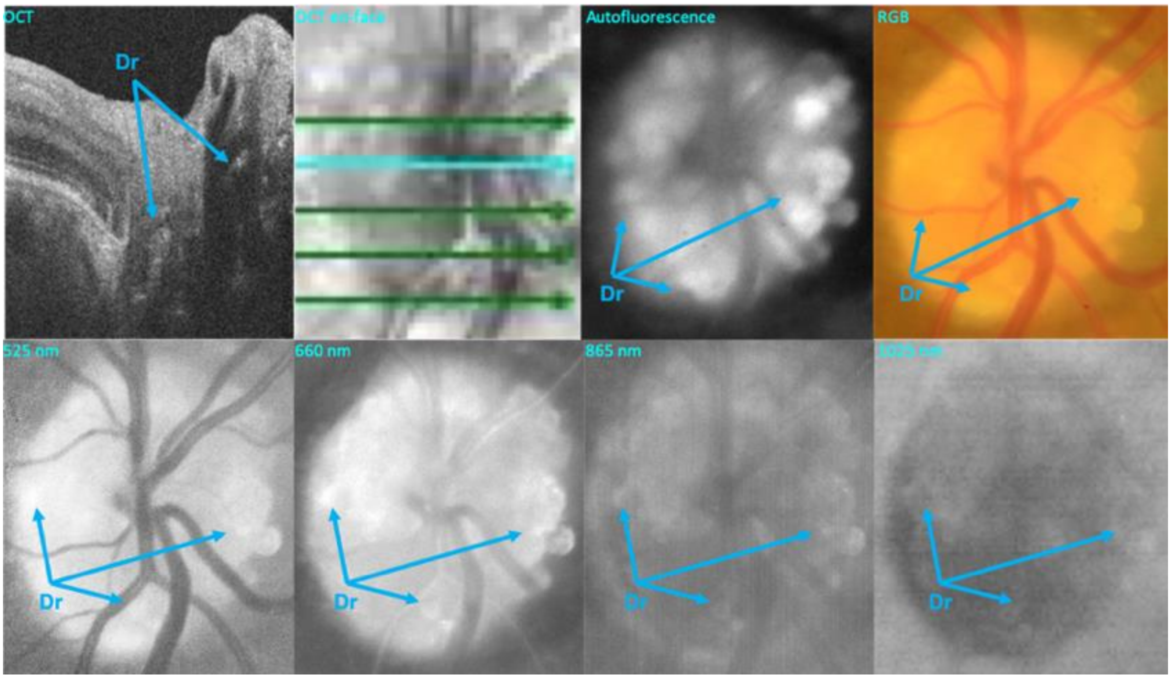

Figure 5.39: Selected zoomed images of the optic disk of the right eye (OD) of the patient with optic disk drusen shown in Figure 5.38. Top panel, from left to right: OCT section and en-face image, autofluorescence image and color fundus image, Bottom panel: selected spectral images acquired with the HSI fundus camera.

Although the number of eyes with optic disk drusen included in our study was low (only 2 eyes from 1 patient), it is still worth to show the spectral curves using as many drusen as possible to enlarge the statistical sample (Figure 5.40).

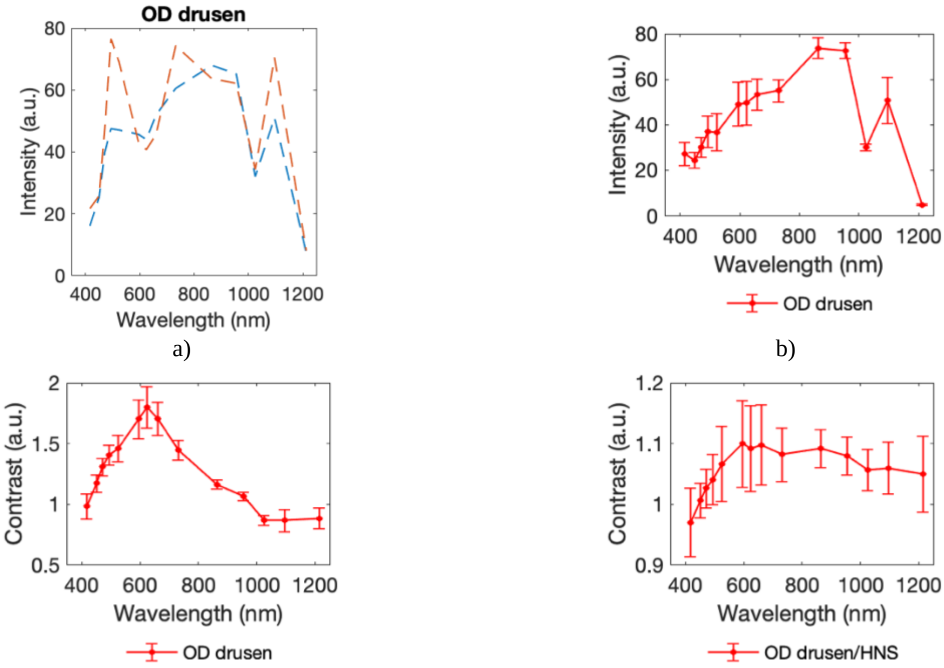

a) b) c) d)

Figure 5.40: Spectral analysis of optic disk drusen performed over 2 eyes. a) Intensity curves calculated as the average of all drusen found in each eye. b) Mean intensity curve. c) GC contrast curve. d) LC contrast curve. In b) and c) the mean and standard error were calculated from 28 ROIs (diameter 0.2°) centered on different drusen collected from each eye. In d) the mean and standard error were calculated from 23 ROIs (diameter 0.2°) centered on different drusen collected from the two eyes. In this case, 4 ROIs of diameter 0.2° in the HNS of the drusen were collected, averaged and used to calculate LC.

According to the results, differences between the healthy tissue of the optic disk and drusen are noticeable within the range comprised from 500 nm to 900 nm, presenting GC and LC contrasts higher than 1 beyond 450 nm, with a shape that resembles that of retinal drusen. Differently from the latter (maximum contrast at 550 nm) the maximum peak of optic disk drusen is around 660 nm. This could probably be caused by the different depth of the drusen, which can influence the intensity recorded besides the chemical composition itself. Thanks to the increased penetration depth, the HSI system could be used as a complementary tool for the precise screening of optic disk drusen, also in the childhood when these are buried and both the OCT and the autofluorescent screening are insufficient.

5.2.3 Glaucoma

Glaucoma is an eye disease often associated with elevated intraocular pressure, in which damage to the optic nerve can lead to loss of vision and even blindness. In fact, it is the leading cause of irreversible blindness worldwide [158]. Glaucoma usually causes no symptoms early in its course, at which time it can only be diagnosed by regular eye examinations (screenings with the frequency of examination based on age and the presence of other risk factors). Intraocular pressure increases when either too much fluid is produced in the eye or the drainage or outflow channels (trabecular meshwork) become blocked. The two main types of glaucoma are open-angle glaucoma, which has several variants and is a long duration (chronic) condition, and angle-closure glaucoma, which may be either a sudden (acute) condition or a chronic disease. Zoomed images of the optic disk of glaucomatous eyes are shown in Figure 5.41.

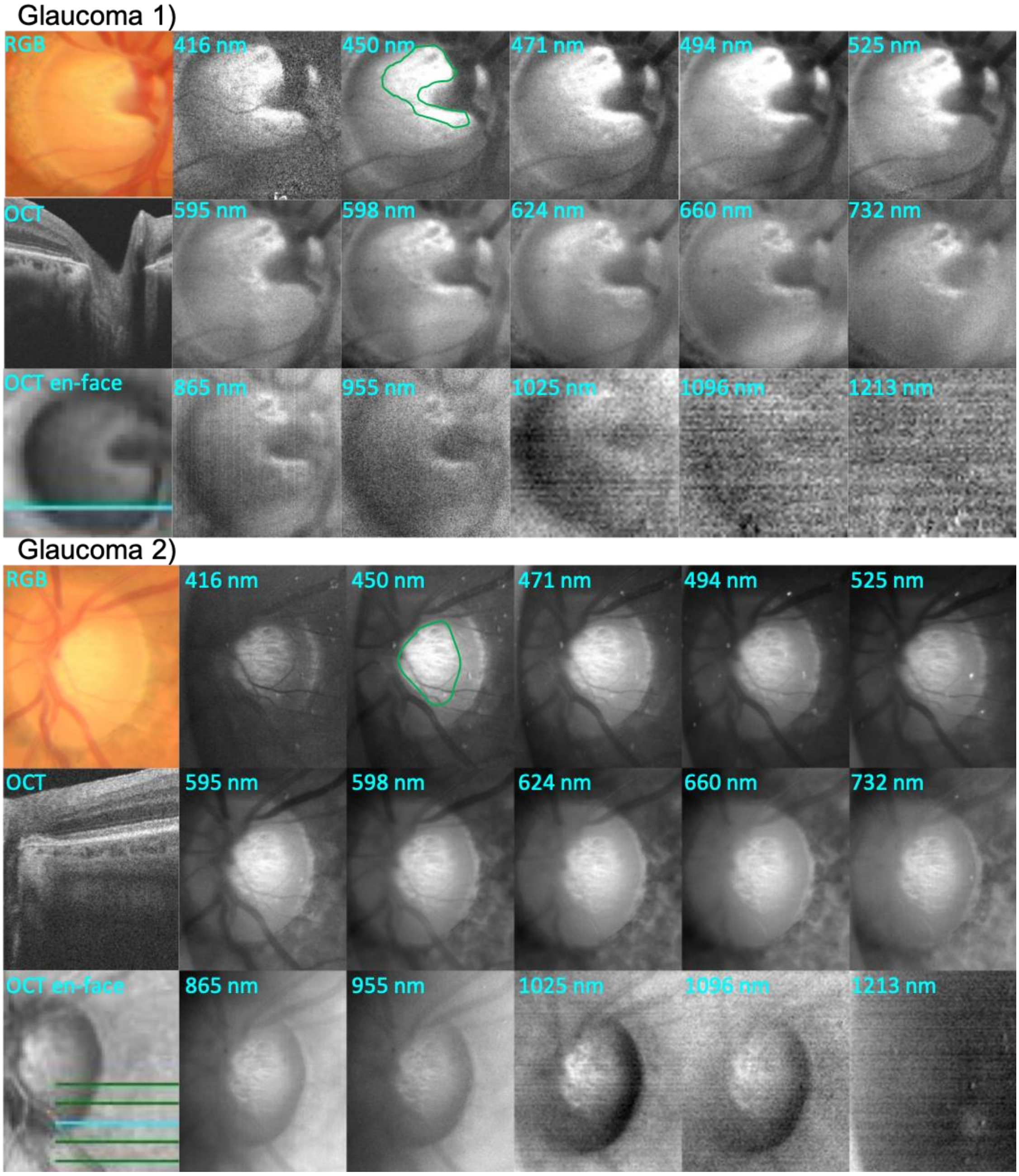

Figure 5.41: Zoomed ROIs centered on the optic disks of two eyes of two patients with glaucoma (Glaucoma 1 and 2). Left panel, from top to bottom: Color fundus image, OCT section and en-face image. Right: Complete spectral sequence obtained with the HSI fundus camera. In green in 450 nm images, anomalous regions with higher intensity levels manually segmented.

According to the literature, the optic nerve presents a larger cup with higher intensity levels and reduced NFs. This can be noticed in the spectral images (segmented green region) of Figure 5.41 all over the entire spectral range (especially in Glaucoma 2). Thanks to the enhanced penetration NIR light in the HSI system and the availability of spectral intensity curves, the segmentation of the damaged portion of the optic disk can be done more precisely, which might take to a more robust cup-to-disk assessment than using commercial color fundus cameras.

In Figure 5.42, the quantitative spectral analysis of the eyes with glaucoma is shown. In particular, the spectral analysis was carried out at the periphery and at the center of the optic disk, to be consistent with the analysis carried out for healthy eyes. In fact, it was found that the curves of the center and the periphery had similar spectral patterns with a peak of the GC around 600 - 700 nm and a monotone decreasing contrast below and above it. For glaucomatous eyes, the spectral behavior is different. Contrary to what was expected considering the degeneration of NFs that takes place in glaucoma, the intensity and contrast values were higher at shorter wavelengths (between 400 nm and 550 nm) than in healthy subjects, for both the center and the periphery of the optic disk. For an in-depth analysis on this, Figure 5.43 depicts the LC contrast calculated between the optic disk center and periphery for glaucomatous and healthy eyes.

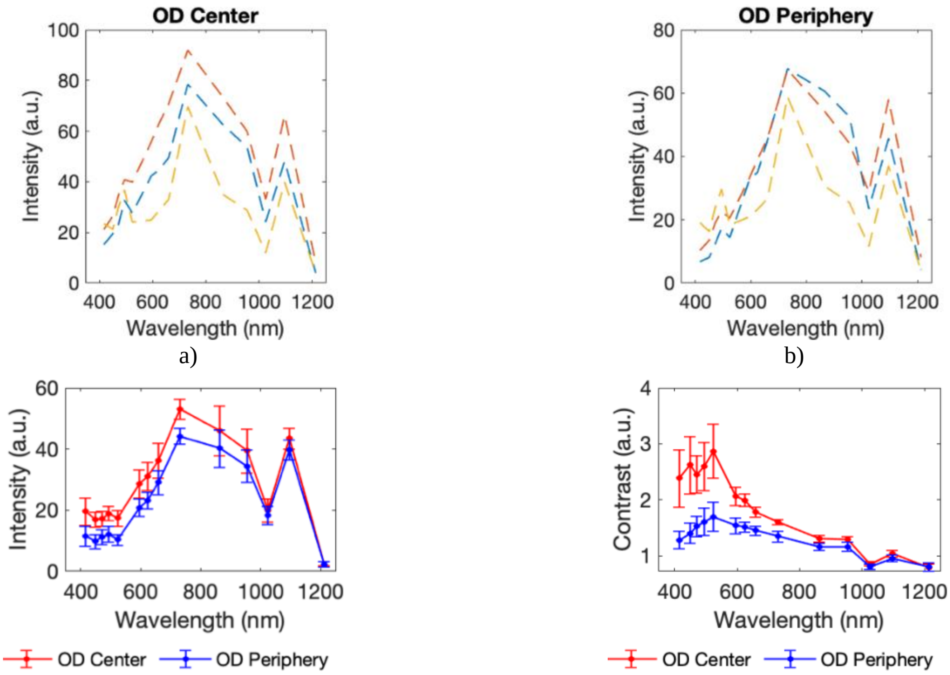

a)

b)

c)

d)

Figure 5.42: Spectral analysis of the center (red curves) and the periphery (blue curves) of glaucomatous optic disks performed on 3 eyes of 2 patients. a, b) Intensity curves calculated as the average of intensity values collected from the center (a) and periphery (b) of each eye. c) Mean intensity curve. d) GC contrast curve. In c) and d) the mean and standard error were calculated from 1 ROI (diameter 0.2°) centered on the optic disk and 3 ROIs (diameter 0.2°) collected from the periphery of each eye.

One hypothesis of this behavior may be that, as glaucoma causes a degeneration of optic disk layers, the lamina cribrosa can be more exposed taking to a different reflectivity. Probably, light at shorter wavelengths (more influenced by scattering and absorption at the first retinal layers) experiences less scattering and absorption, and higher reflection from eroded areas. Our results also show that, at longer wavelengths, there are no substantial differences in terms of spectral reflectivity between glaucomatous and healthy eyes. Probably, thanks to the deeper penetration achieved by NIR light, more information could be found studying the morphological differences between healthy and glaucomatous eyes (assessment of cup to disk ratio). Unfortunately, the number of eyes included in the study is too low to carry out such analysis and no definitive conclusions can be drawn from the current analysis.

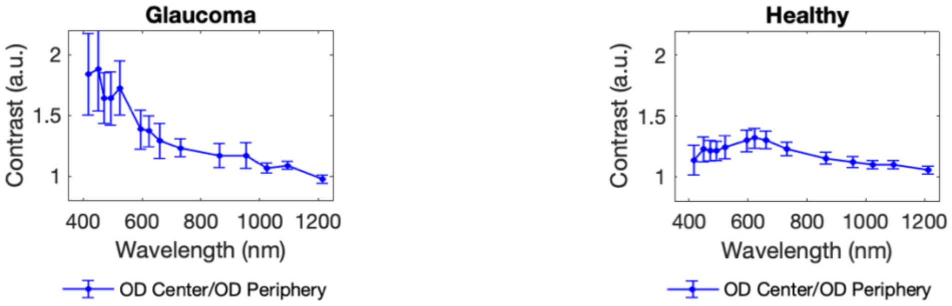

a) b)

Figure 5.43: Mean LC contrast curves calculated dividing averaged values collected from 3 ROIs from the center and 3 ROIs on the periphery of the optic disk of 3 glaucomatous (left) and 60 healthy (right) eyes. The standard errors in a) and b) were calculated using the LC curves from all glaucomatous and healthy eyes, respectively.

5.2.4 Choroidal tumors

A choroidal nevus is a flat, benign pigmented area that appears in the choroid. It is basically an eye freckle caused by the accumulation of pigmented cells. Estimates set occurrence between 2% and 13% of the population, being the most common intraocular tumor. Choroidal nevi rarely evolve into malignant melanomas; the annual rate of malignant transformation is estimated to be 1 in 8.845, [159]. The rate of transformation increases with age; it has been estimated that by the age of 80, the risk for malignant transformation of a choroidal nevus is of 0.78%, [160]. Nevertheless, choroidal melanomas can spread to other parts of the body. Accordingly, care must be taken and nevi should be closely monitored.

Images of a patient with a choroidal nevus are shown in Figure 5.44. As can be seen, in the RGB image the nevus is not as contrasted as in the case of red-NIR images. In fact, the depth at which the nevus is located might play a role in the spectral intensities registered. As its formation is not superficial, red-NIR wavelengths (mainly from 600 nm to 800 nm) reach the nevus thanks to their enhanced penetration. As a consequence, the nevus is neither displayed at shorter wavelengths nor in the color image.

Moreover, it is to be highlighted that the contrast of the nevus changes from negative to positive between 955 nm and 1025 nm. This transition might be related with the etiology and state of the nevus as well as the state of the RPE tissue in its near surrounding, as in the case of atrophy.

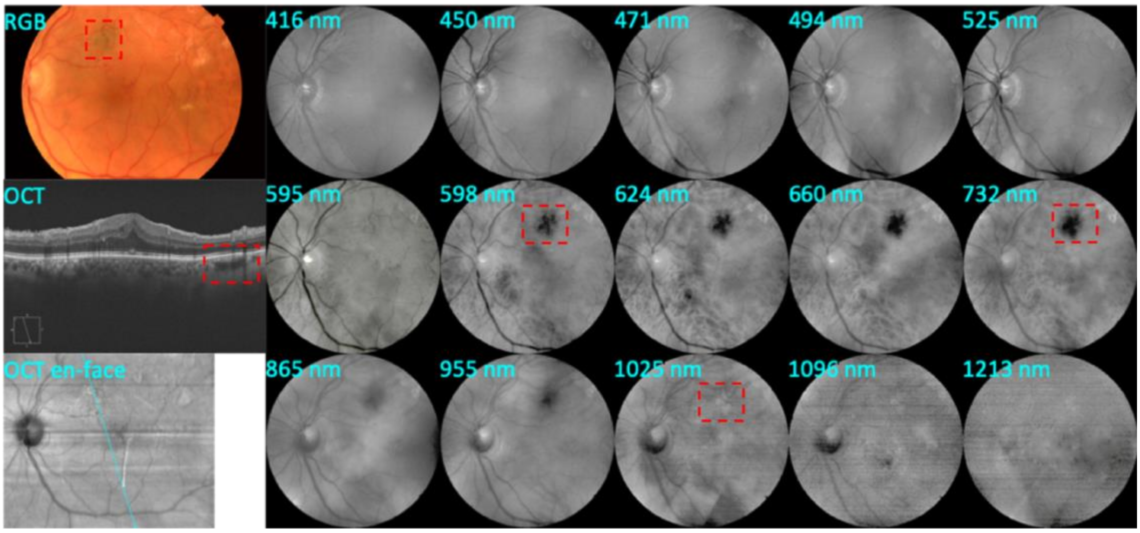

Figure 5.44: Eye with a choroidal tumor. Left panel from top to bottom: Color fundus image, OCT section and en-face image. Right: Complete spectral sequence obtained with the HSI fundus camera.

In the OCT image, taken at 850 nm approx., a black absorptive area can be seen in the deep choroid, confirming that the nevus affects the deepest layers of the fundus. The image taken at 865 nm confirms the absorptive behavior of the nevus but at longer wavelengths (above 1000 nm), the contrast changes to positive. In the clinical study, three eyes had choroidal nevi, which are shown in Figure 5.45. As can be noticed, all are well contrasted in the spectral region between 600 nm and 950 nm, especially at 732 nm. But in the NIR region, differences in visibility, contrast and texture are better revealed as light reaches the layers where the nevi are. In particular, Nevus #1 and #2 are brighter than the surrounding at long wavelengths while #3 keeps its dark color and contrast.

The spectral differences found among lesions are in line with differences in reflectivity of nevi reported by other authors (see section 2.3.2.3), [118]. In particular, in the article from Shields et al. [161], differences in nevi were related to differences in pigmentation. These authors concluded that pigmented choroidal nevus surrounded by a halo or circular band of depigmentation have a low possibility to turn in melanoma, while nevus without halo reach a value of 7%. The use of spectral images might help in discerning between benign and malignant nevi thanks to the increased information on the pigmentation state of the nevus, although the low number included in this study limits this analysis. Another interesting spectral feature that can be seen in Figure 5.45, is the different wavelength at which each nevus seems to have the highest contrast. Nevus #1 shows the highest negative contrast around 624 nm whereas nevus #2 and #3 at 732 nm. This difference is probably related with a different depth. This type of information, when contrasted with precise location with OCT records, might be another starting point for future characterization of choroidal tumors.

Additionally, a quantitative spectral analysis on these three nevi is presented below (Figure 5.46):

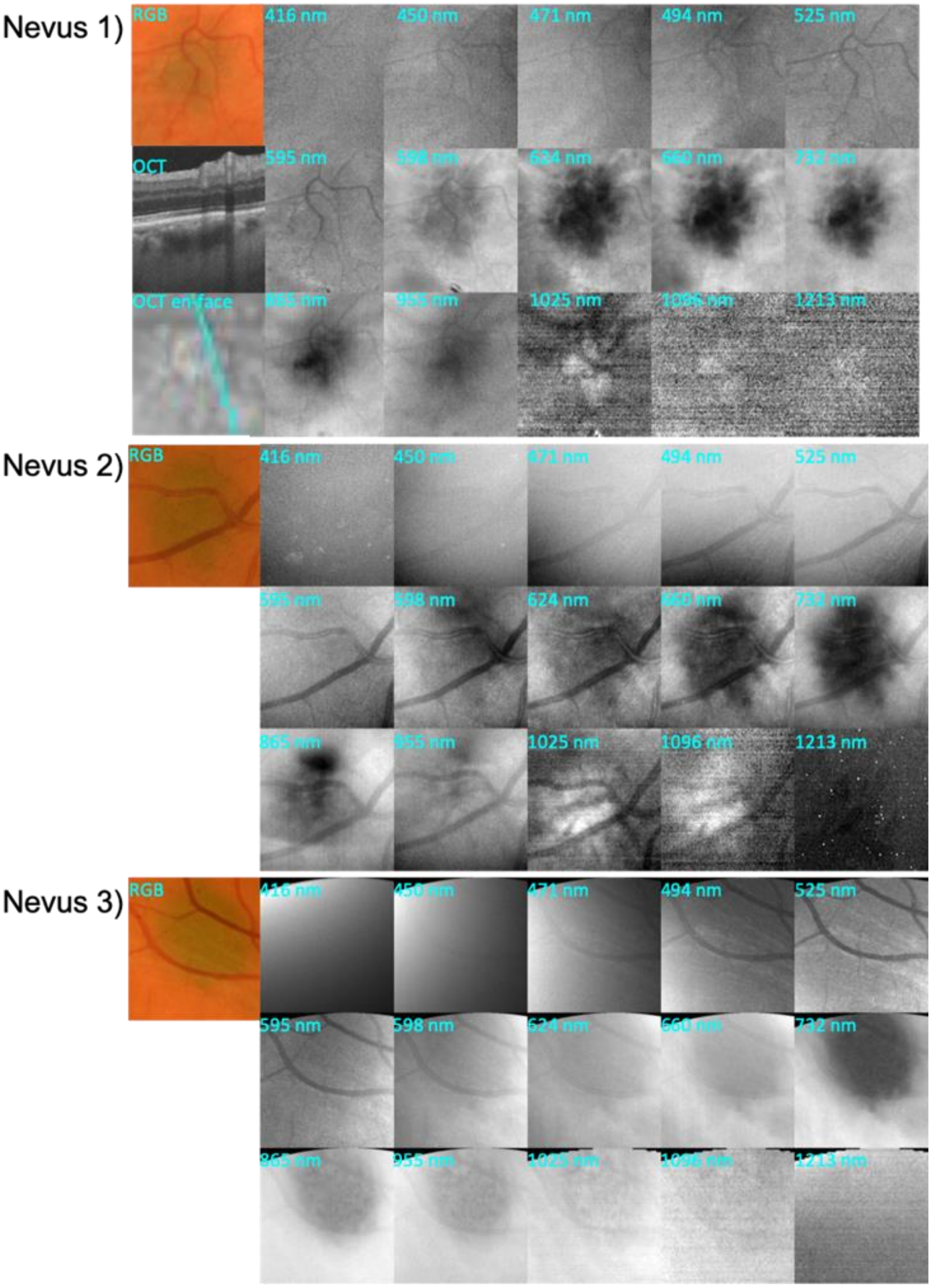

Figure 5.45: a) Zoomed ROIs centered on regions with choroidal tumors of three patients (Nevus # 1, 2 and 3). Left column: color fundus image, OCT section and en-face image (only available for patient a). Right columns: complete spectral sequence obtained with the HSI fundus camera.

There are differences among nevi in terms of spectral reflectivity (Figure 5.46 a). In fact, the three different lesions show notable differences of intensity at NIR wavelengths. This is also confirmed in the statistical analysis in Figure 5.46 b as the standard error is bigger at wavelengths above 950 nm. Values close to 1 at short wavelengths were expected as the nevi visibility is null or low because of the poor penetration of light.

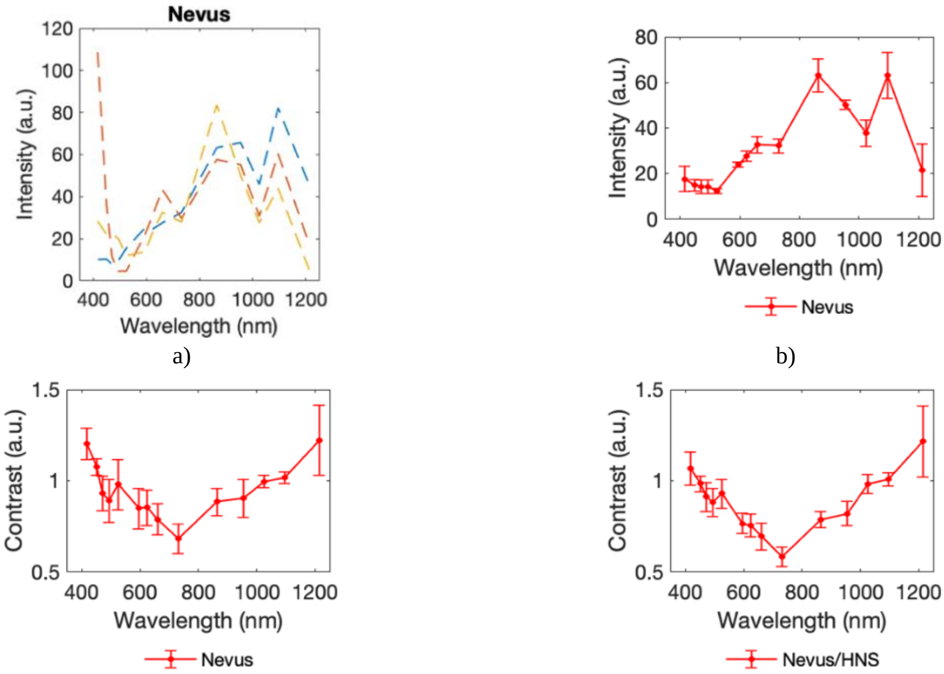

a) b)

c) d)

Figure 5.46: Spectral analysis of nevi performed on 3 eyes. a) Intensity curves calculated as the average of all sampled regions of the nevus in each eye. b) Mean intensity curve. c) GC contrast curve. d) LC contrast curve. In b) and c) the mean and standard error were calculated from 24 ROIs (8 ROIs of diameter 0.2° for each nevus) centered on different regions collected from the 3 lesions. In d) the mean and standard error were calculated from 17 ROIs (diameter 0.2°) centered on different nevus collected from all eyes. In this case, 4 ROIs of diameter 0.2° in the HNS of the lesion were collected, averaged and used to calculate LC. In a), one of the curves (Nevus #3) deviates considerably from the others at 400 nm, which is clearly a consequence of non-uniformities in the illumination as can be confirmed with the image shown in Figure 5.45. In fact, this nevus is located more peripherally than the others, and thus inhomogeneities are stronger.

The spectral curves resemble well the spectral behavior of common skin nevi, despite here they are also affected by the ocular media transmission and the fundus reflectance, [161]. In our study, choroidal nevi present stronger absorbance around 600 and 800 nm and then increased reflectance (intensity and contrast) at longer wavelengths, similarly to skin ones. In fact, few information about spectral features of choroidal nevi can be found in the literature, [162]. The differences reported in our study might offer complementary information to evaluate nevi features and their risk of turning into melanomas.

5.2.5 Photocoagulation

Another interesting case consisting of an eye that underwent photocoagulation therapy after thrombosis is shown in Figure 5.47.

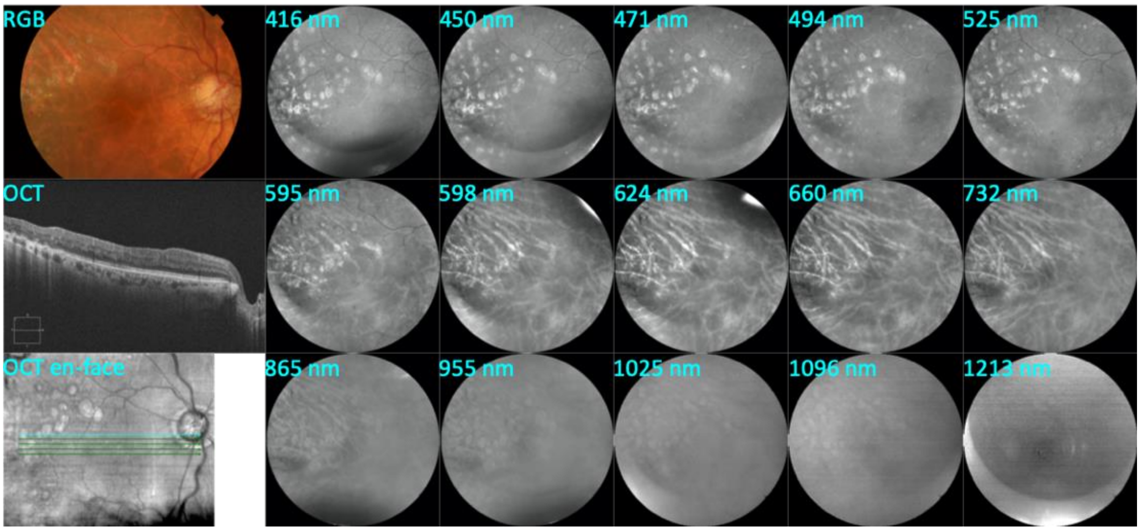

Figure 5.47: Eye undergoing photocoagulation due to thrombosis. Left panel from top to bottom: Color fundus image, OCT section and en-face image. Right: Complete spectral sequence obtained with the HSI fundus camera.

Photocoagulation was applied to avoid degeneration caused by a retinal vein thrombosis. In the color image, photocoagulated areas are not well contrasted, appearing as just slightly yellow regions. In the OCT records, these lesions are positively contrasted with respect to the surrounding and hyperreflective zones can be recognized at the interface between the choroid and the retina. In the spectral sequence, they are well contrasted over the entire spectral range, but especially at shorter wavelengths, as well as residuals of retinal hemorrhages. The fact that these lesions are observable at NIR wavelengths indicates that the RPE absorbance is reduced and, thus, that the scleral reflected signal is less attenuated. This might indicate that photocoagulation has an effect not only at the retinal but also at deeper layers, thus affecting the choroid. In order to highlight this, zoomed images of this eye are shown in Figure 5.48. The figure also includes a preliminary quantitative analysis carried out on some regions (photocoagulated areas and hemorrhages). The curves obtained are in line with the former findings in terms of absorption for damaged RPE and hemorrhages. As in the case of RPE atrophy, both the intensity and contrast curves of the photocoagulated areas are above the values of the HNS. The hemorrhages present higher absorbance and the characteristic minimum around 600 nm.

On the other hand, the LC curve shown in Figure 5.49 resembles that found for RPE atrophies, where a depigmentation is present. At short wavelengths, the curves are similar to those for soft drusen and autofluorescent lesions, caused by accumulation of lipofuscin. As described elsewhere [163], photocoagulation process takes to the production of autofluorescent substances, explaining the high levels of contrast at short wavelengths.

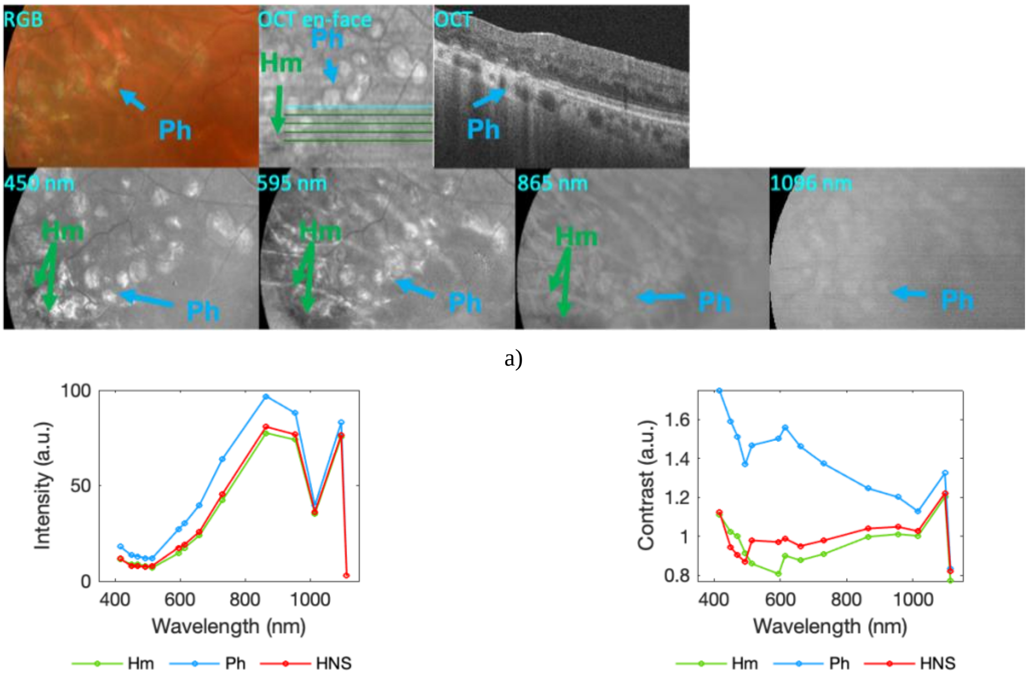

a)

b)

c)

Figure 5.48: Zoomed ROI centered on a region with several photocoagulated areas of the eye shown in Figure 5.47. Top row from left to right: color fundus image, OCT en-face image and section. Bottom row: selected spectral images acquired with the HSI fundus camera. b) Intensity curves and c) GC contrast curves of the areas indicated. Labels: Ph (Photocoagulation), Hm (Hemorrhage), HNS (Healthy Near Surroundings).

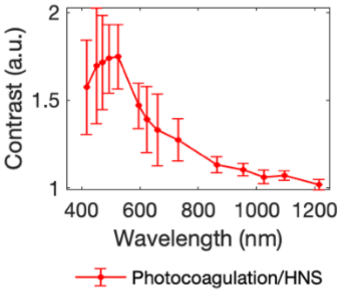

Figure 5.49: LC contrast curve computed on different photocoagulated areas over the FOV of the eye shown in Figure 5.47. The mean and standard error were calculated from 7 ROIs (diameter 0.1°) centered on different photocoagulated areas. In this case, 4 ROIs of diameter 0.1° in the HNS of the lesion were collected, averaged and used to calculate LC.

It is to be commented that during the clinical study other retinal lesions and diagnosis were found such as thrombosis, RAP, amblyopia, edema, diabetic retinopathy, and a macular hole. However, they are not analyzed here because the fundus images did not show any particular characteristic or their quality was too poor to carry out a proper analysis.

5.2.6 Summary

Finally, as for the healthy eyes, the averaged spectral curves of intensity and the GC for all the abnormal structures analyzed are presented in Figure 5.50. Additionally, zoomed curves in the NIR (from 800 nm to 1200 nm) are depicted in Figure 5.51. As a reference, the curve of the healthy background was appended to the plots, too.

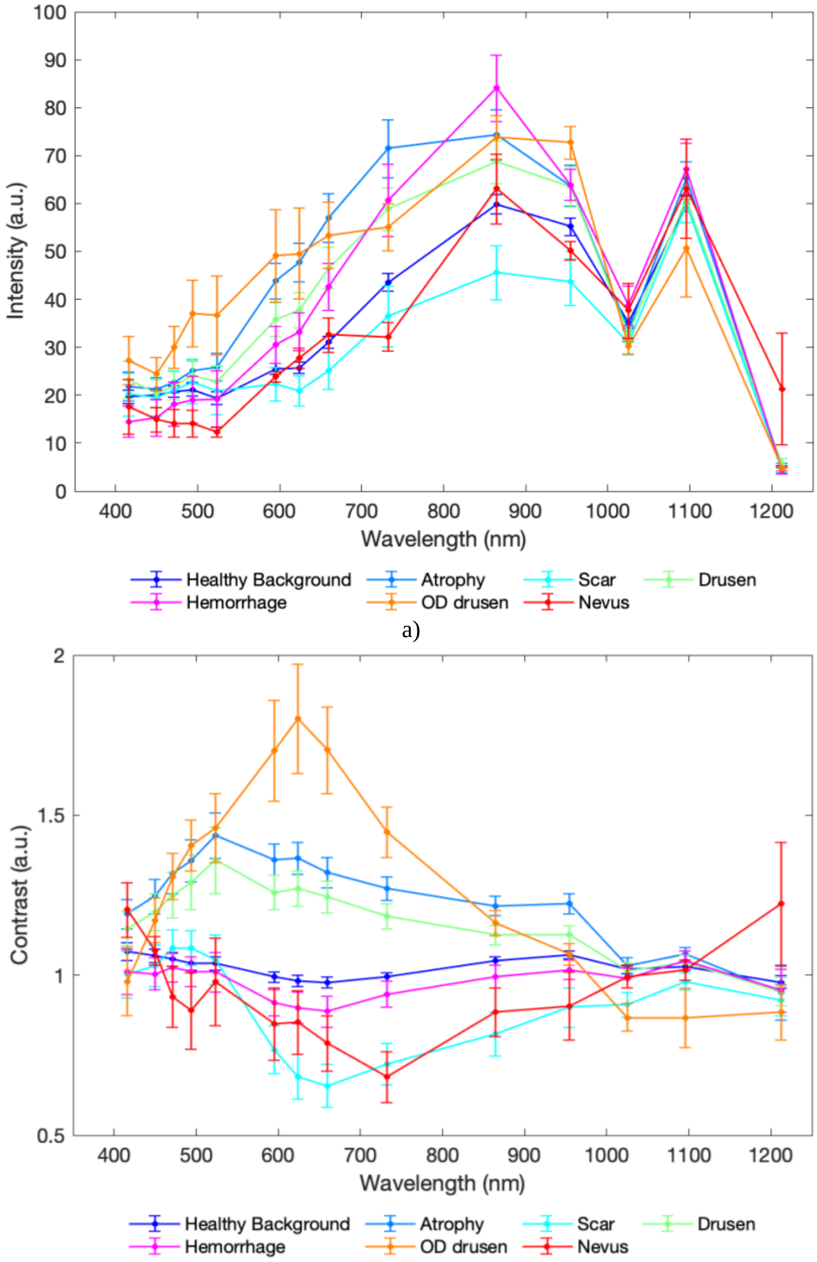

a)

b)

Figure 5.50: a) Averaged intensity curves and b) GC contrast curves from all fundus structures analyzed for diseased eyes.

As can be noticed, both the intensities and contrasts can be well differentiated among structures of different nature. In the case of RPE degeneration such as drusen, atrophy and optic disk drusen, the intensity levels are the highest and the contrasts are above the threshold of 1 over the entire spectral range.

In the case of atrophies and drusen, differences (with respect to the healthy background) are especially noticeable at short wavelengths, but also through all VIS range. In particular, higher values of intensity and contrast registered at short wavelengths (below 500 nm) correlate with the emission of fluorescent compounds associated to photoreceptors damage (e.g., lipofuscin). Additionally, some differences between drusen and atrophy can be noticed in the NIR. Atrophies show a positive contrast with respect to the surrounding tissue and higher values of intensity and contrast even at 1096 nm. As commented, atrophied regions are associated with complete RPE depigmentation and thus its power of absorbing light, being therefore the reflected light coming from the sclera higher than in the case of drusen, which still preserve some pigment (see Figure 5.36)

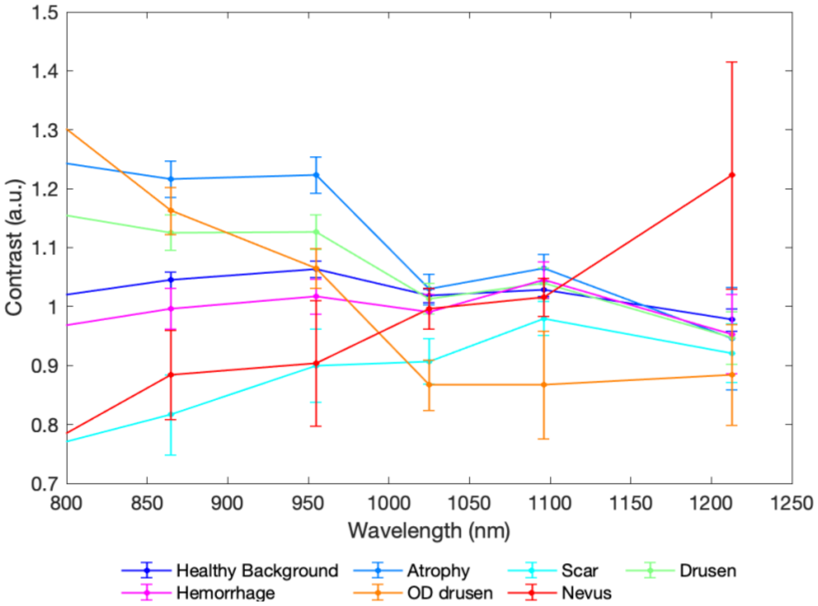

Figure 5.51: Zoom of Figure 5.50 b. in the NIR-IR range.

In the case of blood-related structures such as scars and hemorrhages, the overall absorptive behavior of hemoglobin is clear. Both scars and hemorrhages show a minimum of reflectance around 600 nm. In scars, the contrast remains well below 1 for all the spectral range whereas hemorrhages absorb less as the wavelength increases, and the contrast above 800 nm is near 1. Scars, due to the fibrotic and scattering nature of the coagulated blood, scatter more light than hemorrhages and thus, the back reflected light is low even at wavelengths beyond 900 nm.

The minimum contrast of nevi is recorded at the red-NIR wavelengths, as a consequence of the depth at which they are located in combination with their spectral absorption. As the wavelength increases, their GC values also increase, which might be related to the lesion etiology.

In the case of optic disk drusen, values of contrast well above 1 are registered up to 950 nm, firstly increasing and then decreasing. As already explained, drusen are more reflective than healthy tissue, probably because of autofluorescence, that takes place at wavelengths below 500 nm. Spectral images at longer wavelengths (above 700 nm), not exciting autofluorescence and collecting light from deeper layers, reveal the real extent of the lesions and can be helpful to better localize them.

Finally, spectral imaging in the NIR spectral range (above 700 nm) allows an easier differentiation of healthy/injured zones, especially caused by RPE dystrophies (atrophies, drusen, etc.).

6 CONCLUSIONS

This PhD project was carried out within the framework of the European Project BE-OPTICAL “Advanced BiomEdical OPTICAL Imaging and Data Analysis” (EU European Commission, Innovative Training Networks [ITN] call H2020-MSCA-ITN-2015) (2015-2019), which aimed to share and improve knowledge of imaging technologies and data analysis for biomedical applications.

In particular, the goal of this thesis was to build a novel hyperspectral fundus camera allowing for the fast imaging of the retina in the visible and in the near infrared regions of the spectrum through a considerable number of spectral bands. Accordingly, a fundus camera with sensitivity from 400 nm to 1300 nm and 15 spectral bands was developed. Such system had never been conceived before and new methods to perform imaging in such a broad spectral range and useful for outcomes analysis, especially between 700 nm and 1300 nm, were built (including both hardware and software).

The prototype was carefully designed, implemented and tested in the laboratory. Then, the system was extensively characterized, taking as reference applicable international ISO standards. Later, it was submitted to the evaluation of an ethical committee. After the approval, the system was used in a clinical environment to acquire hyperspectral image sequences of healthy and diseased retinas. Finally, the analysis of the acquired data was carried out both qualitatively and quantitatively.

The specific achievements of this thesis as well as the most relevant conclusions obtained are outlined in more detail below.

1. Design of the hyperspectral fundus camera.

    a) Starting from the literature and using only commercial optical elements, the design of the hyperspectral fundus camera was achieved by means of optical simulations using Zemax software (Radiant Zemax, USA). In particular, a non-mydriatic retinograph with two optically independent paths, one for the illumination and one for the detection, was used. The selected illumination was based on a standard Maxwellian illumination, using LEDs. The detection optical path is composed by two optical arms: one to cover the spectral range from 400 nm to 950 nm (VIS-NIR arm) and another to cover the spectral range from 950 nm to 1300 nm (NIR-IR arm). Each detection arm used a different camera sensor: a CMOS and an InGaAs for the VIS-NIR and NIR-IR, respectively. The detection pupil diameter was 1.75 mm. The compensation of chromatic aberrations and field curvature was critical in the design.

    The designed detection system grants:

    - A Field Of View (FOV) of 30°.
    - Optical resolution better than 76.9 lp/mm and 25 lp/mm (limits imposed by the sensors) for the VIS-NIR and the NIR-IR detection arms, respectively.
    - Good optical quality (Strehl ratio > 0.8) within 24° FOV, except for wavelengths below 450 nm.

- Low image distortion at the full FOV with a maximum of -1.45% and -1.92% for the VIS-NIR and NIR-IR arms, respectively.

The designed illumination system uses custom-made rings of LEDs. Each ring includes LEDs with different wavelengths welded in a symmetrical configuration to provide a homogeneous illumination. In particular, 3 LED rings with 15 wavelengths (channels) comprised between 400 nm and 1300 nm, were combined. For each spectral band, at least 2 identical LEDs were placed symmetrically on the ring. This cost-effective configuration grants at least the 1% of light collection efficiency (from the source to the retina).

b) Non-sequential simulations of the system were carried out in order to test its performance as a whole, ensuring the elimination of cornea, crystalline and objective lens back reflections.

2. Implementation of the hyperspectral fundus camera system.

a) The hyperspectral fundus camera was implemented in accordance with the design. The system makes only use of commercial optical components, custom and commercial opto-mechanics and a custom holed mirror to join the illumination and detection optical paths, ensuring geometrical pupil separation. A fixation target was coupled to the illumination optical path ensuring the proper alignment between the patient's eye and the system during the measure.

b) A tailored hardware was implemented to orchestrate the synchronization between illumination and image acquisition during the tests. In particular, thanks to a custom electronic principal board, the computer, the LEDs and the two cameras were triggered by programmed synchronized voltage signals. The computer was especially designed by Hamamatsu to be used with two cameras at their maximum frame rates simultaneously. The electronic principal board was developed internally.

c) A user-friendly control software was built in MATLAB to control each unit of the system. It allows controlling single LEDs or to program illumination and acquisition of spectral sequences.

3. System characterization.

a) An exhaustive optical characterization was carried out following the guidelines given by the ISO 10940:2009 "Ophthalmic instruments — Fundus cameras". The ISO describes the requirements of both the illumination and the detection systems of fundus cameras.

Listed below are the measured optical characteristics of the implemented system:

- FOV: 30.4° and 31.1° for the VIS-NIR and the NIR-IR spectral ranges, respectively.
- Pixel side length (retinal plane): 5.4 μm and 23 μm for the CMOS and the InGaAs sensors, respectively.

- Lateral resolutions above the limits established by the standard for both center and periphery.

b) A full radiometric characterization was carried out to guarantee the safeness of the systems in regards of light hazard, following the guidelines of ISO 15004-2:2007 “Ophthalmic instruments -- Fundamental requirements and test methods -- Part 2: Light hazard protection”. From this analysis, the instrument was classified as group 1 (non-hazardous) in both the fixation and measure phases.

c) An analysis of short- and mid-term repeatability was carried out to ensure the stability of the system. The percentage of variation for each channel was lower than 3%.

4. Clinical study, image processing and spectral analysis.

a) The system was validated through clinical studies conducted at the Instituto de Microcirugía Ocular (IMO) in Barcelona (Spain), under the supervision of an ophthalmologist (C.M), and the University Vision Center (CUV) of the Universitat Politècnica de Catalunya (UPC) in Terrassa (Spain). Accordingly, the ethical committee approval was obtained.

b) In both studies an exhaustive sample of image sequences was acquired from healthy (36 patients, 72 eyes) and diseased (100 patients, 200 eyes) subjects. Due to eye misalignment and critical system positioning, the final sample analyzed was reduced to61 healthy and 60 diseased eyes.

c) Image processing tools were developed with MATLAB. They permit to remove illumination and sensor inhomogeneities, residual back reflections and artifacts, and to compensate for the spectral response of the system, essential to convert digital levels into spectral intensity or reflectivity values.

d) Spectral analysis tools were developed and used to compute the intensity levels from all acquired images. The software allows the registration and remapping of images acquired by the two sensors. During data collection, a complete data archive was generated, including all spectral intensity values, the image coordinates and the ROIs of all analyzed retinal regions, which are labeled and organized for future studies.

e) As the obtained intensity values also include the transmission of the preceding ocular media (cornea, lens, aqueous humor and vitreous) for each individual, besides the reflectance of the retina itself, global and local contrast analysis were also carried out rather than only using intensity values; the first is computed referencing intensity values to that obtained over the entire FOV of the eye under analysis while in the second, a local quantification is carried out to compare two different structures near to each other. In the analysis of diseased eyes, the ratio between two intensity curves (specific contrast) that correspond to two far and different structures on the same eye is sometimes also used, in order to compare their spectroscopic features.

5. Results.

a) A qualitative and quantitative spectral analysis was carried out for the healthy and diseased eyes.

b) We observed that all intensity curves were dominated by the water-like transmission of the ocular media preceding the fundus. Different subjects show shifted or scaled intensity values due to the differences in their ocular transmittance. Consequently, an analysis based on contrasts was judged as more appropriate to mitigate disparities among patients, as previously reported, despite the fact of reducing illumination inhomogeneities.

c) The developed system permitted to highlight different fundus structures depending on the used wavelength: shorter wavelengths permit to contrast superficial layers of the retina (nerve fibers, retinal arteries and veins, pigments, etc..), while longer ones, thanks to the increased penetration capability of NIR-IR light, give access to the deepest layers of the ocular fundus (retinal pigment epithelium (RPE), choroid, sclera, etc..).

Remarkable observations and conclusions based on records of healthy eyes are outlined below.

- The nerve fibers are better observed at shorter wavelengths (400 nm to 500 nm), showing a monotone overall decrease in terms of contrast as a function of the wavelength.
- Subjects with different pigmentation show differences in the reflectance/absorbance of the ocular fundus. Higher melanin concentrations lead to reduced or null visibility of the choroid and its vasculature in the VIS-NIR range. In the IR, the choroidal vasculature of all subjects is negatively contrasted with respect to the background (the crossing point from positive (>1) to negative (<1) contrast takes place between 950 nm and 1000 nm). We concluded that, as the melanin absorbs progressively less as the wavelength increases, above 950 nm the sclera reflects most of light causing this contrast shift.
- Retinal arteries (oxygenated blood) and veins (de-oxygenated blood) show different spectral response through the spectral range with a peak of absorption (minimum in reflected intensity) around 525 nm, thus correlating with hemoglobin peaks.
- A maximum absorption was observed between 500 nm and 600 nm in the spectral curves of the fovea. This was assumed to be related with the spectral characteristics of macular pigments and capillaries, whose concentration in the fovea is higher.
- The optic disk is the brightest structure of the ocular fundus up to 955 nm. Above this wavelength, a change of contrast from positive to negative was observed. It was inferred that this is due to the optic disk morphology (optic disk pit) at deep layers since IR light is not reflected as in the other parts of the retina where the sclera is homogeneous.
- In the IR range, besides small differences among the choroidal vasculature, the background and the optic disk, no substantial differences were found between

other structures of the retina. Above 1000 nm, the ocular fundus appears as a homogeneous carpet, dominated by the reflectance of the sclera.

d) The system had a good performance when analyzing abnormal structures and lesions of diseased ocular fundus. The system was able to better contour some of them and give a superior contrast at specific channels. Remarkable examples of this are scars, atrophies, macular dystrophies, soft and hard drusen, optic disk drusen, hemorrhages and nevi. Although in most of the analyzed pathologies, further studies are necessary to corroborate the clinical findings of this work, the spectral quantitative and qualitative analysis on diseased eyes definitely gives new insights, opening possibilities for the study, diagnosis and prognosis of ocular disorders. In particular, the spectral outcomes allow obtaining information on the chemical characterization and location of structures, sometimes allowing for a better differentiation between substances that show the same color in traditional fundus cameras (e.g., soft and hard drusen). It also allows the observation of damaged tissue beyond the RPE, giving access to choroidal tumors, scars and hemorrhages, among others.

A list of conclusions drawn from the qualitative and quantitative analysis of diseased eyes is reported here.

- The system shows particular usefulness for the observation of lesions that affect the RPE or deeper layers, especially of interest in diseases like ARMD, eyes with drusen and other macular dystrophies. It is known that some of these are linked to the leakage of autofluorescent compounds (e.g., lipofuscin) and, accordingly, higher intensity values at short wavelengths are recorded due to fluorescence excitation. Other lesions of the RPE do not show fluorescent emission but higher levels of intensity in the NIR-IR spectral range. In these cases, it was concluded that the local degeneration of RPE cells diminishes the melanin concentration, thus decreasing absorption, leaving the sclera more exposed. Examples of the first kind are soft drusen that can aggregate and evolve in large atrophied regions. The second kind of behavior was observed in atrophies and hard drusen (less dangerous).
  These conclusions were confirmed with OCT and autofluorescence records. Color retinography in many of these cases fails in contrasting some of these lesions due to metamerism. Therefore, besides helping in distinguishing among lesions, the analysis of this spectral information over time might be used for a predictive analysis of RPE evolution and disease prognosis.
- Scars and hemorrhages show the spectral fingerprint of blood in the VIS, with a minimum contrast within 500 nm and 600 nm. At NIR wavelengths, hemorrhages are almost transparent (low absorption) while scars are better contrasted and contoured with respect to the surrounding than in common RGB. This might be because of the depth at which the blood lays, being the scars located near the RPE interface.
- Optic disk drusen show strong differences along the spectral bands of the system. In the autofluorescence image, drusen seem to be clustered and present high values of intensity with blurred contours; RGB retinography fails in contrasting them. In the OCT image, drusen can be recognized at different depths of the nerve, but they generate a shadow that obscure all layers behind. In the

hyperspectral sequence: at short wavelengths the drusen are blurry, clustered and the signal is higher than the optic disk surrounding (due to autofluorescence emission); from 500 nm to 660 nm the drusen contrast is low and they can be hardly recognized; in the NIR-IR range (well above autofluorescence excitation), many isolated drusen can be distinguished as hyperreflective regions inside the disk. The deeper penetration capability of light and the reflectivity of these structures above 732 nm give superior contrast and definition to these lesions.

- Only three eyes affected by glaucoma were included in the study so that no conclusion could be drawn. However, differences in spectral response and appearance between glaucomatous and healthy eyes were reported. In particular, we observed extended hyperreflective optic disk cups (with respect to healthy ones) through the entire spectral range, in line with the cup-to-disk ratio analysis performed to diagnose and follow up of glaucoma with OCTs. We assumed these differences to be related with the erosion of the superficial NF layer and the increased exposure of the lamina cribrosa (reached with IR light).
- Three nevi were included in the analysis. The three had different overall spectral behaviors and appearances, especially in the IR. This could be related with different etiologies and locations, and might help in the evaluation of the risk for them to evolve into melanomas; nevertheless, the limited number of samples is judged to be a bias and thus, no conclusions can be drawn.
- Images acquired of an eye undergoing photocoagulation were also reported. According to literature, the contrast analysis shows high levels of photocoagulated areas at short wavelengths, which can be attributed to autofluorescent emission of the photodamaged retina. In addition, contrasts above 1 and well distinguishable lesions can be observed in longest wavelength NIR images. This suggest that a damage at the level of the RPE is present, leading to a decrease of absorption, as in atrophies and drusen.

7 FUTURE WORK

In this chapter, possible new research lines and system improvements are suggested for future work related with this thesis.

1. Hyperspectral system improvements.

   a) A single lens custom objective would reduce considerably the back reflections compared to the current achromatic doublet-based approach. However, it would require the design of a complex detection system to compensate for the aberrations (especially the chromatic component in such a broadband instrument).
   b) Using a continuous illumination ring instead of discontinuous LEDs would reduce illumination inhomogeneities on the fundus image. Nevertheless, this solution is not recommended unless (a) is accomplished due to the back reflections removal complexity it would imply.
   c) The next generation of the hyperspectral fundus camera should include an alignment platform that permits to move and rotate the entire system independently to the patient's fixation, as in commercial systems. This would considerably increase the quality of the acquired images and avoid misalignment errors.
   d) A Hartmann (Scheiner) mask, inserted after the refraction compensation module, would increase the focusing precision of the system, allowing for fine adjustments while the operator is acquiring the hyperspectral sequence.
   e) An electro-mechanical translational stage would avoid to manually correct for patient's refraction and could work together with an autofocus algorithm.
   f) An adaptive optical system coupled with a zoom would improve image quality (correcting for patient's astigmatism and higher order aberrations). Moreover, it would allow investigating specific regions of the FOV in detail.
   g) Selective-wavelength filters could be inserted in the VIS-NIR detection path. This would allow the acquisition and reconstruction of autofluorescent spectra for a quantitative estimation of the amount of fluorescence in damaged retinal areas.

2. Further analysis using the available data archive.

   a) In cases where a large data sample is available (e.g., healthy structures, RPE atrophies, drusen, etc.) as well as diagnostic information, the ROIs and the labels of the data archive could be used to train machine learning algorithms to recognize and associate different lesions with specific diseases.
   b) Using the spectral information, a segmentation algorithm for specific regions could be developed. For example, retinal and choroidal vasculature could be independently segmented using VIS-NIR and NIR-IR spectral range, respectively.
   c) After a careful revision of the literature on spectral models of ocular media and retina, spectra of substances such as melanin, macular pigments or hemoglobin could be isolated to provide absolute reflectance information and increase the clinical capability of the system. For instance, a robust estimation of the state of the RPE degeneration could be assessed using isolated spectral information of melanin.

3. Future studies and novel research lines using the developed hyperspectral system.

   a) The system has shown to add remarkable information to standard diagnostic methods. Specific clinical studies should be carried out to extend and corroborate the use of such broadband technology to image the retina.

      Below a list of some possible further investigations is presented.

      - Further cases of dry and wet ARMD could be acquired in order to discriminate them using spectral information.
      - The differentiation between hard and soft drusen could be reinforced and the risk of soft drusen evolution could be assessed from their spectra.
      - Correlating autofluorescence emission intensities with spectra from healthy and diseased retinal regions could take to a robust prediction of RPE degeneration.
      - Dystrophies of the macula could be automatically classified using spectral information, rather than shapes.
      - Extending the study on glaucoma, morphological and spectral hints of its state and evolution could be found using the enhanced penetration depth of IR wavelengths.
      - A broader spectral study of optics disk drusen in the NIR-IR spectral region could be carried out. This would be interesting especially in young subjects where the optic disk drusen are buried in the nerve, being difficult to image them with conventional instrumentation.
      - Oximetry studies could be done for the retinal and choroidal vasculature using the entire spectral range and a proper calibration/model. In particular, the results of this thesis suggest that an estimation of choroidal and retinal oxygenation in blood vessels could be possible in the NIR-IR. This study could give, for the first time, a live video monitoring of the oxygenation of the ocular fundus without using mydriatic drugs or high visible light radiation (which disturb the patient and bleach photoreceptors).
      - Extending the study on choroidal tumors, subjects with melanomas should be included. NIR-IR light is very promising in giving new information on tumors evolution and prognosis.

   b) Sequences of spectral images of subjects affected by other retinal and choroidal disorders, not present in our study, should be acquired to further investigate the applicability of the system. Examples are diabetic retinopathy, RAP, retinitis pigmentosa, retinoblastoma, etc.

8 PUBLICATIONS AND CONFERENCE PRESENTATIONS

Journal articles

- 2019. Alterini, T., Diaz, F., Burgos-Fernandez F.J., Gonzalez L., Mateo C., Vilaseca, M., “Fast visible and extended near-infrared multispectral fundus camera”, Journal of Biomedical Optics 24(9):1-7.

Conference presentations

International conferences

- 2019. Alterini, T., Diaz, F., Vilaseca, M., “Hyperspectral eye fundus imaging with extended spectral range towards the near infrared”, European Conferences on Biomedical Optics, Munich (Germany), 23-27 June, Proceedings of SPIE-OSA, SPIE Vol. 11073, pages. 110730Y-1-5 (Oral presentation).

- 2019. Alterini, T., Diaz, F., Vilaseca, M., “Spectral analysis of the retina and the choroid in the visible and near infrared: preliminary results of a clinical study”, New trends in biomedical imaging and data analysis, Be-Optical Final conference, Göttingen (Germany), 3-4 July, Book of abstracts, 19-20 (Oral presentation).

- 2019. Alterini, T., Diaz, F., Vilaseca, M., “Fast visible and near-infrared extended hyperspectral fundus camera”, 4th Be-Optical Workshop, Berlin (Germany), 11-12 March (Oral presentation).

- 2018. Alterini, T., Diaz, F., Vilaseca, M., “One-shot hyperspectral fundus camera with visible and infrared image sensors”, International Conference on Fluorescence Super-Resolution Microscopy, Spectroscopy, Molecular Cell Mechanics and Theoretical Neurophysics (Biophysics by the sea), Alcudia (Spain), 7-12 October, Book of abstracts (Oral presentation).

- 2018. Alterini, T., Diaz, F., Vilaseca, M., “Hyperspectral fundus camera with sensibility beyond the visible range: a pilot study”, The Association for research in Vision and Ophthalmology Annual Meeting, Honolulu (Hawaii, USA), 29 April - 3 May, Book of abstracts (Poster presentation).

- 2018. Alterini, T., Diaz, F., Vilaseca, M., “Custom made LED-based system for extended hyperspectral retinal imaging”, International Conference on BioMedical Photonics (ICBP 2018), 2nd Be-Optical Workshop, La Grande-Motte, Montpellier (France), 18-19 March, Book of abstracts, pag.103 (Oral Presentation).

National conferences

- 2019. Alterini, T., Diaz, F., Burgos-Fernández F. J., Vilaseca, M., “Medidas hiperespectrales de fondo de ojo: una nueva herramienta para el diagnóstico oftalmológico”, XII Congreso Nacional de Color (CNC 2019), Actas del congreso, pags. 161-164.

- 2018. Alterini, T., Diaz, F., Vilaseca, M., “Retinógrafo hiperespectral basado en LEDs para la obtención de imágenes de fondo de ojo en el visible e infrarrojo”, XII Reunión Nacional de Óptica, Castellón (Spain), Libro de resúmenes, pag. 127.

Awards

- SPIE 2018 Student Prize received at the XII Reunión Nacional de Óptica held in Castellón and granted by the SPIE (The International Society for Optics and Photonics). The work presented was entitled "Hyperspectral retinoscope based on LEDs for obtaining fundus images in the visible and infrared" and was authored by: Tommaso Alterini, Fernando Díaz Doutón and Meritxell Vilaseca.

9 BIBLIOGRAPHY

[1] M. Kaschke, K. H. Donnerhacke, and M. S. Rill, *Optical Devices in Ophthalmology and Optometry: Technology, Design Principles and Clinical Applications*, 1st ed. WILEY-VCHVerlag GmbH, 2014.

[2] D. J. Creel, "Visual and Auditory Anomalies Associated with Albinism," in *The Organization of the Retina and Visual System*, Helga Kolb. Ralph Nelso. Eduardo Fernandez. Bryan William Jones., Ed. Webdivision, 2014, pp. 193–200.

[3] D. M. W. D. J. Brenguier, *Airborne Measurements for Environmental Research: Methods and Instruments*, 1st ed. Wiley-VCH Verlag GmbH & Co. KGa, 2013.

[4] M. E. Martin *et al.*, "Development of an advanced Hyperspectral Imaging (HSI) system with applications for cancer detection," *Ann. Biomed. Eng.*, vol. 34, no. 6, pp. 1061–1068, 2006.

[5] D. Lorente, N. Aleixos, J. Gómez-Sanchis, S. Cubero, O. L. García-Navarrete, and J. Blasco, "Recent Advances and Applications of Hyperspectral Imaging for Fruit and Vegetable Quality Assessment," *Food Bioprocess Technol.*, vol. 5, no. 4, pp. 1121–1142, 2012.

[6] A. A. Gowen, C. P. O'Donnell, P. J. Cullen, G. Downey, and J. M. Frias, "Hyperspectral imaging - an emerging process analytical tool for food quality and safety control," *Trends Food Sci. Technol.*, vol. 18, no. 12, pp. 590–598, 2007.

[7] M. Govender, K. Chetty, and H. Bulcock, "A review of hyperspectral remote sensing and its application in vegetation and water resource studies," *Water SA*, vol. 33, no. 2, pp. 145–151, 2007.

[8] C. Fischer and I. Kakoulli, "Multispectral and hyperspectral imaging technologies in conservation: current research and potential applications," *Rev. Conserv.*, vol. 7, no. 7, pp. 3–16, 2006.

[9] G. Elmasry, D. W. Sun, and P. Allen, "Near-infrared hyperspectral imaging for predicting colour, pH and tenderness of fresh beef," *J. Food Eng.*, vol. 110, no. 1, pp. 127–140, 2012.

[10] F. J. Burgos-Fernández, M. Vilaseca, E. Perales, J. A. Herrera-Ramírez, F. M. Martínez-Verdú, and J. Pujol, "Spectrally tunable light source based on light-emitting diodes for custom lighting solutions," *Opt. Appl.*, vol. 46, no. 1, pp. 117–129, 2016.

[11] G. Lu and B. Fei, "Medical hyperspectral imaging: a review," *J. Biomed. Opt.*, vol. 19, no. 1, p. 23, 2014.

[12] L. Gao, R. T. Smith, and T. S. Tkaczyk, "Snapshot hyperspectral retinal camera with the Image Mapping Spectrometer (IMS)," *Biomed. Opt. Express*, vol. 3, no. 1, p. 48, 2012.

[13] V. Nourrit *et al.*, "High-resolution hyperspectral imaging of the retina with a modified fundus camera," *J. Fr. Ophtalmol.*, vol. 33, no. 10, pp. 686–692, 2010.

[14] N. L. Everdell, I. B. Styles, A. Calcagni, J. Gibson, J. Hebden, and E. Claridge, "Multispectral

imaging of the ocular fundus using light emitting diode illumination," *Rev. Sci. Instrum.*, vol. 81, no. 9, pp. 1–9, 2010.

[15] Y. Xu, X. Liu, L. Cheng, L. Su, and X. Xu, "A light-emitting diode (LED)-based multispectral imaging system in evaluating retinal vein occlusion," *Lasers Surg. Med.*, vol. 47, no. 7, pp. 549–558, 2015.

[16] H2020-EU.1.3.1 funding from the European Union's Horizon 2020 Programme for research technological development and demonstration under grant agreement no. 675512, "Be-Optical, Advanced BiomEdical OPTICAL Imaging and Data Analysis,." [Online]. Available: http://beoptical.eu/. [Accessed: 09-Jan-2021].

[17] J. Y. Hardeberg, *Acquisition and Reproduction of Color Images: Colorimetric and Multispectral Approaches*, 1st ed. Dissertation.com, 2002.

[18] W. A. Thornton, "How Strong Metamerism Disturbs Color Spaces," *Color Res. Appl.*, vol. 23, no. 6, pp. 402–407, 1998.

[19] M. Born and E. Wolf, *Principles of optics*, 7th ed. Cambridge Univesity Press, 2003.

[20] J. Mertz, *Introduction to Optical Microscopy*, 1st ed. Roberts and Co Publishers, 2010.

[21] V. Tuchin, *Tissue optics : light scattering methods and instruments for medical diagnosis*, 3rd ed. SPIE, 2015.

[22] B. H. Bransden and C. J. Joachain, *Physics of Atoms and Molecules*, 2nd ed. Longman scientific & Technical, 2003.

[23] F. Nicodemus, J. Richmond, and J. Hsia, *Geometrical considerations and nomenclature for reflectance*, vol. 60, no. October. National Bureau of Standards, 1977.

[24] Hecht E., *Optics*, 4th ed. Addison Wesley, 2002.

[25] G. Zonios, J. Bykowski, and N. Kollias, "Skin melanin, hemoglobin, and light scattering properties can be quantitatively assessed in vivo using diffuse reflectance spectroscopy," *J. Invest. Dermatol.*, vol. 117, no. 6, pp. 1452–1457, 2001.

[26] X. Delpueyo *et al.*, "Hyperspectral Imaging System for the Detection of Skin handheld," in *Color and Image AIC2015 TOKIO*, 2015, pp. 385–390.

[27] N. Hagen and M. W. Kudenov, "Review of snapshot spectral imaging technologies," *Opt. Eng.*, vol. 52, no. 9, pp. 900–901, 2013.

[28] P. Mishra, M. S. M. Asaari, A. Herrero-Langreo, S. Lohumi, B. Diezma, and P. Scheunders, "Close range hyperspectral imaging of plants: A review," *Biosyst. Eng.*, vol. 164, pp. 49–67, 2017.

[29] Q. Li, X. He, Y. Wang, H. Liu, D. Xu, and F. Guo, "Review of spectral imaging technology in biomedical engineering: achievements and challenges," *J Biomed Opt*, vol. 18, no. 10, p. 100901, 2013.

[30] H. R. Morris and C. C. Hoyt, "Imaging Spectrometers for Fluorescence and Raman Microscopy :

Acousto-Optics and Liquid Crystal Tunable Filters," *Appl. Spectrosc.*, vol. 48, no. 7, p. 847, 1994.

[31] C. Palmer, "Types of Diffraction Gratings," *Spectroscopy*, vol. 10, pp. 14–15, 1995.

[32] M. C. T. Bahaa E. A. Saleh, *Fundamentals of Photonics*, Wiley-Inte. Wiley Series in Pure and Applied Optics, 2007.

[33] Hamamatsu Photonics, "Hamamatsu cameras," *Hamamatsu*. [Online]. Available: http://www.hamamatsu.com/eu/en/product/category/5000/5005/index.html. [Accessed: 01-Sep-2016].

[34] D. Wu and D.-W. Sun, "Advanced applications of hyperspectral imaging technology for food quality and safety analysis and assessment: A review — Part II: Applications," *Innov. Food Sci. Emerg. Technol.*, vol. 19, pp. 15–28, 2013.

[35] C. Yu *et al.*, "Quantitative spectroscopic imaging for non-invasive early cancer detection," *Opt Express*, vol. 16, no. 20, pp. 16227–16239, 2008.

[36] P. Constantinou, T. Nicklee, D. W. Hedley, S. Damaskinos, and B. C. Wilson, "A high-resolution MACROscope with differential phase contrast, transmitted light, confocal fluorescence, and hyperspectral capabilities for large-area tissue imaging," *IEEE J. Sel. Top. Quantum Electron.*, vol. 11, no. 4, pp. 766–777, 2005.

[37] M. B. Sinclair, D. M. Haaland, J. A. Timlin, and H. D. T. Jones, "Hyperspectral confocal microscope," *Appl. Opt.*, vol. 45, no. 24, pp. 6283–6291, 2006.

[38] P. De Beule, "Rapid Hyperspectral Fluorescence Lifetime Imaging," *Microsc. Res. Tech.*, vol. 70, no. 3, pp. 481–484, 2007.

[39] M. Vilaseca *et al.*, "Characterization of the human iris spectral reflectance with a multispectral imaging system.," *Appl. Opt.*, vol. 47, no. 30, pp. 5622–30, 2008.

[40] M. B. Bouchard, B. R. Chen, S. a Burgess, and E. M. C. Hillman, "Ultra-fast multispectral optical imaging of cortical oxygenation, blood flow, and intracellular calcium dynamics.," *Opt. Express*, vol. 17, no. 18, pp. 15670–15678, 2009.

[41] L. Gao, R. T. Kester, N. Hagen, and T. S. Tkaczyk, "Snapshot Image Mapping Spectrometer (IMS) with high sampling density for hyperspectral microscopy," *Opt. Express*, vol. 18, no. 14, p. 14330, 2010.

[42] L. Gao, R. T. Kester, and T. S. Tkaczyk, "Compact Image Slicing Spectrometer (ISS) for hyperspectral fluorescence microscopy," *Opt. Express*, vol. 17, no. 15, pp. 12293–12308, 2009.

[43] N. Hagen, T. R. Kester, G. Liang, and T. S. Tkaczyk, "Snapshot advantage: a review of the light collection improvement for parallel high-dimensional measurement systems," *Opt. Eng.*, vol. 51, no. 11, p. 111702, 2012.

[44] A. Wagadarikar, R. John, R. Willett, and D. Brady, "Single disperser design for coded aperture snapshot spectral imaging," *Appl. Opt.*, vol. 47, pp. B44–B51, 2008.

[45] L. Gao, N. Bedard, N. Hagen, R. T. Kester, and T. S. Tkaczyk, "Depth-resolved image mapping

spectrometer (IMS) with structured illumination," *Opt. Express*, vol. 19, no. 18, pp. 17439–17452, 2011.

[46] R. Shrestha and J. Y. Hardeberg, "Multispectral imaging using LED illumination and an RGB camera," in *21st Color and Imaging Conference Final Program and Proceedings*, 2013, pp. 8–13.

[47] S. A. Mathews, "Design and fabrication of a low-cost, multispectral imaging system," *Appl. Opt.*, vol. 47, no. 28, pp. F71–F76, 2008.

[48] A. Basiri *et al.*, "Use of a multi-spectral camera in the characterization of skin wounds," *Opt. Express*, vol. 18, no. 4, pp. 3244–3257, 2010.

[49] E. DeHoog and J. Schwiegerling, "Fundus camera systems: a comparative analysis," *Appl. Opt.*, vol. 48, no. 2, pp. 221–228, 2009.

[50] E. DeHoog and J. Schwiegerling, "Optimal parameters for retinal illumination and imaging in fundus cameras," *Appl. Opt.*, vol. 47, no. 36, pp. 6769–6777, 2008.

[51] B. Dobbin, "Kodak engineer had revolutionary idea: the first digital camera.," *Seattle Post-Intelligencer*, Sep-2005.

[52] N. Panwar *et al.*, "Fundus Photography in the 21st Century—A Review of Recent Technological Advances and Their Implications for Worldwide Healthcare," *Telemedicine and e-Health*, vol. 22, pp. 198–208, Aug-2015.

[53] C. Zimmer, D. Kahn, R. Clayton, P. Dugel, and K. B. Freund, "Innovation in Diagnostic Retinal Imaging: Multispectral Imaging," *Retin. Today*, pp. 94–99, 2014.

[54] F. C. Delori and K. P. Pflibsen, "Spectral reflectance of the human ocular fundus," *Appl. Opt.*, vol. 28, no. 6, pp. 1061–1077, 1989.

[55] J. Cuba and F. Gómez-Ulla, "Fundus autofluorescence : Applications and perspectives," *Arch. Soc. Esp. Oftalmol.*, vol. 8, no. 2, pp. 50–55, 2013.

[56] F. Fercher, W. Drexler, C. K. Hitzenberger, and T. Lasser, "Optical coherence tomography - principles and applications," *Reports Prog. Phys.*, vol. 66, no. 2, p. 239, 2003.

[57] W. Drexler and J. G. Fujimoto, "State-of-the-art retinal optical coherence tomography," *Prog. Retin. Eye Res.*, vol. 27, no. 1, pp. 45–88, 2008.

[58] R. H. Webb and G. W. Hughes, "Scanning laser ophthalmoscope.," *IEEE Trans. Biomed. Eng.*, vol. 28, no. 7, pp. 488–492, 1981.

[59] T. Bennett, "Scanning Laser Ophthalmoscopy." [Online]. Available: https://www.opsweb.org/page/SLO. [Accessed: 01-Jun-2017].

[60] A. Roorda, F. Romero-Borja, W. Donnelly, H. Queener, T. Hebert, and M. Campbell, "Adaptive optics scanning laser ophthalmoscopy.," *Opt. Express*, vol. 10, no. 9, pp. 405–412, 2002.

[61] A. Roorda, "Adaptive optics ophthalmoscopy.," *Annu. Rev. Vis. Sci.*, vol. 1, no. Sec 3, pp. 19–50, 2000.

[62] A. E. Elsner *et al.*, “Multiply scattered light tomography and confocal imaging: detecting neovascularization in age-related macular degeneration.,” *Opt. Express*, vol. 7, no. 2, pp. 95–106, 2000.

[63] F. Reinholz, R. A. Ashman, and R. H. Eikelboom, “Simultaneous three wavelength imaging with a scanning laser ophthalmoscope,” *Cytometry*, vol. 37, no. 3, pp. 165–170, 1999.

[64] P. Vieira, A. Manivannan, C. S. Lim, P. Sharp, and J. V Forrester, “Tomographic reconstruction of the retina using a confocal scanning laser ophthalmoscope,” *Physiol Meas.*, vol. 20, no. 0967–3334, pp. 1–19, 1999.

[65] A. E. Elsner, S. A. Burns, J. J. Weiter, and F. C. Delori, “Infrared imaging of sub-retinal structures in the human ocular fundus.,” *Vis. Res*, vol. 36, no. 1, pp. 191–205, 1996.

[66] P. Hansell and E. J. G. Beeson, “Retinal photography in colour,” *Brit. J. Ophthal.*, vol. 37, no. 65., pp. 65–69, 1953.

[67] D. D. Donaldson, “A New Camera for Stereoscopic Fundus Photography,” *Trans. Am. Ophthalmol. Soc.*, vol. 62, pp. 429–458, 1964.

[68] T. J. Bennett and C. J. Barry, “Ophthalmic imaging today: An ophthalmic photographer’s viewpoint - A review,” *Clin. Exp. Ophthalmol.*, vol. 37, no. 1, pp. 2–13, 2009.

[69] D. Sliney *et al.*, “Adjustment of guidelines for exposure of the eye to optical radiation from ocular instruments: statement from a task group of the International Commission on Non-Ionizing Radiation Protection (ICNIRP),” *Appl. Opt.*, vol. 44, no. 11, pp. 2162–2176, 2005.

[70] O. Pomerantzeff, R. H. Webb, and F. C. Delori, “Image formation in fundus cameras,” *Investig. Ophthalmol. Vis. Sci.*, vol. 18, no. 6, pp. 630–637, 1979.

[71] ISO 10940:2009, *Ophthalmic instruments—fundus cameras*. International Organization for Standardization, 2009.

[72] ISO 15004-2:2007, *Ophthalmic instruments—fundamental requirements and test methods—part 2: light hazard protection*. International Organization for Standardization, 2007.

[73] F. C. Delori, R. H. Webb, and D. H. Sliney, “Maximum permissible exposures for ocular safety (ANSI 2000), with emphasis on ophthalmic devices.,” *J. Opt. Soc. Am. A. Opt. Image Sci. Vis.*, vol. 24, no. 5, pp. 1250–1265, 2007.

[74] E. A. Boettner and J. R. Wolter, “Transmission of the Ocular Media,” *Invest. Ophthalmol. Vis. Sci.*, vol. 1, no. 6, pp. 776–783, 1962.

[75] T. J. M. Berendschot, P. J. DeLintb, and D. V Norren, “Fundus reflectance—historical and present ideas,” *Prog. Retin. Eye Res.*, vol. 22, no. 2, pp. 171–200, 2003.

[76] J.-M. Gorrand, “Separation of the reflection by the inner limiting membrane,” *Ophthalmic Physiol. Opt.*, vol. 6, no. 2, pp. 187–196, 1984.

[77] R. W. Knighton, S. G. Jacobson, and C. M. Kemp, “The spectral reflectance of the nerve fiber layer in macaque reina.,” *J. Glaucoma*, vol. 30, no. 11, pp. 2389-, 1989.

[78] R. W. Knighton and C. Qian, “An Optical Model of the Human Retinal Nerver Fiber Layer: Implications of Directional Reflectance for Variability of Clinical Measurements,” *Journal of Glaucoma*, vol. 9. pp. 56–62, 2000.

[79] T. Kubena, M. Kofronova, and P. Cernosek, “Nerve Fiber Layer Defects Imaging in Glaucoma,” in *The Mystery of Glaucoma*, 1st ed., Dr. Tomas Kubena, Ed. InTech Europe, 2011.

[80] W. S. Stiles, “The Luminous Efficiency of Monochromatic Rays Entering the Eye Pupil at Different Points and a New Colour Effect,” *Proc. R. Soc. B Biol. Sci.*, vol. 123, no. 830, pp. 90–118, 1937.

[81] J. M. Gorrand and F. Delori, “A reflectometric technique for assessing photoreceptor alignment,” *Vision Res.*, vol. 35, no. 7, pp. 999–1010, 1995.

[82] G. J. Van Blokland, “Directionality and alignment of the foveal receptors, assessed with light scattered from the human fundus in vivo,” *Vision Res.*, vol. 26, no. 3, pp. 495–500, 1986.

[83] S. A. Burns, S. Wu, F. Delori, and a E. Elsner, “Direct measurement of human-cone-photoreceptor alignment,” *ournal Opt. Soc. Am. A*, vol. 12, no. 10, pp. 2329–2338, 1995.

[84] N. P. A. Zagers, J. van de Kraats, T. T. J. M. Berendschot, and D. van Norren, “Simultaneous measurement of foveal spectral reflectance and cone-photoreceptor directionality,” *Appl. Opt.*, vol. 41, no. 22, pp. 4686–4696, 2002.

[85] W. A. H. Rushton and G. H. Henry, “Bleaching and regeneration of cone pigments in man,” *Vision Res.*, vol. 8, no. 6, pp. 617–631, 1968.

[86] O. Strauss, “The Retinal Pigment Epithelium in Visual Function,” *Physiol. Rev.*, vol. 85, pp. 845–881, 2005.

[87] J. T. Landrum and R. Bone, “Lutein, zeaxanthin, and the macular pigment.,” *Arch. Biochem. Biophys.*, vol. 385, no. 1, pp. 28–40, 2001.

[88] J. R. Sparrow, K. Nakanishi, and C. A. Parish, “The Lipofuscin Fluorophore A2E Mediates Blue Light– Induced Damage to Retinal Pigmented Epithelial Cells,” *Invest. Ophthalmol. Vis. Sci.*, vol. 41, no. 7, pp. 1981–1989, 2000.

[89] R. A. Bone, J. T. Landrum, L. H. Guerra, and C. A. Ruiz, “Lutein and Zeaxanthin Dietary Supplements Raise Macular Pigment Density and Serum Concentrations of these Carotenoids in Humans,” *Biochem. Mol. Actions Nutr. Lutein*, vol. 133, no. 1953, pp. 992–999, 2003.

[90] B. R. Hammond and C.-A. Mary, “Macular Pigment Optical Density in a Southwestern sample,” *Invest. Ophthalmol. Vis. Sci.*, vol. 41, no. 6, pp. 1492–1497, 2000.

[91] V. C. Lima, R. B. Rosen, and M. Farah, “Macular pigment in retinal health and disease,” *Int. J. Retin. Vitr.*, vol. 2, no. 1, p. 19, 2016.

[92] R. A. Weale, “From the Department of Physiological Optics , Institute of,” *J. Physiol.*, pp. 175–186, 1966.

[93] C. J. Kennedy, P. E. Rakoczy, and I. J. Constable, “Lipofuscin of the retinal pigment epithelium: A review,” *Eye*, vol. 9, no. 6, pp. 763–771, 1995.

[94] C. Delori, D. G. Goger, and C. K. Dorey, “Age-Related Accumulation and Spatial Distribution of Lipofuscin in RPE of Normal Subjects Franc,” *IOVS*, vol. 42, no. 8, 2001.

[95] J. R. Sparrow and M. Boulton, “RPE lipofuscin and its role in retinal pathobiology,” *Exp. Eye Res.*, vol. 80, pp. 595–606, 2005.

[96] J. J. Reinboth, K. Gautschi, K. Munz, G. E. Eldred, and C. E. Remè, “Lipofuscin in the Retina : Quantitative Assay for an Unprecedented Autofluorescent Compound (Pyridinium Bis-Retinoid , A2-E) of Ocular Age Pigment,” *Exp. Eye Res.*, vol. 65, pp. 639–643, 1997.

[97] J. J. Weiter, F. C. Delori, L. W. Glenn, and K. A. Fitch, “Retinal Pigment Epithelial Lipofuscin and Melanin and Choroidal Melanin in Human Eyes,” *Invest. Ophthalmol. Vis. Sci.*, pp. 145–152, 1984.

[98] K. A. Firn, B. Khoobehi, and S. C. Ave, “Novel , Noninvasive Multispectral Snapshot Imaging System to Measure and Map the Distribution of Human Retinal Vessel and Tissue Hemoglobin Oxygen Saturation,” *Int. J. Ophthalmic Res.*, vol. 1, no. 2, pp. 48–58, 2015.

[99] D. J. Mordant *et al.*, “Spectral imaging of the retina.,” *Eye (Lond).*, vol. 25, no. 3, pp. 309–20, 2011.

[100] C. Regillo, T. Chang, and M. Johnson, “Retina and vitreous,” in *Basic and Clinical Science Course*, Revised ed., American Academy of Ophthalmology, 2011, p. 424.

[101] J. Salmon, *Kanski’s Clinical Ophthalmology*, 9th ed., vol. 69, no. 2. Elsevier, 2019.

[102] M. Yanoff and J. W. Sassani, “Optic Nerve,” in *Ocular Pathology*, 7th ed., London: W.B. Saunders, 2015, pp. 441–465.

[103] J. Gloster and D. G. Parry, “Use of photographs for measuring cupping in the optic disc,” *Br. J. Ophthalmol.*, vol. 58, no. 10, pp. 850–862, 1974.

[104] X. R. Huang, Y. Zhou, R. W. Knighton, W. Kong, and W. J. Feuer, “Wavelength-dependent change of retinal nerve fiber layer reflectance in glaucomatous retinas,” *Investig. Ophthalmol. Vis. Sci.*, vol. 53, no. 9, pp. 5869–5876, 2012.

[105] A. Tuulonen, P. J. Airaksinen, A. Montagna, and H. Nieminen, “Screening for glaucoma with a non-mydriatic fundus camera,” *Acta Ophthalmol.*, vol. 68, no. 4, pp. 445–449, 1990.

[106] H. R. Coleman, C.-C. Chan, F. L. 3rd Ferris, and E. Y. Chew, “Age-related macular degeneration,” *Lancet*, vol. 372, no. 9652, pp. 1835–1845, Nov. 2008.

[107] A. Ly, L. Nivison-smith, N. Assaad, and M. Kalloniatis, “Infrared reflectance imaging in age-related macular degeneration,” vol. 36, no. 2016, pp. 303–316, 2017.

[108] A. Abdelsalam, L. Del Priore, and M. A. Zarbin, “Drusen in age-related macular degeneration: pathogenesis, natural course, and laser photocoagulation-induced regression.,” *Surv. Ophthalmol.*, vol. 44, no. 1, pp. 1–29, 1999.

[109] D. J. Taylor, N. D. Smith, A. M. Binns, and D. P. Crabb, “The effect of non-neovascular age-related macular degeneration on face recognition performance,” *Graefe’s Arch. Clin. Exp. Ophthalmol.*, vol. 256, no. 4, pp. 815–821, Apr. 2018.

[110] S. B. ManojKumar, R. Manjunath, and H. S. Sheshadri, “Feature extraction from the fundus images for the diagnosis of Diabetic Retinopathy,” in *International Conference on Emerging Research in Electronics, Computer Science and Technology*, 2015, pp. 240–245.

[111] P. Bartczak, P. Falt, and M. Hauta-Kasari, “Applicability of LED-Based Light Sources for Diabetic Retinopathy Detection in Retinal Imaging,” *2016 IEEE 29th Int. Symp. Comput. Med. Syst.*, pp. 355–360, 2016.

[112] D. Schweitzer, C. Schrödel, A. Jütte, F. Blaschke, E. Königsdörffer, and W. Vilser, “Reflectance spectrophotometry in the human ocular fundus,” *Graefe’s Arch. Clin. Exp. Ophthalmol.*, vol. 223, no. 4, pp. 207–210, 1985.

[113] I. Y. Wong, H. Koizumi, and W. W. Lai, “Enhanced depth imaging optical coherence tomography.,” *Ophthalmic surgery, lasers & imaging*, vol. 42, pp. S75-84, Jul. 2011.

[114] J. P. Ehlers, “The OCT Angiography Revolution: Five Emerging Themes.,” *Ophthalmol. Retin.*, vol. 1, no. 6, pp. 457–460, 2017.

[115] R. F. Spaide, J. G. Fujimoto, and N. K. Waheed, “Image artifacts in optical coherence tomography angiography,” *Retina*, vol. 35, no. 11, pp. 2163–2180, 2015.

[116] F. Semeraro *et al.*, “Central Serous Chorioretinopathy: Pathogenesis and Management.,” *Clin. Ophthalmol.*, vol. 13, pp. 2341–2352, 2019.

[117] R. S. Moorthy, H. Inomata, and N. A. Rao, “Vogt-Koyanagi-Harada syndrome.,” *Surv. Ophthalmol.*, vol. 39, no. 4, pp. 265–292, 1995.

[118] C. L. Shields *et al.*, “Choroidal nevus transformation into melanoma: analysis of 2514 consecutive cases.,” *Arch. Ophthalmol.*, vol. 127, no. 8, pp. 981–987, 2009.

[119] V. L. L. Torres, N. Brugnoni, P. K. Kaiser, and A. D. Singh, “Optical Coherence Tomography Enhanced Depth Imaging of Choroidal Tumors,” *Am. J. Ophthalmol.*, vol. 151, no. 4, pp. 586–593, 2011.

[120] C. Riva, “New ocular fundus reflectometer,” *Appl. Opt.*, vol. 11, no. 8, pp. 1845–9, 1972.

[121] M. Hammer, “Imaging spectroscopy of the human ocular fundus in vivo,” *J. Biomed. Opt.*, vol. 2, no. 4, pp. 418–425, 1997.

[122] S. Li *et al.*, “In vivo study of retinal transmission function in different sections of the choroidal structure using multispectral imaging,” *Investig. Ophthalmol. Vis. Sci.*, vol. 56, no. 6, pp. 3731–3742, 2015.

[123] G. Y. Li, S. Al-Wesabi, and H. Zhang, “Retinal and choroidal oxygen saturation of the optic nerve head in open-angle glaucoma subjects by multispectral imaging,” *Medicine (Baltimore).*, vol. 95, no. 52, 2016.

[124] J. Lin *et al.*, “Groupwise registration of sequential images from multispectral imaging (MSI) of the retina and choroid,” *Opt. Express*, vol. 24, no. 22, p. 25277, 2016.

[125] L. Li, P. Zhang, H. Liu, Y.-H. Liu, and L. Gao, “Evaluation of Multispectral Imaging in Diagnosing Diabetic Retinopathy,” *Retina*, p. 1, 2018.

[126] J. Lian *et al.*, “Measuring Spectral Inconsistency of Multispectral Images for Detection and Segmentation of Retinal Degenerative Changes,” *Sci. Rep.*, vol. 7, no. 1, pp. 1–8, 2017.

[127] C. E. Pang, Y. Suqin, J. Sherman, and K. B. Freund, “New insights into stargardt disease with multimodal imaging,” *Ophthalmic Surg. Lasers Imaging Retin.*, vol. 46, no. 2, pp. 257–261, 2015.

[128] L. Feng, G. L. Fan, J. Zhang, X. Wang, and J. Zhu, “Retinal and choroidal abnormalities identified by multispectral imaging in patients with uveitis: Three case reports,” *Medicine (Baltimore).*, vol. 98, no. 20, p. 15655, 2019.

[129] J. Zhang, Y. B. Chen, Z. K. Yu, and L. Liu, “Multispectral imaging in detecting early retinal pigment epithelial atrophy,” *Int. J. Ophthalmol.*, vol. 11, no. 6, pp. 1071–1074, 2018.

[130] J. Lian, Y. Zheng, W. Jiao, F. Yan, and B. Zhao, “Deblurring sequential ocular images from multi-spectral imaging (MSI) via mutual information,” *Med. Biol. Eng. Comput.*, vol. 56, no. 6, pp. 1107–1113, 2018.

[131] M. Tocci, “How to model the human eye in OpticStudio,” *Zemax Knowledgebase*, 2007. [Online]. Available: https://customers.zemax.com/os/resources/learn/knowledgebase/how-to-model-the-human-eye-in-zemax. [Accessed: 15-Jan-2021].

[132] A. Ly, L. Nivison-Smith, N. Assaad, and M. Kalloniatis, “Infrared reflectance imaging in age-related macular degeneration.,” *Ophthalmic Physiol. Opt.*, vol. 36, no. 3, pp. 303–16, 2016.

[133] “Thorlabs Gmbh Webpage.” [Online]. Available: https://www.thorlabs.com/index.cfm. [Accessed: 05-Jan-2021].

[134] M. Y. B. Daniel Salo, David Kim, Qian Cao, “Multispectral imaging/deep tissue imaging: extended near-infrared: a new window on in vivo bioimaging,” *BioOpt. World*, vol. 7, pp. 22–25, 2014.

[135] J. B. Jonas, W. M. Budde, and S. Panda-Jonas, “Ophthalmoscopic Evaluation of the Optic Nerve Head,” *Surv. Ophthalmol.*, vol. 43, no. 4, pp. 293–320, Jan. 1999.

[136] J. J. Shelke, A. R. , Roscoe, J. A. , Morrow, G. R. , Colman, L. K. , Banerjee, T. K. , & Kirshner, “Optic Disk Size and Glaucoma,” *Bone*, vol. 23, no. 1, pp. 1–7, 2008.

[137] J. R. H. Kumar, C. S. Seelamantula, Y. S. Kamath, and R. Jampala, “Rim-to-Disc Ratio Outperforms Cup-to-Disc Ratio for Glaucoma Prescreening,” *Sci. Rep.*, vol. 9, no. 1, pp. 1–9, 2019.

[138] C. D. Hanning and J. M. Alexander-Williams, “Pulse oximetry: A practical review,” *Bmj*, vol. 311, no. 7001, p. 367, 1995.

[139] M. Hammer, E. Thamm, and D. Schweitzer, “A simple algorithm for in vivo ocular fundus oximetry compensating for non-haemoglobin absorption and scattering.,” *Phys. Med. Biol.*, vol. 47, no. 17, pp. N233-8, 2002.

[140] R. Poplin *et al.*, “Prediction of cardiovascular risk factors from retinal fundus photographs via deep learning,” *Nat. Biomed. Eng.*, vol. 2, no. 3, pp. 158–164, 2018.

[141] K. Zhang, D. C. Garibaldi, Y. Li, W. R. Green, and D. J. Zack, “Butterfly-Shaped Pattern Dystrophy: A Genetic, Clinical, and Histopathological Report,” *Arch. Ophthalmol.*, vol. 120, no. 4, pp. 485–490, 2002.

[142] R. J. Talbert, S. H. Holan, and J. A. Viator, “Photoacoustic discrimination of viable and thermally coagulated blood using a two-wavelength method for burn injury monitoring,” *Phys. Med. Biol.*, vol. 52, no. 7, pp. 1815–1829, 2007.

[143] S. M. Waldstein *et al.*, “Comparison of penetration depth in choroidal imaging using swept source vs spectral domain optical coherence tomography,” *Eye*, vol. 29, no. 3, pp. 409–415, 2015.

[144] M. Esmaeelpour *et al.*, “Three-Dimensional 1060-nm OCT: Choroidal Thickness Maps in Normal Subjects and Improved Posterior Segment Visualization in Cataract Patients,” *Invest. Ophthalmol. Vis. Sci.*, vol. 51, no. 10, pp. 5260–5266, 2010.

[145] T. Alterini, F. Díaz-Doutón, F. J. Burgos-Fernández, L. González, C. Mateo, and M. Vilaseca, “Fast visible and extended near-infrared multispectral fundus camera,” *J. Biomed. Opt.*, vol. 24, no. 9, pp. 1–7, 2019.

[146] M. Rudolf, M. E. Clark, M. F. Chimento, C. M. Li, N. E. Medeiros, and C. A. Curcio, “Prevalence and morphology of druse types in the macula and periphery of eyes with age-related maculopathy,” *Investig. Ophthalmol. Vis. Sci.*, vol. 49, no. 3, pp. 1200–1209, 2008.

[147] A. von Rückmann, F. W. Fitzke, and A. C. Bird, “Distribution of fundus autofluorescence with a scanning laser ophthalmoscope.,” *Br. J. Ophthalmol.*, vol. 79, no. 5, pp. 407–412, May 1995.

[148] C. J. F. Boon, B. Jeroen Klevering, J. E. E. Keunen, C. B. Hoyng, and T. Theelen, “Fundus autofluorescence imaging of retinal dystrophies,” *Vision Res.*, vol. 48, no. 26, pp. 2569–2577, 2008.

[149] N. Lee *et al.*, “In vivo snapshot hyperspectral image analysis of age-related macular degeneration,” *IEEE Eng. Med. Biol. Soc. Annu. Int. Conf.*, vol. 2010, pp. 5363–5366, 2010.

[150] V. Purvin, R. King, A. Kawasaki, and R. Yee, “Anterior ischemic optic neuropathy in eyes with optic disc drusen.,” *Arch. Ophthalmol.*, vol. 122, no. 1, pp. 48–53, Jan. 2004.

[151] A. Chang and M. Flaherty, “Disc drusen: a headache for child and clinician,” *Aust. N. Z. J. Ophthalmol.*, vol. 24, no. 4, pp. 381–384, 1996.

[152] A. H. Friedman, S. Gartner, and S. S. Modi, “Drusen of the optic disc. A retrospective study in cadaver eyes.,” *Br. J. Ophthalmol.*, vol. 59, no. 8, pp. 413–421, Aug. 1975.

[153] M. K. Erol, D. T. Coban, B. B. Ceran, and M. Bulut, “Enhanced depth imaging optical coherence tomography and fundus autofluorescence findings in bilateral choroidal osteoma: a case report,” *Arq. Bras. Oftalmol.*, vol. 76, no. 3, pp. 189–191, 2013.

[154] T. Sato, S. Mrejen, and R. F. Spaide, “Multimodal imaging of optic disc drusen.,” *Am. J. Ophthalmol.*, vol. 156, no. 2, pp. 275-282.e1, 2013.

[155] Sowka Joseph Gurwood Andrew Kabat Alan, “Optic Nerve Head Drusen,” in *Handbook of Ocular Disease Management*, 19th ed., Jobson Publishing L.L.C., 2018.

[156] S. Hamann, L. Malmqvist, and F. Costello, “Optic disc drusen: understanding an old problem from a new perspective,” *Acta Ophthalmol.*, vol. 96, no. 7, pp. 673–684, 2018.

[157] C. Calvo-González *et al.*, “Optic nerve drusen and deep visual fields defects,” *Arch. Soc. Esp. Oftalmol.*, vol. 81, no. 5, pp. 269–273, May 2006.

[158] R. N. Weinreb, T. Aung, and F. A. Medeiros, “The Pathophysiology and Treatment of Glaucoma: A Review,” *JAMA*, vol. 311, no. 18, pp. 1901–1911, 2014.

[159] A. D. Singh, P. Kalyani, and A. Topham, “Estimating the risk of malignant transformation of a choroidal nevus,” *Ophthalmology*, vol. 112, no. 10, pp. 1784–1789, 2005.

[160] T. Kivelä and S. Eskelin, “Transformation of nevus to melanoma.,” *Ophthalmology*, vol. 113, no. 5. United States, pp. 887–8.e1, May-2006.

[161] X. Delpueyo *et al.*, “Multispectral imaging system based on light-emitting diodes for the detection of melanomas and basal cell carcinomas: a pilot study,” *J. Biomed. Opt.*, vol. 22, no. 6, pp. 1–9, 2017.

[162] N. A. Vallabh, J. N. Sahni, C. K. Parkes, G. Czanner, H. Heimann, and B. Damato, “Near-infrared reflectance and autofluorescence imaging characteristics of choroidal nevi,” *Eye*, vol. 30, no. 12, pp. 1593–1597, 2016.

[163] C. Framme, R. Brinkmann, R. Birngruber, and J. Roider, “Autofluorescence imaging after selective RPE laser treatment in macular diseases and clinical outcome: a pilot study,” *Br. J. Ophthalmol.*, vol. 86, no. 10, pp. 1099–1106, 2002.

ACKNOWLEDGMENTS

Never have we felt like citizens of the world, as today.

We could study and grow with infinite possibilities and resources for our future. Then, an unprecedented global pandemic hit us. When this crisis will be over, we will have an opportunity that few generations have had, that of rebuilding. For this, it is necessary to immediately recognize our mistakes and commit ourselves to a wiser, more responsible, and united world.

Personally, the possibility of doing the PhD program in Catalonia allowed me to mature, making me overcome many prejudices and fears. For this, I would like to thank the European Commission which funded my PhD and continues to make this incredible cultural exchange possible.

I am infinitely grateful to my precious supervisors, Prof. Dr. Meritxell Vilaseca Ricart and Dr. Fernando Díaz Doutón. You have been my guides and my teachers. Thanks to your intelligence and patience, you have always been able to give me the help and support I needed. It was an honor and a fortune to have you with me on this journey.

I thank all the members of the European Be-Optical Project, the whole color and vision group, all the CD6 and the PhD students for the advice, discussions and moments of fun.

Thanks to the staff of the Institute of Ocular Microsurgery of Barcelona, ophthalmologist Dr. Carlos Mateo and optometrist Laura González for all the support during the clinical trial.

Thanks to Prof. Dr. Jaume Pujol, Dr. Clara Mestre and Dr. Francisco Javier Burgos Fernández for all the help in the testing phase and for the always productive discussions.

Thanks to Fermín Alarcón, Xavier Murcia, Cristina Cusidó and Julia Sebastián without whom this project would have been impossible.

I wish all the best to former students Laura, Natalia and Astrid. Thanks for your invaluable help.

I sincerely thank my friends Jesus and Pau who immediately made me feel part of the city.

A special hug to Alessandro, alias Sardo, for being one of the people closest to me in all aspects of life.

A hug to all the friends of Barcelona Giulio, Berta, Anna, Andrea, Walter and Barbara for making me feel at home.

To Oriol, Marta, Jorge, Nina for all the affection and experiences shared together.

A special thanks goes to the colla Castellera de Sants for making me part of an incredible family.

Thanks to my family who never made me miss their closeness and affection.

Finally, with all my heart, I want to thank the best part of my life, Michela Ravera. Every day, you give me strength and courage and encourage me to be a better person.

Mai come oggi ci dobbiamo sentire cittadini del mondo.

Potevamo studiare e crescere con infinite possibilità e risorse per il nostro futuro. Poi, una pandemia globale senza precedenti ci ha colpiti. Quando questa crisi sarà giunta al termine, avremo un'opportunità che poche generazioni hanno avuto, quella di ricostruire. Per questo, è necessario fin da subito riconoscere i nostri errori e impegnarsi per un mondo più saggio, responsabile e unito.

Personalmente, la possibilità di fare il percorso di dottorato in Catalogna mi ha permesso di maturare, facendomi superare molti pregiudizi e paure. Per questo vorrei ringraziare la Commissione Europea che ha finanziato il mio dottorato e continua a rendere possibile questo incredibile scambio culturale.

Ringrazio infinitamente i miei preziosi supervisori, la Prof. Dr. Meritxell Vilaseca Ricart e il Dr. Fernando Díaz Doutón. Siete stati le mie guide e i miei insegnanti. Grazie alla vostra intelligenza e pazienza avete saputo sempre darmi l'aiuto e il sostegno di cui avevo bisogno. È stato un onore e una fortuna avervi con me in questo percorso.

Ringrazio tutti i membri del Progetto Europeo Be-Optical, tutto il gruppo di colore e visione, tutto il CD6 e la sala dottorandi per i consigli, le discussioni e i momenti di divertimento.

Grazie allo staff dell'Istituto di Microchirurgia Oculare di Barcelona, all'oftalmologo Dr. Carlos Mateo e l'optometrista Laura González per tutto il sostegno durante lo studio clinico.

Grazie al Prof. Dr. Jaume Pujol, la Dr. Clara Mestre e il Dr Francisco Javier Burgos Fernández per tutto l'aiuto in fase di test e per i confronti sempre produttivi.

Grazie a Fermín Alarcón, Xavier Murcia, Cristina Cusidó e Julia Sebastián senza i quali questo progetto non sarebbe stato possibile.

Auguro tutto il meglio alle ex-studentesse Laura, Natalia e Astrid. Grazie per il vostro prezioso aiuto.

Ringrazio di cuore gli amici Jesus e Pau che fin da subito mi hanno fatto sentire parte della città.

Un abbraccio speciale ad Alessandro, alias Sardo, per esser stato una delle persone a me più vicine in tutto e per tutto.

Un abbraccio a tutti gli amici di Barcelona Giulio, Berta, Andrea, Anna, Walter e Barbara per avermi fatto sentire a casa.

A Oriol, Marta, Jorge, Nina per tutto l'affetto e le esperienze condivise insieme.

Un ringraziamento speciale va alla colla Castellera de Sants per avermi fatto partecipe di una famiglia e un'esperienza unica al mondo.

Un ringraziamento alla mia famiglia che non mi ha fatto mai mancare la sua vicinanza e il suo affetto.

Infine, con tutto il cuore, voglio ringraziare la parte migliore della mia vita, Michela Ravera. Ogni giorno mi regali forza e coraggio e mi sproni ad essere una persona migliore.

Avui, més que mai, ens hem de sentir ciutadans del món.

Hem pogut estudiar i créixer amb possibilitats i recursos infinits per al nostre futur. Tot seguit, una pandèmia mundial sense precedents ens ha colpejat. Quan aquesta crisi haurà acabat, tindrem una oportunitat que poques generacions han tingut, la de reconstruir. Per això, és necessari reconèixer els nostres errors de forma immediata, i comprometre'ns a construir un món més savi, unit i responsable.

Personalment, la possibilitat de fer el doctorat a Catalunya m'ha permès madurar, fent-me superar molts prejudicis i pors. Per això, voldria agrair a la Comissió Europea que ha finançat la meva tesi, i que fa possible aquests increïbles intercanvis culturals.

Estic infinitament agraït als meus preuats supervisors, la Prof. Dra. Meritxell Vilaseca Ricart i el Dr. Fernando Díaz Doutón. Heu estat els meus guies i els meus mestres. Gràcies a la vostra intel·ligència i paciència, sempre heu estat capaços de proporcionar-me l'ajut i el suport que he necessitat. Ha estat un honor i una sort tenir-vos amb mi en aquest camí.

Agraeixo a tots els membres del projecte europeu Be-Optical, a tot el grup de color i visió, a tot el CD6 i a la sala de doctorands pels consells, les discussions i els moments de diversió.

Gràcies al personal de l'Institut de Microcirurgia Ocular de Barcelona, a l'oftalmòleg Dr. Carlos Mateo i a l'optometrista Laura González, per tot el suport durant l'assaig clínic.

Gràcies al Prof. Dr. Jaume Pujol, la Dra. Clara Mestre i al Dr. Francisco Javier Burgos Fernández, per tota l'ajuda durant la fase de proves i per les discussions sempre tan productives.

Gràcies a Fermín Alarcón, Xavier Murcia, Cristina Cusidó i Julia Sebastián, sense els quals aquest projecte no hagués estat possible.

Desitjo tot el millor a les ex alumnes Laura, Natalia i Astrid. Gràcies per la vostra inestimable ajuda.

Agraeixo sincerament als meus amics Jesús i Pau, que de seguida em van fer sentir part de la ciutat.

Una abraçada especial a l'Alessandro, àlies Sardo, per ser una de les persones més properes a mi, en tots els aspectes.

Una abraçada a tots els amics de Barcelona Giulio, Berta, Andrea, Anna, Walter i Barbara, per fer-me sentir com a casa.

A l'Oriol, la Marta, el Jorge i la Nina, per tot l'afecte i les experiències compartides.

Un agraïment especial als Castellers de Sants, per haver-me fet partícip d´una família i una experiència única al món.

Gràcies a la meva família, ja que no m'ha mancat mai el seu suport i la seva estima.

Finalment i de tot cor, vull donar les gràcies a la millor part de la meva vida, Michela Ravera. Cada dia em dones força i coratge i m'animes a ser millor persona.

Hoy más que nunca hay que sentirse ciudadanos del mundo.

Podíamos estudiar y crecer teniendo infinitas posibilidades y recursos para nuestro futuro. Entonces, una pandemia sin precedentes nos ha golpeado. En cuanto esta crisis llegue a su final tendremos una oportunidad que pocas generaciones han tenido, reconstruir. Por eso, es necesario reconocer nuestros errores y comprometerse por un mundo más sabio, responsable y unido.
Personalmente, la posibilidad de llevar a cabo este doctorado en Cataluña me ha permitido crecer como persona, enfrentándome a mis prejuicios y miedos. Por ello deseo darle las gracias a la Comisión Europea por financiar mi doctorado y seguir haciendo que sea posible este increíble intercambio cultural.

Muchísimas gracias a mis preciados supervisores, la Prof. Dra. Meritxell Vilaseca Ricart y el Dr. Fernando Díaz Doutón. Habéis sido mis guías y mis profesores. Gracias a vuestra inteligencia y paciencia, sempre habéis sido capaces de proporcionarme la ayuda y el soporte que he necesitado. Ha sido un honor teneros a mi lado en este camino.

Quiero darle las gracias también a todos los miembros del proyecto europeo Be-Optical, al grupo de color y visión, al CD6 y a todos los estudiantes de doctorado por los consejos, las discusiones y los momentos de diversión.

Gracias al equipo del Instituto de Microcirugía Ocular de Barcelona, al oftalmólogo Dr. Carlos Mateo y a la optometrista Laura González por todo su apoyo durante el ensayo clínico.

Gracias al Prof. Dr. Jaume Pujol, la Dr. Clara Mestre y el Dr. Francisco Javier Burgos Fernández por su ayuda durante las pruebas y los debates siempre productivos.

Gracias a Fermín Alarcón, Xavier Murcia, Cristina Cusidó y Julia Sebastián, sin los que este proyecto no habría sido posible.

Deseo todo lo mejor a las antiguas estudiantes de máster; Laura, Natalia y Astrid. Gracias por vuestra inestimable ayuda.

Gracias de corazón a mis amigos Jesús y Pau, que desde el principio han hecho que me sintiese parte de esta ciudad única.

Un abrazo especial a Alessandro, alias Sardo, por haber sido una de las personas más cercanas a mí en todos los aspectos.

Un abrazo a todos los amigos de Barcelona: Giulio, Berta, Andrea, Anna, Walter y Barbara por hacer que me sintiera como en casa.
A Oriol, Marta, Jorge y Nina por todo el cariño y las experiencias que hemos vivido juntos.

Quiero hacer un agradecimiento especial a la colla de los Castellers de Sants por acogerme en su familia y por la increíble experiencia que he podido vivir con ellos.

Gracias a mi familia, jamás me ha faltado su amor y su apoyo.

Finalmente, con todo mi corazón, le doy las gracias a lo mejor que me pasó en la vida, Michela Ravera, por regalarme fuerza, valentía y por animarme a ser mejor persona día tras día.

APPENDIX A

Table A.1: CMOS camera specs.

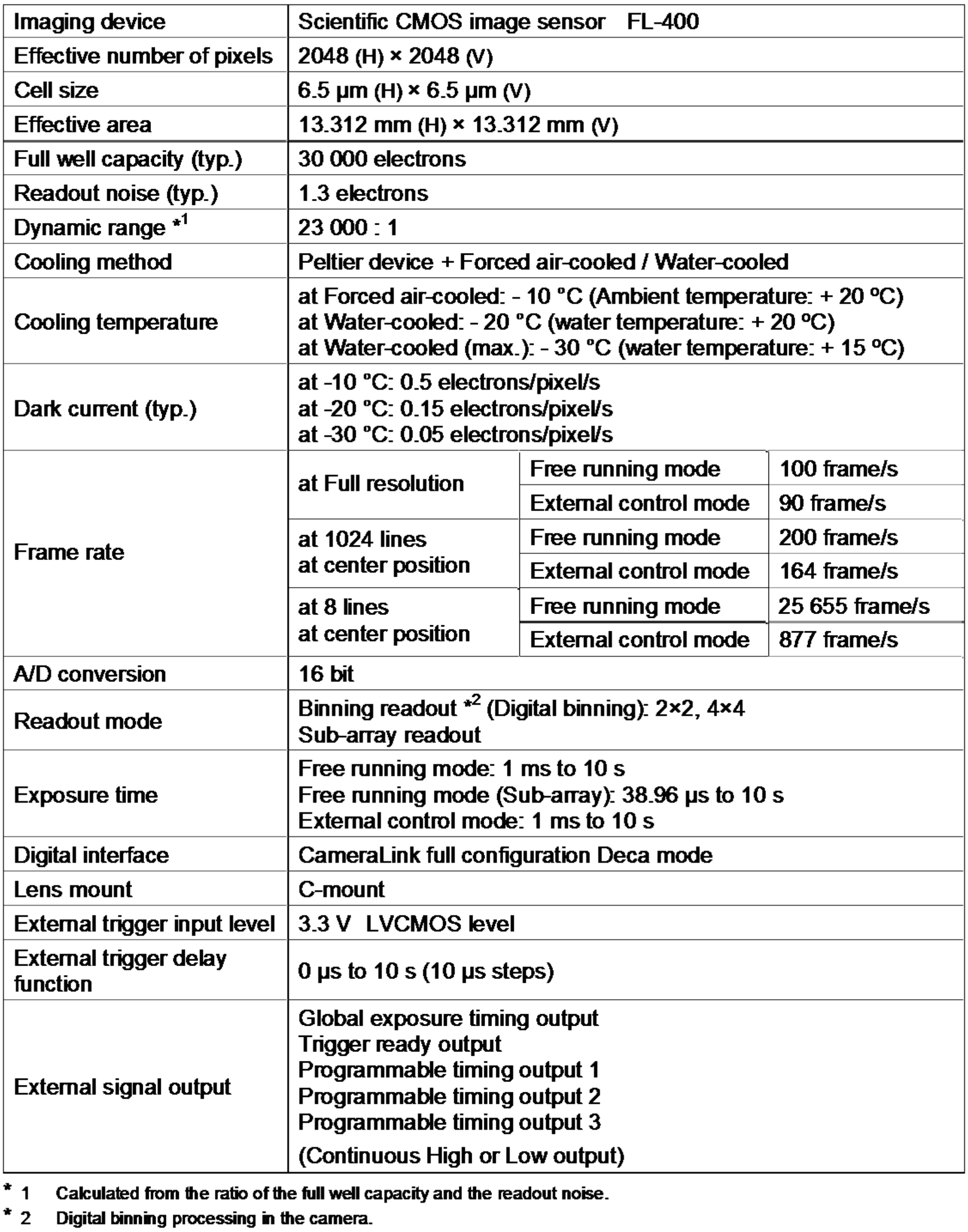

Imaging device	Scientific CMOS image sensor FL-400		
Effective number of pixels	2048 (H) × 2048 (V)		
Cell size	6.5 μm (H) × 6.5 μm (V)		
Effective area	13.312 mm (H) × 13.312 mm (V)		
Full well capacity (typ.)	30 000 electrons		
Readout noise (typ.)	1.3 electrons		
Dynamic range *[1]	23 000 : 1		
Cooling method	Peltier device + Forced air-cooled / Water-cooled		
Cooling temperature	at Forced air-cooled: - 10 °C (Ambient temperature: + 20 °C) at Water-cooled: - 20 °C (water temperature: + 20 °C) at Water-cooled (max.): - 30 °C (water temperature: + 15 °C)		
Dark current (typ.)	at -10 °C: 0.5 electrons/pixel/s at -20 °C: 0.15 electrons/pixel/s at -30 °C: 0.05 electrons/pixel/s		
Frame rate	at Full resolution	Free running mode	100 frame/s
		External control mode	90 frame/s
	at 1024 lines at center position	Free running mode	200 frame/s
		External control mode	164 frame/s
	at 8 lines at center position	Free running mode	25 655 frame/s
		External control mode	877 frame/s
A/D conversion	16 bit		
Readout mode	Binning readout *[2] (Digital binning): 2×2, 4×4 Sub-array readout		
Exposure time	Free running mode: 1 ms to 10 s Free running mode (Sub-array): 38.96 μs to 10 s External control mode: 1 ms to 10 s		
Digital interface	CameraLink full configuration Deca mode		
Lens mount	C-mount		
External trigger input level	3.3 V LVCMOS level		
External trigger delay function	0 μs to 10 s (10 μs steps)		
External signal output	Global exposure timing output Trigger ready output Programmable timing output 1 Programmable timing output 2 Programmable timing output 3 (Continuous High or Low output)		

* 1 Calculated from the ratio of the full well capacity and the readout noise.

* 2 Digital binning processing in the camera.

Table A.2: InGaAs camera specs

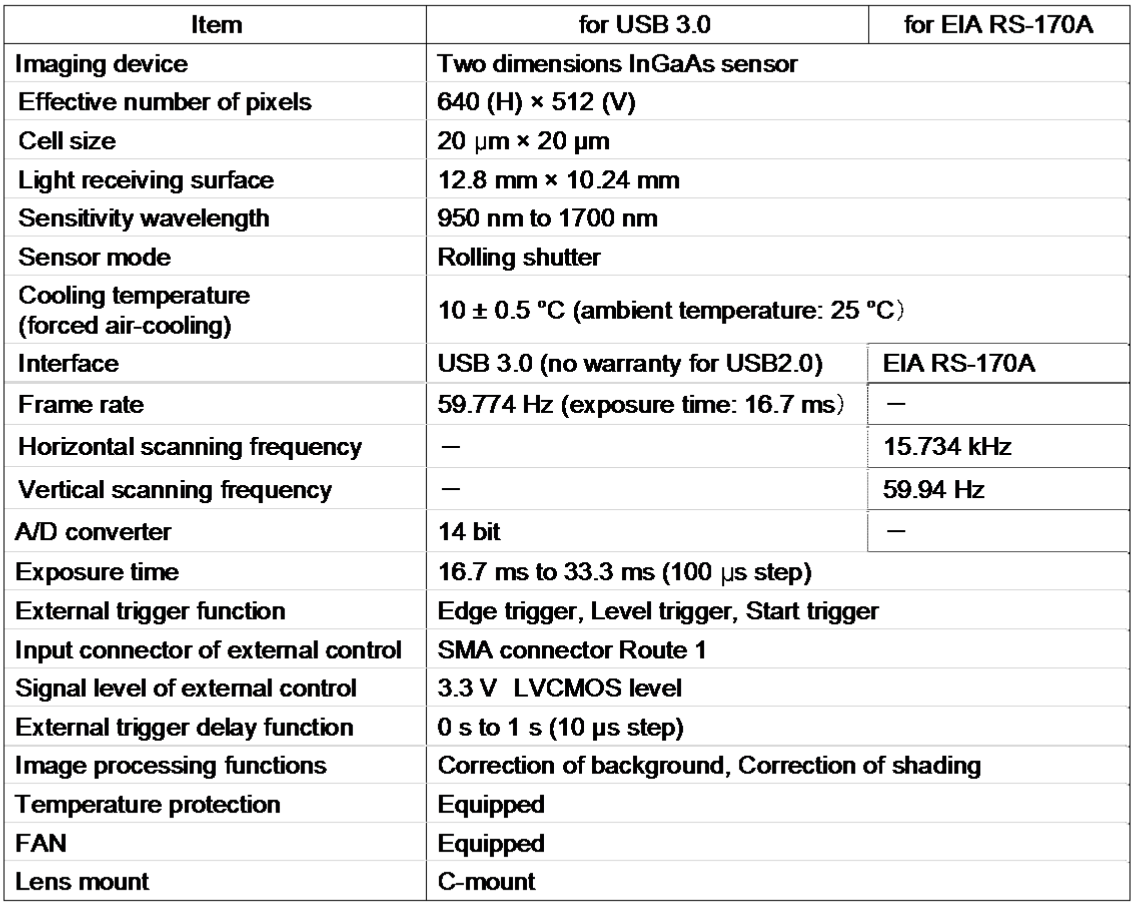

Item	for USB 3.0	for EIA RS-170A
Imaging device	Two dimensions InGaAs sensor	
Effective number of pixels	640 (H) × 512 (V)	
Cell size	20 μm × 20 μm	
Light receiving surface	12.8 mm × 10.24 mm	
Sensitivity wavelength	950 nm to 1700 nm	
Sensor mode	Rolling shutter	
Cooling temperature (forced air-cooling)	10 ± 0.5 °C (ambient temperature: 25 °C）	
Interface	USB 3.0 (no warranty for USB2.0)	EIA RS-170A
Frame rate	59.774 Hz (exposure time: 16.7 ms）	—
Horizontal scanning frequency	—	15.734 kHz
Vertical scanning frequency	—	59.94 Hz
A/D converter	14 bit	—
Exposure time	16.7 ms to 33.3 ms (100 μs step)	
External trigger function	Edge trigger, Level trigger, Start trigger	
Input connector of external control	SMA connector Route 1	
Signal level of external control	3.3 V LVCMOS level	
External trigger delay function	0 s to 1 s (10 μs step)	
Image processing functions	Correction of background, Correction of shading	
Temperature protection	Equipped	
FAN	Equipped	
Lens mount	C-mount	

APPENDIX B

Table B.1 Details of the components of the set-up (Figure 3.10) with references and descriptions.

Component	Manufacturer	Reference	Description
1	Custom made	-	LED aluminum cage
2 a	Custom made	VIS ring	Visible illumination ring
2 b	Custom made	NIR ring	Near InfraRed illumination ring
2 c	Custom made	IR ring	InfraRed illumination ring
3	EDMUND	86-697	Short-pass filter, 25x36 mm, cut-off wavelength 1100 nm
4	EDMUND	64-449	Cold mirror, 30x30 mm, cut-off wavelength 730 nm
5 a, b	EDMUND	49-390	50mm Dia. x 100mm FL, VIS-NIR Coated, Achromatic Lens
6	THORLABS	ID50/M	Mounted Standard Iris, Ø50 mm Max Aperture, TR75/M Post
7	2CI	-	Plastic printed binary mask
8	Custom made	-	Fixation target
9	EDMUND	01-914-522	2" Dia. Protected Aluminum, λ/10 Flat Fused Silica
10	Custom made	-	Methacrylate optical window
11	EDMUND	49-371	30mm Dia. x 50mm FL, VIS-NIR Coated, Achromatic Lens
12	EDMUND	49-389	50mm Dia. x 75mm FL, VIS-NIR Coated, Achromatic Lens
13	ALTECHNA	-	25.4 mm diameter, protected aluminum holed mirror
14	EDMUND	67-422	25 x 50mm EFL Steinheil Triplet Achromatic Lens
15	THORLABS	DMLP950R	25 mm x 36 mm Longpass Dichroic Mirror 950 nm Cutoff
16	EDMUND	45-221	25mm Dia x -50mm FL Negative Doublet Lens MgF Coated
17	Custom made	-	VIS and NIR detection field diaphragm, 14 mm diameter
18 a	EDMUND	49-384	40mm Dia. x 250mm FL, VIS-NIR Coated, Achromatic Lens
18 b	EDMUND	63-725	40mm Dia. x 100mm FL, VIS-NIR Coated, Achromatic Lens
19	Custom made	-	Aluminum optical platform
20	Custom made	-	VIS and NIR detection aperture diaphragm, 7 mm diameter
21	Hamamatsu	C11440-22C	CMOS camera
22	Custom made	-	NIR and IR detection field diaphragm, 11 mm diameter
23	THORLABS	PF20-03-M01	Ø2" (Ø50.8 mm) Protected Gold Mirror
24	EDMUND	55-282	25mm Travel, Metric Micrometer, Solid Top Ball Bearing Stage
25 a	THORLABS	AC254-125-C	f=125.0 mm Ø1" Achromatic Doublet ARC: 1050-1700 nm
25 b	THORLABS	AC254-075-C	f=75.0 mm Ø1" Achromatic Doublet ARC: 1050-1700 nm
26	Custom made	-	NIR and IR detection aperture diaphragm, 6 mm diameter

APPENDIX C

HOJA DE INFORMACIÓN AL PACIENTE Y CONSENTIMIENTO INFORMADO,

Modelo para pacientes con enfermedades o alteraciones retinianas

Estudio del fondo de ojo con un retinógrafo multiespectral para la detección de enfermedades de retina

Descripción

Usted está invitado a participar en un proyecto de investigación para comprobar la validez para uso clínico de una nueva técnica experimental. Ésta técnica consiste en analizar el fondo de ojo con una cámara multiespectral que registra fotografías del fondo de ojo a diferentes longitudes de onda (colores). El propósito de este estudio es comprobar si a partir de dichas imágenes se puede obtener información que queda escondida en las imágenes de color convencionales disponibles en la actualidad, y que puede ser relevante para el diagnóstico de enfermedades de retina.

Se realizarán medidas del fondo de ojo con una cámara multiespectral. Para las medidas usted deberá apoyar su barbilla en la mentonera de los instrumentos, fijando su vista en un test de fijación. Una vez el examinador ha alineado el instrumento con su ojo, se realizará la medida correspondiente. La duración de cada medida es de 1 minuto aproximadamente. Podrá parpadear normalmente. En ningún momento se realiza contacto con su ojo.

El objetivo es poder comparar estas imágenes con las imágenes de retinografía y OCT que se le hayan tomado dentro de la práctica habitual para el diagnóstico y seguimiento de la enfermedad.

Ninguna de las pruebas que le realicemos fuera de la práctica habitual le supondrán un gasto adicional.

El participar en este estudio le tomará aproximadamente *15 minutos.*

Riesgos y beneficios

Las medidas no son invasivas (no existe contacto con su ojo) y no representan ningún riesgo. El material utilizado ha sido diseñado para cumplir con un muy amplio margen la normativa Europea en materia de seguridad. Los beneficios esperados de esta investigación son mejorar el diagnóstico de patologías de retina.

Derechos

Si ha leído este documento y ha decidido participar, por favor entienda que su participación es voluntaria y que usted tiene derecho a abstenerse de participar o retirarse del estudio en cualquier momento, sin ninguna penalización. Tiene derecho a no contestar alguna pregunta en particular. También tiene derecho a recibir una copia de este documento.

Confidencialidad

Su participación en este estudio será tratada con total confidencialidad según lo dispuesto en el reglamento (UE) 2016/679 del Parlamento Europeo y del Consejo, de 27 de abril de 2016, relativo a la protección de las personas físicas en lo que respecta al tratamiento de datos personales y a la libre circulación de estos datos y por el que se deroga la Directiva 95/46/CE (Reglamento general de protección de datos*)

La cumplimentación y entrega de este documento implica su **consentimiento** para participar en este estudio.

Si tiene alguna pregunta o queja, por favor comuníquese ____________--TElf____________

______________________________ ____________________________ ______________________________

Nombre del paciente Firma Fecha

He discutido el contenido de esta Hoja de Consentimiento con el arriba firmante. Le he explicado los riesgos y beneficios del estudio.

______________________________ ____________________________ ______________________________

Nombre del investigador Firma Fecha

o persona designada

HOJA DE INFORMACIÓN AL PACIENTE Y CONSENTIMIENTO INFORMADO

Modelo para sujetos voluntarios sanos

Estudio del fondo de ojo con un retinógrafo multiespectral para la detección de enfermedades de retina

Descripción

Usted está invitado a participar en un proyecto de investigación para comprobar la validez para uso clínico de una nueva técnica experimental. Ésta técnica consiste en analizar el fondo de ojo con una cámara multiespectral que registra fotografías del fondo de ojo a diferentes longitudes de onda (colores). El propósito de este estudio es comprobar si a partir de dichas imágenes se puede obtener información que queda escondida en las imágenes de color convencionales disponibles en la actualidad, y que puede ser relevante para el diagnóstico de enfermedades de retina.

El objetivo es poder comparar estas imágenes con imágenes de retinografía y OCT , es por ello que le pedimos autorización para realizarle estas pruebas adicionales.

Se realizarán medidas del fondo de ojo con una cámara multiespectral.Para las medidas usted deberá apoyar su barbilla en la mentonera de los instrumentos, fijando su vista en un test de fijación. Una vez el examinador ha alineado el instrumento con su ojo, se realizará la medida correspondiente. La duración de cada medida es de 1 minuto aproximadamente. Podrá parpadear normalmente. En ningún momento se realiza contacto con su ojo.

Con el retinógrafo convencional y el OCT el paciente debe apoyar su barbilla en la mentonera del equipo, fijando su vista en un test de fijación. Una vez el examinador ha alineado el instrumento con su ojo, el equipo realizará la medida. La duración de cada medida es de 1 minuto aproximadamente. Podrá parpadear normalmente. En ningún momento se realiza contacto con su ojo . No será necesario dilatar la pupila.

Ninguna de las pruebas que le realicemos fuera de la práctica habitual le supondrán un gasto adicional.

El participar en este estudio le tomará aproximadamente *25 minutos.*

Riesgos y beneficios

Las medidas no son invasivas (no existe contacto con su ojo) y no representan ningún riesgo. El material utilizado ha sido diseñado para cumplir con un muy amplio margen la normativa Europea en materia de seguridad. Los beneficios esperados de esta investigación son mejorar el diagnóstico de patologías de retina.

Derechos

Si ha leído este documento y ha decidido participar, por favor entienda que su participación es voluntaria y que usted tiene derecho a abstenerse de participar o retirarse del estudio en cualquier momento, sin ninguna penalización. Tiene derecho a no contestar alguna pregunta en particular. También tiene derecho a recibir una copia de este documento.

Confidencialidad

Su participación en este estudio será tratada con total confidencialidad según lo dispuesto en el reglamento (UE) 2016/679 del Parlamento Europeo y del Consejo, de 27 de abril de 2016, relativo a la protección de las personas físicas en lo que respecta al tratamiento de datos personales y a la libre circulación de estos datos y por el que se deroga la Directiva 95/46/CE (Reglamento general de protección de datos*)

La cumplimentación y entrega de este documento implica su **consentimiento** para participar en este estudio.

Si tiene alguna pregunta o queja, por favor comuníquese con ______________telf____________

__________________________ _________________________ __________________________

Nombre del paciente Firma Fecha

He discutido el contenido de esta Hoja de Consentimiento con el arriba firmante. Le he explicado los riesgos y beneficios del estudio.

__________________________ _________________________ __________________________

Nombre del investigador Firma Fecha

o persona designada
